University of Oxford

Balliol College
Department of Chemistry
Bayley Group

Light-activated ATP synthesis in droplet networks

Matthew Cornall

A thesis submitted for the degree of
Doctor of Philosophy

Trinity Term 2022

Abstract

The fabrication of synthetic tissues that mimic the complex collective functionality of living tissues is the central objective of synthetic biology. A key step in this endeavour is the construction of an energy production system. Energised synthetic tissues could produce therapeutic oligonucleotides and proteins on demand, or transport substrates to modulate the behaviour of interfaced living tissues. This thesis describes the assembly of synthetic tissues with an encapsulated light-activated adenosine triphosphate (ATP) production system. The synthetic tissues comprised droplet networks, assemblies of aqueous droplets in a lipid-containing oil separated and stabilised by droplet interface bilayers (DIBs). Two membrane proteins were reconstituted into proteoliposomes to create a synthetic organelle able to generate ATP on demand: a modified light-activated proton pump, proteorhodopsin-mCherry and *E. coli* F_1F_O ATP synthase. An ATP synthesis rate of 53.2 nmol ATP.min^{-1}.mgF_1F_O-^{1} was achieved in bulk studies. Transfer of the energy generating proteoliposomes to pL-sized droplets created a system capable of light-activated transcription of a ribonucleic acid (RNA) aptamer, which was detected with a novel hydrophilic analogue of the cognate fluorophore, DFHBI. To facilitate small molecule communication between compartments of the synthetic tissue, DIBs were permeabilised with a pore forming protein, alpha-hemolysin (αHL). ATP synthesised under control by light could then be transferred to and used in a neighbouring compartment.

Acknowledgements

I would like to thank everyone who has contributed towards my DPhil. Unfortunately, there are too many I need to thank and I cannot possibly fit them all onto this page, so a general thank you to everyone who has provided support and encouragement throughout my DPhil.

Firstly, to Prof. Hagan Bayley, for the opportunity of a lifetime to undertake a DPhil in his lab. His advice and mentorship have been invaluable. He has taught me his approach towards research, of relishing the freedom to scientific curiosities, all the while staying in sight of the bigger picture. It was a privilege to be named Entertainment Director.

I am equally indebted to the Bayley and Booth groups for making LG6, 7, & 11 enjoyable places to work. Special thanks go to Pablo, Jack, Jeff, Razia, Rav, and Assala, I don't know what I would have done without you all. Honourable mention to Hafez for the warm introduction to CMP. Jia Jia, the lab would fall apart without you, thank you for always being there for everyone. You are an excellent teacher and we're lucky to have you. Thank you for taking the time to proofread this thesis.

Without a good supervisor at the start of my DPhil I would have been lost, and so I was extremely lucky to be under the guidance of Dr Robert Ishmukhametov, one of the hardest working and dedicated scientists I know. Always on hand with another tip, trick, or proverb, thank you for teaching me the secrets of F_1F_O.

To my friends from Wheatley, who have tried yet failed to help me with my DPhil, thank you. Chris, George, Jake, Dan, Flo and Henri, each one of you have been there when things haven't gone to plan, I can only hope I can return the favour one day.

I would like to thank my family, in particular my Mum and Dad for allowing me to live at home over the past four years.

Writing this thesis has been arduous, but writing in Mauritius made it slightly more manageable. For this I have to thank Susanna, I could not have done it without your endless support and encouragement.

Table of Contents

Abbreviations

θ_{DIB}	Equilibrium contact angle
2-NBDG	2-(N-(7-Nitrobenz-2-oxa-1,3-diazol-4-yl)Amino)-2-Deoxyglucose
2D	Two dimensional
3D	Three dimensional
αHL	Alpha-hemolysin
ABC	ATP binding cassette
ACMA	9-amino-6-chloro-2-methoxyacridine
ADP	Adenosine diphosphate
ADP_{HK}	Hexokinase-purified adenosine diphosphate
AR20	Silicone oil AR20
ATP	Adenosine triphosphate
bR	Bacteriorhodopsin
CETCH	Crotonyl–coenzyme A (CoA)/ethylmalonyl-CoA/hydroxybutyryl-CoA
CCP	Cell-penetrating peptide
CMC	Critical micellar concentration
DDM	n-Dodecyl-β-D-Maltoside
DIB	Droplet interface bilayer
DMSO	Dimethyl sulfoxide
DOPC	1,2-dioleoyl-sn-glycero-3-phosphocholine
DOPG	1,2-dioleoyl-sn-glycero-3-phospho-(1'-rac-glycerol)

DPPE-PEG2000	1,2-dipalmitoyl-sn-glycero-3-phosphoethanolamine-N-[methoxy(polyethylene glycol)-2000
DPhPC	2-diphytanoyl-sn-glycero-3-phosphocholine
EtOH	Ethanol
F_1F_O	F_1F_O ATP synthase
GFP	Green fluorescent protein
GUV	Giant unilamellar vesicle
Hx	Hexadecane
IPTG	isopropyl β-D-1-thiogalactopyranoside
IVT	*In-vitro* transcription
IVTT	*In-vitro* transcription translation
LB	Lysogeny broth
LMCA1	*Listeria monocytogenes* Ca^{2+}-ATPase 1
LN2	Liquid nitrogen
LUV	Large unilamellar vesicle
Mant-ATP	2′/3′-O-(N-Methylanthraniloyl)adenosine 5′-triphosphate
MDR1	Multidrug resistant protein 1/ P-glycoprotein
MQ	Milli-Q®
MS	Mass spectrometry
NEB	New England Biolabs
Ni-NTA	Nickel-nitrilotriacetic acid
nL	Nanolitre
NMR	Nuclear magnetic resonance
NTP	Nucleoside triphosphates
OG	n-Octyl-β-D-Glucopyranoside

ONT	Oxford Nanopore Technologies
PCR	Polymerase chain reaction
PEG	Poly(ethylene glycol)
P_i	Inorganic phosphate
pL	Picolitre
PMF	Proton motive force
PMMA	Poly(methyl methacrylate)
RNA	Ribonucleic acid
RNAP	Ribonucleic acid polymerase
POPA	1-palmitoyl-2-oleoyl-sn-glycero-3-phosphate
POPC	Palmitoyl-2-oleoyl-sn-glycero-3-phosphocholine
pR	Proteorhodopsin
pR-mCherry	Proteorhodopsin-mCherry fusion construct
S. aureus	*Staphylococcus aureus*
SDS-PAGE	Sodium dodecyl-sulfate polyacrylamide gel
SERCA	Sarco(endo)plasmic reticulum Ca^{2+}-ATPase
SUV	Small unilamellar vesicle
TFA	Trifluoroacetic acid
Tris	Tris(hydroxymethyl)aminomethane
UV	Ultraviolet
v/v	Volume per volume
WT	Wild-type
w/v	Weight per volume

1 Introduction

1.1 Synthetic cells and tissues

A key challenge facing bottom-up synthetic biology is the construction of synthetic cells and tissues. Synthetic cells and tissues mimic a selection of natural functionality in an artificial system, and have the potential to be used as smart delivery systems[1,2], biocompatible devices[3], and as tools for studying the origins of life[4].

The simplest form of synthetic cellular structure consists of sequestering a biochemical process within a semi-permeable membrane. The membrane structure and composition can vary across a wide range of lipids, proteins, and amphiphilic polymers monomers, for liposomes[5], proteinosomes[6], and polymersomes[7] respectively. Both coacervates[8] and water-in-oil emulsions[9] have been developed as liquid-liquid phase separated synthetic cells, and the latter are the focus of this thesis. Such synthetic cells are commonly stabilised against coalescence into a bulk liquid phase by a polymer[10] or lipid [9] membrane located at the liquid-liquid interface.

To date the majority of work in this field has focused on synthetic cells, in both homo- and heterogeneous[11] populations. A wide variety of cell-like functions have been demonstrated in synthetic cells, such as carbon fixation[12], actin polymerisation[12], RNA synthesis[8], protein synthesis[13], energy generation[14], cell division[15,16], motion[17], and protein secretion[13,18]. Higher order structures have been

achieved through the compartmentalisation of synthetic organelles within synthetic cells, in the form of vesicles[12,14] or coacervates[5,19].

While the field of synthetic cell research has achieved promising results, advancements in the area of synthetic tissues have remained limited. Synthetic tissues consist of collections of synthetic cells working synergistically to reveal emergent properties[20] and are a key next step towards the distant goal of developing bottom-up synthetic organs. To construct synthetic tissues, biological functions that can facilitate the cooperation between synthetic cells are required, including inter-cellular communication. Examples of such communication across lipid bilayers include chemical communication through transporters (e.g. the archaeal light-activated proton pump bacteriorhodopsin, bR[9]), channels (e.g. the pore forming protein alpha-hemolysin, αHL[21]), and artificial receptors (e.g. the small molecule membrane-bound esterase from the group of Professor Christopher Hunter, to name one example)[22,23]. The ability to create tissue-like systems would support the design of soft, biocompatible devices that readily interface and communicate with living tissues to monitor and control their biological activity.

Previous work has centred around clustered populations of dispersed liposomal synthetic cells[24–26] in solution, leading to structures with no patterning. In nature, however, the emergent properties of tissues arise from the precisely controlled 3D distribution, communication, and cooperation of multiple distinct cell types and this must be replicated in the context of synthetic tissues. Patterned structures comprised of liposomes have been manufactured with optical tweezers, albeit with

low complexity and throughput[26]. Water-in-oil emulsions, stabilised by lipid monolayers surrounding each droplet, present the most advanced platform for synthesising synthetic tissues with a defined architecture[27].

1.2 Droplet interface bilayers

When an aqueous solution is dispensed in a lipid-containing oil, a lipid monolayer spontaneously self-assembles at the oil-water interface[9]. When two such droplets are brought into contact, the lipid monolayers form a droplet interface bilayer (DIB), separating the two aqueous compartments ("lipid-out" method[27]) (**Figure 1.1A**). Lipids can also be added to the system in the form of liposomes ("lipid-in" method[28,29]) (**Figure 1.1B**). Here, liposomes in the aqueous droplet burst at the oil-water interface, coating the interface with a lipid monolayer. The advantage of this method is the ability to form asymmetric DIBs through encapsulation of liposomes of two distinct lipid compositions in either droplet, a valuable tool when desiring to study membrane proteins in their native state[30,31].

DIB technology was originally developed as a means to miniaturise the electrophysiological study of membrane proteins and biological samples when material was scarce; femtolitre to microlitre sized droplets can form DIBs, in contrast to the millilitre volumes required for planar lipid bilayer recordings. Robustness against hydrostatic pressure and the aforementioned flexibility in the composition of the two leaflets of the lipid bilayer are additional benefits over traditional planar lipid bilayers[32]. Upon DIB formation and insertion of electrodes, an ionic current could be recorded flowing through αHL[9]. Proteins, including αHL,

can be incorporated into DIBs using proteoliposomes and the lipid-in method[33], inserted upon *in-vitro* transcription/translation (IVTT)[34], and the spontaneous insertion of detergent solubilised proteins from solution[3]. Investigations into a wide variety of membrane proteins have been performed using DIBs, such as on bacterial rhodopsins[3,9], transporters[33], and channels[31,35].

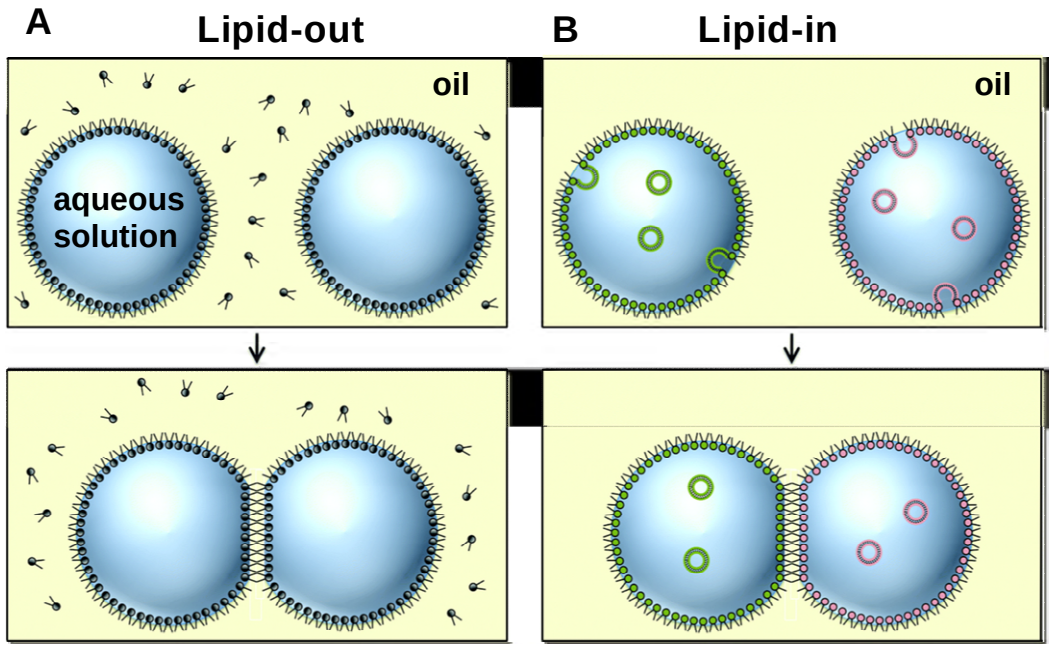

Figure 1.1. Droplet interface bilayer formation. Droplet interface bilayers (DIBs) formation through the ”lipid-out” (**A**) or “lipid-in” (**B**) methods. In the ”lipid-out” method, lipids, dissolved in oil, self-assemble into a monolayer at the interface of aqueous droplets and the oil phase **(A**). In the ”lipid-in” method, the lipid monolayer forms due to fusion of lipid vesicles, encapsulated within the aqueous droplets, at the oil-water interface (**B**). With both methods, upon bringing droplets into contact with one another, a kinetically stable lipid bilayer forms between the two droplets. By using the ”lipid-in” method and vesicles of two lipid compositions, asymmetric bilayers may be formed (**B**). Reproduced from Booth et al.[27]

However, DIBs are not without their limitations. Suspended in oil, droplets are susceptible to dehydration, resulting in droplet shrinkage. This is less of an issue with planar lipid bilayers or liposomes which are immersed in aqueous solution. To counter this, droplets are typically kept under high humidity e.g. by housing the droplet-containing chamber in a petri dish filled with water[2]. While the solution on either side of a planar lipid bilayer can be perfused to introduce and remove

chemicals and proteins, this is not facile with DIBs. This is in part because of the smaller volumes involved – in the nL range for DIBs[27] against the mL range for planar lipid bilayer systems - making manual manipulations difficult. Further, the oil environment surrounding DIBs makes accessing the aqueous compartment difficult. Further, the aqueous compartments separated by a bilayer is surrounded by oil and hard to access. This also makes reconstitution of membrane proteins into a DIB challenging by the conventional detergent-mediated strategy[38], where detergent-solubilised proteins are introduced to the aqueous solution followed by detergent removal by gel filtration, dialysis, or dilution[38]. These techniques are not possible with DIBs and thus detergent cannot be readily removed from a DIB system. Depending on the concentration, residual detergent may permeabilise DIBs and proteoliposomes to small molecules, or result in droplet pair coalescence[39]. As expanded upon in **Chapter 1.3**, this oil environment makes interfacing droplet networks with external solutions and living systems challenging. Furthermore, DIBs exist in a local energy minimum and are thermodynamically unstable towards coalescence into a single droplet[27]. Careful handling must therefore be ensured when assembling DIBs and an appropriate lipid composition is required. For example, lipids that favour monolayer formation (e.g. 1,2-dioleoyl-sn-glycero-3-phosphocholine (DOPC)), or lipids with steric features (e.g. lipids with poly(ethylene glycol) (PEG) headgroups) have been used to promote formation and stabilise DIBs[40,41]. Decreasing droplet volume also increases the rate of monolayer assembly, thereby decreasing the time required for DIB formation[42].

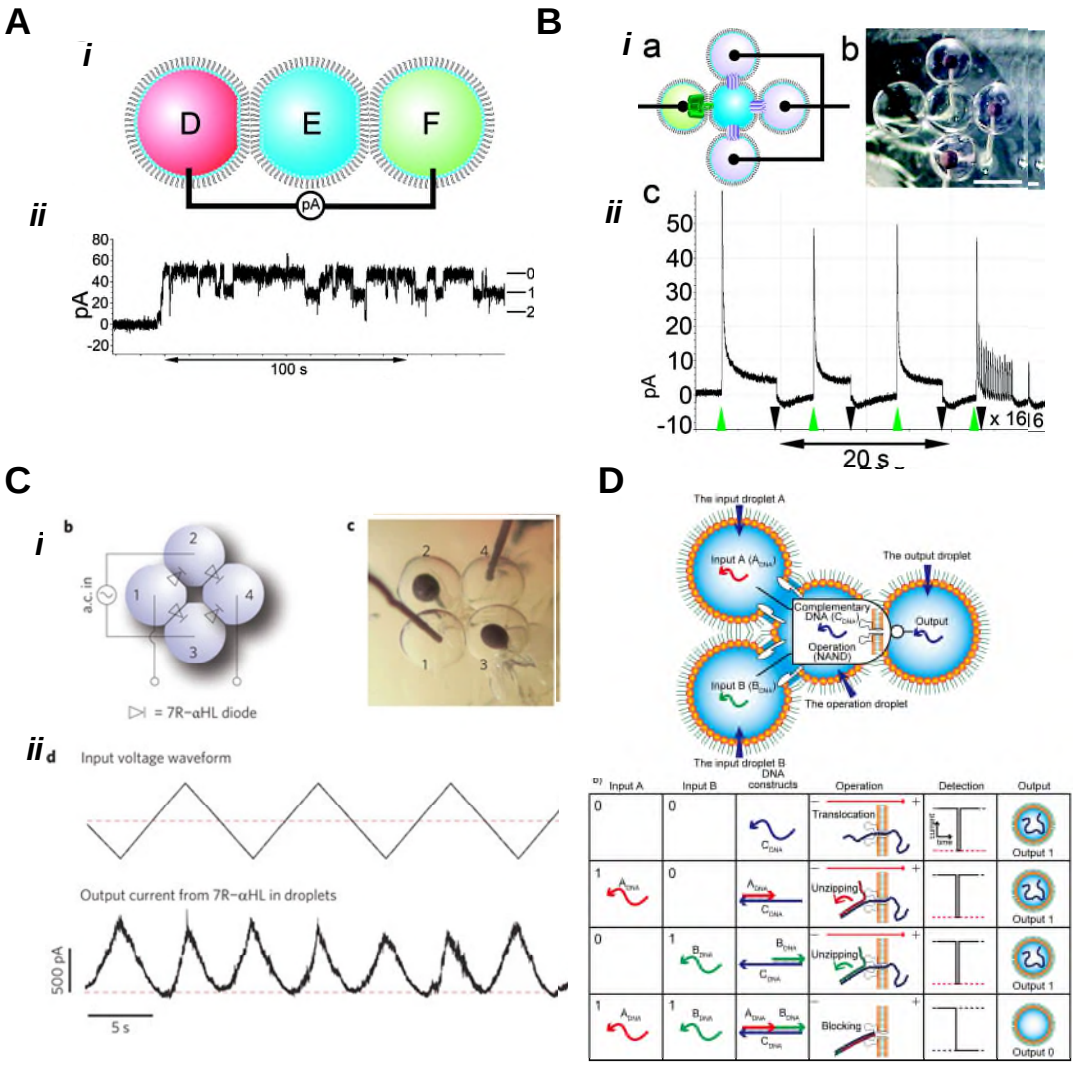

Figure 1.2. Soft biodevices made from 2D droplet networks. (**A**) A DIB-based bio-battery. A voltage is generated by forming a droplet chain with droplets containing a low salt concentration (100 mM NaCl) and the anion-selective N123R αHL (droplet D) and a high salt concentration (1 M NaCl) (droplets E and F) **(i).** Blocking events by β-cyclodextrin are observed in the two WT αHL pores are inserted into the DIB separating droplets E and F (**ii**). (**B**) A DIB-based light detector. The light-activated proton pump, bacteriorhodopsin (bR), was incorporated into DIBs separating purple and blue droplets (**i**)**.** Green light illumination triggers formation of ionic current that is recorded by an electrode placed in the αHL-containing green droplet (**ii**). (**C**) A DIB-based full-wave rectifier. Four droplets with DIBs functionalised by the 7R αHL mutant create a bridge rectifier (**i**)**,** converting alternating current to direct current (**ii**). (**D**) A DIB-based Boolean logic gate. A NAND logic gate was created from two input droplets encapsulating short single-stranded DNA molecules (the input signals), an operation droplet encapsulating a single-stranded DNA molecule complementary to both input signals, and an output droplet. When both are present, input single-stranded DNA hybridise with the single-stranded DNA in the operation droplet with the resulting double-stranded DNA unable to translocate to the output droplet. (**A**), (**B**) Reproduced from Holden et al.[9], (**C**) Maglia et al.[43], and (**D**) Yasuga et al.[44]

Forming two-dimensional (2D) structures containing multiple droplets interfaced by DIBs gives rise to a number of interesting avenues of investigation. These

structures, termed droplet networks, possess emergent properties not found in simple droplet pair systems. For example, droplet networks functionalised with membrane proteins have been used to form a number of bio-electronic devices, such as light sensors[3,9], a bio-battery[9], a current rectifier[43], and Boolean logic gates[44] (**Figure 1.2**).

In a demonstration of the functionality of 2D droplet networks, Dupin et al. showed that nanolitre droplets (200 μm in diameter) could be assembled into compartmentalised gene circuits with ordered spatial arrangements and morphogen gradients, originating from remote "organiser cells", controlling a gene circuit response[41] (**Figure 1.3A**). Amphiphilic signalling molecules (e.g. isopropyl β-D-1-thiogalactopyranoside (IPTG)) diffused across DIBs, whereas membrane impermeable hydrophilic molecules (e.g. arabinose) required transmembrane protein channels (e.g. αHL) to facilitate communication between droplets across DIBs (**Figure 1.3B**). In this manner, a pulse of fluorescence was sequentially activated by fluorophore-RNA binding and deactivated by subsequent *in-vitro* transcription (IVT), releasing the fluorophore to diffuse into neighbouring droplets. This was performed in both a linear chain and a grid of droplets, visualised with a fluorescent ribonucleic acid (RNA) aptamer and its cognate fluorophore, (5Z)-5-[(3,5-difluoro-4-hydroxyphenyl)methylene]-3,5-dihydro-2,3-dimethyl-4H-Imidazol-4-one (DFHBI) (**Figure 1.3C**). While the authors found that the lipid used, 2-diphytanoyl-sn-glycero-3-phosphocholine (DPhPC), was sufficient to rapidly form a monolayer when encapsulating proteins, oligonucleotides, and bacteria, the relatively slow monolayer formation was deleterious to droplet function and DIB formation when attempting to encapsulate cell extract in droplets. In this instance

attempting to form a DIB shortly after droplet formation led to fusion due to incomplete monolayer coverage, while longer incubation times led to droplet deformation. The authors hypothesised that protein denaturing at the oil-water interface was interfering with monolayer. To overcome this limitation, a novel lipid composition was developed containing lipids with a faster rate of monolayer assembly, such as 1,2-dioleoyl-sn-glycero-3-phosphocholine (DOPC), and negatively charged lipids, such as 1,2-dioleoyl-sn-glycero-3-phospho-(1'-rac-glycerol) (DOPG). Negatively charged lipids were proposed to stabilise DIBs via charge repulsion of anionic biomolecules.

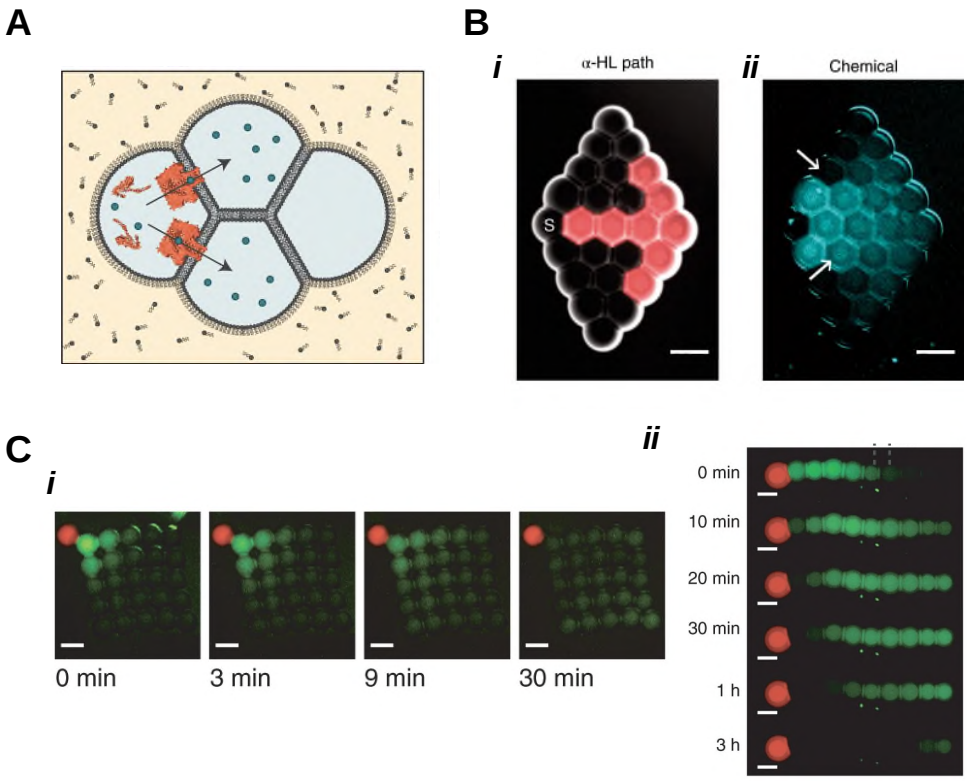

Figure 1.3. Gene circuits in 2D droplet networks. (**A**) Droplet networks consisting of nL droplets were prepared using the lipid-out method. (**B**) αHL, patterned throughout the network **(i),** mediated small molecule diffusion across lipid bilayers **(ii)**. (**C**) A pulse of *in-vitro* transcription activity visualised by DFHBI is observed over a grid (**ii**) and chain of droplets (**iii**). DFHBI binds to RNA, increasing fluorescence and displacing a small single-stranded DNA molecule. This single-stranded DNA hybridises with and activates the double-stranded DNA template. The resulting RNA molecule hybridises with Spinach, displacing DFHBI to begin the cycle over again in the neighbouring droplet. Scale bars 200 μm. Reproduced from Dupin et al.[41]

The small 2D droplet networks described in this early work were typically constructed using manually manipulated nanolitre sized droplets[9,28,34,43]. Simple three-dimensional (3D) droplet networks were also constructed using this method; individual droplets dispensed by micropipettes or Hamilton® syringes were positioned using either electrodes connected to micro-manipulators or pipette tips and pulled glass capillaries[21,27,45] (**Figure 1.4A**).

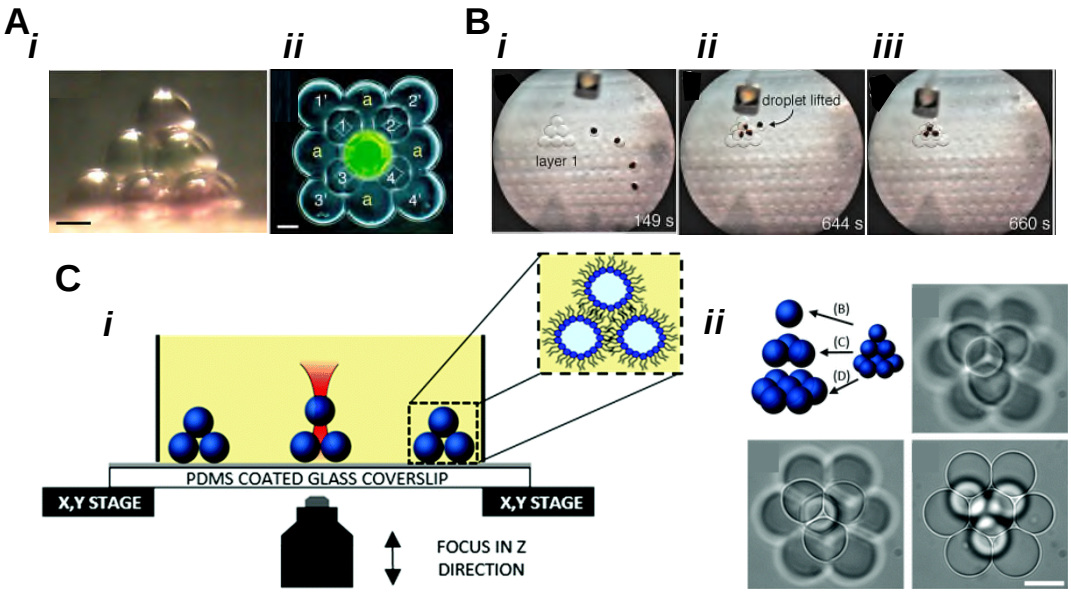

Figure 1.4 Construction of simple 3D droplet networks. (**A**) **i** Bright field image of ten aqueous droplets of nanoliter volume forming a pyramid structure (side view). **ii** Fluorescent microscopy image of a fourteen-droplet pyramid (top view). Scale bars 200 μm. (**B**) Droplet manipulation with a Nd magnet. Droplets containing paramagnetic particles (black dots) were levitated by a Nd magnet to form a three-layered pyramid. (**C**) Optical tweezers manipulate sucrose droplets. **i** Diagram showing 3D droplet network construction. **ii** Eleven droplets are positioned with optical tweezers to form a three-layered pyramid. Scale bars 15 μm. (**A**), (**B**) Reproduced from Wauer et al.[21], and (**C**) Friddin et al.[46]

Another technique has involved positioning droplets containing paramagnetic beads with sub-millimetre precision using a Nd magnet[21] (**Figure 1.4B**). Building droplet networks devoid of paramagnetic beads was possible; empty droplets were manipulated upon DIB formation with a droplet containing magnetic beads. In this way droplet networks consisting of nine droplets in three layers could be constructed and reordered. Separately, single-beam optical traps have been

applied to droplet network construction, manipulating droplets <15 pL in volume - 11 droplets of identical composition have been arranged in this manner in a pyramid structure[46] (**Figure 1.4C**).

While these examples highlight a number of impressive techniques, they suffer from poor throughput and limit the number of droplets within networks. New techniques are required to build synthetic tissues from cell-sized droplets and with a defined architecture. Currently the most advanced technique in 3D droplet network construction is the droplet-based 3D printer developed within the Bayley group[42] (**Figure 1.5**). With this technology tens of thousands of heterologous droplets can be printed to form precisely patterned synthetic tissues in an automated fashion. The aqueous solutions to be printed, so-called “inks”, are loaded into nozzles custom-made from pulled glass capillaries with an internal tip diameter of around 100 μm. Nozzles are attached to a poly(methyl methacrylate) (PMMA) chamber containing a piezoelectric transducer (piezo). Droplets are dispensed upon activation of the piezo with droplet size ranging from 10 – 200 μm in diameter (0.5 pL – 4 nL), dependent on the voltage applied to the piezo. Patterned structures are obtained by the harmonious movement of a motorised micro-manipulator stage that houses the oil bath, in parallel with droplet ejection. The printing set-up has so far been limited to printing two aqueous solutions from two nozzles at any one time, however it is relatively easy to generate droplets networks containing multiple inks by cleaning and refilling nozzles with appropriate solutions[47]. To decrease the building time of large (cm-scale) droplet networks, multiple pre-formed mm-sized droplet networks can be adhered to one another, with DIBs forming between droplets located at the boundary between networks[48].

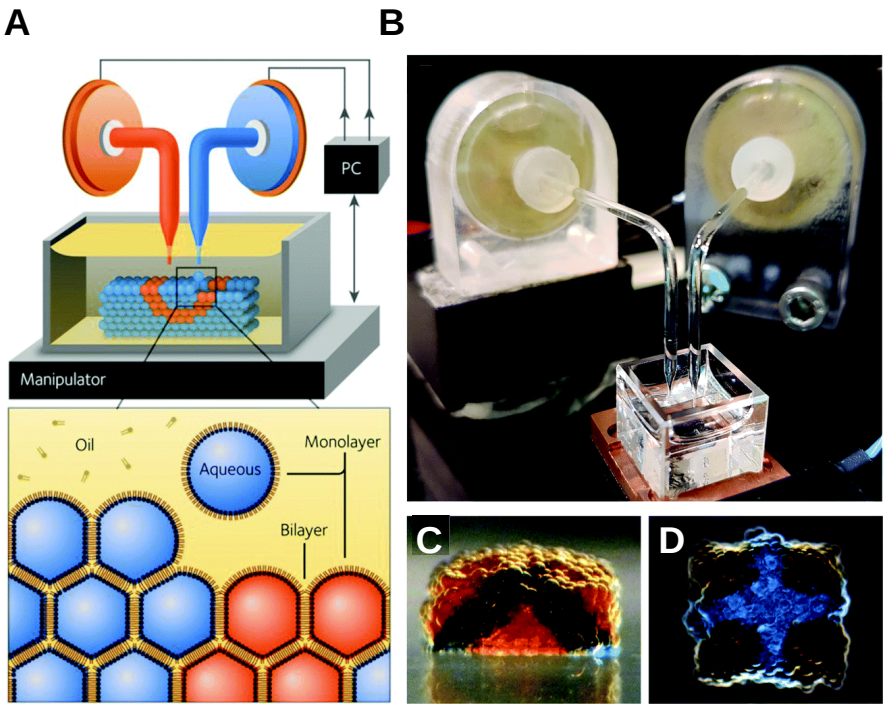

Figure 1.5. A 3D droplet printer. (**A**) Diagram of a 3D droplet printer with two nozzles in operation, constructing a droplet network by dispensing droplets of aqueous solution in lipid-containing oil. (**B**) Photograph of the 3D droplet printer and lipid-in-oil-containing cuvette. (**C**) A patterned 3D droplet network comprised of two distinct solutions as viewed from the side. (**D**) As in **C** but viewed from the top. Reproduced from Booth et al.[27]

Accurate patterning of the first layer of droplets is crucial to the final architecture of 3D droplet networks, because mispacking or unalignment of droplets in this bottom layer propagates throughout the network. Achieving a large fraction of hexagonal close packing of the final droplet network would enable patterning of the structure down to single droplet resolution, enabling channels one droplet wide to be printed. A key parameter that dictates droplet packing is the equilibrium contact angle of the DIB (θ_{DIB}) (**Figure 1.6A**). In a system of four droplets arranged in a pyramid (**Figure 1.6B**), when θ_{DIB} approaches the critical angle (θ_c) of 35.3º, the subsequent droplet network will have a regular hexagonal close-packed (hcp) structure with lipid monolayers between all four droplets touching at a point (**Figure 1.6C**). At a contact angle lower than 35.3º, a continuous oil phase will exist at the centre of this tetrahedral pocket[49]. It is important to remove this oil phase to ensure that the

system is physiologically relevant. When the contact angle equals 35.3^{o} a droplet network will have the largest fraction of hexagonal close packing (0.43 ± 0.06 area fraction) compared to that at a contact angle below (θ_c = 9.9^{o}, hcp = 0.28 ± 0.08 area fraction) or above ((θ_c = 57.5^{o}, hcp = 0.17 ± 0.06 area fraction) the critical angle (**Figure 1.6D**)[49]. Packing imperfections are present in part due to the drag of the nozzle as it moves through the oil and droplets at the edge of networks rolling before DIB formation can occur [49].

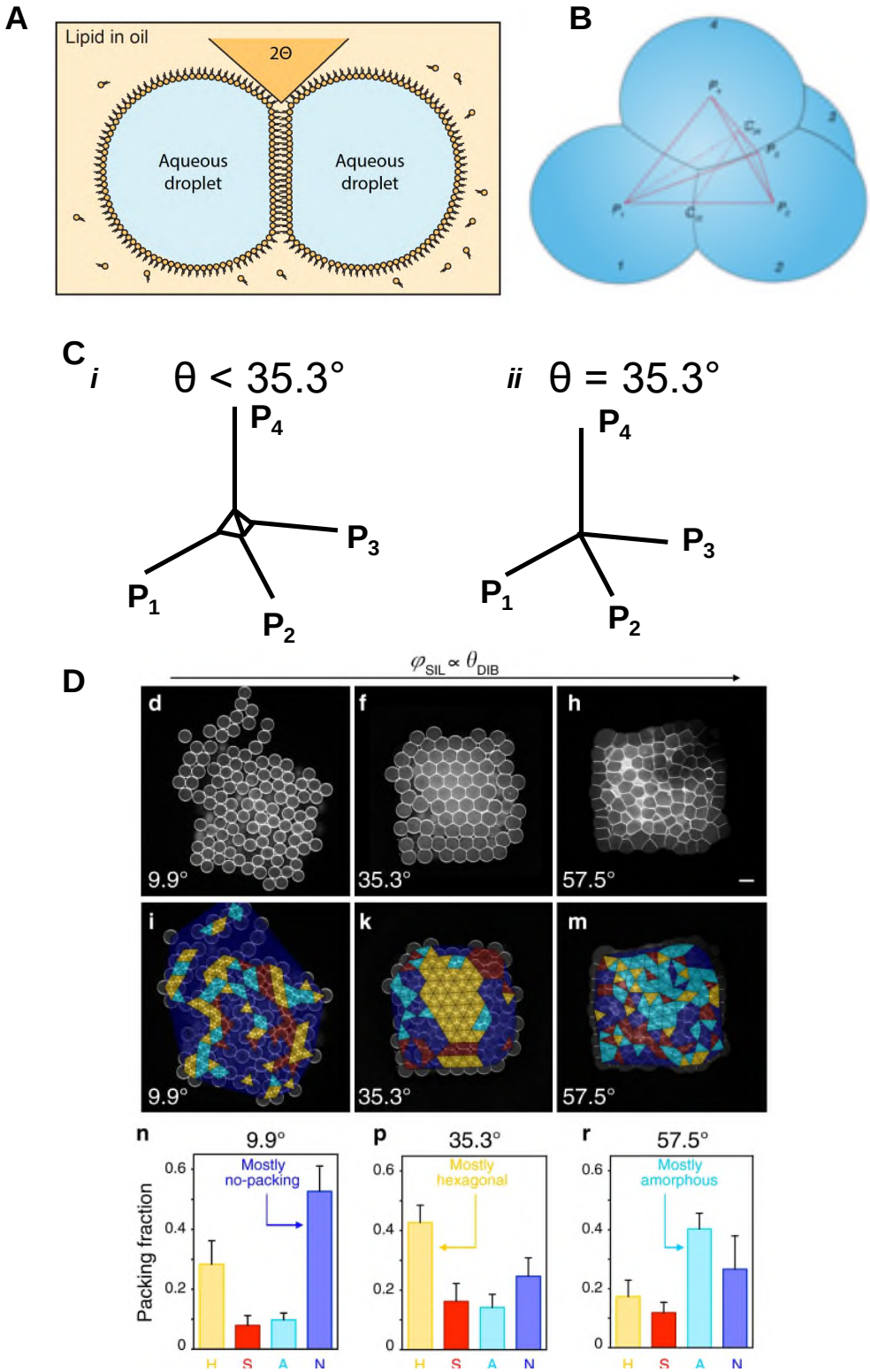

Figure 1.6. The contact angle (**A**) Schematic of a pair of aqueous droplets forming a DIB in a lipid-in-oil solution highlighting the contact angle (θ). (**B**) Schematic showing the packing of a four-droplet network arranged with their centre-to-centre distances at the corners of a regular tetrahedron. (**C**) ***i*** At θ < 35.3°, the droplet monolayers of the droplets do not touch at the centre, and a continuous oil phase exists in the centre of the tetrahedral pocket ***ii*** When θ = 35.3°, the droplets meet at a point and the oil phase is excluded from the droplet network. (**D**) The highest fraction of hexagonal close packing is found when θ = 35.3°. **B** and **D** reproduced from Alcinesio et al[49].

Choice of oils, and ratio thereof, is the simplest way to adjust θ_{DIB} without adjusting any variables that influence the aqueous phase[49]. A typical choice of oils would be a linear alkane, such as hexadecane or undecane, mixed with a more hydrophilic oil such as silicone oil AR20 (AR20)[27]. AR20 is used both to increase the density of the oil phase, and encourage bilayer formation, as the fatty acid tails of lipids are less soluble in AR20 compared to alkanes. Increasing the ratio of AR20 relative to linear alkane increases θ_{DIB} and thus bilayer area[49]. θ_{DIB} is also strongly dependent on the nature of the lipid used, for example palmitoyl-2-oleoyl-sn-glycero-3-phosphocholine (POPC) gives rise to larger bilayers relative to DPhPC[49], presumably due to differences in their relative solubilities in oil.

The variation between droplet volume is also an important factor in achieving patterned droplet networks as a difference between volumes of droplets could prevent a regular hexagonal close packing structure. Changing droplet volumes during experiments is also an issue as this could lead to the dilution or concentration of droplet contents. Variation in the volume of droplets can occur initially upon droplet formation and care and expertise must be used to form droplets of a uniform size. Droplet volumes can also change *in-situ* for a variety of potential reasons. Firstly, dehydration of droplets, resulting from the movement of water from the aqueous phase to the oil phase, leads to a decrease in droplet volume. DIBs prepared in the lipid-out method buckle upon dehydration (**Figure 1.7Ai**), while DIBs prepared by the lipid-in method have been shown to shrink uniformly in size (**Figure 1.7A*ii***)[50]. Osmosis is another factor that may lead to changing droplet sizes. Diffusion of water from a droplet of low solute concentration, across the semi-permeable DIB, to droplets of high solute

concentration will cause an increase in the volume of the high-solute droplets, and a decrease in the volume of the low-solute droplets[9,51]. In an interesting example, this phenomenon was utilised to create a droplet network containing droplets with two osmolarities that underwent an osmotic-driven shape change (**Figure 1.7B**)[51]. Ostwald ripening is another potential cause of droplet size variation. Ostwald ripening occurs whereby larger droplets increase in volume at the expense of smaller ones, as the solubility of the aqueous phase within a droplet increases in the oil as the interfacial curvature increase; the Kelvin-Thompson effect[52]. As a result of small droplets becoming smaller, and large droplets becoming larger, there is a reduction in the interfacial area. A theoretical description of Ostwald ripening was provided by Lifshitz, Slyozov and Wagner, who described the LSW theory[52], which states that a stationary state is achieved whereby:

$$\omega = \frac{da_N^3}{dt} = \frac{8\gamma V_m^2 D_m C_{(\infty)}}{9RT}$$

Where ω is the ripening rate, $a_N$is the average particle radius, V_m and D_m are the molar volume and molecular diffusion coefficient of the dispersed phase, $C_{(\infty)}$is the bulk solubility of the dispersed phase through the continuous phase, γ is the interfacial tension, and R and T are the gas constant and absolute temperature[52]. If droplet volumes are changing over the course of the experiment and having a detrimental effect on outputs, then measures could be taken to prevent this, such as by balancing the osmolarity across DIBs[41].

A range of aqueous solutions have been utilised in printed 3D droplet networks, from the original work performed on salt solutions[42], to IVTT machinery[40], hydrogels[47], bacterial cells[47], and eukaryotic cells[53].

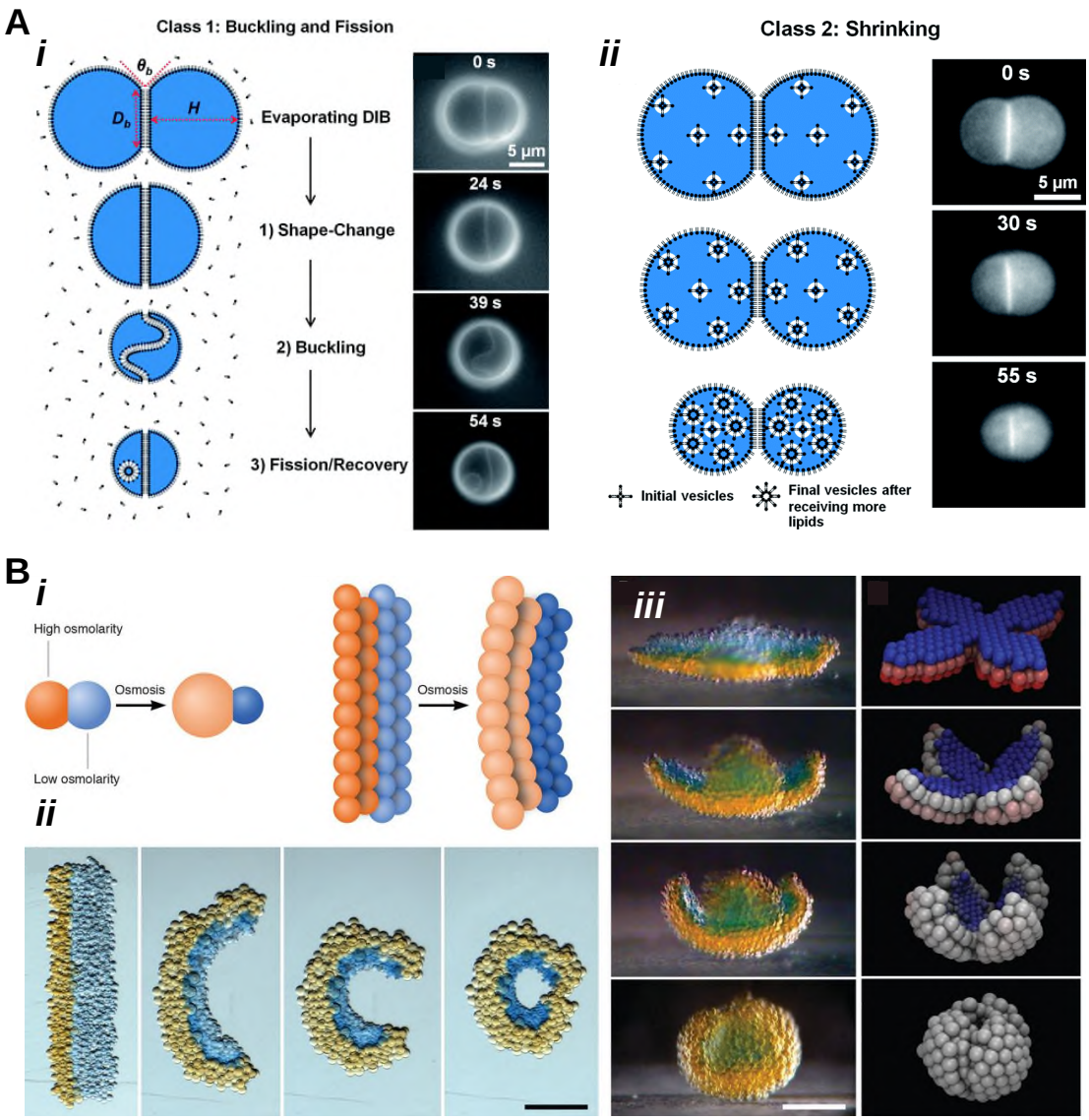

Figure 1.7 Changing droplet volume. (**A**) Dehydration lowers droplet volume. DIBs made from femtolitre droplet pairs with the ***i*** lipid-out buckle upon droplet shrinkage before vesicles are ejected from the DIB. ***ii*** DIBs made from the lipid-out method undergo uniform shrinkage upon dehydration. (**B**) ***i*** Osmotic effects change droplet volume. A droplet network containing high (orange) and low (blue) concentration salt droplets undergo osmotic shape change to form ***ii*** a ring and ***iii*** a sphere. **A** reproduced from Mruetusatorn et al.[50], **B** reproduced from Villar et al.[51]

1.3 Interfacing droplet networks with external solutions

Droplet networks represent an adaptable platform to build soft devices and compartmentalised synthetic tissues. Historically, one of the main limitations of this technology was the oil environment in which they are formed. The oil phase

surrounding droplet networks would limit the hybridisation of droplet networks with living tissues and hinder the development of biologically relevant applications.

An early strategy to overcome this problem was to develop multisomes, aqueous droplets formed within an oil droplet, which is itself suspended within a bulk aqueous phase (**Figure 1.8A**). Droplets made in this manner form bilayers with both each other and the external solution. Initial work demonstrated the controlled, but irreversible, droplet bursting and subsequent release of internal contents upon pH or temperature triggers in the external solution [54].

An ensuing work utilised αHL pores for the uptake, processing, and release of chemical signals to and from the external bulk solution[1] (**Figure 1.8B**). This work lead to the development of a soft bio-processor unit, constructed from a droplet network, able to process external ionic signals and activating multiple biological functions including sugar hydrolysis and DNA cleavage in a parallel and orthogonal manner[1].

Functionalising droplet networks with hydrogels is another way to enable interactions with an external bulk aqueous phase[45]. Droplet networks were assembled from aqueous solutions containing a hydrogel precursor, that after photopolymerisation generated micrometre to millimetre sized hydrogels with defined patterns[45] (**Figure 1.8C**). Polymerisation broke the network of DIBs across the structure, in its place forming a continuous hydrogel transferrable to aqueous solutions. By incorporating thermal- and magnetic- responsive hydrogel droplets,

an object was picked up, carried through a maze, and deposited by a carrier hydrogel droplet network[45].

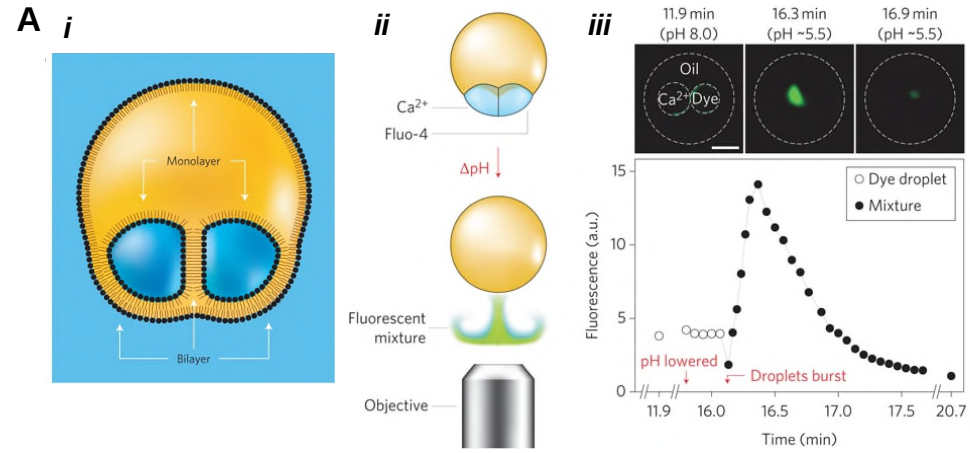
A
i
ii
iii
Monolayer
Bilayer
Ca2+
Fluo-4
ΔpH
Fluorescent mixture
Objective
11.9 min (pH 8.0)
16.3 min (pH ~5.5)
16.9 min (pH ~5.5)
Oil
Ca2+ Dye
Dye droplet
Mixture
Fluorescence (a.u.)
pH lowered
Droplets burst
Time (min)

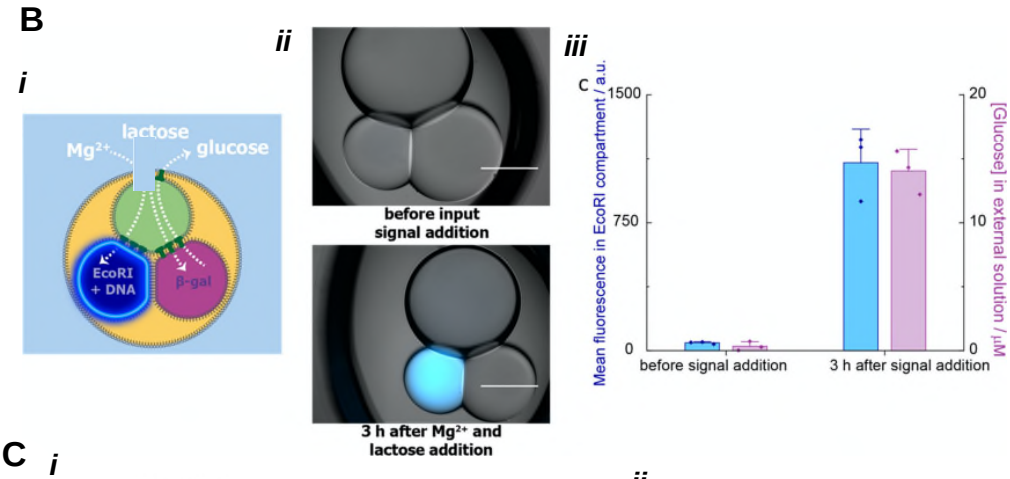
B
i
ii
iii
lactose
Mg2+
glucose
EcoRI + DNA
β-gal
before input signal addition
3 h after Mg2+ and lactose addition
C
Mean fluorescence in EcoRI compartment / a.u.
[Glucose] in external solution / μM
before signal addition
3 h after signal addition

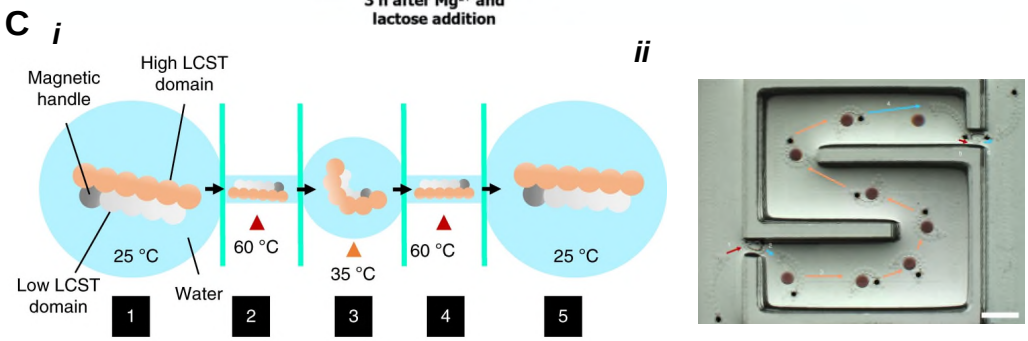
C
i
ii
Magnetic handle
High LCST domain
Low LCST domain
Water
25 °C
60 °C
35 °C
60 °C
25 °C
1
2
3
4
5

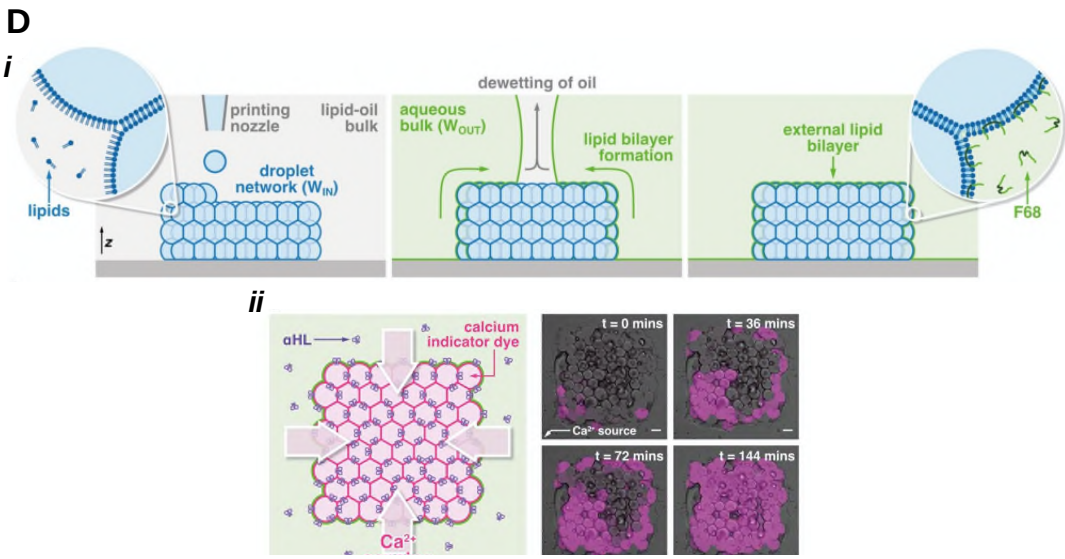
D
i
ii
printing nozzle
lipid-oil bulk
droplet network (WIN)
lipids
dewetting of oil
aqueous bulk (WOUT)
lipid bilayer formation
external lipid bilayer
F68
αHL
calcium indicator dye
Ca2+
Ca2+ source
t = 0 mins
t = 36 mins
t = 72 mins
t = 144 mins

Figure 1.8 Interfacing droplet networks with external environment. (**A**) **i** Diagram of a multisome, a water-in-oil-in-water emulsion. **ii** Schematic of the pH-mediated bursting of multisomes and the contents release. **iii** Upon multisome bursting, Ca^{2+} and Fluo-4, a Ca^{2+} fluorophore, mix and produce a fluorescent signal. Subsequent diffusion of fluorophore and Ca^{2+} lowers fluorescence. Scale bar, 500 μm. (**B**) **i** Diagram detailing signal processing in multisomes. Separate compartments hydrolyse lactose and activate DNA cleavage. **ii** Image of multisome showing DNA cleavage-induced fluorescence upon addition of Mg^{2+} addition to the external solution. **iii** Quantification of fluorescence in **ii** before and after Mg^{2+} addition. Externally supplied lactose diffuses into the multisome and is enzymatically cleaved to produce glucose. Glucose concentration is measured from the external solution after product secretion. Scale bar, 300 μm. (**C**) **i** Diagram of a controllable hydrogel droplet network. Hydrogel volume is controlled by temperature while position is magnetically controlled. **ii** The hydrogel structure was used to pick up and carry a cargo through a maze. Scale bar, 4 mm. (**D**) Phase transferring printed droplet networks. **i** nL droplets containing surfactant, F68, mediated the dewetting oil from droplet networks. An external lipid bilayer forms around the periphery of the droplet network. **ii** External Ca^{2+} diffused into the droplet network through αHL embedded in the newly formed external bilayer. Scale bar, 100 μm. (**A**) reproduced from Villar et al.[54], (**B**) Cazimoglu et al.[1], (**C**) Downs et al.[45], and (**D**) Alcinesio et al.[55]

Phase transferring droplet networks to an aqueous phase while maintaining DIB architecture and compartmentalisation is an attractive next step. Recently, in a surfactant-mediated dewetting approach, the external oil solution surrounding a printed 3D droplet network was displaced by an aqueous solution (**Figure 1.8D**). Bilayers formed around edge droplets to enclose the droplet network in a continuous lipid bilayer[55].

Remarkably, the precise internal patterning of the 3D droplet network was conserved during this process. αHL pores embedded in the newly formed bilayers enabled Ca^{2+} from the external solution to diffuse into the structure[55]. Unfortunately, this dewetting technique did not disrupt the bilayer between the bottom layer of droplets and the glass, and so the networks could not be transported.

1.4 Energy generation in vitro

As discussed previously, a goal of the field is to reconstitute life-like processes inside synthetic cells and tissues, and the generation and consumption of energy is key amongst these. Simple droplet networks have been constructed into biobatteries, based on concentration cells, in an early example of power generation in synthetic cells and tissues[9]. Three droplets were brought into contact to form a linear droplet network separated by two DIBs, one of which was functionalised by an anion-selective αHL mutant. With a NaCl gradient present between the two compartments adjacent to the functionalised DIB, a current could be recorded due to Cl^- freely diffusing through the pore, while Na^+ could not[9]. As the salt gradient rapidly reached equilibrium, due to ion transport and osmosis, the biobattery ran for less than an hour.

Making use of a renewable energy source, light, bR was incorporated into a simple 2D droplet network which upon illumination generated a current[9] (**Figure 1.2B**). One proton is transported for every photon absorbed by the retinal cofactor of bR, resulting in a ΔpH build-up across the bilayer, assuming that the protein is unidirectionally inserted. Correct orientation of membrane proteins in artificial lipid bilayers is an ongoing challenge in the field[56]. Orientated insertion can be achieved through fusion of a hydrophilic domain attached to either the C- or N-terminus of the protein, as shown for another light-activated proton pump, green-light absorbing proteorhodopsin (pR), a 27 kDa bacterial membrane protein, with the unoccupied terminal facing the lumen of vesicles[57]. Patterned power generation was accomplished using a photomask placed above a 4 x 4 array of droplets, each

containing bR, and embedded in a hydrogel structure[3]. Electrodes inserted in each droplet recorded 16-pixel grey-scale images based on current generation levels, as well as moving images.

It is desirable to undertake the conversion of ΔpH into an energy form capable of performing useful work, for example the powering of biochemical transformations. To do so ΔpH can be converted into adenosine triphosphate (ATP) through the membrane protein F_1F_O ATP synthase (F_1F_O)[58] (**Figure 1.9A**). ATP is ubiquitous in all known forms of life[59], and it is the hydrolysis of the γ-phosphate ester that releases the energy used to maintain homeostasis[60]. F_1F_O consists of two opposing rotary proteins, the hydrophobic membrane bound F_O and hydrophilic F_1[61]. F_1F_O is powered by the proton motive force (PMF), a combination of both ΔpH and membrane potential, ΔΨ.

The two can be written as follows:

$$\Delta\mathrm{pH} = pH_{external} - pH_{internal}$$

And when the membrane is in thermodynamic equilibrium and assuming the membrane is permeable to one type of ion, the membrane potential can be given by:

$$\Delta\Psi = 2.3\frac{RT}{zF}log_{10}\left\{\frac{X^z_{out}}{X^z_{in}}\right\}$$

Where R is the gas constant, T is the absolute temperature, z is the charge on ion X, and F is the Faraday constant[62]. The two variables and can be linked through the following equation:

$$PMF = \Delta\Psi - 2.3RT\Delta\mathrm{pH}$$

Where, R is the gas constant, and T is the absolute temperature. $\Delta\Psi$ and ΔpH are intrinsically linked, as protons are cationic, affording $\Delta\Psi$ upon transport across a bilayer, and the chemical separation across the bilayer generates ΔpH - for a change in ΔpH -0.1 units, there is an increased contribution to PMF of 6 mV[63]. Other ions such as sodium or potassium can influence $\Delta\Psi$ but not ΔpH[62]. The exact contributions of $\Delta\Psi$ and ΔpH to ATP synthesis rates are unknown, however it is known that these components effect the rate of ATP synthesis dependent on the specific type of F_1F_O. For example, *E. coli* and mitochondrial F_1F_O maintain a high PMF primarily in the form of $\Delta\Psi$, while with chloroplast F_1F_O, PMF is maintained predominantly in the form of ΔpH[58]. After building of the PMF, protons flow down their electrochemical gradients at the interface of subunits a and c of the transmembrane F_O. The torque generated through this process is transferred to the γ subunit of F_1, in turn powering ATP synthesis from adenosine diphosphate (ADP) and inorganic phosphate (P_i) at the catalytic interfaces of the α and β subunits of F_1. A hexameric assembly of alternating α and β subunits around the γ subunit reveals six nucleotide binding sites at the α-β interfaces[64], although only three are catalytically active[65]. The β subunits undergo a conformational change required for ATP synthesis upon rotation of the central γ subunit, resulting in a maximum of one molecule of ATP synthesised per 120^o rotation[58].

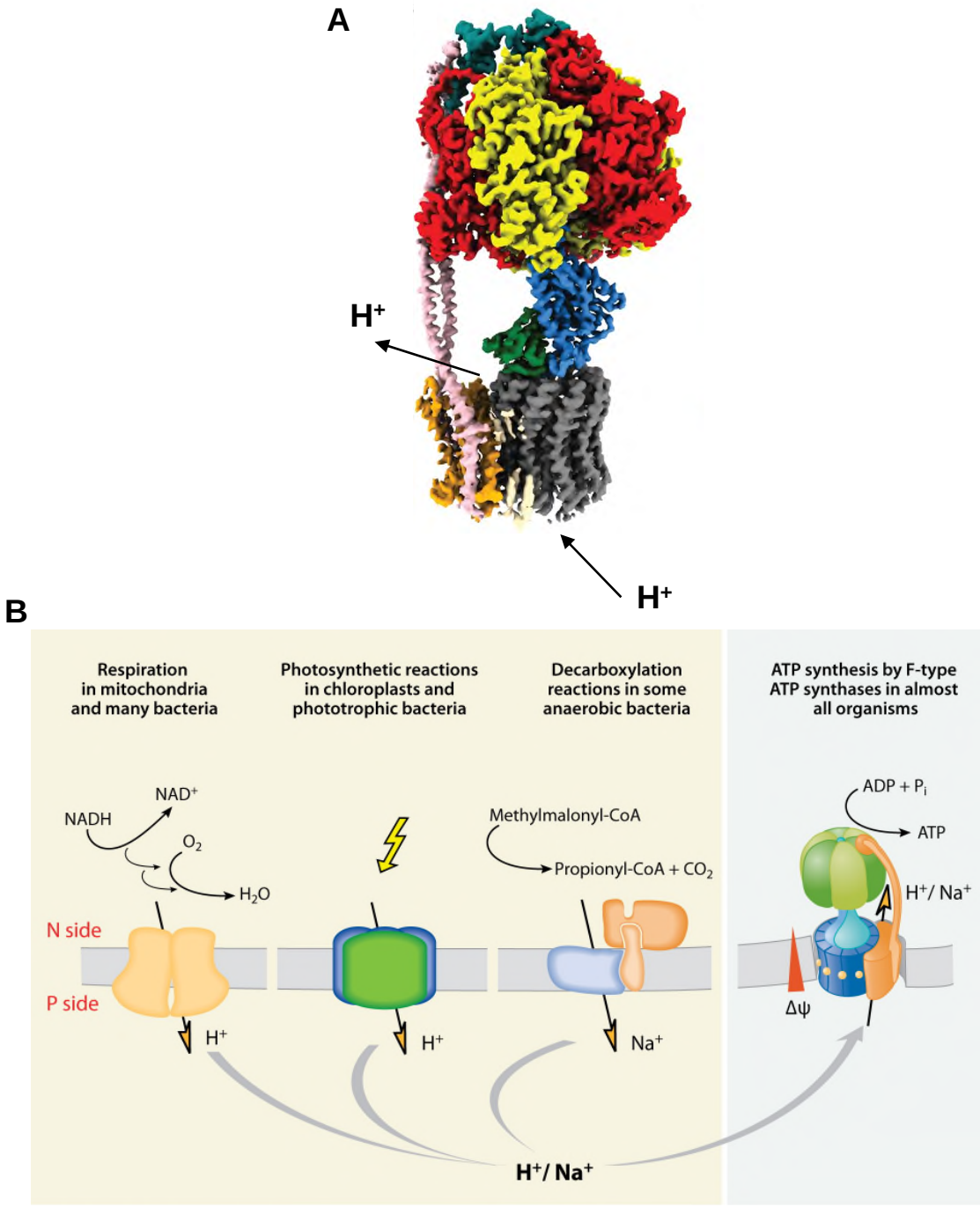

Figure 1.9 F_1F_O ATP synthase. (**A**) Cryo-EM map of *E. coli* F_1F_O ATP synthase. F_O consists of a, b, and c subunit (orange, purple, and grey, respectively). F_1 consists of α, β, δ, ε, and γ (in red, yellow, teal, green, and blue, respectively). Protons translocate between the a subunit and the c ring This creates torque in the γ subunit of F_1 which in turn generates conformational changes in the catalytic sites of the β subunits, synthesising ATP. (**B**) The proton motive force (PMF) necessary to power F_1F_O ATP synthase is generated through respiration chain proteins, photosynthetic reaction centres, sodium pumps, and other proton pumps. P side refers to positive side of the membrane, N side is negative. (**A**) reproduced from Sobti et al.[66], and (**B**) from von Ballmoos et al.[58]

In bacterial F_1F_O, ATP synthesis is a reversible process; in the absence of a PMF but presence of ATP, the F_1 rotor can turn in the opposite direction, undergoing up to 350 revolutions per second, hydrolysing ATP and acidifying the transmembrane compartment[67]. ATP hydrolysis can be activated *in vitro* for other classes of F_1F_O. For example, F_1F_O from the thermoalkaliphilic bacteria *Bacillus subtilis* hydrolyses ATP at very low rates unless activated by the detergent lauryldimethylamine oxide[68]. F_1F_O are found in the thylakoid membrane of chloroplasts, the cristae of mitochondria, and the plasma membrane of bacteria[69], with the PMF supplied by photosystem II, electron transport chain proteins, and a variety of ion pumps, including a Na^+ pump in one bacterial species[70] (**Figure 1.9B**).

Early work investigating F_1F_O in artificial systems focused on understanding the function of F_1F_O using small unilamellar vesicles (SUVs). To do so, one needs to reconstitute F_1F_O into a bilayer along with a means of generating PMF. Artificial methods of inducing the PMF include acid-base transitions[71], boric acid ester formation[72], glucose oxidation[73], electric fields[74], Janus metal-organic layers[75], and photoacids[76]. However, the majority of work historically has focused on generating a PMF via membrane proteins. In 1974, Racker and Stoeckenius performed the first co-reconstitution of bovine F_1F_O and purple membrane containing bR by sonicating the proteins in sodium cholate and a crude mixture of soybean lipids[77]. The resulting proteoliposomes were shown to synthesise ATP upon illumination and were sensitive to PMF uncouplers.

Later, Pitard and co-workers performed a comprehensive screening regarding the optimal conditions for the detergent-based liposomal co-reconstitution of F_1F_O and

bR[78]. Important variables included detergent type and concentration, reconstitution buffer composition and temperature, bR structure (added as purple membrane or monomers), lipid composition and rate of detergent removal. It was noted that optimal reconstitution conditions for each F_1F_O (from thermophilic bacteria, chloroplast, mitochondria) had to be determined experimentally; while a mixture of Triton X-100 and octyl glucoside (OG) provided the highest rate of ATP synthesis in a bacterial F_1F_O (*from Bacillus subtilis* PS3), OG was deleterious towards chloroplast and mitochondrial F_1F_O[78].

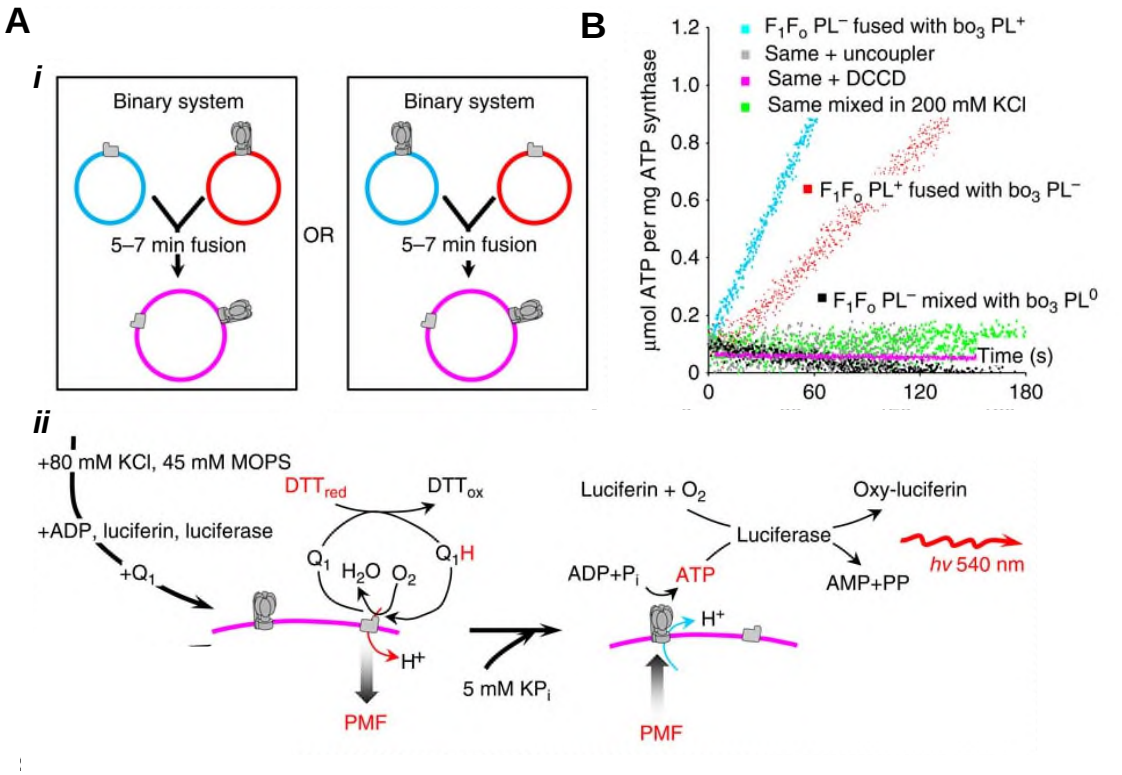

Figure 1.10 Fusiogenic proteoliposomes construct ATP synthesizing organelles. (**A**) ***i*** Positive (red) and negative (blue) proteoliposomes were prepared with either *E. coli* F_1F_O or bo_3 oxidase. Fusion occurs in low salt conditions. ***ii*** Upon addition of a quinol, PMF is generated by bo_3 oxidase, driving ATP synthesis via F_1F_O. (**B**) Luminescence traces of ATP synthesis. Maximal ATP synthesis rates are achieved when F_1F_O is initially reconstituted in anionic proteoliposomes (blue trace) than in cationic proteoliposomes (red trace). No ATP synthesis is observed when non-fusiogenic proteoliposomes are used, or when PMF uncouplers are present. Reproduced from Ishmukhametov et al.[79]

Cytochrome bo_3 oxidase, a proton pump found in bacterial electron transport chains, has been reconstituted into SUVs to generate a PMF across and power F_1F_O[79]. Two populations of fusiogenic SUVs, with lipid compositions of opposite charges, were mixed to form proteoliposomes containing both cytochrome bo_3-oxidase and F_1F_O (**Figure 1.10A**). This redox protein is highly dependent on membrane quinols, such as coenzyme Q_{10}, and molecular oxygen as donors and acceptor of electrons, respectively. Activity of bo_3 oxidase is such that upon activation, a rate of stable ATP synthesis was maintained for only 5-7 minutes, before depletion of oxygen lowered the synthesis rate[79].

1.5 ATP synthesis and consumption in synthetic cells

While the examples described previously within this thesis (see **Chapter 1.4**) demonstrated that ATP can be made in vitro, ATP production was not coupled to any interesting biological functions in synthetic systems. Sequestering ATP synthesising proteoliposomes and ATP in synthetic cells is advantageous for downstream biological applications as a high concentration of ATP can be achieved. In one example, microfluidic systems were used to generate synthetic cells encapsulating ATP synthesising machinery. Here, F_1F_O was reconstituted into large unilamellar vesicles (LUVs) and added to water-in-oil droplets by pico-injection, with droplets stabilised against coalescence by a perfluorinated polyether[80]. Upon addition of $MgCl_2$ to the droplets, LUVs within the droplets fused to form a supported lipid bilayer at the copolymer layer functionalised with F_1F_O, with F_1 facing the lumen of the droplet. Acidification of the oil by trifluoroacetic acid (TFA) rapidly increased the PMF across the supported lipid bilayer, driving ATP

synthesis. ATP synthesis was subsequently coupled to actin polymerisation and microtubule formation[80].

Recent work has focused on more biomimetic systems that can sustain ATP synthesis, namely synthetic organelles encapsulated within synthetic cells in the form of giant unilamellar vesicles (GUVs). In 2018, F_1F_O was reconstituted into SUVs with two photoconverters, photosystem II and pR, to generate synthetic organelles capable of ATP synthesis under a complete optical control within GUV-based synthetic cells[12] (**Figure 1.11A**). At high pH, photosystem II and pR work synergistically, acidifying the interior of SUVs and inducing a PMF, under red and green light respectively. However, at low pH pR exhibits a reversal in proton-pumping directionality[81]; here green light still generates PMF and activates F_1F_O while red light rapidly dissipates the PMF as protons are exported from the lumen of SUVs. This marks a major improvement over previous light-driven ATP synthesising synthetic organelles, where cessation of light resulted in a slow decline of ATP synthesis as ΔpH dissipates through F_1F_O. ATP produced by synthetic organelles powered actin polymerisation and asymmetrically deformed the GUV in a crude mimic of cellular movement. Buffering of metal ions was essential to perform actin filamentation and was accomplished with Ca^{2+} and Mg^{2+} ionophores embedded in the GUV bilayer. Fortuitously, no transfer of ionophores to synthetic organelles was observed, as this would have the effect of collapsing the membrane potential, $\Delta\Psi$, by dissipating the build-up of charge across the bilayer (see page 17) and thus would have destroyed ATP synthesis.

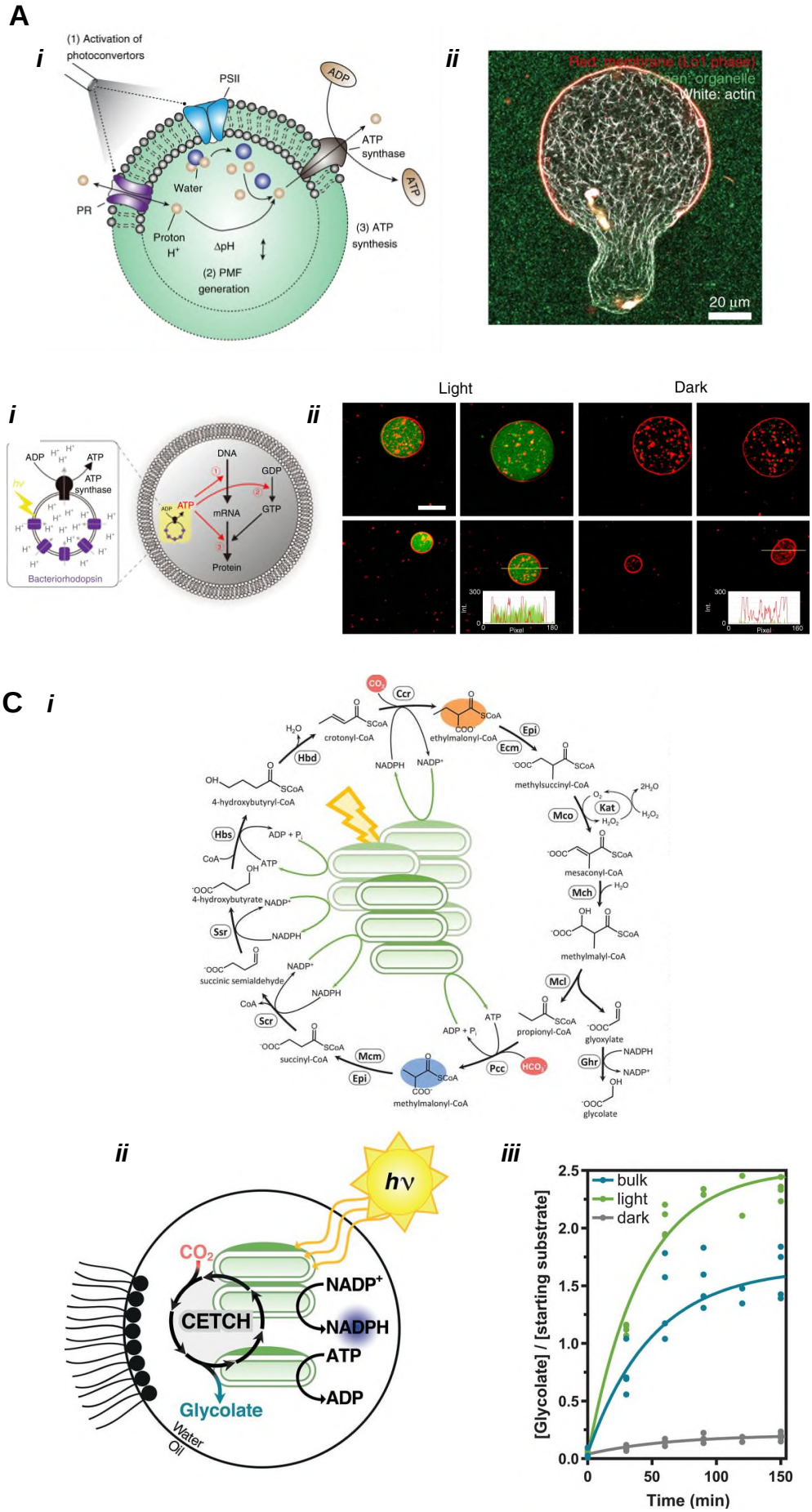
A
i
(1) Activation of photoconvertors
PSII
ADP
ATP synthase
ATP
Water
PR
Proton H+
ΔpH
(2) PMF generation
(3) ATP synthesis
ii
Red: membrane (Lo1 phase)
White: actin
20 μm
B
i
ADP
ATP
ATP synthase
hν
Bacteriorhodopsin
DNA
GDP
GTP
mRNA
Protein
ii
Light
Dark
C
i
CO2
Ccr
crotonyl-CoA
ethylmalonyl-CoA
Epi
Ecm
methylsuccinyl-CoA
Mco
Kat
mesaconyl-CoA
Mch
methylmalyl-CoA
Mcl
glyoxylate
Ghr
glycolate
propionyl-CoA
Pcc
methylmalonyl-CoA
Mcm
succinyl-CoA
Scr
succinic semialdehyde
Ssr
4-hydroxybutyrate
Hbs
4-hydroxybutyryl-CoA
Hbd
NADPH
NADP+
ATP
ADP + Pi
ii
hν
CO2
CETCH
NADP+
NADPH
ATP
ADP
Glycolate
Water
Oil
iii
bulk
light
dark
[Glycolate] / [starting substrate]
Time (min)

Figure 1.11 Light-activated ATP synthesis in synthetic cells. (**A**) ***i*** Diagram of the co-reconstitution of F_1F_O, photosystem II (PSII), and proteorhodopsin (pR). Upon illumination, PSII and pR generate the PMF inside proteoliposomes, powering ATP synthesis through F_1F_O. ***ii*** Synthesised ATP drives actin filamentation in synthetic cells, in a crude mimic of cellular movement. (**B**) ***i*** Diagram of the co-reconstitution of F_1F_O and bacteriorhodopsin into proteoliposomes and their encapsulation in synthetic cells. **ii** Upon illumination, proteoliposomes synthesise ATP and power IVTT of GFP. Scale bar 10 μm. (**C**) ***i*** Schematic of the carbon-fixing CETCH cycle. ***ii*** Upon illumination, thylakoid membranes produce ATP and NADPH. ***iii*** Synthesised ATP and NADPH power the CETCH cycle, driving the formation of glycolate. (**A**) Reproduced from Lee et al.[12], (**B**) Berhanu et al.[14], and (**C**) Miller at al.[82]

In 2019, artificial chloroplasts were coupled with an IVTT kit in synthetic cells to enable light-driven protein synthesis[14] (**Figure 1.11B*i***). Again, co-reconstitution of F_1F_O and bR into SUVs constructed synthetic organelles which upon illumination powered the IVTT of bR (**Figure 1.11B*ii***). Remarkably, synthesised bR spontaneously inserted in a vectoral manner into the synthetic organelles, enhancing the rate of ATP synthesis. Towards the same goal, F_1F_O was produced through light-activated IVTT but the much larger protein complex (520 kDa vs 25 kDa for bR) hindered insertion into the SUV bilayer. Instead, F_O was isolated from F_1 and reconstituted into synthetic organelles, alongside F_1F_O and bR. Reconstituted F_O provided a platform for IVTT produced F_1 docking, again enhancing ATP synthesis rates synthesis[14].

In 2020, Miller and co-workers assembled synthetic cells capable of carbon fixation[82]. A 16-enzyme synthetic network, the crotonyl–coenzyme A (CoA)/ethylmalonyl-CoA/hydroxybutyryl-CoA (CETCH) cycle (**Figure 1.11C*i***), was coupled to light-driven NADPH and ATP regeneration by isolated thylakoid membranes, converting CO_2 to glycolate (**Figure 1.11C*ii* - *iii***). Residual ATP synthesis in the dark, attributed to membrane-bound adenylate kinases[83], was suppressed by diadenosine pentaphosphate, an adenylate kinase specific

inhibitor. Synthetic cells were produced microfluidically in a fluorinated oil and stabilised by a perfluoropolyether-polyethyleneglycol block-copolymer surfactant. While stabilising against droplet coalescence, the surfactant inhibits any attempt at communication between synthetic cells in a tissue, preventing synthesised small molecules, ATP, and NADPH performing work at distal sites.

1.6 Summary of thesis work

This thesis describes the development of novel synthetic tissues containing compartmentalised ATP-synthesising organelles and ATP-driven biological functionality. There are three main areas of investigation within this thesis, that must be optimised and combined to achieve the final aim of light-driven ATP synthesis powering a biological function in a remote compartment. The first objective is to achieve light-dependent ATP synthesis via the generation of proteoliposomes. ATP should be generated in micromolar concentrations to sufficiently power biological functions. The second objective is to optimise an ATP-dependent biological process that can be powered by light-activated ATP synthesis and are functional within the water-in-oil emulsions that constitute our droplet networks. The final objective is to use ATP-synthesising proteoliposomes described in objective one to power the biological process optimised in objective two in a compartment separated by a lipid bilayer. To accomplish this, the lipid bilayer must be stabilised to avoid coalescence of droplets, and permeabilised with protein nanopores to facilitate the diffusion of hydrophilic chemicals across the DIB.

In **Chapter 2**, I describe the manufacturing and optimisation of synthetic organelles in the form of proteoliposomes with the ability to convert light energy to chemical energy: ATP.

In **Chapter 3**, I discuss the ATP dependent biological function under investigation: IVT. After detailing optimisation of bulk studies, I will show that transferring the system to aqueous droplets in oil requires solutions to a number of challenges.

Chapter 4 brings the previous chapters together, as I will outline a synthetic tissue capable of light-activated ATP synthesis coupled to IVT. Lipid bilayers must be functionalised to allow permeation of hydrophilic biomolecules and for this I will explore the purification and use of protein pores.

Lastly, in **Chapter 5**, I summaries the outcomes of the presented work and discuss possible future lines of investigation, such as additional ATP dependent functionality and communication between synthetic tissues and living cells.

2 Synthetic organelles capable of light-activated ATP synthesis

In this chapter, I will discuss the development of proteoliposomes capable of light-activated ATP synthesis. To create these synthetic organelles, I reconstituted two classes of membrane proteins into liposomes: *E. coli* F_1F_O ATP synthase and a light-activated proton pump. Proteoliposomes containing the light-activated proton pump pR precipitated after detergent removal to form 2D crystal sheets. Substitution of a fusion construct of pR attached to the fluorescent protein mCherry generated proteoliposomes that were stable for multiple days. The functional activity of pR-mCherry and F_1F_O as reconstituted membrane proteins was assayed using light and ATP-induced acidification of proteoliposomes, respectively. Micromolar concentrations of ATP were achieved in bulk experiments, synthesised from proteoliposomes upon illumination. Lastly, I will discuss factors leading to the stable storage of proteoliposomes.

Acknowledgement of collaboration

The research described within this chapter was carried out in collaboration with Dr Robert Ishmukhametov, a former postdoctoral research assistant in the Bayley laboratory.

2.1 Introduction

To produce ATP enzymatically in vitro, two criteria must be met. Firstly, an F_1F_O ATP synthase must be purified in an active state and secondly, the F_1F_O ATP synthase must be energised by an external force[84]. Examples exist of powering F_1F_O through the magnetic field-driven rotation of F_1[85], and application of electrical fields[86], however these are niche examples in highly constrained systems, unusable in the context of synthetic cells.

A more general approach and one used widely, is to power F_1F_O by the PMF, a combination of ΔpH and $\Delta\Psi$, the proton and electrochemical gradients respectively (see page 22). To generate a PMF, F_1F_O must first be reconstituted into a semi-permeable membrane. Membrane compositions typically attempt to recapitulate natural systems and are therefore comprised of lipids[12,14,77,79,84,87]. However, these systems are not confined to using lipids membranes, and polymer membranes have also housed F_1F_O[88]. Reconstitution of F_1F_O into a membrane is typically performed in a detergent-mediated process, with initial destabilisation of small unilamellar vesicles (SUVs) by detergent, protein addition and incorporation in membranes, and finally detergent removal[38].

While an alternative method to incorporate membrane proteins in droplet networks would be to functionalise the lipid bilayers already present – namely, the DIBs separating compartments - there are numerous drawbacks to this approach. Firstly, the surface area to volume ratio of SUVs is larger than that of a droplet – a surface area to volume ratio 1000 times higher for a 100 nm diameter SUV

compared to a 100 μm diameter droplet. This can be calculated from the following equations:

$$Volume\ of\ sphere = \frac{4}{3}\pi r^3$$

$$Surface\ area\ of\ sphere = 4\pi r^2$$

A higher surface area to volume ratio affords a faster increase in the PMF as a higher number of proton-pumping membrane proteins can be inserted into the bilayer, relative to the interior volume, leading to faster acidification.

Secondly, a larger surface area for protein insertion is available when using SUVs encapsulated in a droplet compared to the total available DIB area, which can be approximated to the surface area of the droplet. The available lipid bilayer area presented by 200 nm diameter SUVs at a concentration of 5 mg/mL within 100 μm diameter droplets is 21 times higher than the droplet surface area.

This can be estimated as follows. First, we estimate the concentration of SUVs. The surface area of a 200 nm diameter SUV can be calculated from:

$$SA = 4\pi r^2$$

Which gives a surface area of 1.26×10^{-13} m^2. As there are two lipid leaflets in a unilamellar liposome, the total surface area that is covered by lipids is approximately double this value at 2.52×10^{-13} m^2. The lipids used in this thesis, DOPC and POPA, have masses of 786.11 and 696.91 Da, and areas of 72[89] and 50[90], $Å^2$, respectively. We can calculate the mass and area of an averaged lipid molecule in this system as we know the molar ratio of DOPC:POPA – 3:1. This gives an averaged lipid with mass 763.81 Da and area 67 $Å^2$. Thus, we can estimate the number of lipids per SUV:

$$Number\ of\ lipids\ per\ SUV = \frac{SA_{exterior\ leaflet} + SA_{interior\ leaflet}}{Area\ of\ one\ lipid}$$

Giving a value of 3.9×10^5 lipids per SUV. As we know the concentration of lipid used (5 mg/mL) we can calculate the concentration of SUVs (in molar units) by rearranging:

$$mol = \frac{mass}{mw}$$

$$mol = concentration \times volume$$

$$lipid\ concentration = \frac{mass}{mw \times volume}$$

And as we know there are 3.9×10^5 lipids per SUV:

$$SUV\ concentration = \left(\frac{mass}{mw \times volume}\right) \div 3.9 \times 10^5$$

Where mass is the mass of lipid (5 mg) per volume (1 mL) and mw is the molecular weight of the average lipid (763.81 Da). This affords an approximate SUV concentration of 17 nM. We can then calculate the number of SUVs in a 200 μm diameter droplet by first calculating the volume of said droplet with:

$$Volume = \frac{4}{3}\pi r^3$$

Which gives a volume of 5.23 pL. Knowing the concentration of SUVs and the volume of SUVs, we can calculate the number of SUVs per droplet:

$$SUV_{Number\ per\ droplet} = Concentration_{SUV} \times Volume_{Droplet} \times N_A$$

Where N_A is Avogadro's number – 6.022×10^{23} mol^{-1}. Using the values established previously, one can calculate 5.25×10^6 SUVs per droplet. With a surface area 1.26×10^{-13} m^2 calculated previously, we obtain a total surface area of 6.62×10^{-7} m^2. Finally, we can calculate the surface area of the 200 μm diameter droplet from:

$$SA = 4\pi r^2$$

To be 3.14×10^{-8} m^2. Thus, we can calculate the combined surface areas of SUVs to be 21 times that of the droplet by simply:

$$SA_{ratio} = \frac{Total\ SA_{SUV}}{SA_{Droplet}}$$

Lastly is the challenge of inserting membrane proteins into a DIB. Insertion of membrane proteins into SUVs is facilitated by detergents which are subsequently removed by a variety of methods[38]; whereas, in droplet networks the detergent would remain in the system, potentially permeabilising or destabilising DIBs. Small membrane proteins such as bR have been incorporated into DIBs by diluting the sample to below the critical micellar concentration (CMC) before droplet formation[3]. It is unclear whether a large, multi-subunit protein such as F_1F_O would survive these denaturing conditions. Therefore, I decided to use proteoliposomes as the ATP synthesising machinery for the work described in this thesis.

Historically, in the field of synthetic biology, the PMF has been generated through the formation of a proton gradient across a membrane alongside the associated build-up of charge. However, one can achieve the same goal by producing a charge imbalance through selective ion transport[70]. Generating a proton gradient to power F_1F_O has been achieved through a number of methods, including acid/base transitions[71], photoacids[91], and chemically, for example boric acid esterification[72]. While successfully powering ATP production, these methods suffer from a finite lifetime of ATP synthesis as they are unable to continuously regenerate ΔpH.

An improvement to these systems is to co-reconstitute a second class of membrane protein alongside F_1F_O in proteoliposomes; proteins capable of generating ΔpH. Such proteins can produce protons through the oxidisation of water, in the case of photosystem II[12], but more commonly are proton pumps such

as bR[14,77], pR[12], and bo_3 oxidase[79]. For the work described in this thesis pR, a green-light activated proton pump found in bacteria[92] was selected for initial investigations. A light-activated proton pump affords the ability to selectively activate ATP production in specific compartments of synthetic tissues, depending on the applied stimulus, whereas a protein such as bo_3 oxidase would be in an active state constitutively[83]. To synthesise ATP, an extremely well-studied protein, the 520 kDa F_1F_O ATP synthase from *E. coli* was selected for use in this study[64,79,93,94].

2.2 Results and discussion

2.2.1 Purifying membrane proteins

The first step towards reconstituting membrane proteins into proteoliposomes is their purification in an active state. His-tagged *E. coli* F_1F_O was solubilised from native lipid membranes through a cholate mediated extraction and purified on nickel-nitrilotriacetic acid (Ni-NTA) resin, using an adapted protocol[93]. To purify pR, *E. coli* strain C43(DE3) expressing His-tagged pR were lysed via two passages through a French Press pressure cell at 16,000 psi, with the resulting inverted membrane vesicles harbouring pR solubilised by homogenisation in buffer containing 1.5% weight per volume (w/v) n-dodecyl-β-D-maltoside (DDM). Solubilised pR was charged to Ni-NTA resin and washed with solubilisation buffer before elution with buffer containing 180 mM imidazole. I observed a portion of solubilised pR to undergo irreversible binding to Ni-NTA resin, with 500 mM imidazole unable to elute this fraction of pR (**Figure 7.1*i***). At 1.5% w/v, DDM was

well above its CMC of 0.0087%[95] and it was hypothesised that the high number of DDM micelles present could be a contributing factor. Indeed, upon 10-fold dilution of solubilised pR with a DDM-free buffer prior to Ni-NTA binding, complete elution was achieved with 180 mM imidazole (**Figure 7.1*ii***). While DDM is a detergent known for its low denaturing potential[96], making it an ideal choice for membrane protein purification, its low CMC and large micelle size of 72 kDa[97] render it extremely difficult to remove from a protein sample. Due to these factors, once immobilised on Ni-NTA resin, I washed solubilised pR with a buffer containing 1% w/v n-octyl-β-D-glucopyranoside (OG) an alkyl glucoside detergent with higher CMC (0.53%)[98] and lower micelle size (8 – 29 kDa)[98] for ease of removal downstream.

With these adjustments I obtained solubilised F_1F_O and pR at an acceptable level of purity, though whether they were isolated in an active state was yet to be determined. While F_1F_O and pR required reconstitution into lipid bilayers to assay activity levels, F_1 could be investigated through an ATP hydrolysis assay. In this assay ADP, formed by the hydrolysis of ATP by F_1, was converted back to ATP at the expense of NADH. Changes in NADH fluorescence were observed on a fluorometer. Upon addition of ATP to a cocktail of F_1F_O, NADH, pyruvate kinase, and lactate dehydrogenase, as well as some small molecules, a decrease in NADH fluorescence was observed, indicating the hydrolysis of ATP. This highlighted that I had isolated at least F_1 in an active manner.

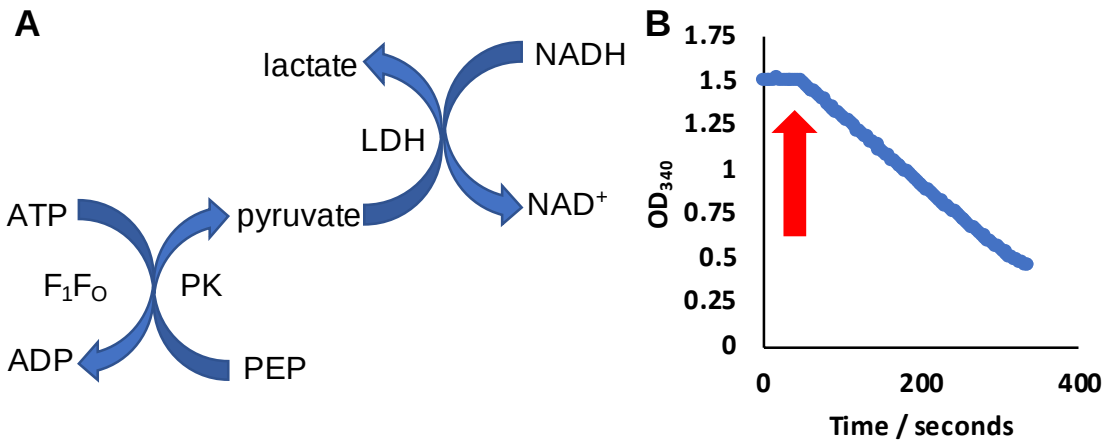

Figure 2.1 Solubilised F_1F_O ATPase activity. (**A**) ATP regenerating assay. PEP – phosphoenolpyruvate. PK – pyruvate kinase. LDH – lactatedehydrogenase. (**B**) NADH fluorescence. Red arrow indicates addition of F_1F_O.

2.2.2 Reconstitution of pR and F_1F_O

Reconstitution of membrane proteins into liposomal bilayers followed a detergent-mediated process, as outlined in the seminal work of Professor Jean-Louis Rigaud[38]. I chose a lipid composition of 3:1 DOPC:1-palmitoyl-2-oleoyl-sn-glycero-3-phosphate (POPA) as a biomimetic mimic of the anionic bacterial cell membrane[99], with previous studies validating the activity of *E. coli* F_1F_O in this lipid composition[79]. Pre-formed 200 nm SUVs were destabilised by addition of 1% w/v OG and incubated with both pR and F_1F_O for 15 minutes. Passing the lipid/protein/detergent micelles through Sephadex G50 resin assured a rapid and total removal of detergent. I performed a co-reconstitution with pR and F_1F_O. 300 μg of F_1F_O and 300 μg pR were added to 3 mg of 200 nm SUVs, to give roughly 60 F_1F_O and 1200 pR per SUV, in a 1:20 ratio, assuming complete reconstitution. This can be estimated as follows. First, we must estimate the concentration of SUVs. The number of lipids per SUV was previously calculated in **Chapter 2.1** at

a value of $3.9x10^5$ lipids per SUV. As we know the mass of lipid used per reconstitution (3 mg) we know the number of lipids to be:

$$Number\ of\ lipids = \frac{Mass}{mw} \times N_A$$

Where N_A is Avogadro's number, $6.022x10^{23}$ mol^{-1}. Using the molecular weight described in **Chapter 2.1** (763.81 Da), we obtain a value of $2.37x10^{18}$ as the number of lipids in the reconstitution. We can then calculate the number of SUVs:

$$Number\ of\ SUVs = \frac{Number\ of\ lipids}{Lipids\ per\ SUV}$$

Which gives a value of $6.06x10^{12}$ SUVs per reconstitution.

Using:

$$Number\ of\ proteins = \frac{Mass}{mw} \times N_A$$

And molecular weights of 520 kDa and 25 kDa for F_1F_O and pR respectively, we can estimate there to be $3.56x10^{14}$ and $7.23x10^{15}$ molecules of F_1F_O and pR per reconstitution. Finally:

$$Proteins\ per\ SUV = \frac{Number\ of\ proteins}{Number\ of\ SUVs}$$

To give roughly 57 molecules of F_1F_O and 1192 molecules of pR per SUV.

I investigated the activity of proteins independently before proceeding to ATP synthesis. To do so I monitored the acidification of proteoliposomes. pR and F_1F_O would acidify the lumen of proteoliposomes if reconstituted in an active state upon illumination or the addition of ATP, respectively (**Figure 2.2A**). Reconstitution of pR was successful, as quenching of a pH sensitive dye, 9-amino-6-chloro-2-methoxyacridine, ACMA[100], was observed upon illumination by a 532 nm laser (Thor labs) at an intensity of 500 mW cm^{-2} (Beam area of 3 mm^2. Upon hitting the cuvette filled the beam diffracted to illuminate the majority of the solution) (**Figure**

2.2B, green bars). Generating a pH gradient revealed that pR was inserted into the lipid bilayer vectorially, with a preference of the N-terminus facing in to the lumen of the proteoliposomes, although what proportion remained unclear.

Acidification of the lumen via F_1F_O mediated ATP hydrolysis was observed only weakly, indicative of a non-functional reconstitution (**Figure 2.2B**, red arrow). In an effort to determine the cause for this loss of activity, F_1F_O was reconstituted into proteoliposomes through a cholate-mediated reconstitution as had been performed in the literature[79]. Here, excellent ACMA quenching was observed upon addition of ATP (**Figure 2.2C**). To ensure it was not the addition of pR reducing activity, F_1F_O was reconstituted alone into proteoliposomes through an OG mediated procedure. Once again, minimal changes in ACMA fluorescence were observed (**Figure 2.2C**). Thus, it was clear that while normally considered a mild detergent[96], OG reduced F_1F_O activity and could not be used in the reconstitution protocol. OG has been known to inhibit ATP synthesis by bacterial F_1F_O's[101].

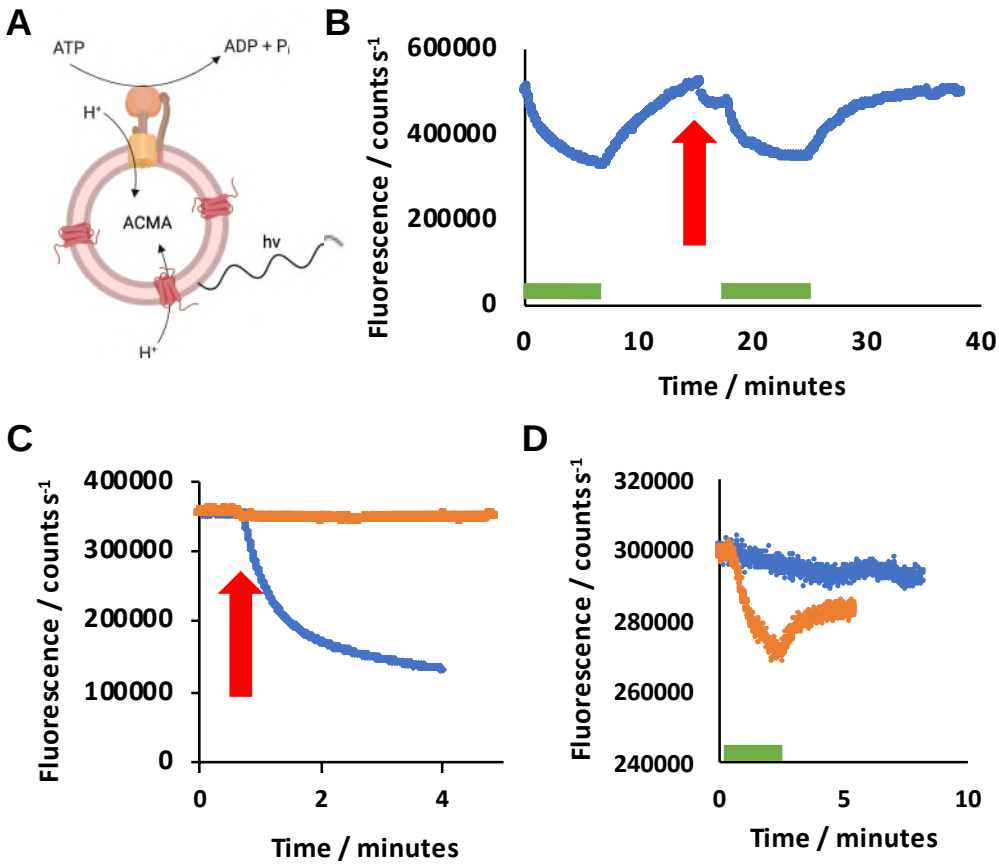

Figure 2.2 Proteoliposome acidification. (**A**) F_1F_O and pR acidify the proteoliposome lumen upon addition of ATP or light, respectively. This is visualised by ACMA, a pH sensitive fluorophore. (**B**) ACMA fluorescence in F_1F_O and pR proteoliposomes upon illumination (green bars) and ATP addition (red arrow) (**C**) ACMA fluorescence in F_1F_O proteoliposomes upon ATP addition. F_1F_O reconstituted with sodium cholate (blue) or OG (orange). (**D**) ACMA fluorescence in pR proteoliposomes upon illumination (green bars). pR reconstituted with sodium cholate (blue) or OG (orange).

As cholate facilitated the functional reconstitution of F_1F_O, I knew that if pR was in an active state in a bilayer following a similar cholate-mediated reconstitution, proteoliposomes with ATP synthesis functionality would be achieved. However, on performing reconstitutions with these parameters, it was apparent that addition of cholate severely reduced the ability of pR to generate ΔpH (**Figure 2.2D**). This led me to conclude the two proteins possessed mutually incompatible detergent requirements: pR required alkyl glucosides for activity and was inactive in cholate; while F_1F_O was non-functional in the OG tested but functional in cholate.

While these studies regarding detergent incompatibility were underway, I began to notice a different problem regarding the proteoliposomes. Proteoliposomes should remain in a homogeneous dispersion in solution, and so it was worrying to observe precipitation upon proteoliposomes containing pR. Precipitation occurred with and without F_1F_O co-reconstituted but did not occur in proteoliposomes constructed via the same protocol but containing only F_1F_O. Onset of precipitation varied between reconstitutions but always occurred after detergent removal was initiated. Precipitation on Sephadex G50 resin was common, after which a reddish band, indicative of pR, would remain immobilised (**Figure 2.3A**). When eluted, proteoliposomes would precipitate over time (**Figure 2.3B**), with no ACMA quenching observed from a sample taken from this layer. Cryo-EM studies of these particulates suggested 2D crystal sheets were forming upon detergent removal (**Figure 2.3C**). Indeed, removal of detergent from solubilised membrane proteins in the presence of lipids has been a classic method for obtaining crystal structures[102] and has been used to crystallise pR in the presence of DOPC[103].

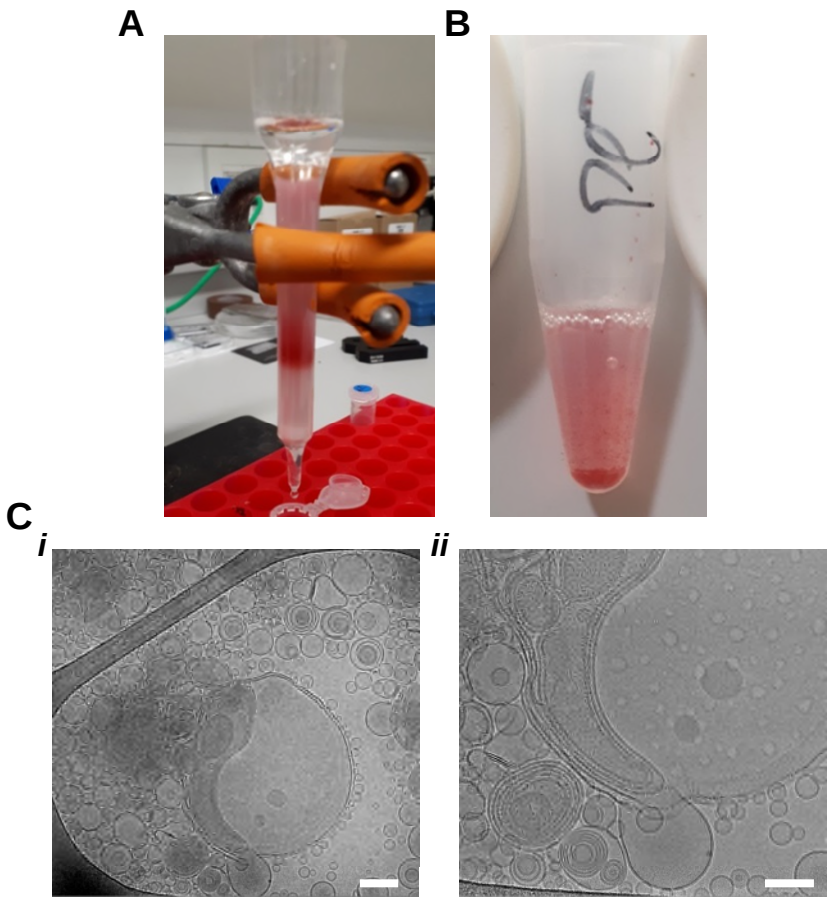

Figure 2.3 Proteoliposome precipitation. (**A**) Proteoliposome precipitation upon addition Sephadex G50 resin. (**B**) Proteoliposomes sediment after elution from Sephadex G50 resin. (**C**) Cryo-EM images of the sample from **B**. ***i*** Scale bar 500 nm. ***ii*** Scale bar 100 nm.

2.2.3 Functional co-reconstitution

As previously discussed (see **Chapter 2.2.2**) pR generated ΔpH across proteoliposome bilayers, suggesting the insertion of pR was proceeding with a bias towards one orientation; however, the exact ratio was unknown and the gradient was weak. A lack of control over membrane protein orientation in bilayers is a common issue in the development of proteoliposomes[56], and much work has gone into controlling the direction of protein insertion. This is not of concern for asymmetric proteins, such as *E. coli* F_1F_O, possessing large hydrophilic domains that are unable to penetrate the membrane – upon reconstitution over 97% of F_1F_O

is orientated with F_1 facing out[104] – but for smaller, symmetric proteins lacking large hydrophilic domains, such pR, this is a problem. One approach to bias the orientation of insertion is to use charged lipids complementary to the charge of the protein terminus one wants to be orientated facing inwards in a proteoliposome[105]. In one report, reconstituting pR with positively charged lipids resulted in a six-fold increase of N-terminus insertion compared to that using negatively charged lipids[105]. However, this was at odds to the results I observed, where pR was orientated with the N-terminus facing the lumen of the proteoliposomes, as evidenced by the acidification of proteoliposomes upon illumination.

Charged bilayers offer some control over membrane protein orientation in lipid bilayers. A more elegant approach is to use fusion constructs consisting of the desired membrane protein and a fused hydrophilic domain. One such protein was described for pR, with either mCherry or GFP fused to the N- or C- terminus respectively, which was insertion selective and in opposite directions for the two constructs[57]. pR pumps from the C to the N terminus, and so I required a construct with the fluorescent protein attached to the C-terminus. As the output of a downstream assay described later in this thesis produces green fluorescent, a new construct was designed with mCherry fused to the C-terminus (pR-mCherry).

Purification proceeded according to previously published protocols[57] with pR-mCherry solubilised in a buffer containing 3% w/v OG, with complete elution from Ni-NTA resin achieved with 250 mM imidazole. Importantly, no precipitation of proteoliposomes was observed upon reconstitution. Fortuitously, while OG was initially used to facilitate reconstitution, cholate facilitated the reconstitution of pR-

mCherry into proteoliposomes without loss of activity. Here 300 μg of F_1F_O and 600 μg pR-mCherry were added to 3 mg of 200 nm SUVs, to give roughly 60 F_1F_O and 1200 pR per SUV, in a 1:20 ratio, assuming complete reconstitution (for calculations please see **Chapter 2.2.2**). Upon illumination from a new, 530 nm LED at a power intensity of 50 mW cm^{-2}, a large pH gradient was observed across the membrane, as indicated by ACMA quenching (**Figure 2.4B**).

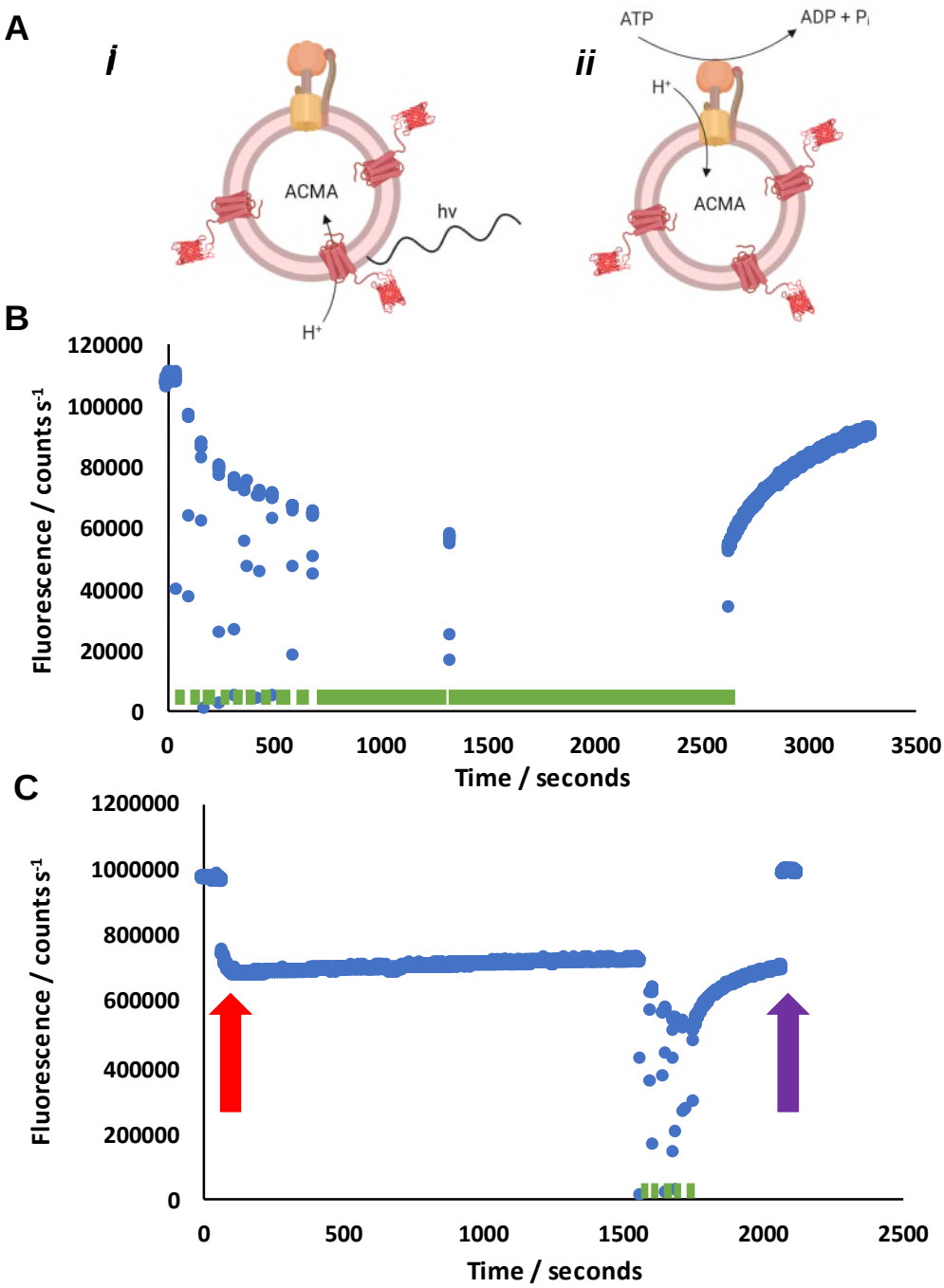

Figure 2.4 Cholate-mediated co-reconstitution. (A) ***i*** Light-dependent and ***ii*** ATP-dependent acidification of proteoliposomes is visualised by the pH sensitive fluorophore ACMA (B) ACMA fluorescence in pR-mCherry proteoliposomes, reconstituted with cholate, upon illumination (green bars). (C) ACMA fluorescence in F_1F_O and pR proteoliposomes upon illumination (green bars) and ATP addition (red arrow). CCCP dissipated the pH gradient (purple arrow). Spikes in the trace during periods of illumination (green bars) were due the manual closing and opening of a shutter that separated the sample compartment from the detector. As the closing of the shutter is not instantaneous, a gradual decrease in the detected signal was observed. The inverse is true when opening the shutter. The use of the shutter was required to not oversaturate the detector when the LED was illuminated. Data points below a set threshold of 5000 $counts^{-1}$ (representing when the shutter was fully closed) were removed for clarity.

Obtaining a cholate-tolerant pR construct enabled the co-reconstitution of pR-mCherry and F_1F_O into proteoliposomes following cholate-mediated liposome destabilisation. Both addition of ATP and illumination of the sample gave a decrease in ACMA fluorescence, highlighting the procedure had successfully maintained protein activity of F_1F_O and pR-mCherry, respectively (**Figure 2.4C**). The slow equilibration of ΔpH in **Figure 2.4C** was noticeable compared to **Figure 2.4B**, presumably due to the ATP present in the system continually powering F_1F_O acidification of proteoliposomes, opposing proton leakage across bilayers.

2.2.4 ADP purification

Having produced proteoliposomes with reconstituted F_1F_O and pR-mCherry in an active state, the next challenge was to perform ATP synthesis de novo. Here, adenosine diphosphate (ADP) and inorganic phosphate (P_i) is converted to ATP, catalysed by F_1F_O that is itself powered by the pR-mCherry induced PMF. ATP would be quantified through a bioluminescent luciferase assay[106].

Before ATP synthesis experiments, it was important to calculate the background level of ATP, either bound to the nucleotide binding domains of F_1 or impurities within ADP. Initial experiments showed that there existed a large percentage of ATP contamination in commercial ADP - 1.4% (**Figure 2.5A**). ATP contamination has been noted in the literature and in these cases, ADP has been purified through anion exchange chromatography[14], and enzymatic conversion[79].

I first attempted to purify ADP through anion exchange chromatography. A Mono Q^{TM} column was used, with ADP eluted with triethyl ammonium bicarbonate (TEAB). TEAB was selected due to it being a volatile buffer and thus removable from purified ADP stocks. An eluent high in NaCl could prove detrimental to downstream assays due to the large amount of salt brought into reactions with ADP. A considerable reduction in ATP contamination to 0.23% was observed by luciferase assay, corresponding to 23 μM in 10 mM ADP (**Figure 2.5A**). I had chosen to use a concentration 10 mM ADP due to the requirements of a downstream assay for specific nucleoside phosphate concentrations (see **Chapter 3.2.1**). This remaining ATP contamination caused me concern, as this value was close to the K_M of T7 RNA polymerase (RNAP) for ATP, which is 76 ± 22 μM[107], and this enzyme was used to carry out the IVT assays (explored in depth in **Chapter 3**). Indeed, as confirmation, this level of impurity could be detected by the IVT of a fluorescent RNA aptamer, when the reaction was deficient in ATP and supplemented with 10 mM ADP_{HPLC} (**Figure 2.5B**)

While purification via anion exchange considerably lowered ATP contamination, ATP was still present in sufficient quantities to give a poor “off” state in downstream assays. An alternative method to remove ATP impurities was to enzymatically convert ATP to ADP. In this biochemical process, hexokinase converted ATP to ADP by phosphorylating glucose to glucose-6-phosphate. After incubation at 37 ^{o}C for one hour, hexokinase was denatured at 99 ^{o}C. This was to prevent any subsequent consumption of ATP by hexokinase downstream, as the hexokinase-purified ADP was not further purified to remove hexokinase. Whilst this ADP stock was free from ATP there were impurities present: denatured hexokinase, glucose,

and glucose-6-phosphate. If the presence of these molecules proves detrimental to downstream applications there existed the option to further purify this sample, through anion exchange chromatography, as described above. ATP contamination in hexokinase-purified ADP was reduced to 0.007%, corresponding to 7 μM in 10 mM ADP (**Figure 2.5A**), and this high purity was demonstrated in the low fluorescent output seen from IVT similar to the innate fluorescence of the fluorophore (**Figure 2.5B**).

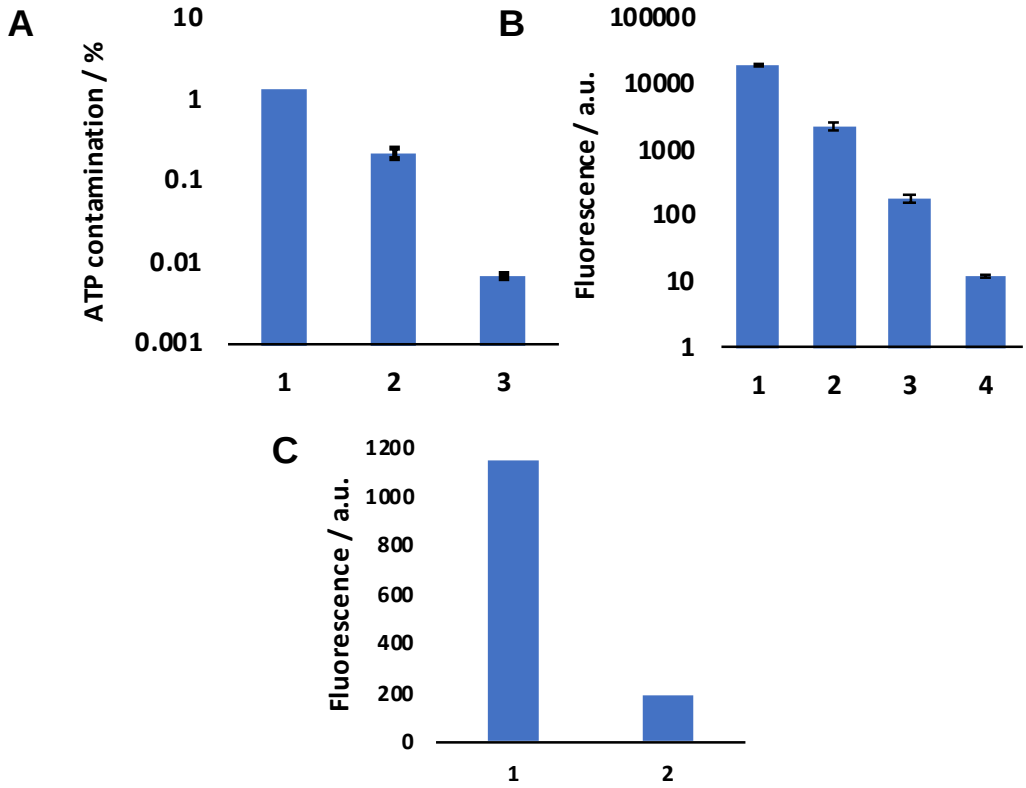

Figure 2.5 ATP-contaminated commercial ADP. (**A**) ATP impurities in **1**. Unpurified ADP, **2.** HPLC-purified ADP (ADP_{HPLC}) **3**. Hexokinase-purified ADP. (ADP_{HK}) (**B**) Fluorescence output of the IVT of the Broccoli aptamer in bulk with **1**. 10 mM ATP **2**. 10 mM unpurified ADP **3**. 10 mM ADP_{HPLC} **4**. 10 mM ADP_{HK}. (**C**) Fluorescence output of the IVT of the Broccoli aptamer in bulk with **1**. 10 mM ADP_{HK} (lyophilised) **2**. 10 mM ADP_{HK} (non-lyophilised). For **A** and **B** data points (apart from **A1**) represent the mean value from three repeats of the same experiment. Error bars represent one standard deviation about the mean.

Interestingly, upon lyophilisation of ADP samples an increase in ATP was observed in hexokinase purified ADP (**Figure 2.5C**). No increase in ATP

concentrations occurred with ADP purified by anion exchange chromatography. Glucose-6-phosphate remained in hexokinase-treated ADP and I hypothesised that this source of phosphate was facilitating ATP formation upon the sample becoming overconcentrated at the ice-water interface. This would explain why there was no increase in ATP concentration in ADP purified by anion exchange chromatography as all sources of phosphate, other than ADP, were removed. While hexokinase-treated ADP could be further purified to remove glucose-6-phosphate, I decided that this additional step was not necessary at this stage and instead I would forgo lyophilisation. Instead, hexokinase-treated ADP was pH adjusted to pH 8.00 and stored at -20 ^{o}C, with no noticeable increase in ATP concentrations observed over a year.

2.2.5 Light-activated ATP synthesis

With this newly purified ADP in hand, I turned my focus towards ATP synthesis via pR-mCherry/F_1F_O proteoliposomes (**Figure 2.6A**). Due to the sensitivity of the luciferase assay to ATP and the limited amount I possessed, proteoliposomes were diluted to a lipid concentration of 0.2 mg/mL, 20 times lower than the stock proteoliposome concentration, assuming all lipids are incorporated during reconstitution. Initial trials were promising: proteoliposomes reconstituted with 300 μg F_1F_O and 600 μg pR-mCherry achieving a concentration of 4.0 μM ATP after 30 minutes with an average initial rate of ATP synthesis of 11.6 nanomoles ATP.min^{-1}.mg $F_1F_O^{-1}$ over the first five minutes (**Figure 2.6B**). Next, I repeated this assay with proteoliposomes nearer to their working concentration. Here proteoliposomes were diluted by a factor of two before ATP synthesis was initiated.

Synthesised ATP was in this way diluted 10-fold before addition to the luciferin/luciferase cocktail, to ensure the luminometer was not oversaturated. Micromolar concentrations of ATP were observed once more, reaching a plateau of around 22.5 μM after approximately one-hour illumination, with 17.5 μM achieved after 30 minutes (**Figure 2.6C**). While the increase in ATP concentration was not proportional to the increased proteoliposome concentration, the concentration reached was in the range sufficient to power biological functions[107,108].

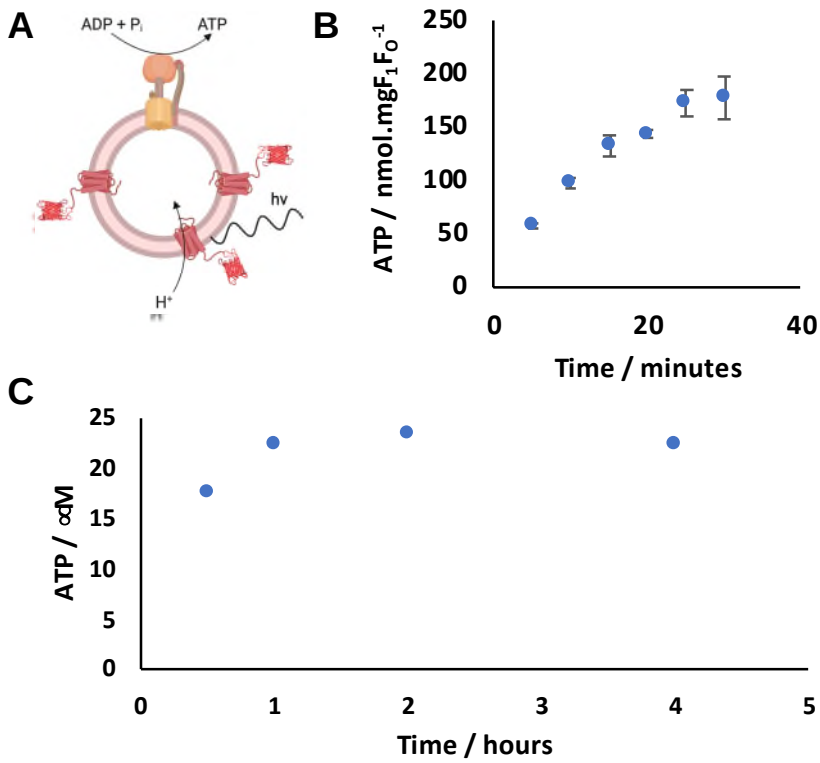

Figure 2.6 Light-activated ATP synthesis. (**A**) Upon illumination pR-mCherry generates ΔpH across the proteoliposome bilayer. Resulting PMF powers F_1F_O to synthesise ATP. (**B**) Luminescence quantification of ATP synthesis by proteoliposomes, diluted 20-fold from the working concentration. N = 2. Error bars represent one standard deviation about the mean. (**C**) Luminescence quantification of ATP synthesis by proteoliposomes, diluted 2-fold from the working concentration. N = 1.

Nevertheless, I knew improvements to ATP synthesis rates would increase the output of downstream assays. To this end, cholesterol was added to the lipid

composition of proteoliposome bilayers. Cholesterol, one of the main components of many eukaryotic membranes at between 10 – 45%[109], is known to decrease proton flux across bilayers[110,111], decrease membrane deformability[110], and modulate the activity of some membrane proteins[112]. Proteoliposomes produced with 15 and 30 mol% cholesterol showed a 2.3-fold and 5.3-fold increase in ATP synthesis over 30 minutes compared to the initial lipid composition, respectively (**Figure 2.7B**). The highest ATP synthesis rates achieved thus far, from proteoliposomes with a lipid composition of 30 mol% cholesterol and diluted twenty times before illumination, resulted in 17.5 μM ATP after 30 minutes and an initial rate of 53.2 nanomoles ATP.min^{-1}.mg $F_1F_O^{-1}$ in the first five minutes. These results are comparable to previous examples of ATP synthesis from proteoliposomes in the literature[78].

As cholesterol is known to decrease bilayer permeability[110,111] I hypothesised that this was the cause for increased rate of ATP synthesis. At high ΔpH proton flux out of proteoliposomes occurs via two mechanisms, firstly through F_1F_O, and secondly through the lipid bilayer. This second method of proton flux creates inefficiencies in the system, as some work performed by pR-mCherry is not coupled to ATP synthesis. Limiting this source of proton flux should therefore increase the PMF available to power F_1F_O. To determine whether this hypothesis held true, proton flux was examined through ACMA dequenching after ΔpH was generated via pR-mCherry driven acidification of proteoliposomes lacking F_1F_O. If cholesterol did indeed decrease proton flux, then the increase of ACMA fluorescence should be observed at a slower rate. Interestingly, after the cessation of illumination no discernible difference in proton flux through lipid bilayers was observed for

proteoliposomes with and without 30 mol% cholesterol (**Figure 2.7C**). There are other factors related to the addition of cholesterol that may be causing increased rates of ATP synthesis, such as the final size of proteoliposomes, membrane fluidity, and any potential synergistic effects between cholesterol and membrane proteins. Further work will be undertaken to establish the link between these observations. For example, by analysing the final size of proteoliposomes through dynamic light scattering and comparing with ATP synthesis data.

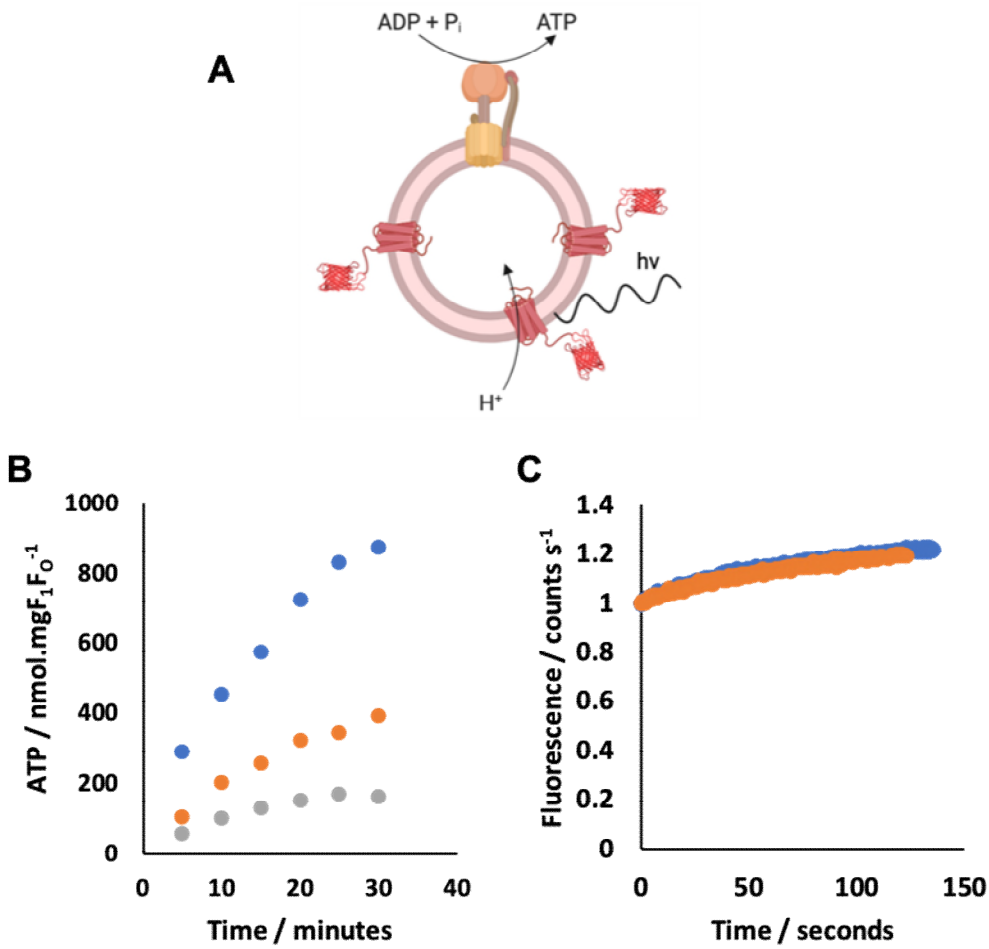

Figure 2.7 Cholesterol enhances ATP synthesis rates. (A) Light-activated ATP synthesis (B) Luminescence quantification of ATP synthesis from proteoliposomes. Proteoliposome lipid composition contain 0 (grey), 15 (orange), 30 (blue) mol% cholesterol. Each trace is from one repeat. (C) ACMA fluorescence in proteoliposomes with a lipid composition containing 0 (blue), or 30 mol% cholesterol, showing ΔpH dissipation. Each trace is from one repeat.

In the future, improvements to the ATP synthesising proteoliposomes will be performed, such as varying the ratio of pR-mCherry to F_1F_O, changing the lipid composition, initial amount and rate of detergent removal, and initial SUV size. However, as the downstream assays to be conducted in droplets had not yet been established, it was unknown what lipid compositions and protein concentrations would be tolerated. Therefore, optimisation of ATP synthesis rates would be revisited at a later date when the resulting proteoliposomes could tested in the appropriate systems.

2.2.6 Stability and storage

Stability of proteoliposomes was of concern as after five days at 4 ^{o}C ATP synthesis had decreased by 44% (**Figure 2.8B**). Initial flash freezing in liquid nitrogen resulted in aggregation of proteoliposomes upon thawing, reminiscent of issues encountered when reconstituting pR (**Figure 2.9A*i***). Aggregation did not prevent nL droplets of proteoliposome solution in a lipid-containing oil forming DIBs, although DIB area shrank over time and complete DIB disruption was observed after nine hours (**Figure 2.9B**). This coincided with sedimentation of proteoliposome aggregates, and what appeared to be association of proteoliposomes to the lipid monolayer at the oil-water interface.

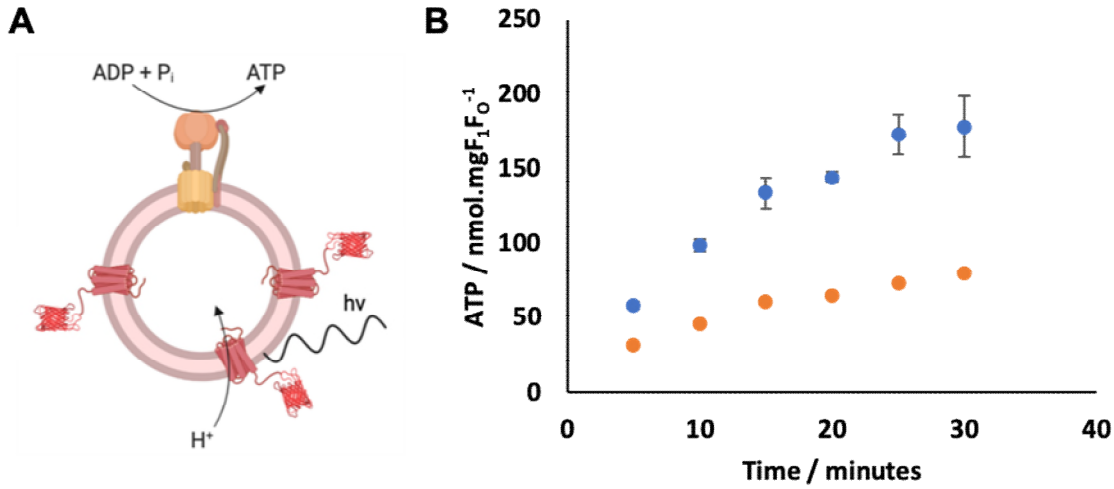

Figure 2.8 Proteoliposome stability. (**A**) Light-activated ATP synthesis. (**B**) Luminescence quantification of ATP synthesis by fresh proteoliposomes (blue) and five days later (orange). The fresh proteoliposomes are the same as in **Figure 1.6B**. The trace from the five-day old proteoliposomes is from one repeat.

To minimise aggregation, I added a cryo-preservative, glycerol[113], known to prevent protein aggregation[114] at a concentration of 33% (volume per volume) v/v before flash freezing. Upon thawing and droplet formation this new storage protocol provided a homogeneous dispersion of proteoliposomes.(**Figure 2.9A*ii***)

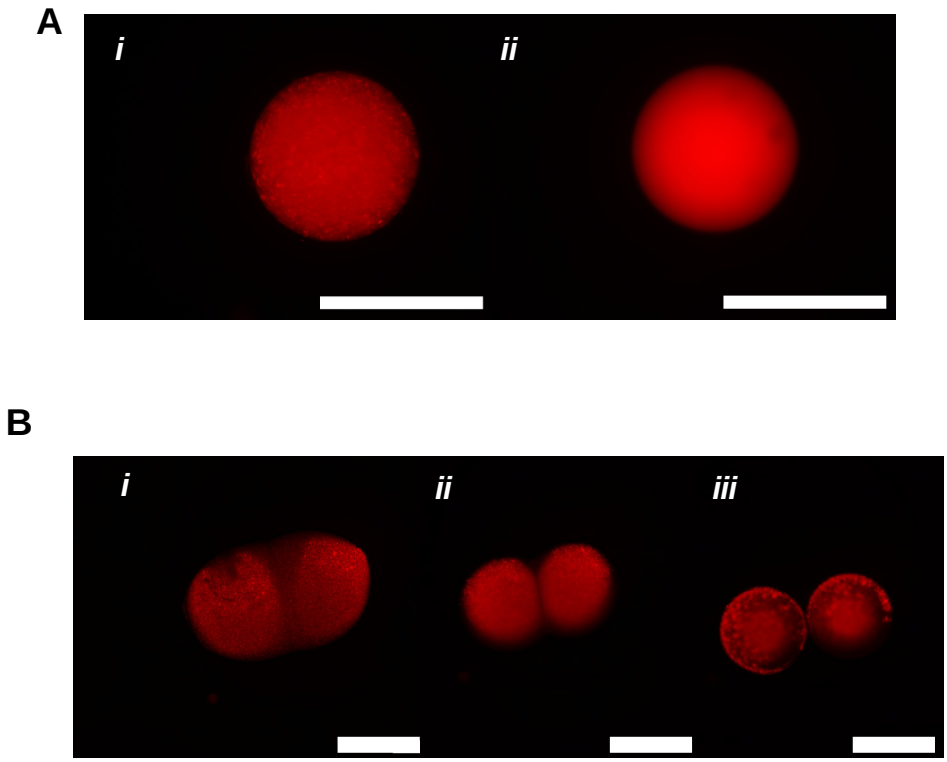

Figure 2.9 Proteoliposome aggregation. (**A**) Fluorescence microscopy image of a droplet of proteoliposomes in oil, in ***i*** the absence or ***ii*** presence of 33% glycerol. (**B**) Fluorescence microscopy images of DIB formation and disassembly with the same solution as in Figure **2.9A*i***- ***i*** Start ***ii*** 2 hours ***iii*** 18 hours. Scale bars are 500 μm.

Interestingly, aggregation of proteoliposomes in glycerol-free buffer had only a slight effect on ATP synthesis; the fluorescent output from IVT powered by proteoliposome-produced ATP is comparable when aggregated and disperse proteoliposomes are used (**Figure 2.10B**) (discussed in detail in **Chapter 3**). However, this assay was performed in single droplets, and as the development of functional tissues is required, DIBs must be formed and sustained over the timeframe of the experiments. Because of this, proteoliposomes were flash frozen in glycerol as standard for the remaining experiments described within this thesis.

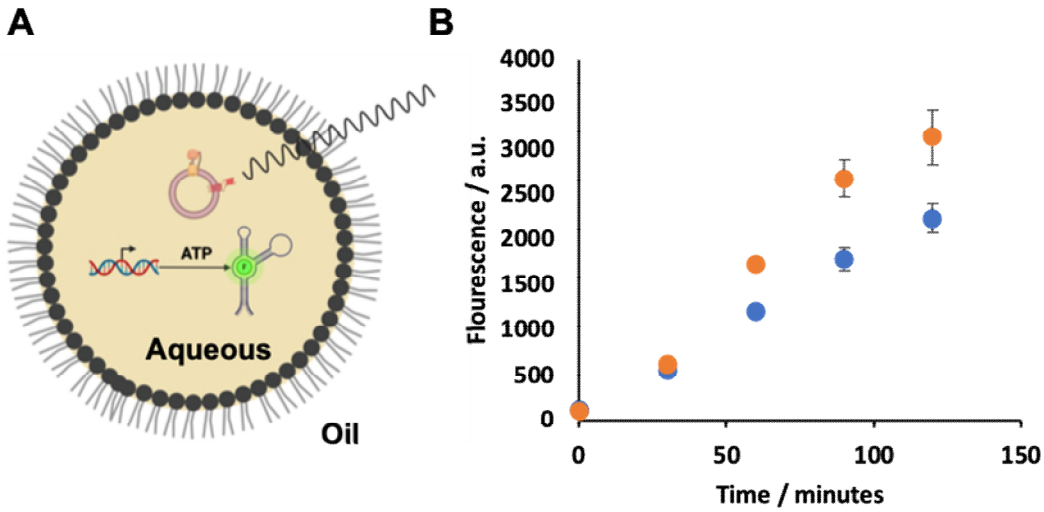

Figure 1.10 ATP synthesis capability of frozen proteoliposomes. (A) Light-activated ATP synthesis by proteoliposomes in a water-in-oil droplet powers the IVT of a fluorescent RNA aptamer (B) Fluorescence output of the IVT of the Broccoli aptamer in nL droplets with light-activated ATP synthesis by proteoliposomes in situ. Proteoliposomes were frozen and thawed once, either with (orange) or without (blue) 33% glycerol. Each data point is the mean fluorescence of three droplets from the same experiment. Error bars represent one stand deviation about the mean.

2.3 Conclusion

This chapter has described the reconstitution of membrane proteins into proteoliposomes demonstrating light-activated ATP synthesis functionality. The success of this was a combination of optimising both the reconstitution procedure and ADP purification.

Firstly, initial reconstitutions failed for two main reasons; orthogonal detergent requirements between pR and F_1F_O, and precipitation of pR proteoliposomes. A new construct, pR-mCherry, was expressed, purified and successfully co-reconstituted, alongside F_1F_O, in an active state as shown by proteoliposome acidification upon light and ATP addition, respectively.

Secondly, ATP impurities were removed from commercial ADP by anion exchange chromatography or hexokinase treatment, enabling ATP synthesis measurements. Of these two methods purer ADP was achieved through enzymatic conversion of ATP. 75:25 DOPC:POPA SUVs afforded moderate rates of ATP synthesis, with an initial rate in the first five minutes of 11.6 nanomoles ATP/min/mg F_1F_O. Addition of 30 mol% cholesterol to the lipid composition of proteoliposomes improved ATP synthesis rates, with an initial rate of 53.2 nanomoles ATP/min/mg F_1F_O, close to the reported literature. As proton flux through the lipid bilayers remains constant with and without cholesterol, the source of this effect is not known.

Lastly, aggregation of proteoliposomes was observed after flash freezing in liquid nitrogen and subsequent thawing. While this did not appear to have a significant impact on ATP synthesis rates, DIB formation was hindered. Addition of 33% v/v glycerol to the sample prior to freezing stabilised proteoliposomes in a homogeneous distribution upon thawing.

With these proteoliposomes in hand, attention will be turned next to powering biologically functionality in droplet networks, which is the focus of **Chapters 3** and **4**.

3 Optimisation of light-activated IVT in nL droplets with ATP synthesising proteoliposomes

In **Chapter 2**, pR-mCherry and *E. coli* F_1F_O were reconstituted into SUVs to generate proteoliposomes capable of light-driven ATP synthesis. This chapter describes the optimisation of a biological function in droplets, IVT, powered by the ATP produced by proteoliposomes described in **Chapter 2**. Through the use of RNA aptamers and their cognate fluorophore, a fluorescent output can be registered from IVT. Observation of a light-dependent fluorescent output in droplets required two major optimisations of the system.

Firstly, it was found that the PMF generated when proteoliposomes were added to the IVT reaction buffer leads to ATP synthesis when the solution was kept in the dark, and that this was due to imbalances in buffer pH. This spontaneous PMF was dissipated by incubating proteoliposomes in ADP_{HK}-free IVT reaction buffer; proton flux across proteoliposome bilayers dissipating the PMF.

Secondly, I found that the canonical fluorophore of the RNA aptamer used in these experiments partitioned into the oil phase of the system. A selection of fluorophores with hydrophilic moieties were synthesised and screened. One of these new fluorophores, termed DFHBI-Choline, was selected for future use as the brightest tested, insoluble in oil, and membrane impermeable. These developments allowed light-activated IVT in pL droplets to be observed and provide a prototype for the

future development of model synthetic tissues, where distinct cells communicate and ATP synthesised in one location is able to perform work in remote cells.

3.1 Introduction

ATP is ubiquitous in nature as a molecular store of energy. Countless pathways and biological functions depend upon the energy released by hydrolysis of the gamma phosphate ester bond. Producing ATP on demand has been made possible with the manufacture of proteoliposomes controlled by light[12,14,77,101] (see **Chapter 2**). Moreover, recent developments have encapsulated ATP synthesising proteoliposomes within GUVs, creating systems resembling synthetic organelles within synthetic cells[12,14]. While biological functionality has been powered within synthetic cells, thus far it has not been possible to trigger energy-dependent functions by communication between synthetic cells, a key property of tissues. In our synthetic tissues, comprised of droplet networks, communication has been enabled between synthetic cells via protein pores[51,115] and membrane proteins[116] embedded in DIBs.

However, before energy-dependent functions can be applied across cells in tissues, ATP synthesis must be demonstrated in the water-in-oil droplets that constitute our synthetic cells. To achieve this requires an ATP dependent biological output. Whilst the luciferase assay described in **Chapter 2** was investigated as a potential solution, the small droplet volume (nL) and oil environment meant signals were hard to detect. This led to the choice of T7 RNAP-dependent IVT as a model ATP-dependent process.

T7 RNAP is a 98 kDa protein isolated from bacteriophage T7-infected *E. coli* in 1970[117], which possesses a number of properties that make it extremely suitable for IVT. It consists of a single polypeptide subunit[118] and requires no additional protein factors[119], in contrast to the multi-subunit prokaryotic and eukaryotic RNAPs. It has high specificity to its cognate T7 promoter[120], and undergoes efficient elongation - around five times faster than *E. coli* RNAP[121].

Whilst in theory an IVT output could be most obviously measured by RNA sequencing, in practice the cost is prohibitive. Instead, a more elegant approach is to utilise the fluorescent RNA aptamers first developed in the laboratory of Professor Samie Jaffrey[122]. In 2011, Jaffrey and co-workers published a seminal study showing that a fluorescent signal could be activated by restricting the free rotation of a mimic of the chromophore of green fluorescent protein (GFP) upon binding of the small molecule to an RNA aptamer (**Figure 3.1A**). Initially this aptamer, termed Spinach, was shown to bind to a range of fluorophores exhibiting a wide range of excitation wavelengths[122]. One such fluorophore, (5Z)-5-[(3,5-Difluoro-4-hydroxyphenyl)methylene]-3,5-dihydro-2,3-dimethyl- 4H-Imidazol-4-one (DFHBI, **Figure 3.1A*i***), with an excitation/emission of 447 and 501 nm, respectively, was selected as the standard for future studies, due to existing predominantly in the more fluorescent phenolate form at physiological pH[122]. Numerous examples of aptamer-fluorophore pairs followed with different spectral properties: for example, Spinach 2[123] and Broccoli using DFHBI has the fluorophore; Mango and TO1-Biotin[124], Corn and DFHO[125,126], and Pepper and HBC[127].

3.2 Results and discussion

3.2.1 Optimising *in vitro* transcription in bulk

The aptamer construct used in this thesis was first described in 2016[128] and consisted of a pair of dimeric Broccoli aptamers to give a total of four DFHBI binding pockets. These aptamers were fused to the RNA scaffold F30[129] to facilitate folding and afford protection from RNases[128]. For simplicity this construct will from now on be referred to as Broccoli.

I linearised the gene encoding Broccoli from a plasmid by polymerase chain reaction (PCR). In bulk studies, a titration to ascertain the minimum ATP concentration required to register a fluorescent output revealed that between 10 and 100 μM would be sufficient, when all other nucleoside triphosphates (NTPs) are in excess (**Figure 3.1B**). This correlates with the K_M of T7 RNAP for ATP, 76 ± 22 μM[107] and is similar to the concentrations produced by the proteoliposomes described in **Chapter 2**. This result validated the use of IVT, and the Broccoli aptamer specifically, as a suitable readout for ATP synthesis.

T7 RNAP is supplied commercially in a number of forms from New England Biolabs (NEB). For this work the HiScribe™ T7 High Yield RNA Synthesis kit was initially chosen for use. The differences between the HiScribe™ enzyme supplied in this kit and the regular T7 RNAP sold by NEB are unknown and proprietary, however one consequence is that the former uses a higher concentration of NTPs, 10 mM vs 0.5 mM per NTP respectively. In total 40 mM NTPs, following the

recommendations from the HiScribe™ T7 High Yield RNA Synthesis kit, were hereafter used in this work. it is possible that the higher concentration of NTPs may aid IVT visualisation in synthetic tissues, although this is uncertain as these concentrations are well above the K_m of T7 RNAP[107].

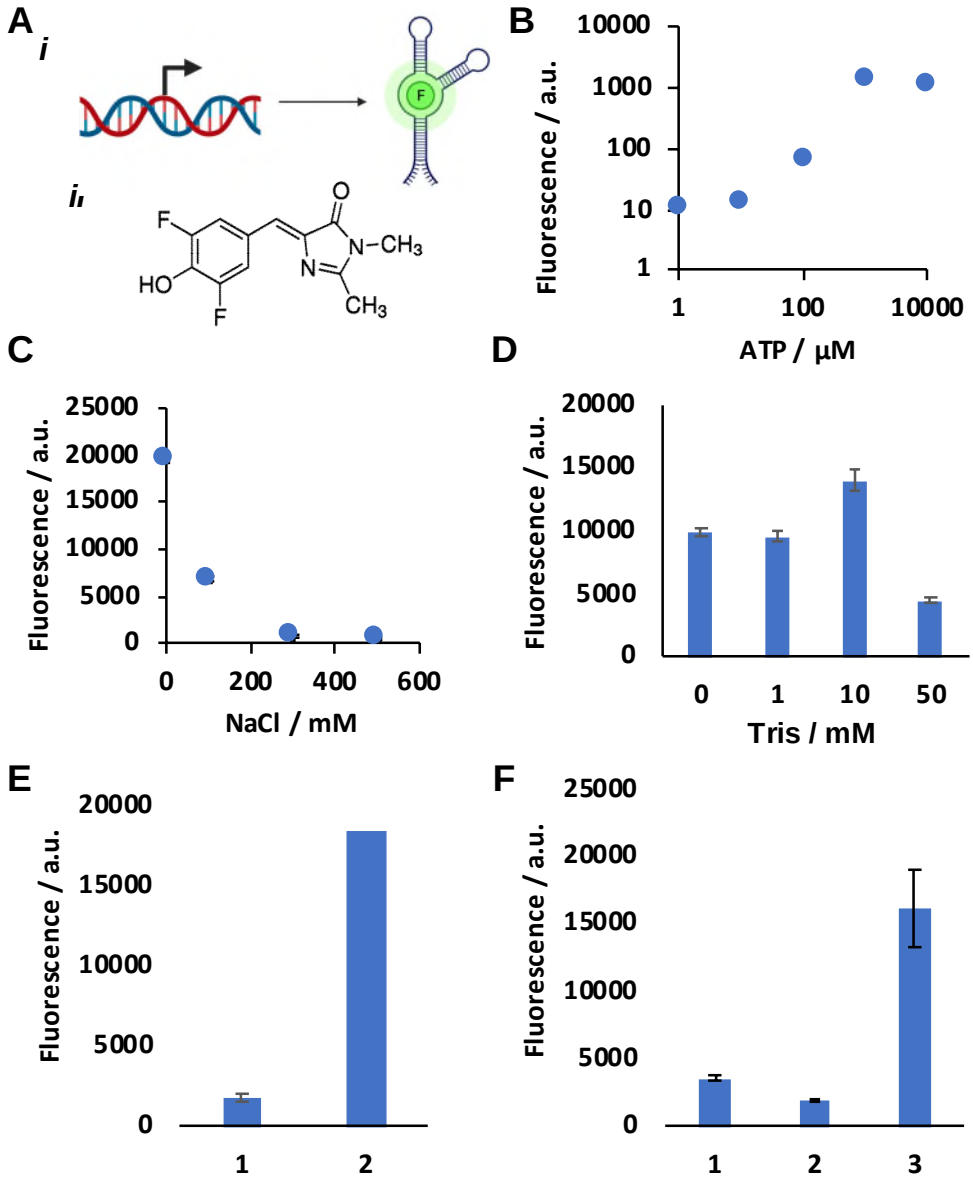

Figure 3.1. Optimising the *in-vitro* transcription of Broccoli aptamer in bulk. (**A**) ***i*** Schematic showing fluorescence activation of a fluorophore upon transcription of its cognate aptamer. ***ii*** The cognate fluorophore for Broccoli, DFHBI. (**B**) Transcription is dependent on ATP concentration, highlighting 10 and 100 µM ATP required to visualise Broccoli transcription. (**C**) Fluorescence output in response to varying concentrations of NaCl. (**D**) Fluorescence output in response to varying concentrations of Tris. (**E**) Fluorescence output with IVT powered by either Tris (**1**) or unbuffered (**2**) NTPs. (**E**) Fluorescence output in one-month old buffer (**1**) or a new buffer with (**2**) or without (**3**) 1 mM DTT. **B** represents one repeat for each data point. **C** – **E** N = 3. Error bars indicate one standard deviation about the mean.

While the HiScribe™ and its buffer are proprietary, it was necessary to have knowledge of the composition of the IVT buffer for a couple of reasons. Firstly, so that the internal and external buffer compositions of proteoliposomes can be matched, to minimise pH imbalances that would give rise to ATP being made in the dark (**see Chapter 3.2.2**) and the osmotic imbalances that could rupture proteoliposomes. The rupture of proteoliposomes would result in loss of IVT function and an increase in ATP hydrolysis from the subsequently unpowered F_1F_O. Secondly, other group members had encountered difficulties caused by NEB's tendency to alter its buffer composition without warning. This fact would make it impossible to compare new experiments with previous work. On these grounds I decided to prepare my own IVT buffer to use going forward.

The new buffer comprised spermidine as an activator of T7 RNAP activity[130], and dithiothreitol (DTT) to keep key cysteines in T7 RNAP reduced[131]. Magnesium ions were required at a higher concentration than the total concentration of NTPs, as magnesium is required for T7 RNAP activity but is chelated by NTPs[132,133]. Accordingly, $MgCl_2$ was added at a concentration of 50 mM, which is 10 mM more than the NTP concentration. Subsequently, a 10 mM excess of magnesium over NTPs has been confirmed in the literature as optimal for IVT yield[134].

I performed a NaCl titration (**Figure 3.1C**), which showed that salt was deleterious to IVT yield, with a 34% reduction of fluorescence output at 100mM NaCl compared to 0 mM NaCl. I therefore did not include NaCl in the buffer composition. While it is known high salt inhibits transcription by the disruption of electrostatic interactions between the positively charged T7 RNAP binding domain and negatively charged

DNA[135,136], the experiments described in Fig 3.1 do not reveal if IVT is inhibited, or Broccoli-DFHBI fluorescence lowered. As both factors must be optimised to visualise IVT in droplets, this ambiguity is not of concern.

I theorised that excess buffer would bring in additional salt, and so looked at changes caused by varying the concentration of tris(hydroxymethyl)aminomethane (Tris) in the reaction (**Figure 3.1D**). 40 mM NTPs were used in the reaction and so 50 mM Tris was used initially; however, as hypothesised, lowering the Tris concentration to 10 mM afforded an increased fluorescent output. Decreasing Tris concentration further proved detrimental to fluorescence, and so 10 mM Tris was used throughout. It is worth noting that NTPs do offer some buffering capacity. Commercial Tris-buffered NTPs from Thermo Scientific™ exhibit a deleterious effect on fluorescence output similar to increasing the Tris concentration (**Figure 3.1E**), and so were not used. Instead NTPs, pH adjusted to around pH 8.00, were purchased from Thermo Scientific™.

Despite these preparations, large variations in fluorescence output were observed between experiments. Remaking the IVT buffer returned fluorescence to its peak, but this was followed by a gradual decline with ageing. Of the buffer components (Tris, $MgCl_2$, Spermidine, DTT), DTT appeared the likely candidate for degradation, with a half-life of 1.4 hours at pH 8.50 and 20 ^{o}C[137]. Indeed, a comparison of one-month old buffer (stored at -20 ^{o}C but undergoing multiple freeze-thaw cycles) showed a similar level low of fluorescence to an IVT buffer deficient in DTT indicating both that DTT was crucial to the reaction, and that DTT was oxidising over time (**Figure 3.1F**). Addition of 1 mM DTT to the buffer before

initiating IVT restored the fluorescence output. I hypothesised buffer with a low concentration of DTT would inhibit transcription via the oxidation of key cysteines in the active site of T7 RNAP. A new protocol was thus established; IVT buffer was prepared with all components minus DTT, aliquoted, and DTT added to an aliquot which was then used for one week before being discarded.

3.2.2 Light-activated ATP synthesis in large, nL, droplets

Having optimised the fluorescence output of the Broccoli aptamer in bulk, I turned my attention to powering IVT in droplets with ATP produced from proteoliposomes. (**Figure 3.2A**). 100 nL droplets of a proteoliposome/IVT solution were dispensed by micropipette into lipid-containing oil in a custom-made poly(methyl methacrylate) (PMMA) well array. For this experiment the 10 mM ATP used in the bulk optimisation studies was replaced with 10 mM ADP_{HK} and 10 mM NaP_i. PMMA well arrays containing droplets were sealed in a hydrated petri dish to minimise droplet dehydration and either illuminated with a 530 nm LED or shielded from light. Unexpectedly, after a two-hour incubation at 37 ^oC a greater fluorescent signal was observed for the control droplets shielded from light than illuminated droplets (**Figure 3.2B**). After ruling out potential sources of ATP contamination (**Figure 3.2C**), it was clear that ATP was being made in the dark.

If there exists a pH imbalance between the proteoliposome lumen and exterior, specifically if the lumen is at lower pH, a PMF will be generated, F_1F_O powered, and ATP synthesised. This concept is similar to an acid/base transition commonly used to artificially power F_1F_O in proteoliposomes[71] whereby proteoliposomes are

incubated in an acidic buffer before being transferred to a basic solution. My decision to prepare custom IVT and reconstitution buffers was performed partly to ensure this pH imbalance did not occur. One solution to this problem was to prepare new IVT and reconstitution buffers with varied pH to minimise the resulting pH gradient across proteoliposome bilayers. However, I hypothesised it was possible, and quicker, to dissipate ∆pH without any corresponding ATP synthesis by incubating proteoliposomes with an IVT cocktail lacking either ADP_{HK} or NaP_i. This method also had the advantage of not consuming any more pR-mCherry or F_1F_O in additional reconstitution attempts. In IVT buffer deficient of the required reagents to make ATP, the PMF would dissipate through spontaneous proton flux across proteoliposome bilayers. I hypothesised that when the missing reagents were added no ATP synthesis would be observed due to the lack of a PMF and any subsequent ATP synthesis would be as a result of the light-driven increase in ∆pH.

I prepared solutions of proteoliposomes with an IVT cocktail containing 10 mM ADP_{HK} but deficient in NaP_i (**Figure 3.2D**). These solutions were incubated in the dark at 37 ^oC for varied lengths of time to dissipate residual ∆pH. Solutions were then charged with 10 mM NaP_i and incubated for a further two hours in the dark before fluorescence was quantified. A positive correlation between ∆pH dissipation time and fluorescence indicated ATP synthesis initiated immediately once solutions were prepared, even in the absence of NaP_i. If instead ATP synthesis initiated upon addition of NaP_i one would expect a uniform level of fluorescence, due to the subsequent two-hour incubation being constant between solutions. This

demonstrated there was an additional source of P_i in the reaction, potentially contamination in the remaining NTPs or from ADP_{HK}.

The above experiment was repeated with ADP_{HK} removed and 10 mM NaP_i added to the initial IVT cocktail during the ∆pH dissipation period. After this varied length of time I then added 10 mM ADP_{HK} and incubated the solutions for a further two hours. Upon fluorescence quantification I observed an exponential decrease in fluorescence relative to the time allowed for ∆pH dissipation, with a 93% decrease in fluorescence after two hours. This indicated that indeed ∆pH was dissipating across the proteoliposome bilayer during this period, and this resulted in lower levels of synthesised ATP in the absence of light. Therefore, before any proteoliposome-driven IVT reactions with this batch of proteoliposomes I performed a two-hour incubation, minus ADP_{HK}, to dissipate ∆pH; the optimal incubation time for individual batches of proteoliposomes varied and was determined experimentally each time.

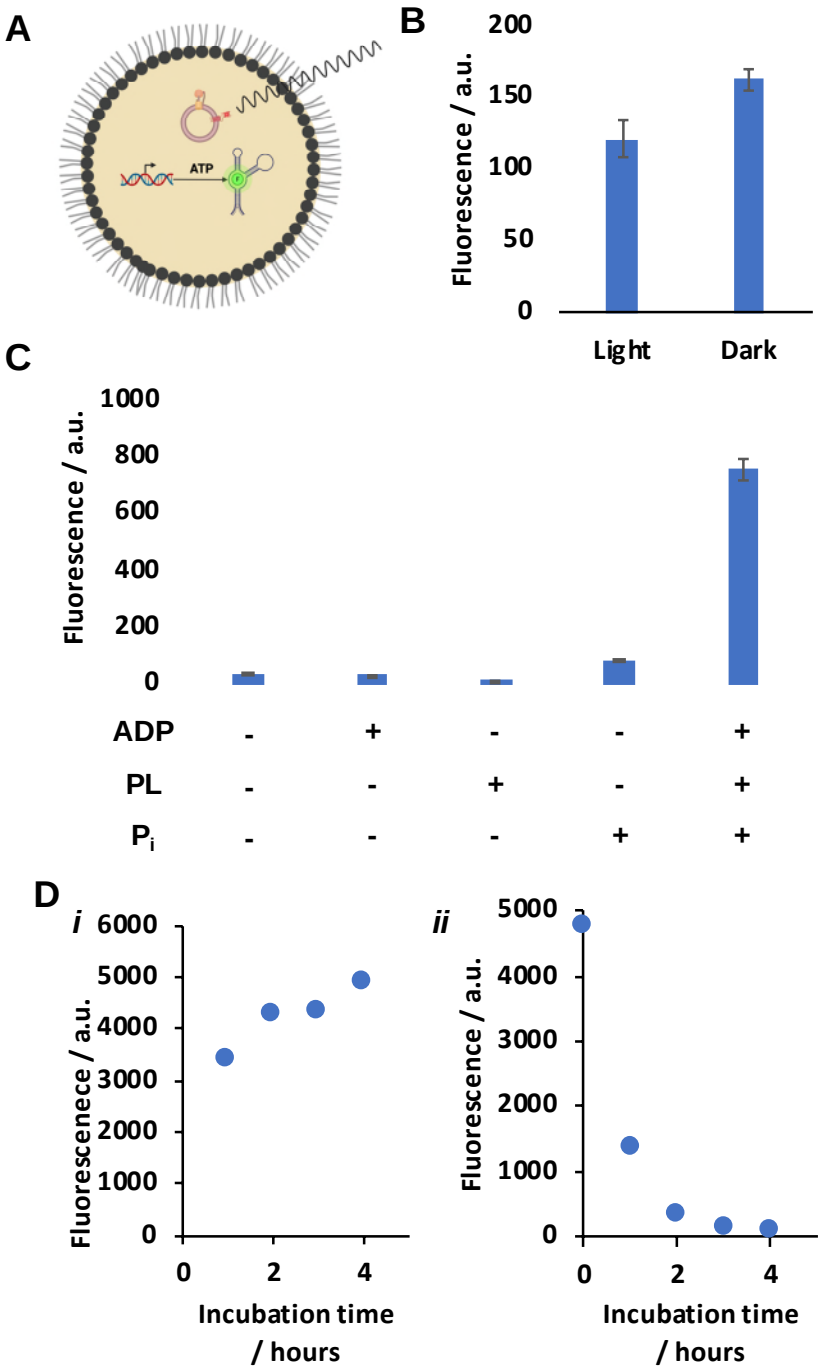

Figure 3.2. Residual pH gradients across proteoliposome bilayers drives ATP synthesis in the dark. (**A**) Diagram detailing light-activated ATP synthesis coupled to IVT in a water-in-oil droplet. (**B**) Fluorescence of droplets either illuminated or shielded from light. (**C**) Investigating sources of potential ATP contamination. Fluorescence observed when all components of ATP synthesis are present indicates ATP made *in situ*. (**D**) Fluorescent IVT output in bulk after an initial incubation period in the absence of ***i*** NaP_i or ***ii*** ADP_{HK} to dissipate proteoliposome pH gradient. In **B** and **C** each data point represents the mean fluorescence of three droplets from the same experiment. Error bars represent one standard deviation about the mean. In **D** each data point is from one repeat.

With this new pre-incubation protocol, proteoliposome-powered IVT was attempted in single, nL, droplets (**Figure 3.3A**). A light-dependent increase in fluorescence was observed (**Figure 3.3B**, grey), while droplets kept in the dark showed an identical level of fluorescence as control IVT droplets lacking proteoliposomes (**Figure 3.3B**, orange and blue, respectively). This demonstrated both light-activated ATP synthesis and the subsequent incorporation of ATP into RNA in synthetic cells; key milestones towards powering biologically relevant functions in synthetic tissues.

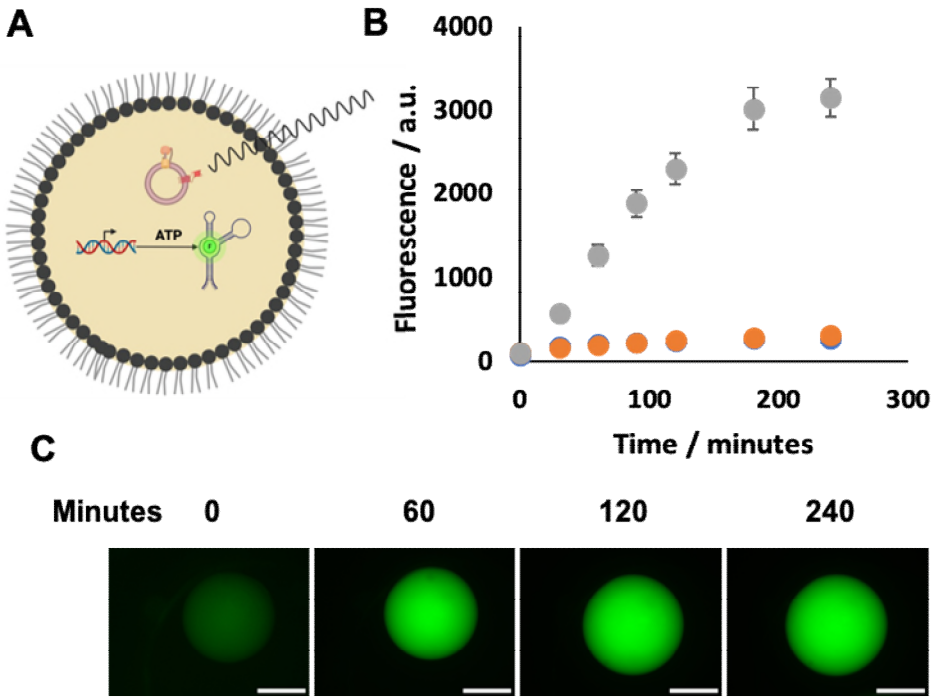

Figure 3.3. Light activated ATP synthesis in nL droplets. (**A)** Light-activated ATP synthesis by proteoliposomes in a water-in-oil droplet powers the IVT of a fluorescent RNA aptamer. (**B**) Fluorescence of droplets illuminated (grey), shielded from light (orange), or in the absence of proteoliposomes (blue). Each data point represents the mean fluorescence of three droplets from the same experiment. Error bars represent one standard deviation about the mean. (**C**) Representative images of illuminated droplets from **B**. Scale bars are 300 μm.

3.2.3 Preventing aggregation of proteoliposomes at the oil-water interface

The structural integrity of proteoliposomes is critical to their function. Not only would ruptured proteoliposomes diminish ATP synthesis rates, any unpowered F_1F_O would hydrolyse ATP. I was therefore concerned to observe an intense fluorescent red band, from pR-mCherry, at the oil-water interface of proteoliposome-containing droplets after two-hours in oil (**Figure 3.4B**). I was unable to determine if proteoliposomes had fused with or aggregated at the oil-water interface from these data, although both were of concern for separate reasons.

In the first example, I hypothesised any potential fusion of proteoliposomes at the interface would occur in a similar fashion to the lipid-in approach to DIB formation[27], where liposomes encapsulated inside a lipid-in-oil droplet fuse at the phase interface to form a lipid monolayer coating the droplet (**Figure 2.1B**). In the case of proteoliposomes, instead of liposomes encapsulated within droplets the resulting monolayer would functionalised with membrane proteins. This technique has been demonstrated by Paula Booth and co-workers with proteoliposomes with a reconstituted sugar transporter, LacY[33]. In my system F_1F_O inserted into the lipid monolayer at the interface would hydrolyse ATP, with corresponding proton transport from the aqueous solution to the oil phase (**Figure 3.4C**). Due to the large volume of oil, negligible ΔpH or $\Delta\Psi$ would be generated by ATP hydrolysis. As a large ΔpH or $\Delta\Psi$ slows the rate of ATP hydrolysis in this case ATP would be

continuously hydrolysed. To prevent F_1F_O ATPase activity I added a known inhibitor of F_1 ATP hydrolysis to the IVT buffer, 10 mM NaN_3[138]. Previously it has been shown this concentration of NaN_3 has no inhibitory effect on IVT function[14]. While NaN_3 addition may prevent ATPase activity, rupturing of proteoliposomes would still be deleterious towards ATP synthesis.

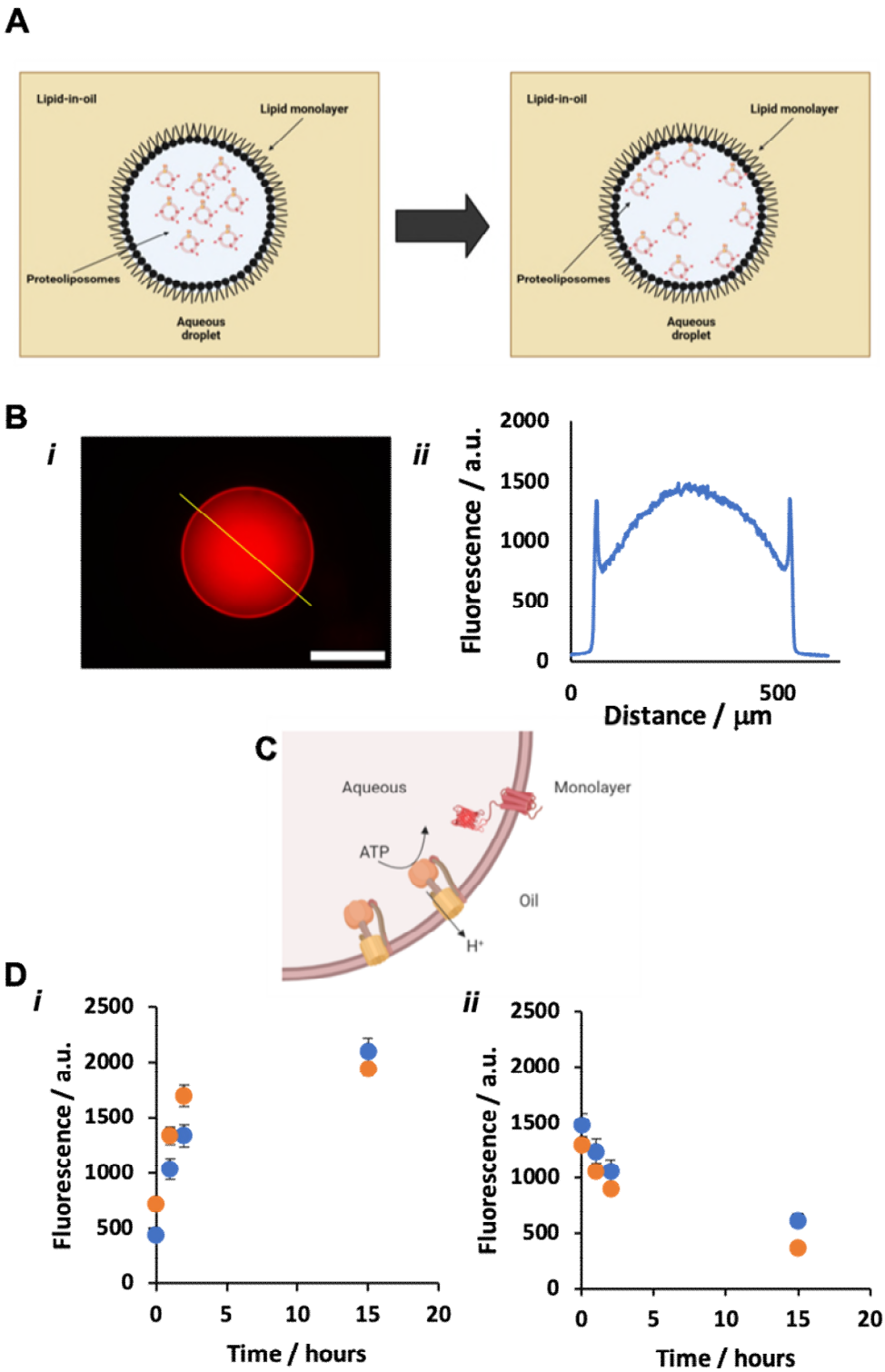

Figure 3.4. Aggregation of proteoliposomes at the oil-water interface. (**A**) Proteoliposomes may associate or aggregate at the oil-water interface. (**B**) ***i*** Representative image showing proteoliposomes aggregation at the periphery of a water-in-oil droplet. ***ii*** Line profile of ***i*** (indicated by yellow line). Scale bar is 300 μm (**C**) Schematic of possible ATPase activity of a F_1F_O functionalised lipid monolayer formed by proteoliposomes fusing with water-oil interface. (**D**) Addition of an anionic lipid, POPA, to the lipid-in-oil does not prevent ***i*** proteoliposome aggregation at the lipid monolayer or ***ii*** proteoliposome depletion from the droplet centre. Each data point represents the mean fluorescence of three droplets from the same experiment. Error bars represent one standard deviation about the mean.

Furthermore, there was cause for concern if proteoliposomes were not fusing but instead aggregating near the lipid monolayer. An aggregation of proteoliposomes near the oil-water interface could form a barrier between the bulk aqueous solution and DIBs, isolating droplets and preventing synthesised ATP from diffusing between compartments and powering biological functions in neighbouring droplets. Therefore, I sought to maintain proteoliposome homogeneity in solution. Two possible solutions came to mind: electrostatic and steric repulsion.

I first attempted to maintain proteoliposome homogeneity through electrostatic repulsion, as proteoliposomes already possessed a net negative charge due to a lipid composition containing 17.5 mol% POPA. I produced an anionic lipid-in-oil solution containing DPhPC:POPA in a 3:1 ratio and formed nL droplets of a proteoliposome-containing solution in this oil and tracked changes in mCherry fluorescence at both the oil-water interface and bulk solution over time. A negligible difference in fluorescence intensities was observed (**Figure 3.4D**) in droplets formed in 3:1 DPhPC:POPA and those formed in DPhPC, both showing a similar trend in fluorescence, indicating that this lipid composition had no effect on proteoliposome aggregation. Thus, I chose to investigate alternative methods of preventing proteoliposome association with the monolayer.

I hypothesised that addition of a PEGylated lipid to the lipid in oil solution would prevent proteoliposome fusion through steric hindrance. At low concentrations PEG chains inserted in a membrane will exist in a mushroom conformation; a bunched, globular structure similar to PEG in solution[139]. A brush regime emerges where, upon reaching a threshold density, polymer chains overlap and linearise[139].

PEGylated lipids have previously been used to modulate the interactions between proteoliposomes and planar bilayers[140]. In this study, I selected 1,2-dipalmitoyl-sn-glycero-3-phosphoethanolamine-N-[methoxy(polyethylene glycol)-2000 (DPPE-PEG2000) as the PEGylated lipid for study due to previous work showing DPPE-PEG2000 stabilised the encapsulation of an IVTT kit within a droplet network[115]. It is known that when it is incorporated in a lipid bilayer at 3 mol%, PEG2000 will exist in the so-called mushroom regime, and at 10 mol% in the so-called brush conformation. I hypothesised that addition of PEG to the lipid monolayer of droplets would, in addition to preventing proteoliposome aggregation, also sterically hinder the insertion of protein pores into DIBs, hindering small molecule diffusion across DIBs. Inhibiting small molecule diffusion between droplets would preclude formation of synthetic tissues, and so chose to incorporate PEG into bilayers at a concentration that would maintain a mushroom conformation. This assumes PEGylated lipids assemble to form the lipid monolayer at an equal rate to DPhPC.

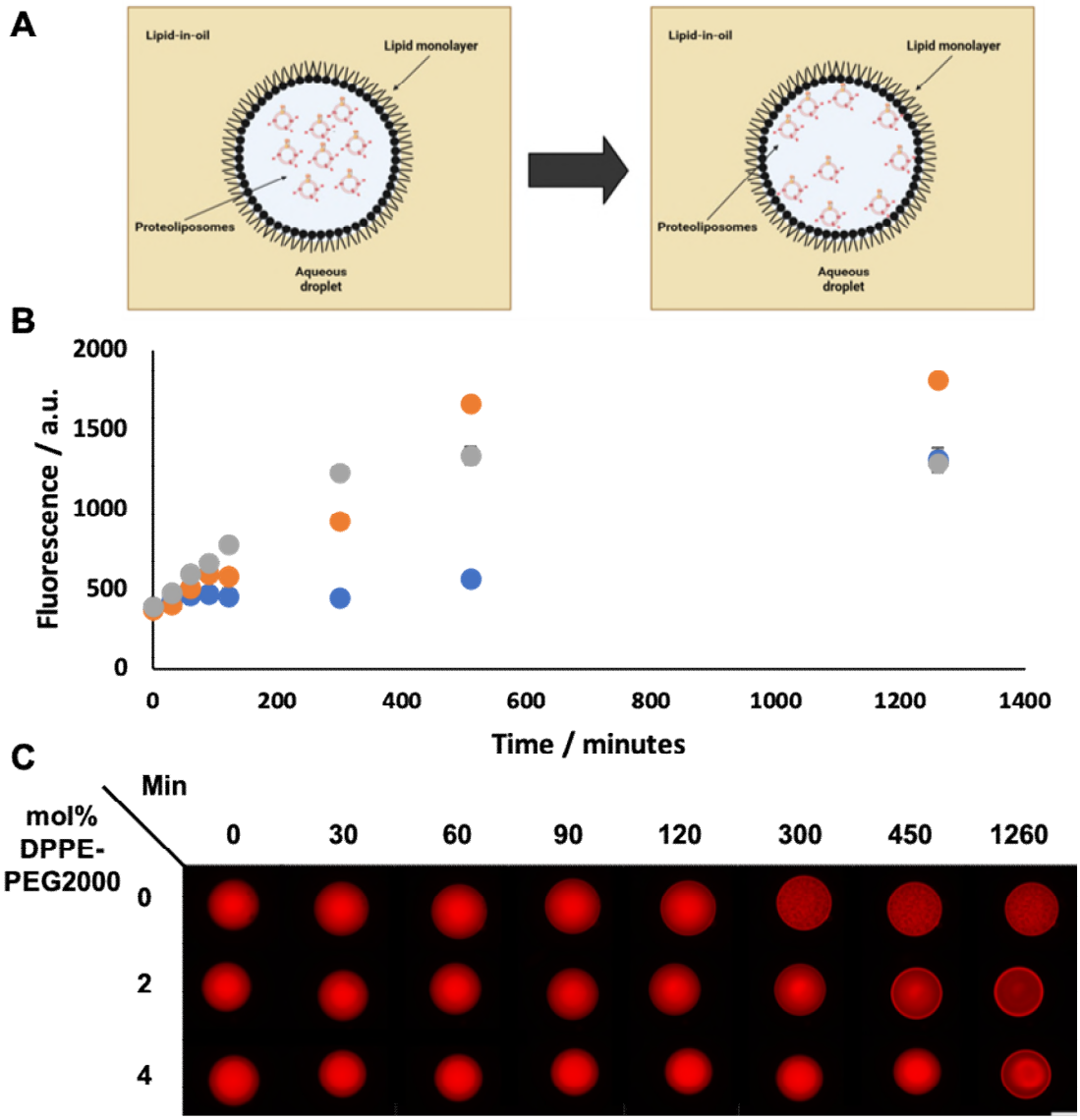

Figure 3.5 PEGylated lipids maintain proteoliposome homogeneity. (**A**) Proteoliposomes may associate or aggregate at the oil-water interface. (**B**) Fluorescence intensity of the oil-water interface. An increase in fluorescence indicates proteoliposome aggregation at the droplet periphery. Droplets were formed in 2 mM total lipid comprised of 0 (grey), 2 (orange), or 4 (blue) mol% DPPE-PEG2000 in DPhPC. Each data point represents the mean of three droplets from the same experiment. Error bars represent one standard deviated about the mean. (**C**) Representative images from **B**. Scale bar is 300 μm.

Upon formation of nL droplets in oils with increasing DPPE-PEG2000 concentrations I observed that addition of a PEGylated lipid decreased aggregation of proteoliposomes at the oil-water interface (**Figure 3.5B**). As expected, after two hours a prominent red ring had formed around droplets formed

in 100% DPhPC. This red ring was visible at the oil-water interface, at the boundary between mCherry fluorescence in red and the black background. A clear example of this phenomenon is present in the droplet formed in 2 mol% DPPE-PEG2000, at T = 1260 minutes. Rather than a homogenous distribution of proteoliposomes, there appears to be an area of low fluorescence adjacent to the oil water interface and a band of high fluorescence at the interface. This can also be seen in both the image and related trace in **Figure 3.4B**). While still visible, the red ring was weaker in droplets formed in 2 and 4 mol% DPPE-PEG2000 (**Figure 3.5C**), indicating that steric hindrance maintained proteoliposome homogeneity. At five hours proteoliposomes in the bulk appeared heterogeneous in 100% DPhPC, an effect not observed before or since. It is unclear as to why this occurred. At five hours an increase in fluorescence at the lipid monolayer of droplets formed in 2 mol% DPPE-PEG2000 revealed an increase in proteoliposomes aggregation, while 4 mol% DPPE-PEG2000 appeared to lower the rate of proteoliposome aggregation the most out of the conditions tested due to the absence of a red ring until 1260 minutes. At this point, a red ring was observed, indicating that 4 mol% DPPE-PEG2000 did not completely prevent proteoliposome aggregation at the oil-water interface. These results were pleasing to see - proteoliposome homogeneity in solution could be altered by varying the concentration of PEGylated lipid. Whether this would be sufficient to afford functional proteoliposomes and DIBs in future experiments remained to be seen, but I chose to proceed with the remaining experiments in order to achieve the final aim of this thesis in a timely manner. If proteoliposome aggregation was to prove an issue going forward, these, and other, lipids would be explored in further detail.

In subsequent work regarding permeabilising DIBs with αHL the molar fraction of DPPE-PEG2000 incorporated into the lipid-in-oil composition would need to be again determined empirically, as I hypothesised insertion efficiency of αHL would decrease with increasing DPPE-PEG2000 concentration (see **Chapter 4.2)**.

3.2.4 DFHBI is an oil-soluble fluorophore

In **Chapter 3.2.2** I demonstrated light-activated ATP synthesis coupled to transcription in single nL droplets. However, during these experiments I had noticed a decrease in fluorescence upon overnight incubation of droplets in oil. This was observed for a solution of proteoliposome/IVT mix, with aptamer generated in situ, (**Figure 3.6A**), and a droplet formed from a solution of pre-transcribed aptamer (**Figure 3.6B**). The fluorescent readout of this assay would depend on the presence of both RNA and fluorophore and at this stage it was unclear which variable, or both, was being affected. RNA hydrolysis, either spontaneous or via ribonuclease (RNase) activity and photobleaching of DFHBI were potential issues in this system. Use of diethyl pyrocarbonate-treated water and addition of a RNase inhibitor, Murine did not affect this decrease in fluorescence (data not shown), suggesting degradation of RNA was not responsible.

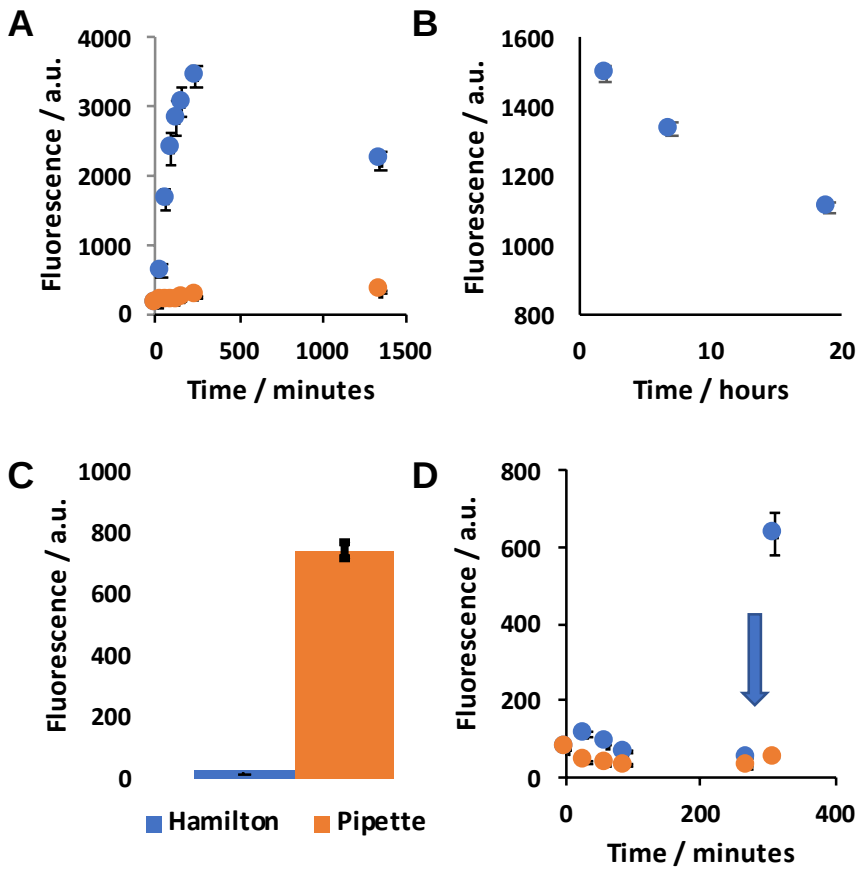

Figure 3.6. DFHBI is an oil-soluble fluorophore. (**A**) Fluorescence of a nL-sized IVT droplets powered by proteoliposome synthesised ATP, incubated in oil and illuminated (blue) or shielded from light (orange). (**B**) Fluorescence of nL-sized droplets in oil of an aptamer-DFHBI solution. (**C**) Fluorescence of nL-sized IVT droplets, with supplied ATP, formed by a Hamilton syringe or micropipette. (**D**) Fluorescence recovery after fusion of a droplet of DFHBI with an IVT droplet containing ATP (blue). No change in fluorescence was observed with a droplet of DFHBI was fused with an IVT-ADP_{HK} droplet (orange). Blue arrow indicated addition of DFHBI. **A – D** each data points represents the mean of three droplets from the same experiment. Error bars represent one standard deviation about the mean.

Interestingly, a striking contrast was exhibited when droplets were formed with either Hamilton® syringes or micropipettes (**Figure 3.6C**). After two hours incubation in oil, droplets formed with micropipettes afforded a 37-times increase in fluorescence over droplets of the same solution dispensed from a Hamilton® syringe. One possible cause for this inhibitory effect was the potential leaching of metal ions from both the stainless-steel tip of the Hamilton® syringe and tungsten plunger into solution. For example, iron potentially leaching into solution resulting in the formation of hexaaquairon ions and subsequent acidification of the solution.

Similar problems with Hamilton® syringes were observed in earlier work in the group[45], and thus I did not use them to form droplets for any further work described in this thesis.

The cognate fluorophore for Broccoli, DFHBI, is a small, membrane permeable molecule. The ability of DFHBI to diffuse freely across cell membranes is a major advantage when imaging RNA in living cells, as this is a ubiquitous, energy-independent method of transportation. However, I hypothesised that DFHBI's amphiphilic nature could be a disadvantage in an oil environment. If soluble in the oil phase, DFHBI encapsulated within a 100 nL droplet formed in 200 μL oil would be diluted 2000 times, assuming equal solubilities of DFHBI in the aqueous and oil phases. To test this theory that DFHBI was being diluted below a critical concentration, I formed 100 nL droplets of two IVT solutions in oil, with either 10 mM ATP or 10 mM ADP_{HK}. Minimal fluorescence was observed for either population of droplets until a 100 nL droplet of 120 μM DFHBI was fused with both populations, whereupon fluorescence greatly increased in the ATP containing sample with only a small change observed in the ADP_{HK} droplets (**Figure 3.6D**). This result confirmed the hypothesis that DFHBI had been partitioning into the oil phase over the course of the experiments, leading to a loss of aptamer-fluorophore binding and a corresponding decrease in fluorescence. The phenolate form of DFHBI is more hydrophilic than the protonated form and thus less soluble in the oil phase. This may explain some observed effects of using a Hamilton® syringe to dispense droplets, as contaminating metal ions from the syringe acidify the solution and keep DFHBI protonated. As I will discuss in **Chapter 4**, consideration of the oil phase is crucial to the successful outcome of experiments.

I planned to counteract loss of DFHBI to the oil phase by saturating the oil with DFHBI before use. In this way any loss of DFHBI from droplets to oil would be counteracted by diffusion of DFHBI from the oil to the aqueous phase. I performed this by dispensing 60 μM DFHBI, dissolved in dimethyl sulfoxide (DMSO), in oil. The oil in this case, as it has been previously, was a one-to-one mixture of hexadecane and silicone oil AR20 (AR20). While DMSO was not miscible in this oil composition, a one-hour incubation at 25 °C led to a significant discolouration of the oil, indicative of an increased DFHBI concentration. This result further provided proof that DFHBI was soluble in the oil phase (**Supplementary Figure 7.3**).

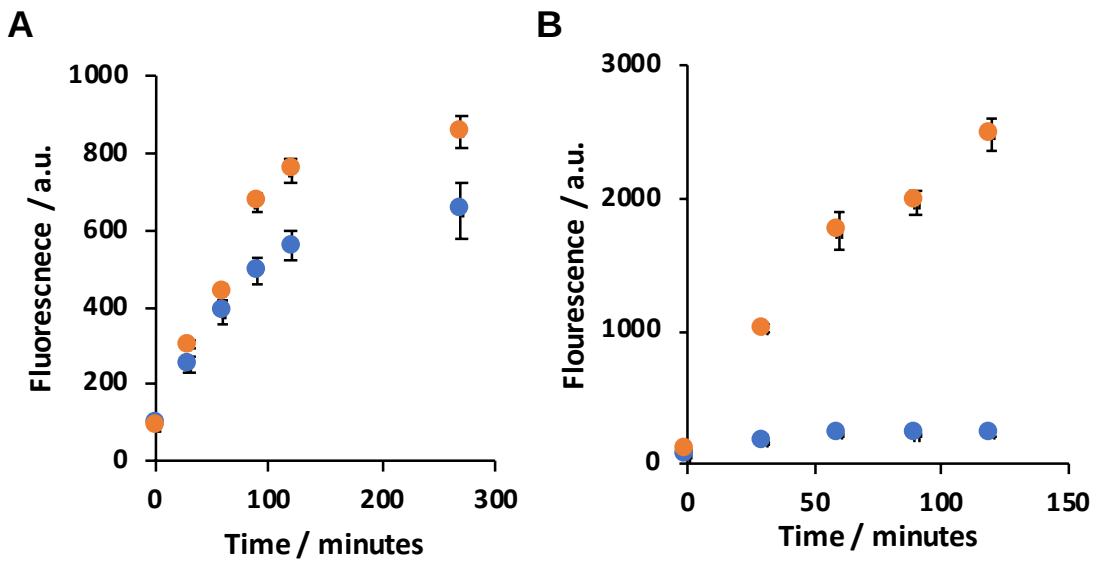

Figure 3.7. Charging oil with DFHBI. (**A**) Fluorescent output of IVT in droplets in a DFHBI-laden oil. Transcription was visualized from IVT solutions made with DFHBI added (orange) and without (blue), highlighting that DFHBI was diffusing from the oil into droplets. (**B**) Aptamer-independent fluorescence was not observed in droplets of IVT solution lacking ATP (blue). **A & B** each data points represents the mean of three droplets from the same experiment. Error bars represent one standard deviation about the mean.

100 nL droplets of an IVT cocktail, with and without 60 μM DFHBI, were dispensed in this DFHBI-laden oil (**Figure 3.7A**). In this experiment solutions were supplied with ATP initially. After incubation at 37 °C fluorescence was observed in both

populations of droplets; confirming the hypothesis that DFHBI from the oil phase can diffuse into droplets to effect visualisation of Broccoli. Preincubating DFHBI with the oil phase for longer should increase DFHBI concentration in oil and thus afford stronger fluorescence of IVT droplets, and indeed that is what was observed (**Figure 3.7B**, orange). DFHBI, incubated with oil for seven hours prior to IVT droplet formation in said oil, afforded higher levels of fluorescence than with an oil incubated with DFHBI for one hour. One potential area of concern was an increase in background fluorescence due to DFHBI precipitating or stacking; both would hinder the free rotation of DFHBI and give rise to fluorescence. Therefore, it was pleasing to observe low fluorescence in a population of ATP-deficient IVT droplets formed in DFHBI-laden oil (**Figure 3.7B**, blue).

The previous work described in this chapter consisted of large droplets, around 100 nL, but the 3D droplet printer developed within the Bayley group[51] (see **section 1.2**) is unable to generate droplets of that volume. The 3D droplet printer is required to manufacture the synthetic tissues and so it was paramount to ensure that biochemical assays functioned in smaller droplets. Typical volumes range from 50 pL to 2 nL. A smaller droplet volume would possess a larger oil-water interface relative to volume for DFHBI diffusion into the oil phase to occur. For example, a 1 nL droplet has a surface area to volume ratio 4.64 times that of a 100 nL droplet. 500 pL (100 μm diameter) droplets were produced by the 3D droplet printer with identical solutions to those of **figure 3.7B** in a DFHBI-laden oil (**Figure 3.8A**). After a two-hour incubation minimal fluorescence was observed in both populations of droplets.

The question remained whether this lack of fluorescence was due to low transcription, or issues with the fluorophore. To remove the variable of transcription efficiency and to investigate the role of DFHBI in Broccoli visualisation in isolation, I transcribed the Broccoli aptamer in bulk in the presence of DFHBI before printing droplets in a DFHBI-laden oil (**Figure 3.8B**). After incubation a decreasing fluorescent signal was observed. It was unlikely that the 3D droplet printer has introduced RNases; rather, it was more likely DFHBI solubility in the aqueous phase had been affected by decreasing droplet volume. One potential cause for this phenomenon - which became apparent later on during the work encompassed within this thesis - was the rapid acidification of pL droplets in comparison to nL by acidic oil. This will be discussed in depth in **section 4.2.6**. As the 3D printer worked with droplets in the pL range, it was of utmost importance to have functional assays in these smaller droplets if I wanted to construct complex synthetic tissues.

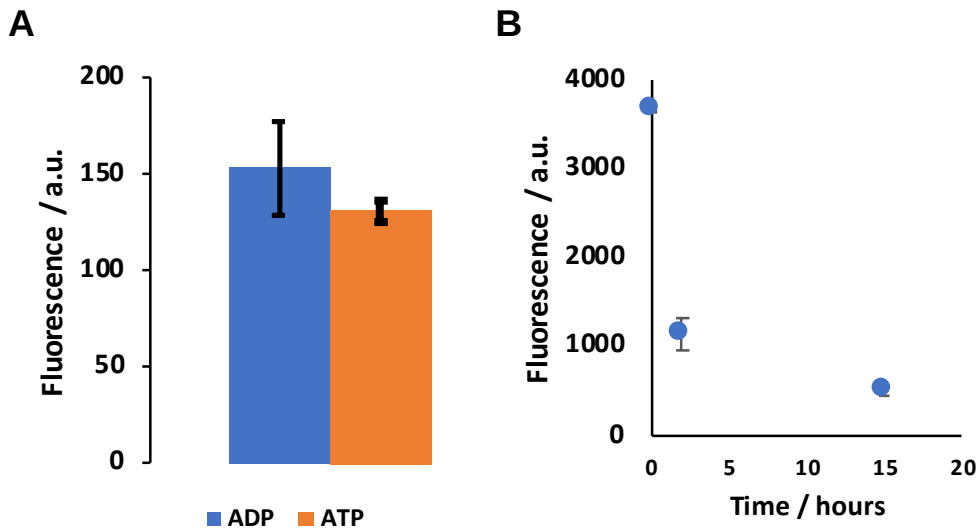

Figure 3.8. IVT assay not functional in printed, pL droplets. (**A**) Fluorescence of pL-sized droplets of an IVT solutions containing either ATP or ADP_{HK} after two-hour incubation. (**B**) Fluorescence of printed droplets containing a preformed Broccoli-DFHBI solution. **A & B** each data point represents the mean fluorescence of ten droplets from the same experiment. Error bars represent one standard deviation about the mean.

3.2.5 A hydrophilic fluorophore for RNA visualisation

Attempts at boosting DFHBI concentration in DFHBI-laden oil by increasing DFHBI concentration and lengthening the incubation time in oil did not afford any detectable fluorescence in 500 pL droplets of an IVT solution after incubation (data not shown). As saturating the oil phase with DFHBI was not achieving the desired results, I looked at other methods of maintaining fluorophore concentration in droplets. A different approach was to increase the solubility of DFHBI in the aqueous phase, which would disfavour partitioning into oil. One possibility would be to attach a hydrophilic protein to DFHBI covalently, similar in concept to the membrane impermeable Rhod-Dextran Ca^{2+} indicator dyes[141]. However, the covalent linking of a large protein to DFHBI might interfere with DFHBI-Broccoli binding. An alternative option was to synthesise an analogue of DFHBI with a hydrophilic side group. Recent work showed that the N1 position of the imidazolinone ring of DFHBI faced a solvent-accessible pocket of Broccoli, so bulky, hydrophobic side groups could be attached at this position without loss of function[142].

As a proof of principle, Lysine-OMe was chosen to as the hydrophilic moiety due to the resulting five-carbon linker between the imidazolinone ring and the bulky hydrophilic group, identical in length to the linker in the optimised molecule (so-called BZ) from [134]. This would lower the possibility of any negative steric interactions between the novel fluorophore and Broccoli. Synthesis proceeded in a two-step procedure, following an adapted published protocol[143]. Due to the zwitterionic nature of the product, termed DLM (**Figure 3.9A**), silica

chromatography was unable to separate the product from impurities and so C18 reverse phase chromatography was employed. While this greatly decreased the yield, I deemed it acceptable in order to obtain a high level of purity, as only a small amount of material was needed for subsequent experiments.

Fluorescence was first investigated in bulk, with fluorescence of DLM-Broccoli found to be 3 times lower than that of DFHBI-Broccoli (**Figure 3.9B**). As in previous experiments, DLM was added to the IVT cocktail prior to transcription. On this basis, the lower fluorescence of DLM-Broccoli could not be solely attributed to a lower brightness or quantum yield of DLM, as DLM may have an inhibitory effect on transcription. As previously discussed, in the context of my experiments this ambiguity was acceptable, as both transcription of the aptamer and fluorescence of the product are required for visualisation and successful assays.

The hydrophilicity of DLM was arguably its most important property, and was investigated next. Here, in a well array a 100 nL droplet of a solution of transcribed Broccoli aptamer was formed in a central well in oil, with the surrounding wells containing 100 nL droplets of 60 μM fluorophore (**Figure 3.9C*i***). If the fluorophore was soluble in oil then one would expect a fluorescence increase in the aptamer droplet over the course of this experiment. As expected, this proved true for the aptamer droplet surrounded by DFHBI, whereas when surrounded by DLM droplets only a small increase in fluorescence was observed after overnight incubation (**Figure 3.9C*ii***). These results indicated that a synthetic approach would be a valid way to obtain Broccoli fluorophores that afforded a detectable level of

fluorescence and were impermeable through oil, although performing a screen to identify a molecule such as this was not within the scope of this thesis.

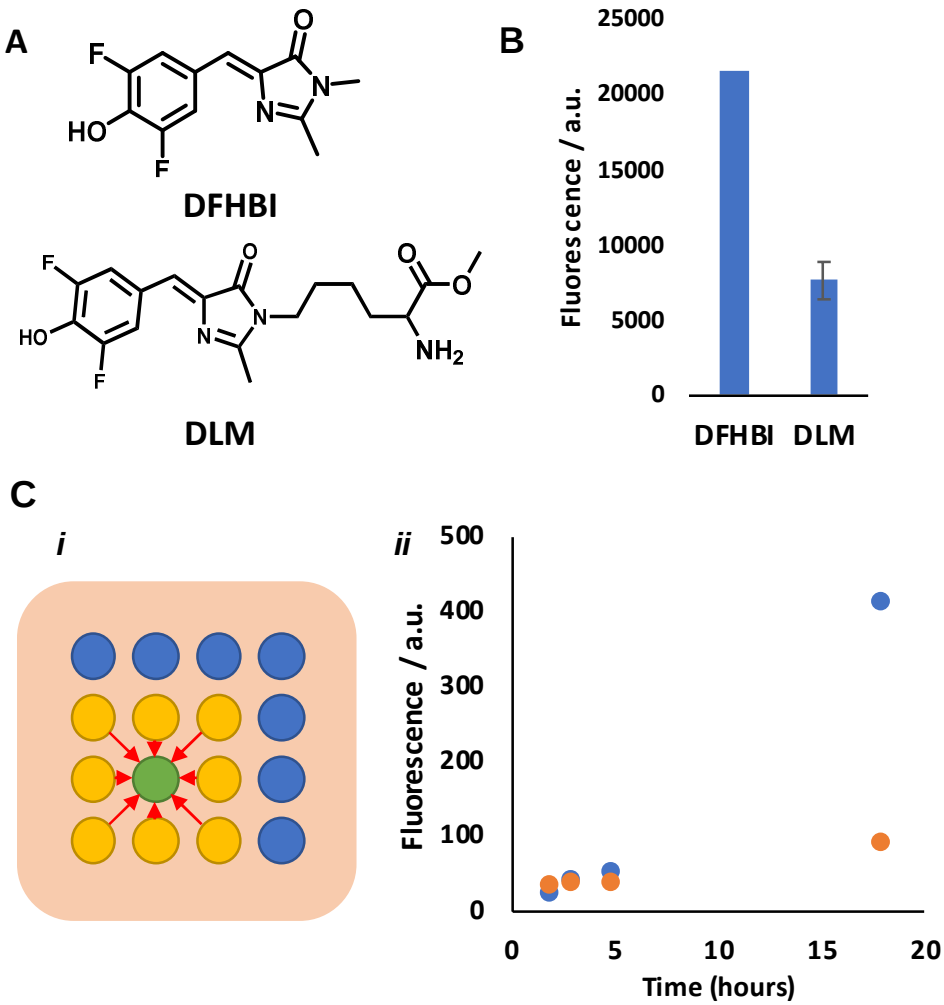

Figure 3.9. A hydrophilic analogue of DFHBI. (**A**) Structures of DFHBI and the novel Broccoli fluorophore, DLM. (**B**) Bulk fluorescence output of an IVT solution prepared with DFHBI or DLM. (**C**) ***i*** Experimental setup. Droplets containing 60 μM fluorophore (yellow) were placed in a well array surrounding a droplet of Broccoli (green). Not to scale. ***ii*** Fluorescence of the central droplet containing Broccoli aptamer when surrounded by DFHBI droplets (blue) or DLM droplets (orange). **B** DFHBI data point is from one repeat, DLM represents the mean fluorescence of three solutions in bulk. Error bars represent one standard deviation about the mean. **C*ii*** Each trace represents the fluorescence of one droplet tracked over time.

After validation of the synthetic approach, I next performed a small screen of DFHBI analogues with hydrophilic side groups attached to the imidazolinone ring (**Figure 3.10**), attempting to enhance fluorescence back to levels observed in

DFHBI-Broccoli while retaining the hydrophilic properties of DLM. Interestingly, deprotecting the carboxylic acid in DLM to afford compound 4 in **Figure 3.10A**, abolished fluorescence, but negatively charged side groups were tolerated in some cases, as in **6**, with similar fluorescence to DLM. However, highest levels of fluorescence were observed with positive charged groups, as in the case for **2**. This choline analogue gave a 270% increase in fluorescence over DFHBI, the highest of any compound tested so far. Compound **5** also possessed a quaternary amine, but it became apparent during the analysis of this experiment that the hydrazine moiety will influence the HOMO-LUMO levels of **5**, and thus the excitation/emission may have been altered. It was decided that **2**, DFHBI-Choline, would be taken forward for further study.

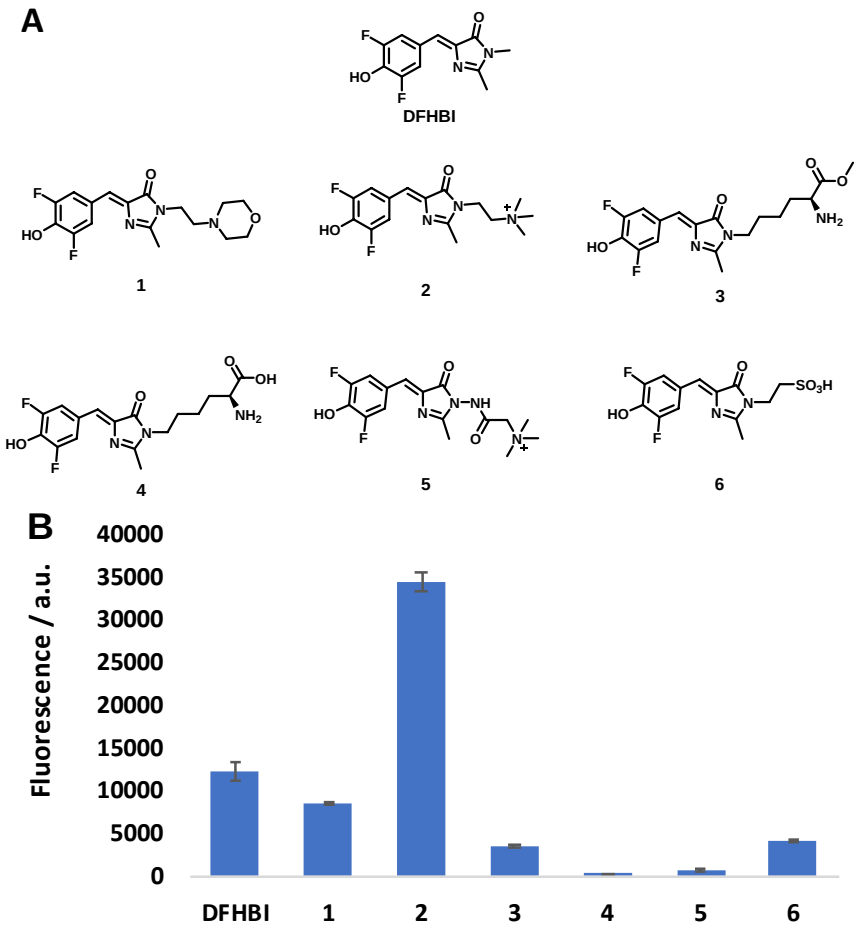

Figure 3.10. A screen of hydrophilic DFHBI analogues. (**A**) The six compounds synthesised and analysed for this screen. (**B**) Fluorescence of each fluorophore incubated with an IVT solution in bulk. Each data point represents three repeats. Error bars represent one standard deviation about the mean.

Repeating the oil permeability experiment described above (**Figure 3.9C**) revealed that DFHBI-Choline possessed a greater hydrophilic nature than DLM, which is expected due to the permanent positive charge (**Figure 3.11)**. A 1.5-fold increase in fluorescence was observed in the aptamer droplet surrounded by droplets of DFHBI-Choline, as opposed to 100-fold for the DFHBI control.

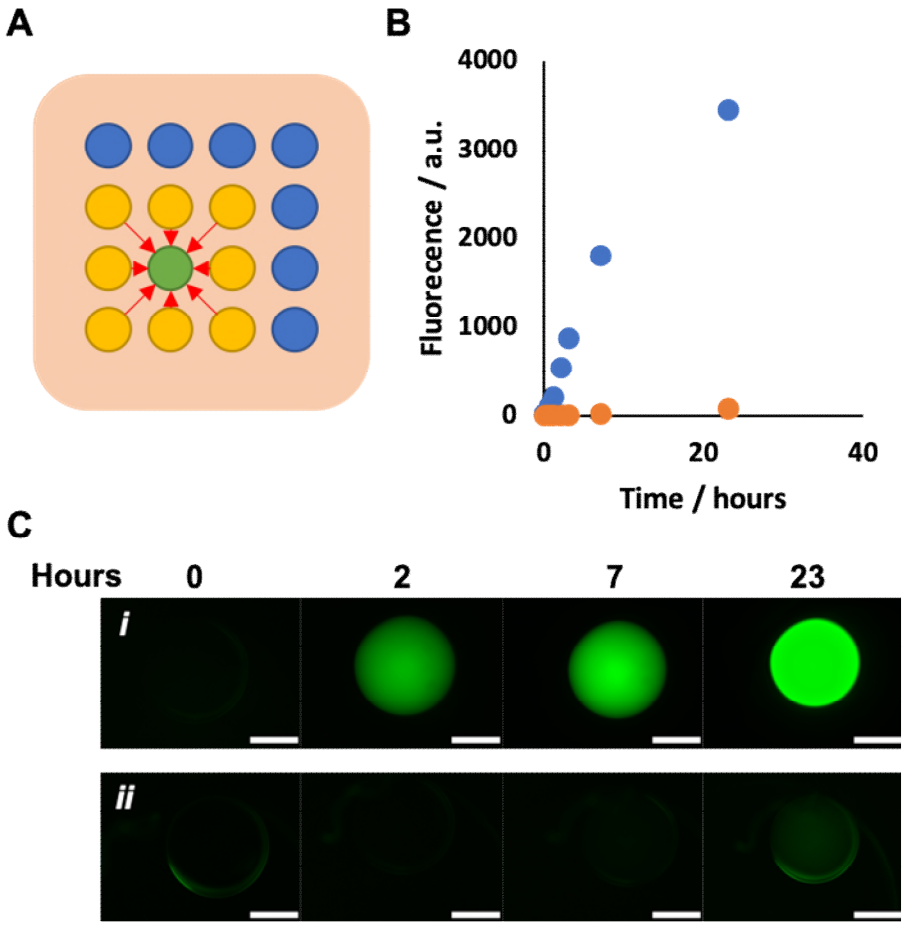

Figure 3.11. DFHBI-Choline is insoluble in oil. (**A**) Experimental setup. Droplets containing 60 μM fluorophore (yellow) were placed in a well array surrounding a droplet of Broccoli (green). Not to scale. (**B**) Repeating the experiment described in **Figure 3.9C**. DFHBI (blue) diffuses to a central droplet containing Broccoli through the oil phase. DFHBI-Choline (orange) is insoluble in oil. (**C**) Fluorescent images from **B** of aptamer droplet surrounded by ***i*** DFHBI or ***ii*** DFHBI-Choline droplets.

I next investigated DFHBI-Choline diffusion across lipid bilayers (**Figure 3.12A)**. DIBs were formed with droplets containing Broccoli and a fluorophore separated by a DPhPC bilayer. DFHBI diffused freely across the DIB to bind with Broccoli, affording a saturating level of fluorescence five minutes post-DIB formation (**Figure 3.12B)**. DFHBI-Choline on the other hand was membrane impermeable, remaining compartmentalised by the lipid bilayer for over 18 hours, as evidenced by only a small increase in fluorescence in the trans droplet. Note that there is a decrease in the volume of the droplet containing DFHBI-Choline (droplet on the left of the

DIB in **Figure 3.12B*ii***), and an increase in droplet containing RNA (droplet on the right of the DIB). I hypothesise the primary cause for this change in size is due to osmosis. RNA was not purified from the IVT kit, and so the RNA droplet contained T7 RNAP, T7 RNAP storage buffer with 5% glycerol (final concentration), in addition to RNA/NTPs and IVT buffer. Conversely, the droplet containing DFHBI-Choline contained just DFHBI-Choline and IVT buffer. This differing osmolarity would create a net flow of water from the DFHBI-Choline droplet to the RNA droplet, resulting in the changing volumes observed. This experiment was designed to examine how membrane permeable DFHBI-Choline was and so no regard was paid to balancing osmolarity. After 18 hours a small increase in fluorescence was observed in the droplet containing RNA adjacent to the DFHBI-Choline droplet, with a net flow of water from the DFHBI-Choline droplet to the RNA droplet. Because of this and with the result observed in **Figure 3.**11, I determined that DFHBI-Choline was hydrophilic enough for the purposes I required. Thus, I proceeded with towards the remaining experiments required to complete the objectives described in **Chapter 1.6**.

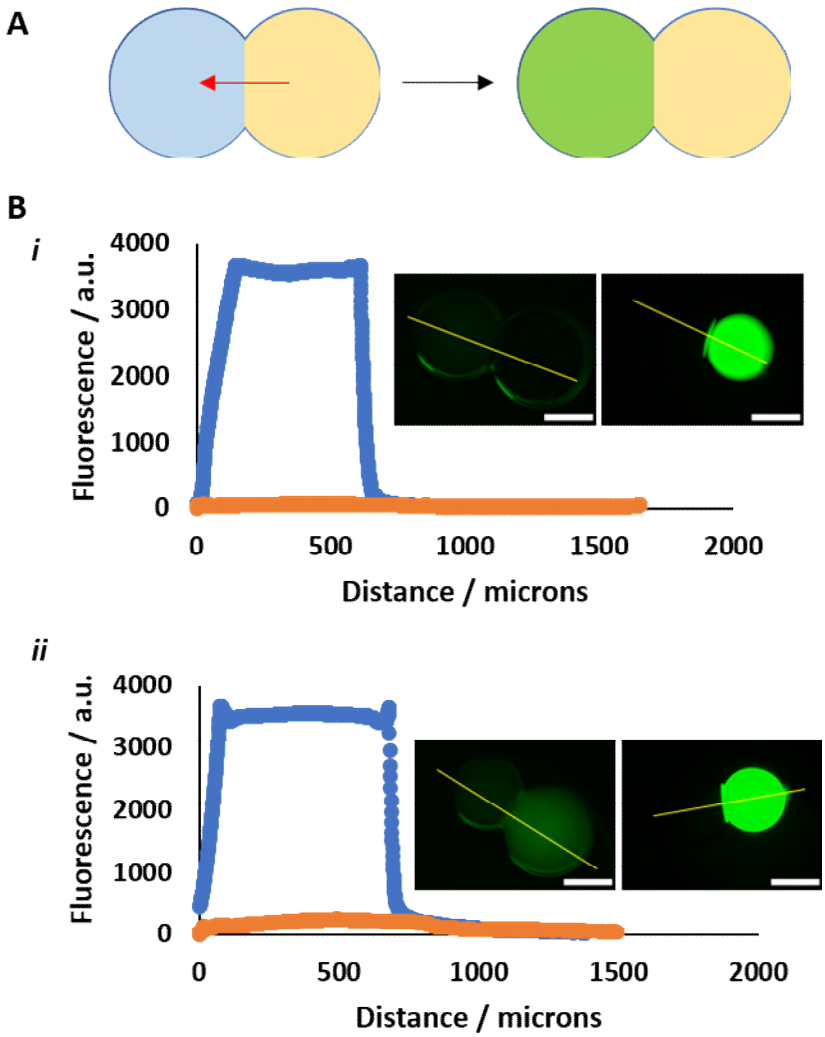

Figure 3.12. DFHBI-Choline is membrane impermeable. (**A**) Diagram of experimental setup. Droplets of Broccoli (blue) and fluorophore (beige) were brought into contact to form a DIB. A membrane permeable fluorophore will diffuse across the DIB (red arrow) to increase fluorescence (green). (**B**) Fluorescence line profile (yellow line) after ***i*** initial DIB formation and ***ii*** 23 hours for droplet pairs containing DFHBI (blue) or DFHBI-Choline (orange). Each trace represents one droplet. Scale bar represents 300 μm.

Finally, I performed IVT in 500 pL printed droplets, with DFHBI-Choline present to visualise transcribed Broccoli (**Figure 3.13)**. Fluorescence was observed after a two-hour incubation and the fluorescence levels stable over 18 hours. This validated the use of DFHBI-Choline as a hydrophilic fluorophore of Broccoli in the water-in-oil emulsions that comprise the synthetic tissues developed within the Bayley group. Having optimised IVT in single droplets, I could now move forward to investigate systems comprised of multiple compartments.

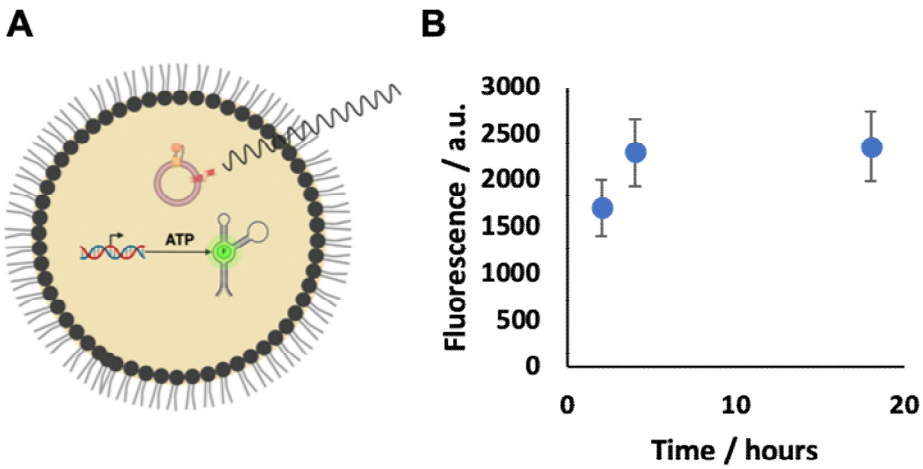

Figure 3.13. IVT in printed droplets visualised by DFHBI-Choline. (**A)** Light-activated ATP synthesis by proteoliposomes in a water-in-oil droplet powers the IVT of a fluorescent RNA aptamer. (**B**) Fluorescence output of printed, pL-sized droplets of an IVT solution with supplied ATP and visualised by DFHBI-Choline. Each data point represents the mean fluorescence of ten droplets from the same experiment. Error bars represent one standard deviation about the mean.

3.3 Conclusion

This chapter has described the IVT of a Broccoli aptamer via light-activated ATP synthesis by proteoliposomes in nL and pL droplets. Both transcription and ATP synthesis were optimised for the final system to be functional.

I first optimised IVT in bulk, with close attention paid to salt concentration and the degradation of IVT output due to DTT oxidation. Next, care was taken to ensure ATP was not synthesised when droplets were not illuminated due to residual pH gradients across proteoliposome bilayers. pH gradients were dissipated by incubating proteoliposomes in an IVT mixture, without ADP_{HK}, allowing proton flux to occur across lipid bilayers. Using this protocol, I successfully performed light-activated IVT in large, 100 nL droplets dispensed in oil.

However, I observed a decrease in fluorescence in droplets containing Broccoli-DFHBI over time and after some investigation determined that solubility of the Broccoli fluorophore, DFHBI, in the oil phase was responsible. While initial attempts at saturating the oil phase with DFHBI were promising for experiments conducted with nL droplets, I was unable to visualise IVT in the smaller, printed droplets that comprise the synthetic tissues used within our laboratory.

To this end, I designed and synthesised a range of novel fluorophores with hydrophilic side groups, based on the structure of DFHBI. DFHBI-Choline, possessing a quaternary amine, afforded the greatest fluorescence when bound to Broccoli in bulk studies, was insoluble in oil and bilayer-impermeable. With DFHBI-Choline I was able to demonstrate IVT in printed droplets, with no decrease in fluorescence observed. DFHBI-Choline will be a valuable tool in future studies investigating IVT in water-in-oil emulsions.

4 Energy generation and communication across lipid bilayers

In **Chapter 3** I detailed the light-activated transcription and visualisation of a Broccoli aptamer in droplets, powered by ATP synthesising proteoliposomes. This required optimising transcription by adjusting the buffer composition and synthesising novel, hydrophilic fluorophores to aid visualisation. The latter was required because the canonical fluorophore for Broccoli, DFHBI, is a small amphiphilic molecule that partitioned into the oil phase of the water-in-oil emulsions that constituted our synthetic cells and tissues.

This chapter describes the construction of compartmentalised systems. Here, synthetic cells containing either ATP synthesising proteoliposomes or transcription machinery were assembled into pairs of synthetic cells separated by a DIB. To permeabilise DIBs to hydrophilic molecules, I purified a pore forming protein, αHL, from *Staphylococcus aureus* (*S. aureus*). I found a concentration of 100 μg/mL αHL optimal for maximum synthetic cell equilibration rates. Initially DIBs formed between nL droplets were susceptible towards coalescence and I found decreasing droplet volume to the pL range was required to stabilise DIBs. A key issue overcome in order to create a functional synthetic tissue was synthetic cell acidification by AR20. I observed that both a lower visualisation of Broccoli and decreasing mCherry fluorescence in synthetic cells in oil over time could be negated with additional washing of the silicone oil prior to use.

Finally, I combined the previous work and themes of this thesis to describe a system capable of light-activated ATP synthesis, with αHL-permeabilised DIBs enabling ATP to perform work in separate synthetic cell. This work, IVT, was visualised with the custom-made fluorophore DFHBI-Choline. This system has a potential to be scaled up with tens to hundreds of synthetic cells forming synthetic tissues. In this scenario, a multitude of biological functionality could be reconstituted within specific synthetic cells in a patterned manner, with activation controlled via light and other external stimuli.

4.1 Introduction

The transition from unicellular to multicellular organisms is regarded as one of the major evolutionary developments of life on Earth, and has occurred independently at least 25 times[144]. Specialisation of cells appears in multicellular organisms giving rise to distinct cell types expressing different phenotypes while containing identical genetic information, resulting in groups of cells able to work cohesively in a wider range of functions, and with emergent properties greater than the sum of their individual parts[145]. However, there needs to be a precise control over cellular location and distribution is critical to proper functionality, examples being the patterning of photoreceptors and ganglion cells in the retina[146], and the layer of epithelial cells in the skin[147], to provide vision and a barrier to pathogens, respectively.

Constructing synthetic tissues comprised of multiple compartments, each performing unique functions in a spatiotemporally controlled manner, would be a

powerful tool towards building soft medical devices and implants. Synthetic tissues comprised of water-in-oil emulsions can be patterned in a variety of ways. Firstly, individual droplets can be manipulated by hand into a desired pattern. Droplets may be formed by pipette[1,45], Hamilton® syringe[45], or microinjector[41] and positioned by hand[1,45] or by micromanipulators[41]. Small droplet networks can be formed quickly in this manner and comprised of a number of different solutions[1]. However, formation of these networks is laborious, technically challenging, and difficult to scale up. Importantly, individual droplets formed in this manner are nanolitre in volume, far more than the volume of most cells[148]. If we try to capture the complexity and density of natural tissues, then we must decrease the cell volume. This is possible by using the 3D droplet printer developed within the Bayley group, discussed in detail in **Chapter 1.2**.

The droplet printer has been used to pattern synthetic tissues comprised of picolitre droplets down to single-droplet resolution, with channels one-droplet wide integrated into synthetic tissues[49]. To date a maximum of three solutions have been patterned in synthetic tissues, and synthetic tissues built on a cm scale, however in theory both of these properties can be increased as required[47].

Intercellular communication is arguably one of the main challenges that must be replicated to transition from single cells to synthetic tissues, without which cells cannot work cohesively. Small, amphiphilic molecules are able to diffuse across lipid bilayers and between synthetic cells, as is the case for DFHBI[41] (**Chapter 3.2.4**). Movement of hydrophilic molecules requires functionalisation of the lipid bilayer separating compartments. As discussed in **Chapter 1.2**, in the context of

synthetic biology communication across lipid bilayers has been achieved through the reconstitution of membrane proteins, such as bR[116], LacY[33], and most commonly, αHL [1,2,41,115,149].

4.2 Results and discussion

4.2.1 Purification of αHL monomers

Secreted from *S. aureus* as 33.2 kDa water-soluble monomers, αHL binds to rabbit and human erythrocytes' cell membranes and oligomerises to form a 232.4 kDa heptameric protein nanopore[150]. The concentration of αHL required for lysis varies considerably, from 1 μM for human erythrocytes to 1 nM for rabbit erythrocytes[151]. The high susceptibility of rabbit erythrocytes towards αHL is afforded by a membrane protein binding target; a sheddase, a disintegrin and metalloproteinase domain-containing protein 10 (ADAM10)[152].

Historically αHL has been used extensively within the Bayley group for both DNA sequencing[153,154] and substrate diffusion across lipid bilayers[21] (**Figure 4.1A)**. Preoligomerised αHL heptamers were used in these experiments due to the requirement of single channels for electrophysiological measurements. Addition of monomers would result in the binding of numerous monomers to the planar lipid bilayer causing the formation of multiple pores. However, DIB permeabilisation proved extremely inefficient when using pre-heptamerised αHL, with the complete equilibration of 400 nL droplets not achieved after five days[21].

An improvement to increase droplet content equilibration is to use αHL monomers. A previous member of the Bayley group showed conclusively that αHL monomers permeabilise DIBs to a greater extent than pre-formed αHL pores. Equilibration of a fluorescent dye between nanolitre droplets was achieved with 200 μg/mL αHL monomers after six minutes; no transfer of fluorescent dye was observed with the equivalent amount of αHL heptamers after three days[1]. Separately, αHL monomers have been shown to facilitate rapid diffusion of transcription inducers in droplet networks[41].

To permeabilise DIBs towards ATP and power biochemical reactions in remote droplets, I thus turned my focus towards purifying αHL monomers. Commercial αHL monomers are available, however concerns over purity and price prohibited their use. Protocols developed within the Bayley group expressed His-tagged αHL in *E. coli*[1]. While purification yields from *E. coli* were high, a significant proportion of αHL was heptamerising, either due to the high intracellular concentration of αHL, or forming on the *E. coli* cell membrane. Removing heptamer from monomer was not possible by gradient elution of a Ni-NTA column, rather a subsequent purification step with size exclusion chromatography was required[1].

To avoid this laborious process and to minimise loss of yield to heptamerisation, I chose to express wild-type (WT) αHL from *S. aureus*. Following *S. aureus* growth, in which αHL was expressed and secreted to the extracellular environment, I collected the cells by centrifugation to afford a αHL-rich supernatant. After adjusting the supernatant pH to below αHL's isoelectric point (5.8) and halving the

NaCl concentration through dilution, I concentrated the protein on a cation exchange column. Elution was performed with a step-wise gradient of NaCl to remove contaminating proteins, with αHL monomer eluted at 250 mM NaCl.

Samples containing αHL were concentrated to 5 mg/mL via ultracentrifugation. The solution was mixed periodically to ensure that the sample did not become overconcentrated near the membrane as this could lead to spontaneous αHL heptamerisation. Having concentrated αHL, size exclusion chromatography further purified αHL. Pure fractions of αHL were concentrated to 1 mg/mL and flash frozen as 20 μL droplets in liquid nitrogen (LN2). Analysis by sodium dodecyl-sulfate polyacrylamide gel (SDS-PAGE) electrophoresis showed that αHL was far purer than that from a commercial source (**Figure 4.1B**, lanes 1-4). For example, αHL from Sigma-Aldrich showed four contaminating proteins, including heptamerised protein (**Figure 4.1B**, lane 5).

Activity of αHL was first assessed through a haemolytic assay. Rabbit erythrocytes incubated with 1.5 nM αHL monomers were fully lysed within 20 minutes, confirming that αHL had been isolated in an active form (**Figure 4.1C**).

Next, I validated αHL monomer activity in artificial lipid bilayers (**Figure 4.1D**). As these bilayers lacked the proposed molecular target of αHL, ADAM10, it was important to confirm αHL activity. DIBs were formed with pairs of droplets containing αHL and 1 mM 2-(N-(7-nitrobenz-2-oxa-1,3-diazol-4-yl)amino)-2-deoxyglucose (2-NBDG), a fluorescent glucose derivative. Droplets were

incubated in lipid-containing oil solution for 10 minutes prior to DIB formation to ensure monolayer formation.

The lowest concentration of αHL monomer used, 10 ug/mL (300 nM), was unable to permeabilise sufficiently DIBs to an acceptable degree, as indicated by the lack of observable diffusion of 2-NBDG across the bilayer (**Figure 4.1D*iii***). This result was surprising, as one would expect to see some transfer of 2-NBDG – approximately 10 times less than in **Figure 4.1D*ii*** where αHL monomer at 100 ug/mL was employed. There is not known to be a critical concentration of αHL monomer needed to form heptameric pores, which made this result puzzling. One factor could be the use of an optical microscope used to image and analyse droplet pairs limiting detection of low concentrations of 2-NBDG. One would imagine that the use of a fluorescent microscope could quantify 2-NBDG movement through αHL at a low concentration. However as 2-NBDG movement across the DIB proceeded with αHL monomer at 100 ug/mL, I decided to use this concentration going forward and continue with the remaining experiments required to achieve the final goal of this thesis, rather than spend too long optimising one minor aspect of the final system. On the other hand, αHL monomer at 1 mg/mL (30 μM) destabilised DIBs greatly, and the one droplet pair that did not coalesce did not equilibrate its contents (**Figure 4.1D*i***). I hypothesised that the instability is caused by αHL monomers and lipids competing to form a monolayer at the oil-water interface; in the absence of a lipid monolayer αHL would denature at the interface, with hydrophobic side groups orientating towards the oil phase and hydrophilic side groups facing inwards. If this occurs and a lipid monolayer unable to subsequently assemble, then when a second droplet is brought into contact a DIB cannot form

resulting in coalescence. Indeed, this competition between proteins and lipids to form a monolayer at the oil-water interface has been observed before. Here the authors were unable to form a monolayer of DPhPC when encapsulating cell-free extract within droplets, and so turned to lipids with faster monolayer assembly time, such as DOPC, and those that offered charge stabilisation effects, such as the anionic DOPG [41].

Optimal results were found when using 100 ug/mL (3 uM) αHL monomer, revealed by a high rate of 2-NBDG equilibration after 70 minutes (**Figure 4.1D*ii***). This indicated that multiple αHL monomers had associated with the DIB and subsequently formed heptameric pores, facilitating the diffusion of the hydrophilic dye. This concentration of αHL monomer was used in all subsequent experiments.

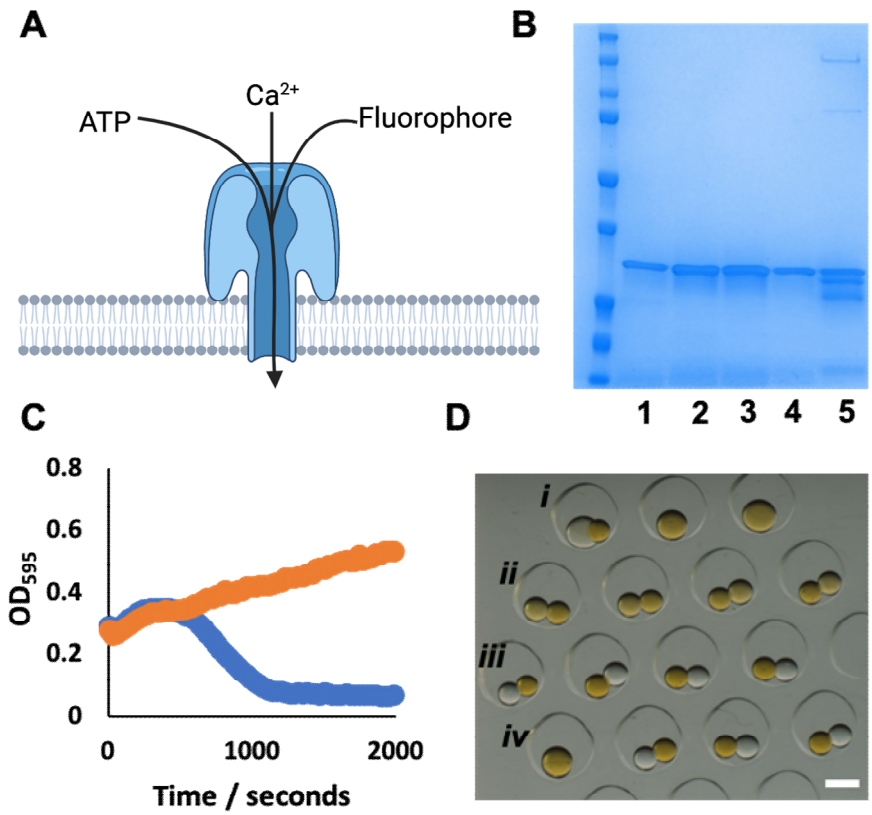

Figure 4.1. αHL purification and activity. (**A**) αHL permeabilises lipid bilayers to small hydrophilic molecules. (**B**) SDS-PAGE gel of purified αHL. Lanes 1-4 are purified αHL. Lane 5 is commercial αHL from Sigma Aldrich. Ladder: 250, 150, 100, 75, 50, 36, 25, 20, 15 kDa. (**C**) Optical density of a solution containing rabbit erythrocytes in the presence of 1.5 nM (50 ng/uL) αHL (blue). Lysis not observed in absence of αHL (orange). Increasing background signal in control due to sedimentation of rabbit erythrocytes. (**D**) Optical microscopy image of αHL-mediation permeabilisation of a DIB highlighting equilibration of a fluorescent dye, 2-NBDG. ***i*** 1 mg/mL αHL ***ii*** 100 μg/mL αHL ***iii*** 10 μg/mL αHL ***iv*** No αHL. Scale bar is 1 mm.

To prevent aggregation of proteoliposomes at the lipid monolayer, PEGylated lipids had been added to the lipid composition of the oil phase (see **Chapter 3.2.4**). As previously mentioned, αHL monomer binding to the lipid monolayer would likewise be affected by the addition of PEGylated lipids. To determine the effect this would have on DIB permeabilisation I repeated the experiment described in **figure 4.2D** with two alterations. First, I added 4 mol% DPPE-PEG2000 to the lipid-in-oil composition, the concentration previously determined in **Chapter 3.2.4**. Secondly, I decreased the concentration of 2-NBDG. The stock concentration of

2-NBDG in ethanol (EtOH) used in the previous experiment was 58 mM and dilution with Milli-Q® (MQ) H_2O to the working concentration of 1 mM brought in 1.7% EtOH. This high amount of EtOH may have influenced the properties of the DIB and aqueous phase, and so these experiments would not give accurate data for downstream assays. In the new protocol a 2 mM stock of 2-NBDG in EtOH was prepared, and diluted 200-fold to 50 uM, making the final concentration of EtOH 0.25% - an acceptable amount.

With a lower concentration of 2-NBDG and EtOH, DIBs formed in pure DPhPC showed minimal 2-NBDG diffusion after three hours (**Figure 4.2B**), compared with the results observed in **Figure 4.1D*ii***. As I hypothesised, addition of DPPE-PEG2000 hindered αHL insertion; 2-NBDG transfer rate was lowered as DPPE-PEG2000 increased to 2 mol%, and in DIBs doped with 4 mol% DPPE-PEG2000 minimal transfer was observed after overnight incubation at 37 ^{o}C. These findings were worrying; without a means to equilibrate droplet contents synthesised ATP would be isolated from the system and unable to power biological functions elsewhere in the synthetic tissue. It was clear DPPE-PEG2000 was detrimental to αHL insertion and I would be faced with two opposing factors to balance; proteoliposome aggregation at the lipid monolayer (see **Chapter 3.2.4**) and αHL insertion.

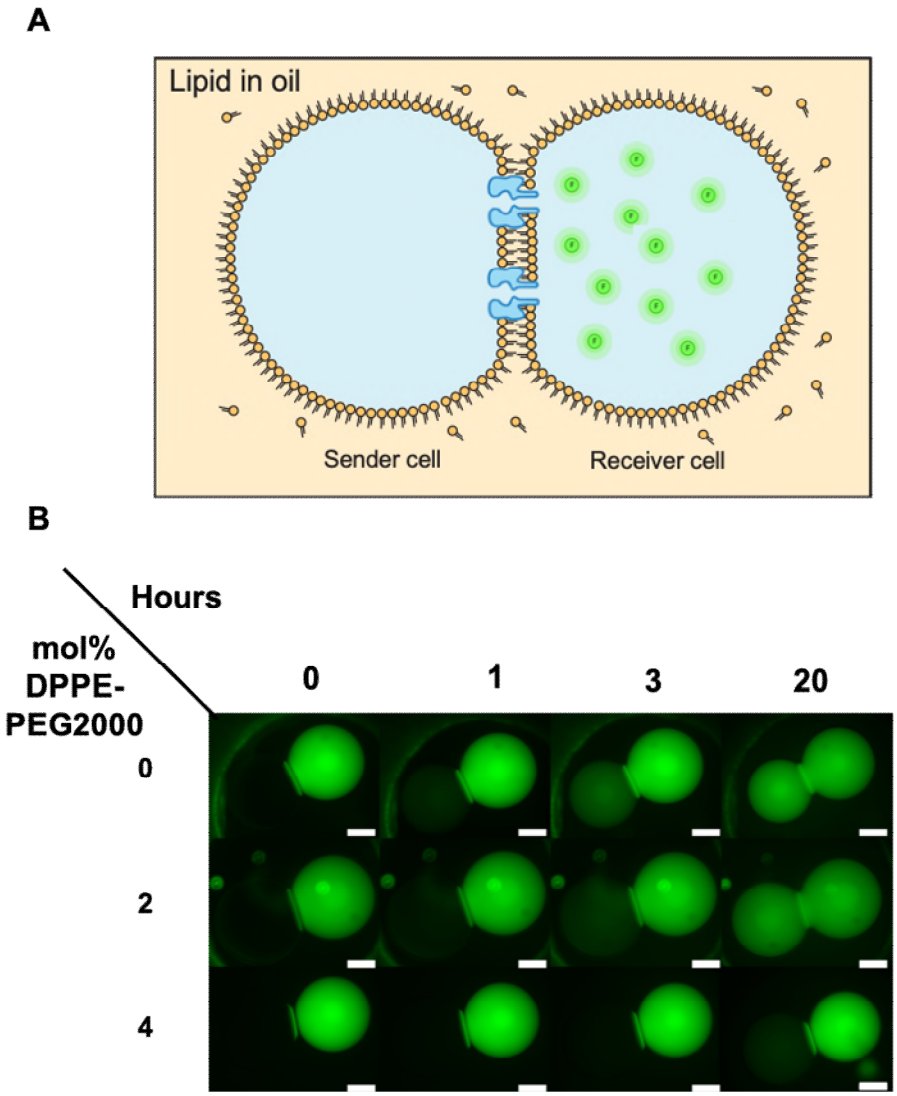

Figure 4.2. DPPE-PEG2000 inhibits αHL insertion. (**A**) αHL permeabilises DIBs to hydrophilic fluorophores (**B**) Increasing the fraction of DPPE-PEG2000 in the lipid-in-oil composition relative to DPhPC slows the equilibration of droplet contents, indicating lower αHL insertion. Scale bar is 200 μm.

4.2.2 Decreasing droplet pair volume enhances equilibration

In addition to investigating αHL-mediated permeabilisation of DIBs, I began to look at the stability of proteoliposome and αHL/T7 RNAP droplet pairs. This was important to consider as previous work in the group described a trend of increasing

DIB instability with increasing protein concentration[115]. When constructing simple structures, consisting of two droplets separated by one DIB, I chose to encapsulate αHL and T7 RNAP in the same droplet. This was because αHL could permeabilise proteoliposomes, if αHL and proteoliposomes were in the same droplet, dissipating the PMF and abolishing ATP synthesis. Structures consisting of two droplets were chosen for both ease of construction and ability to print, as the printer was designed to fabricate synthetic tissues from two solutions. Structures containing three solutions have been printed using the 3D droplet printer, however these were technically challenging to align, especially on a small scale[47].

Attempts to form DIBs with proteoliposome and αHL/T7 RNAP droplet pairs proved challenging. With a five-minute incubation in 2 mM DPhPC droplets coalesced instantly when brought into contact. While increasing the incubation time to 15 minutes prevented coalescence, I was still unable to form DIBs. When in contact but with no DIB formation, incubation of droplet pairs led to the formation of an emulsion, which grew in length over time (**Figure 4.3**). Upon separation of the droplets the emulsion was associated with the αHL/T7 RNAP droplet. I hypothesised the emulsion was caused by the high protein density in the lipid monolayer of both proteoliposome-loaded droplets and αHL-loaded droplets as proteoliposomes fused and αHL inserted at the monolayer, respectively. DIBs would be unable to form with such a high protein concentration, and instead droplets would behave as hard spheres, which would not deform upon contact. I hypothesised that minute vibrations generated when transferring the sample to the microscope sheared small droplets off at the contact interface between the two larger droplets, producing the emulsions shown, and thereby decreasing the

volume of the αHL/T7 RNAP droplet. Dehydration of droplets and osmosis through the emulstion could also effect droplet volume.

It was becoming clear that large, nL droplets would not be suitable for my system due to both to slow equilibration of aqueous content and DIB instability. I hypothesised that decreasing the volume of droplets would be beneficial in combatting these issues. Firstly, lack of equilibration could be attributed to the random diffusion of the molecules through the bulk droplet. By decreasing droplet volume, the required distance that must be overcome by random diffusion is lowered. By taking Fick's first law, diffusion times can be estimated:

$$t \approx \frac{x^2}{2D}$$

Where "t" equals time taken for a molecule with diffusion coefficient "D" to diffuse "x" distance. With a diffusion coefficient of $1x10^{-9}$ m^2s^{-1} (assuming the diffusion coefficients of glucose and its derivative 2-NBDG would be similar), it would take 180 seconds for a molecule to diffuse from the centre of a 100 nL droplet to the centre of a neighbouring 100 nL droplet, assuming diffusion at the DIB is not limiting (conversely, for centre-to-centre diffusion for a 100μm diameter printed droplet pair would take 5 μs). As droplet equilibration was taking far longer than this time scale, diffusion across the membrane could be a limiting factor, potentially caused by low number of αHL inserted.

Secondly, decreasing droplet volume increases the rate of lipid monolayer formation[51]; preventing αHL and proteoliposomes denaturing or fusing at the oil-water interface, respectively.

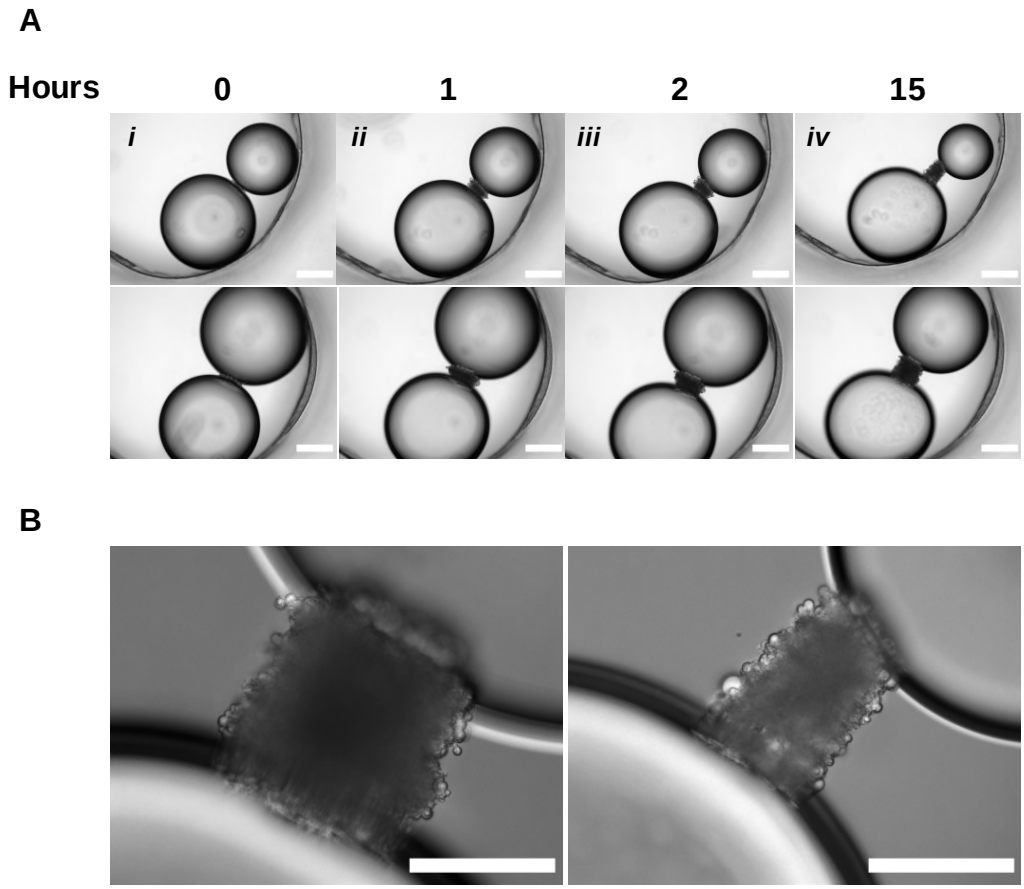

Figure 4.3. Emulsion between droplets containing αHL and proteoliposomes. (**A**) Representative optical microscopy images of nL droplets containing αHL and proteoliposomes. (**B**) Magnified optical image of **A*iv***. Scale bars in **A** 200 μm, **B** 100 μm.

I therefore decided to manufacture DIBs from pL sized droplets using the 3D droplet printer (**Figure 4.4A**). Into a glass cuvette I formed 500 pL (100 μm diameter) droplet pairs containing either 100 μg/mL αHL or 50 μM 2-NBDG (identical solutions to those used in the experiment described in **Figure 4.2**) in an oil containing 2 mM DPhPC. I first printed ten droplets of 2-NBDG before incubating them for five minutes to allow lipid monolayer formation. Droplets containing αHL were then deposited on top of 2-NBDG droplets. Before imaging, droplet pairs were incubated for an addition five minutes to ensure fully formed DIBs. After this five-minute incubation I observed excellent 2-NBDG transfer across the DIB, with

complete equilibration of 2-NBDG achieved across the droplet pair after 15 minutes (**Figure 4.4B**).

While 2-NBDG was a useful probe to investigate DIB permeabilisation, it was chosen precisely due to the knowledge that it translocated through αHL efficiently[1], a property that may not be shared with ATP. To this end I repeated the above experiment with 2′/3′-O-(N-methylanthraniloyl)adenosine 5′-triphosphate (Mant-ATP), a fluorescent ATP analogue (**Figure 4.4C**). Movement of 100 μM Mant-ATP through αHL was slower, and so I decided to ascertain whether DIB permeabilisation was sufficient for the eventual powering of IVT by ATP supplied across a DIB.

To do this I printed droplet pairs consisting of an IVT droplet, containing NTPs (minus ATP), DNA, T7 RNAP, and αHL and a sender droplet containing NTPs and ATP (**Figure 4.4D**). Both droplets contained DLM for Broccoli visualisation. 20 mM ATP was used in this experiment to ensure that the final NTP concentration remained 10 mM below Mg^{2+} concentration. A rapid increase in fluorescence indicating Broccoli transcription was detected after two hours, increasing in intensity over the course of the experiment. This clearly showed that IVT could be successfully energised from a distinct compartment separated by a lipid bilayer. DIBs not permeabilised by αHL showed minimal increase in fluorescence, especially in the early stages of the experiment. Some fluorescence was observed in these non-permeabilised DIB droplet pairs after overnight incubation in oil however, which may be linked to the decreasing droplet volume, caused by droplet dehydration (**Figure 4.4D*ii***). Decreasing droplet volume results in a higher DLM

concentration, assuming DLM is insoluble in oil. This would increase the background fluorescence. Dehydration of water-in-oil emulsions is an issue with these systems[27], and when powering proteoliposomes the extra thermal energy afforded by illumination must be taken into consideration.

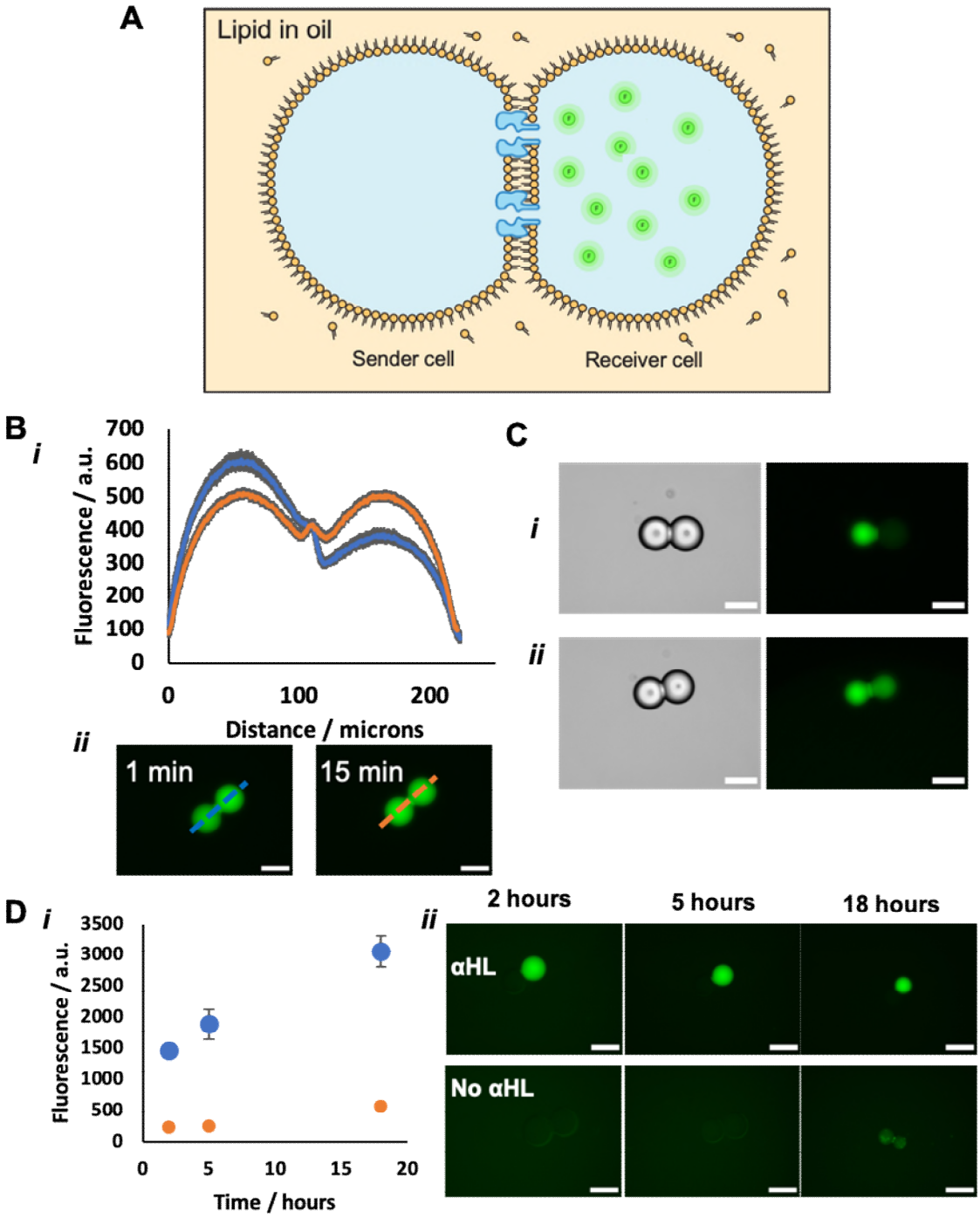

Figure 4.4. Rapid content mixing in pL droplets. (**A**) αHL permeabilises DIBs to hydrophilic fluorophores (**B**) ***i*** Fluorescence line profile of droplet pairs at 1 (blue) and 15 (orange) minutes post DIB formation, highlighting rapid 2-NBDG diffusion through aHL. ***ii*** Representative images from **B*i***. (**C**) Representative images showing Mant-ATP diffusion across aHL-permabilised DIBs after ***i*** 15 and ***ii*** 60 minutes. (**D**) ***i*** IVT fluorescence in a droplet pair with ATP supplied across the DIB. In the presence (blue) or absence (orange) of aHL. ***ii*** Representative images from **D*i***. For **B** and **D**, each data trace represents the mean fluorescence of 10 droplets. Error bars represent one standard deviation about the mean. **B-D** scale bars are 100 μm.

When repeating the above experiment, I observed two populations of IVT droplets with differing levels of fluorescence (**Figure 4.5A**). As these images were captured on an epifluorescence microscope, one would expect there to be a positive correlation between droplet volume and fluorescence, as light is collected in the Z-direction as well as the XY plane on the widefield epifluorescence microscope used to capture these images. Fluorescence quantification was performed by manually drawing a line segment over the centre of the droplet in ImageJ and averaging the range of fluorescent values. When using an epifluorescence microscope, the entire sample is illuminated and all the emitted light is collected, including out-of-focus fluorescent light. This means that fluorescence in the Z-direction is added. An alternative is to use a confocal microscope, where a pinhole aperture removes out of focus light, leaving a focal plane with a thickness of 0.5 μm, however one was not available during the period these experiments described within this thesis were performed. However, the size distribution of IVT droplets were narrow, and there was no correlation between droplet size and fluorescence, indicating another factor was at play here.

Upon further investigation I noticed droplets displaying a high level of fluorescence had a bridging ATP "sender" separating the main droplet of ATP from the IVT droplet (**Figure 4.5*ii-iii***). These small satellite droplets form either due to deformations to the glass nozzle used for printing, or applying too high of a high pulse voltage across the piezo[51]. As αHL was present solely in the IVT droplet, only the DIB between the IVT and small ATP droplet were permeabilised; the larger ATP droplet was isolated from the rest of the system. This observation was puzzling: there should not be a negative correlation between ATP supplied and

fluorescence unless inhibition occurs at high ATP levels. ATP concentration would be above the K_m for T7 RNAP for both cases, and so one would expect similar levels of fluorescence.

I conjured a couple of hypotheses for this observation. Firstly, there was a critical reagent required for transcription in the IVT droplet becoming diluted to below its minimal active concentration after droplet pair equilibration. Secondly, there was a reagent in the ATP sender droplet that was inhibiting transcription at high concentrations.

To test the first theory of there being a dilution of a critical reagent, I compared the solutions for both αHL/IVT and ATP droplets. The main source of imbalance in reagents between solutions was the addition of T7 RNAP in the IVT droplet, more accurately the storage buffer T7 RNAP was supplied in. This storage buffer contained 50 mM Tris-HCl, 100 mM NaCl, 20 mM β-ME, 1 mM EDTA, 50% Glycerol, 0.1% (w/v) Triton® X-100 and was diluted 10-fold into the final solution. To determine whether one of these components was beneficial to transcription and was diluted below its working concentration, I printed a new set of droplet pairs with the ATP droplet containing 10-fold diluted T7 RNAP storage buffer. No difference in fluorescence was observed compared to controls of ATP droplets lacking T7 RNAP storage buffer (**Figure 4.5B**). This demonstrated that excess dilution of T7 RNAP storage buffer was not responsible for lowering Broccoli fluorescence in large droplet pairs, however it did not rule out that another key reagent was diluted by DIB formation with larger ATP droplets.

I next investigated whether there was a chemical species having an inhibitory effect on either transcription or Broccoli fluorescence. As the only chemical present in the ATP droplet not present in the IVT droplet was ATP itself, I started here. Either ATP or the waste products of transcription, AMP and pyrophosphate, could be having inhibitory effects. Assuming total equilibration of the small ATP bridging droplet and the IVT droplet, I calculated the final ATP concentration would be 1 mM, compared to 10 mM when the larger ATP droplet formed a DIB with the IVT droplet. I printed structures with 500 pL αHL/IVT droplets connected by DIBs with equally sized droplets containing 2 mM ATP. $MgCl_2$ concentration in the buffer was lowered to 41 mM to accommodate this decrease in total NTP concentration. No difference in fluorescence was observed after incubation compared to that seen in droplet pairs formed with 20 mM "sender" droplets (**Figure 4.5C**); to be expected if the concentration of ATP in the IVT droplet exceeds the K_M of T7 RNAP for ATP. This suggested ATP was not having an inhibitory effect on transcription.

Finally, I attempted to recapture the conditions of the earlier experiment (**Figure 4.5A**). Forming the structures shown in **Figure 4.5A*ii-iii*** were exceedingly difficult to do on purpose, as a satellite droplet had to be generated and fall in a precise orientation to form a bridge between the larger droplets. Instead, I varied the volume of the ATP-droplet by adjusting the piezo pulse voltage. If indeed there was inhibition originating from the ATP droplet, then by decreasing ATP droplet volume fluorescence should increase. However, instead of a negative correlation between ATP-droplet volume and fluorescence, a positive correlation was observed (**Figure 4.5D**). Alongside the previous experiment, this suggests that there is not an inhibitor inhibiting transcription/fluorescence.

I decided not to pursue this line of investigation any further. While interesting scientifically and a potential method to increase the fluorescence output of my final system I was no closer to answering this question. As it stood I was already achieving acceptable fluorescence by transcription of the Broccoli aptamer in droplet pairs powered by supplied ATP, and it was crucial to optimise the use of proteoliposomes to power IVT in DIBs. Moreover, the development of DFHBI-Choline greatly increased Broccoli visualisation in printed droplets, removing the need somewhat for other methods of boosting fluorescence.

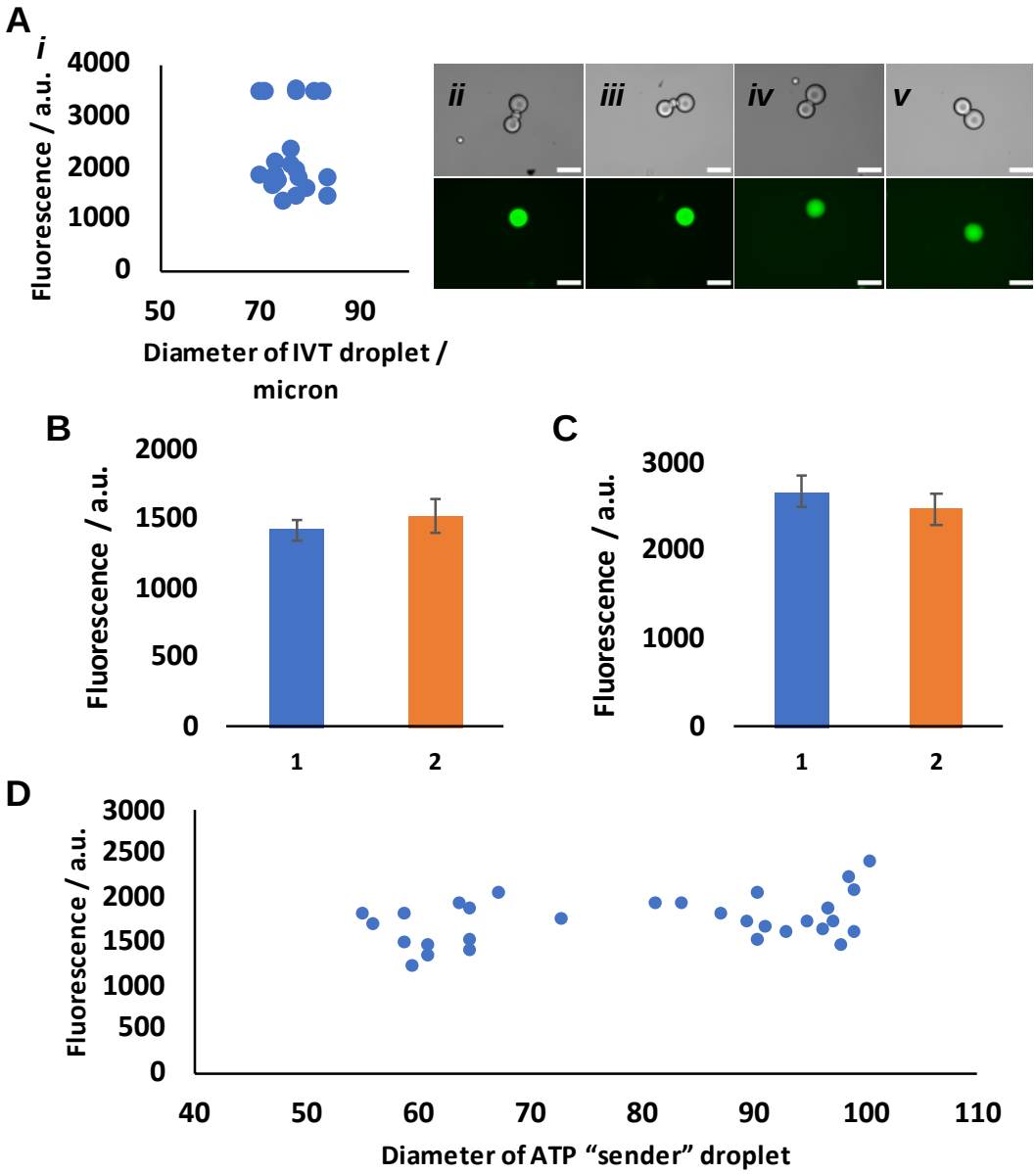

Figure 4.5 Enhanced fluorescence in droplets. (**A**) ***i*** Fluorescence IVT output of pL droplets revealing two populations. Note the detection limit of the microscope has been reached in the population of droplets with high fluorescence. ***ii-v*** Representative optical and fluorescent microscopy images from ***i*** showing saturating fluorescence in presence of bridging ATP sender droplet ***(ii,iii***) compared to those without ***(iv,v*)*.*** Scale bars 100 μm. (**B**) Fluorescence of pL droplet pairs with (blue) and without (orange) T7 RNAP storage buffer added to the ATP sender droplet. (**C**) Fluorescence of pL droplets pairs with either 1 (blue) or 10 (orange) mM ATP (final concentration) supplied from the ATP sender droplet. (**D**) Fluorescence of IVT droplets with varying volume ATP sender droplets. **B** and **C** values represent the mean of 10 droplets from the same experiment. Error bars represent one standard deviation about the mean.

4.2.3 Stabilising proteoliposomes in printed droplets

Decreasing droplet volume greatly enhanced the rate of droplet pair equilibration as seen in **Chapter 4.2.2**. However, the increased surface area to volume ratio of small droplets was of concern; the surface area to volume ratio of a 500 pL droplet is 5.85 times that of a 100 nL droplet. As I discussed in **Chapter 3.2.4**, proteoliposomes tended to aggregate at the lipid monolayer. By increasing the surface area relative to proteoliposome concentration, I was concerned a larger fraction of proteoliposomes would be removed from the bulk solution. Therefore, I turned again to the use of DPPE-PEG2000-containing lipid-in-oil solutions to provide proteoliposome homogeneity. It would be equally important to maintain the rate of small molecule equilibration in droplet pairs observed previously (**Figure 4.4A**).

Interestingly, upon repeating my previous experiment on αHL-mediated droplet pair equilibration with a lipid-in-oil containing pure DPhPC and no DPPE-PEG2000, a slower rate of equilibration was observed (**Figure 4.6A**). Previously, substantial equilibration occurred within 5 minutes (**Figure 4.4A**), and little equilibration was observed in this instance on a corresponding time-scale, with complete equilibration not reached after 35 minutes. However, considerable equilibration occurred after 35 minutes; and I deemed this to be an acceptable level for future experiments. I hypothesised the longer time required for droplet pair equilibration was a decrease in αHL activity. 15 μL aliquots of purified αHL monomer were subjected to multiple rounds of freeze/thawing and while

considered a robust protein, this may have had a detrimental impact on the ability of αHL to permeabilise DIBs.

I then doped the lipid-in-oil with DPPE-PEG2000. Pleasingly, DIBs formed from DPhPC with 2 and 4 mol% DPPE-PEG2000 showed acceptable rates of permeabilisation (**Figure 4.6C-D**). It is worth noting that while equilibration may appear slower for the DIBs formed with 2 mol% DPPE-PEG2000 (**Figure 4.6C**), it is in fact due to droplets containing 2-NBDG formed in 2 mol% DPPE-PEG2000 being 3.4 times larger in volume (1.77 nL vs 520 pL) than the droplets formed in DPhPC or 4 mol% DPPE-PEG2000 (**Figure 4.6B & D**, respectively). This was due to a defect with the glass nozzle when printing droplets. This provided hope that neither the rate of droplet equilibration or proteoliposome stability had to be sacrificed.

Finally, I looked at what I believed would be a DPPE-PEG2000 ratio that would ensure proteoliposome homogeneity, 10 mol%, the concentration used previously to stabilise an IVTT system[115]. In this previous study, αHL generated *in-situ* permeabilised DIBs to facilitate the recording of an electrical current. However, while only a single αHL pore was required for current detection, the high insertion number required for substrate diffusion may suffer due to such a high concentration of DPPE-PEG2000 in the DIB. Indeed, equilibration was severely inhibited with 10 mol% DPPE-PEG2000, with only one droplet pair showing a small amount of equilibration. The remaining 9 DIBs remained intact and impermeable to 2-NBDG. It was clear that a lipid composition with such a high concentration of DPPE-PEG2000 would not be suitable for my system.

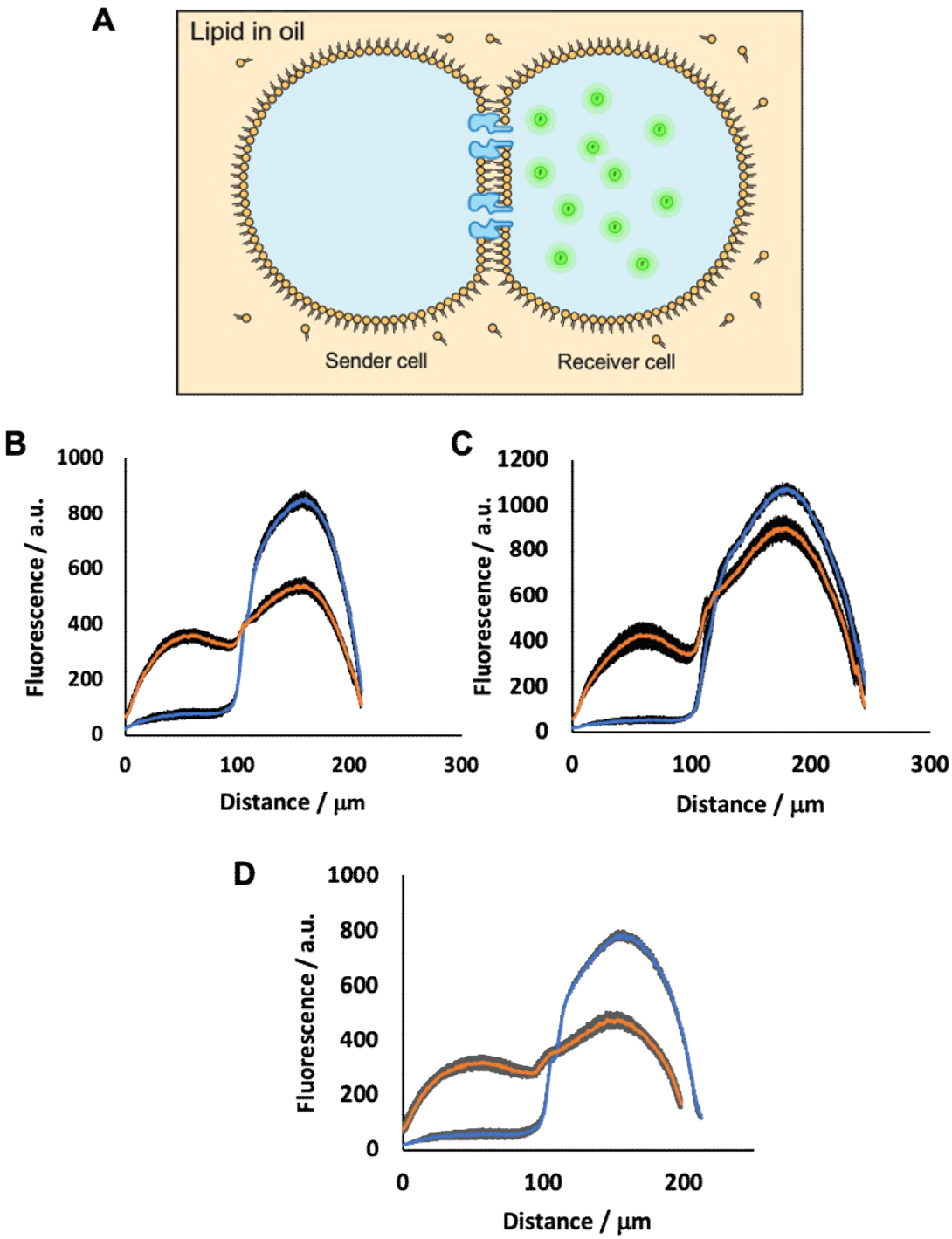

Figure 4.6 PEGylated DIBs. (**A**) αHL permeabilises DIBs to hydrophilic fluorophores. **B-D** Fluorescence line profile of a droplet pair, highlighting aHL-mediated permeabilisation of DIBs facilitating 2-NBDG equilibration. DIBs prepared with a lipid composition containing **(B)** 0, **(C)** 2, **(D)** 4 mol% DPPE-PEG2000.

Increasing the DIB size increases the available surface area for αHL insertion. This would lead to a greater rate of droplet pair equilibration. To this end I investigated

variations in Hx to AR20 ratios. Increasing the ratio of AR20 to Hx decreases the solubility of a lipid's fatty acid tails in the oil and hence promotes larger DIB formation[49]. I therefore looked at αHL permeabilisation of DPPE-PEG2000-containing DIBs in 65:35 Si:Hx. Excellent equilibration was observed in DIBs formed with 2 mol% DPPE-PEG2000 (**Figure 4.7A**), similar in rate to the best results seen so far (**Figure 4.4B**). However, DIB formation proved difficult when using 4 mol% DPPE-PEG2000 (**Figure 4.7B**) and thus equilibration naturally suffered, potentially due to DPPE-PEG2000 insolubility in AR20. It is known that DPPE-PEG2000 will precipitate in pure AR20[115]. While it appeared promising to use this ratio of Hx:AR20 going forward, issues with AR20 contamination and shortages (see **Chapter 4.2.4**) limited this quantity of AR20 available per experiment and so the decision was made to continue using a 1:1 ratio.

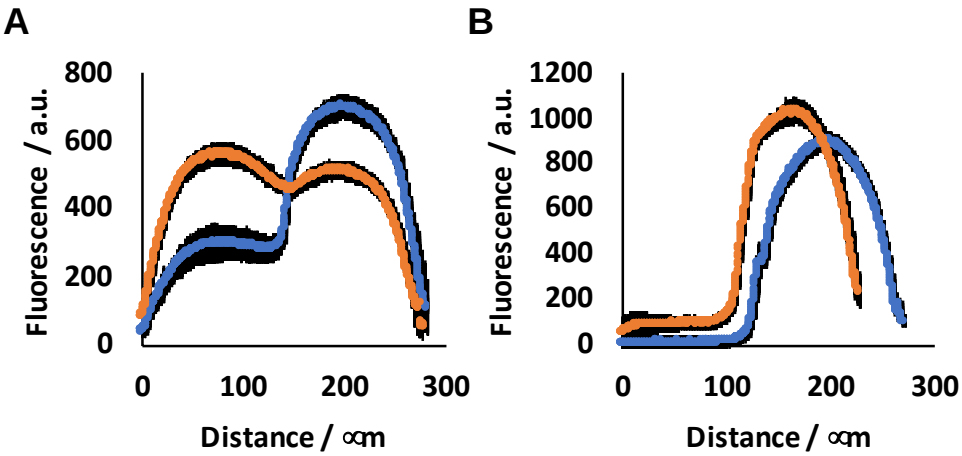

Figure 4.7 Increasing AR20:Hx. Fluorescence line profile of a droplet pair, highlighting αHL-mediated permeabilisation of DIBs facilitating 2-NBDG equilibration. DIBs prepared with a lipid-in-oil of 65:35 AR20:Hx with a composition of DPhPC and **(A)** 0, **(B)** 2 mol% DPPE-PEG2000. Traces represent 5 (blue) and 35 (orange) minutes post DIB formation. Each trace represents the mean fluorescence of 10 droplets. Error bars are one standard deviation about the mean.

Having investigated the effect of DPPE-PEG2000 on αHL-mediated permeabilisation of DIBs, it was now time to relook at proteoliposome stability. Droplets pairs were formed in 1:1 Hx:AR20 with solutions of proteoliposomes, and

a solution of αHL and 2-NBDG (**Figure 4.8A**). Successful DIB formation marked the first time that DIBs were stable in the presence of both proteoliposomes and αHL. Immediately red rings were observed for DIBs formed with both 2 and 4 mol% DPPE-PEG2000 (**Figure 4.8B and C**, respectively), indicating proteoliposomes associating at the oil-water interface. Pleasingly however, proteoliposome aggregation had minimal effect on droplet pair equilibration: as expected, droplet pairs formed in 2 mol% DPPE-PEG2000 possessed a faster rate of equilibration than those formed in higher DPPE-PEG2000. One of the initial concerns I had with proteoliposomes aggregated at the interface was the potential for a lipid/protein barrier to form between a αHL-functionalised DIB and the bulk droplet, preventing small molecule diffusion. These results confirmed that droplet pairs could be stably formed with proteoliposomes and αHL, an important stepping stone to the final experiment of light-activated ATP synthesis and powering of IVT across a DIB.

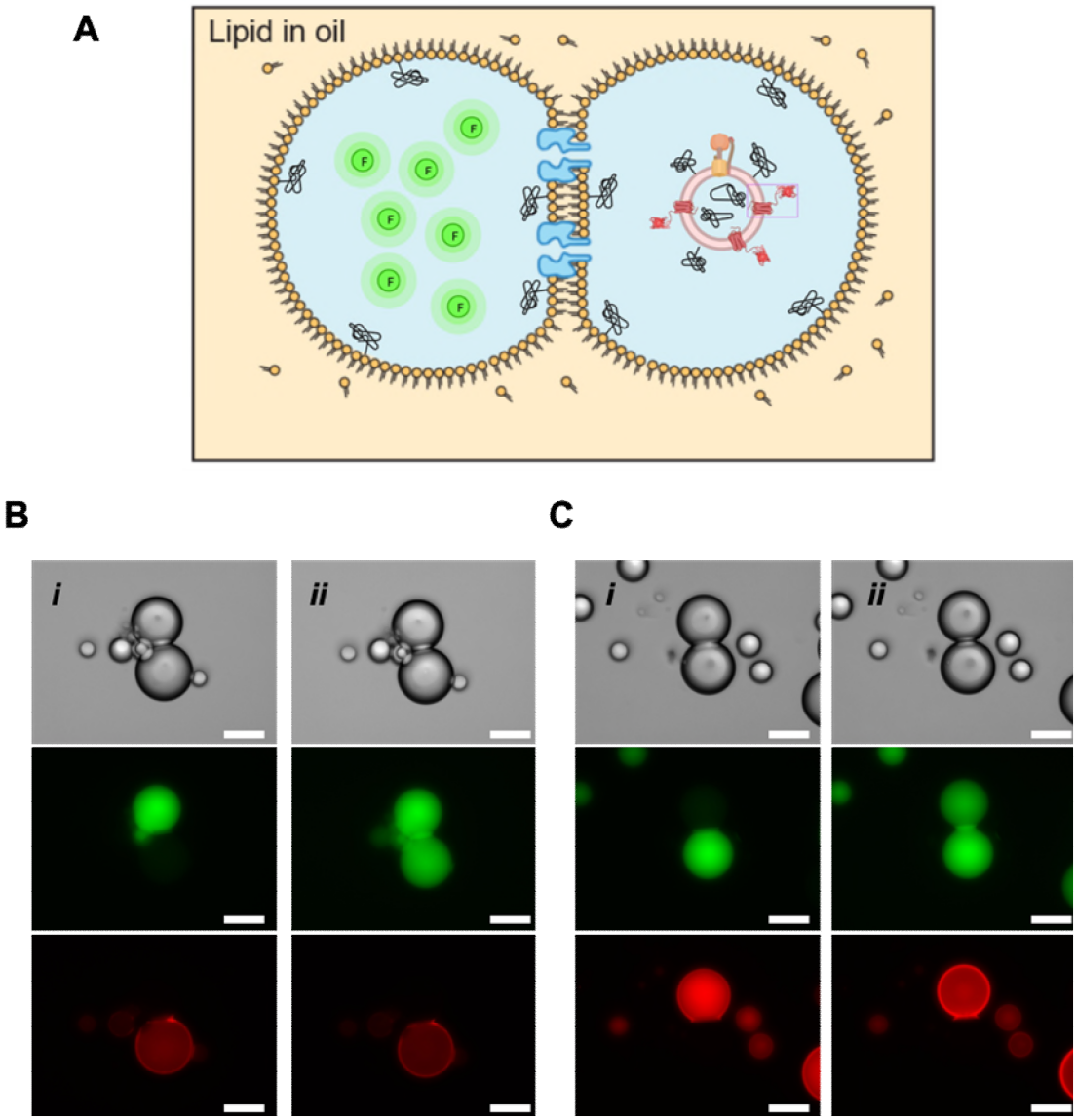

Figure 4.8 Stable αHL and proteoliposome droplet pairs. (**A**) DIBs formation between droplets containing proteoliposomes and droplets containing αHL and a hydrophilic fluorophore. (**B**) Optical and fluorescent microscopy images of a droplet pair in a lipid-in-oil solution containing 2 mol% DPPE-PEG2000 ***i*** 5 minutes and ***ii*** 20 minutes post DIB formation. Fluorescence in the green channel afforded by 2-NBDG, and in the red channel by mCherry. (**C**) As in **B** but the lipid-in-oil solution containing 4 mol% DPPE-PEG2000. Scale bars are 100 μm.

While association of proteoliposomes at the interface did not affect permeabilisation of DIBs, it was still unclear as to how ATP synthesis would be influenced. To this end I sought to prevent proteoliposome-interface association. It was clear that the addition of excess DPPE-PEG2000 in the oil phase inhibited DIB permeabilisation. An alternative solution was to incorporate PEGylated lipids

in the proteoliposome lipid bilayer. However, I was concerned that PEGylated lipids would inhibit membrane protein insertion into lipid-detergent micelles during the proteoliposome formation. Fortuitously, reconstitution efficiency of pR-mCherry into proteoliposomes can be tracked visually. I performed a new reconstitution with liposomes consisting of 3:1 DOPC:POPA, doped with 30 mol% cholesterol and 3 mol% DPPE-PEG2000. After reconstitution proteoliposomes were pelleted and showed a strong pink colour, indicative of successful pR-mCherry insertion. Conversely no pink was seen in the supernatant. ATP synthesis by proteoliposomes was not diminished by incorporation of DPPE-PEG2000 (**Figure 4.9B**). No association of proteoliposomes with the oil-water interface was observed when a solution of PEGylated proteoliposomes was printed in oil (**Figure 4.9C**). I therefore used these proteoliposomes going forward.

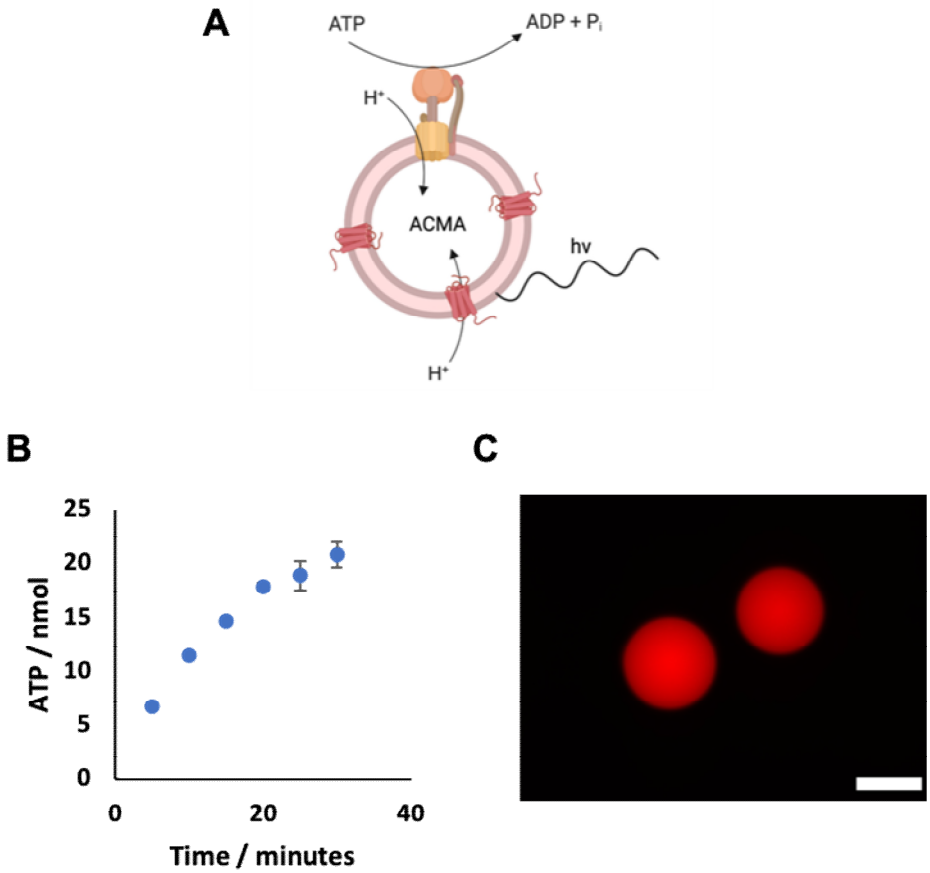

Figure 4.9. Proteoliposomes doped with 3mol% DPPE-PEG2000. (**A**) Light activated ATP synthesis. (**B**) Luminescence trace quantifying light-activated ATP synthesis. Data points represent the mean of two repeats. Error bars represent one standard deviation about the mean. (**C**) Fluorescence microscopy image of a solution of PEGylated proteoliposomes incubated for two hours in a solution of 1:1 Hx:AR20 containing 2 mM DPhPC with 3 mol% DPPE-PEG2000. Scale bar 100

4.2.4 Issues with silicone oil

While the experiments with PEGylated lipids were ongoing, I investigated other methods of maintaining proteoliposome homogeneity and promoting αHL insertion into DIBs. As ATP synthesising proteoliposomes are negatively charged due to the presence POPA, I hypothesised that proteoliposomes could be kept in solution through the addition of a negatively charged lipid to the oil phase. In addition to a

potential increase in stability, I wondered if changing the DIB lipid composition could increase αHL activity by, for example, the addition of negatively charged lipids and cholesterol to recreate a more physiologically relevant membrane[155].

Rather than optimise a novel lipid composition I took inspiration from the literature[41]. Here the authors used a lipid composition of 0.25 mM cholesterol, 0.25 mM DOPG, 4 mM DOPC, 0.5 mM DPhPC to stabilise droplets encapsulating cell extract. I first recreated this lipid composition in 1:1 Hx:Si, and printed 500 pL droplet pairs in order to investigate αHL permeabilisation, in a similar set of experiments to those in **Figure 4.5**. DIBs formed with these lipids exhibited larger bilayers than those formed with pure DPhPC (**Figure 4.10A**). Rapid permeation of 2-NBDG to the neighbouring droplet was observed, with a majority equilibrated after two minutes. IVT was powered across a DIB, with αHL facilitating ATP permeation across the lipid bilayer (**Figure 4.10B**). Membrane structural integrity was observed in DIBs lacking αHL, as indicated by a low fluorescent output.

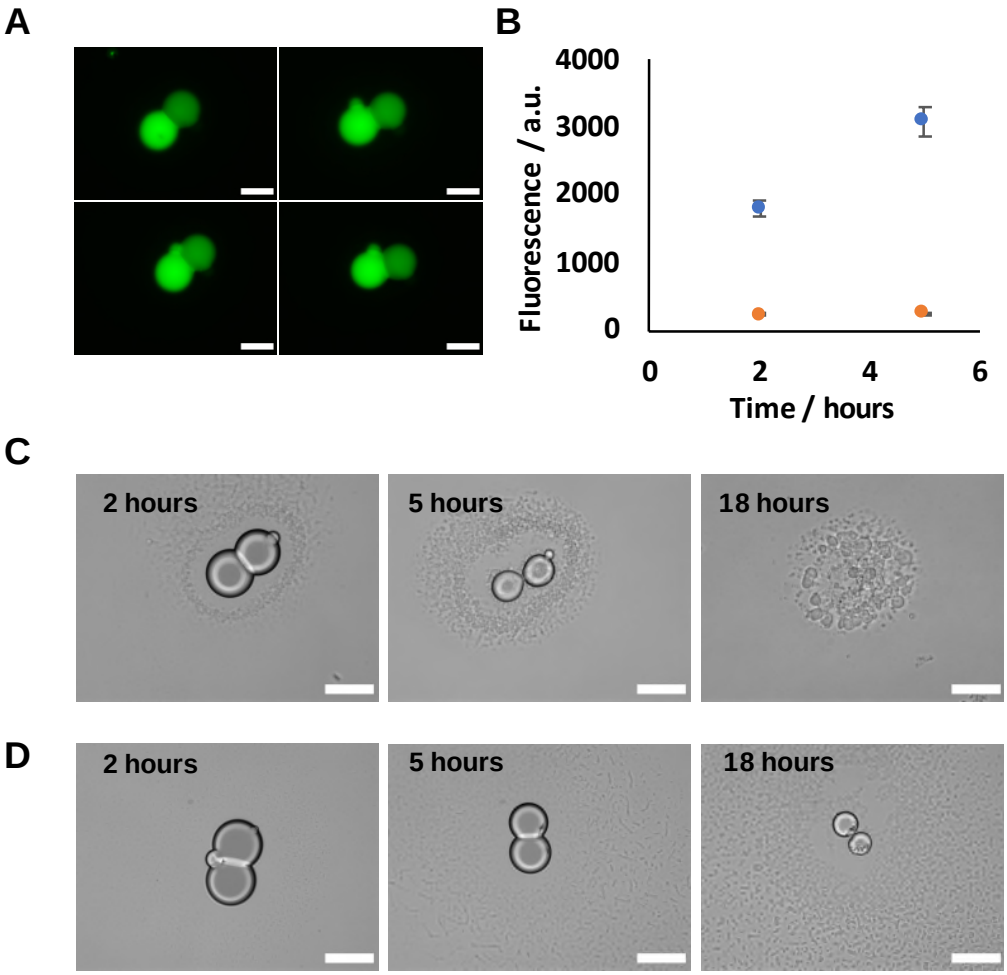

Figure 4.10 An anionic lipid composition. (**A**) Representative fluorescence microscopy images showing the rapid diffusion of 2-NBDG across an anionic DIB. Images taken immediately after DIB formation. (**B**) IVT fluorescence in a pL droplet pair with ATP supplied across an anionic DIB. In the presence (blue) or absence (orange) of αHL. Each data point represents the mean fluorescence of 10 droplets. Error bars represent one standard deviation about the mean. (**C**) Precipitation in 1:1 Hx:ONT AR20. (**D**) Same as in **C**, half lipid concentration. Scale bars 100 μm

However, I would be unable to use this lipid composition going forward. Over the course of the experiments significant precipitation was observed, localised around the droplet pairs (**Figure 4.10C**). Decreasing the total lipid concentration by half slowed but did not prevent lipid precipitation (**Figure 4.10D**). I therefore reverted to using a lipid composition of 2 mM DPhPC with 3 mol% DPPE-PEG2000. Precipitation of this lipid composition had not been noted in the original paper and I believe this is difference could be due to the source of AR20. Historically, the

Bayley group purchased AR20 from Sigma Aldrich without issue. However, in 2019 group members began to notice a white phase-separated liquid forming in bottles of AR20. Multiple bottles of AR20 purchased from Sigma Aldrich all contained these impurities, and attempts to conduct IVT in nanolitre droplets dispensed in these batches of AR20 failed. Unfortunately, all AR20 purchased from Sigma Aldrich came from the same batch and it would be many months before a new batch could be supplied.

The group was fortunate to be also supplied with AR20 from Oxford Nanopore Technologies (ONT). ONT had faced similar problems with contaminated AR20 in the past and so chose to stockpile large quantities of AR20. IVT could be successfully performed in ONT AR20, and no precipitation was observed. However, a colleague from the Bayley group, Dr Ravinash Krishna Kumar, discovered that ONT AR20 was more hydrophilic than AR20 from Sigma Aldrich. When forming a hydrogel structure from droplet networks one must break DIBs by precipitating lipids; this was achieved by replacing the Hx/AR20 mixture with pure of AR20[47]. Dr Krishna Kumar discovered that less ONT AR20 was required to precipitate lipids that for Sigma Aldrich AR20. A lower lipid solubility in ONT AR20 correlates with the precipitation observed in **Figure 4.10C-D**.

Furthermore, forming 500 pL droplets of proteoliposomes in 1:1 Hx:ONT AR20, I observed a worrying trend. Rapid loss of mCherry fluorescence occurred within minutes of droplet formation (**Figure 4.11B**). I was concerned that the other proteins in my system, F_1F_O, T7 RNAP, and αHL, were being similarly affected. I hypothesised that a contaminant present in the ONT AR20 was diffusing in to the

aqueous droplets. I believed this contaminant could be a chemical used during the polymerisation of the silicone chains. To remove any water-soluble chemicals that may have been present, I washed ONT AR20 with MQ water three times. A final wash with 250 mM glucose allowed for a straightforward extraction of the washed ONT AR20. Whereas droplets formed in untreated ONT AR20 and Hx showed a rapid decrease in mCherry fluorescence, washing ONT AR20 prior to droplet formation preserved mCherry fluorescence for at least five hours (**Figure 4.11C**). It was clear that something had been removed from the ONT AR20 by the washing step. I had not observed this effect in nL droplets, presumably due to the lower ratio of oil volume to water volume, as well as the smaller surface are to volume ratio.

Washing with deuterated H_2O and subsequent analysis by mass spectrometry (MS) and nuclear magnetic resonance (NMR) spectroscopy did not reveal any impurities. I stored washed ONT AR20 in a sealed glass vial with MQ water layered on top in order to sequester any residual or newly formed contaminants. However, when forming proteoliposome droplets in this oil a rapid decrease in mCherry fluorescence was once again observed (**Figure 4.11D**).

It was important to ascertain whether the observed effect was limited to mCherry fluorescence or a universal one influencing a multitude of proteins. If the effect was limited to mCherry then this would not be a serious issue, as after mCherry directed insertion of pR into lipid bilayers it became mostly redundant, expect for its uses as a marker. I therefore tested the IVT of Broccoli, visualised with DFHBI-Choline, in washed and unwashed ONT AR20. (**Figure 4.11E**) A striking difference was

observed: a 4.5-fold increase in fluorescence output when droplets were formed in washed ONT AR20. It was clear that this effect was not limited to just mCherry fluorescence, and thus would most likely affect ATP synthesis as well.

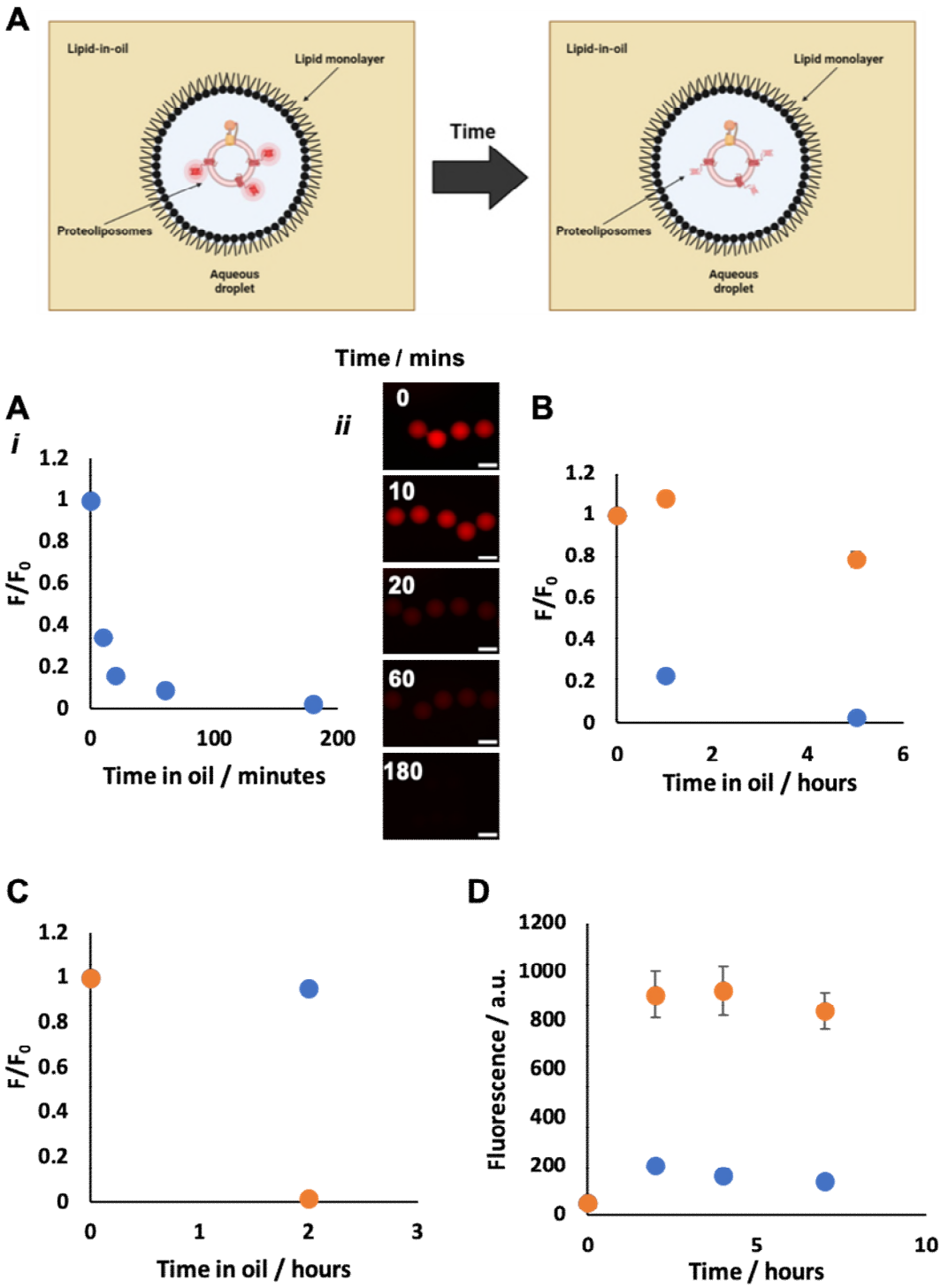

Figure 4.11. Silicone oil inhibits protein function. (A) Lowering mCherry fluorescence upon droplet formation in oil (B) *i* mCherry fluorescence in water-in-oil droplets. *ii* Representative fluorescence microscopy images from *i*. Scale bars 100 μm. (C) mCherry fluorescence in droplets in oil containing washed (orange) and unwashed (blue) AR20. (D) mCherry fluorescence in droplet formed in oil containing AR20 washed five days previously (orange) or washed 30 minutes prior (blue) (E) IVT fluorescence of droplets formed in an oil containing washed (orange) or unwashed (blue) AR20. For B – E, each data point represents the mean fluorescence of 10 droplets. Error bars represent one standard deviation about the mean.

In an effort to remove my dependence on AR20, I trialled DIB formation in a silicone oil with differing molecular structures to AR20 but matching density and viscosity (Silicone oil DC 200®, Sigma Aldrich – viscosity of 20 mPa.s at 25 ^{o}C, density 1.00 g /mL at 20 ^{o}C). The polymer chain contained repeating dimethylsiloxane units with no phenyl moieties, unlike AR20. Unfortunately, DPhPC was not soluble in a 1:1 mixture of this silicone oil and Hx. After sonication, the lipid in oil solution turned cloudy, and under magnification solid particulates were observed (**Figure 4.12**). I therefore returned to the use of ONT AR20, with the intention to determine the mechanism of enzyme inhibition.

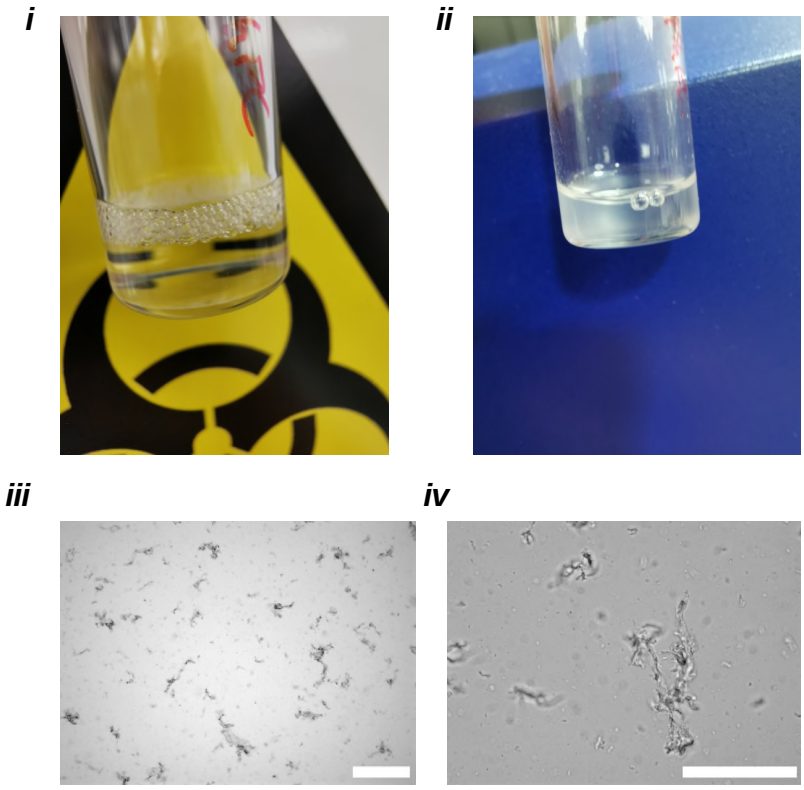

Figure 4.12 Using new formulations of silicone oil. Lipids are readily dissolved in a new silicone oil ***i***, but precipitate after sonication ***ii***. ***iii*** and ***iv*** Magnified images of oil from ***ii***. Scale bars are 200 μm.

As ONT AR20-induced protein inhibition seemed a non-specific phenomenon I now hypothesised that rather than being caused by a small molecule contaminant, the acidity of ONT AR20 could be the driving force behind the decrease in mCherry fluorescence[156] and loss of T7 RNAP function[157]. To test this, I printed 500 pL droplets containing 200 μM pyranine, a pH sensitive fluorophore[158]. Pyranine was selected due to its hydrophilic properties; unlike DFHBI, pyranine should not partition into the oil phase. If droplets were being acidified by ONT AR20 then one would expect a decrease in pyranine fluorescence and indeed that was observed (**Figure 4.13A**). To validate this finding and to ensure that this was not caused by pyranine diffusing into the oil, I varied the concentration of buffer from 0 to 200 mM Tris, pH 8.00. If droplet acidification from the oil was taking place, increasing Tris

concentration should maintain fluorescence. Pleasingly that was observed (**Figure 4.13B**); 200 mM Tris maintained fluorescence over the time frame of the experiment – note the increase in fluorescence due to droplet dehydration. Conversely, droplets formed without Tris showed a steeper rate of fluorescence drop-off compared to solutions with 10 mM Tris, indicative of rapid acidification. These experiments appeared to validate the hypothesis that droplets were becoming acidified, however I still could not rule out that pyranine was partitioning into the oil phase.

I next went to prove that pyranine was still present in aqueous solution by restoring fluorescence through the addition of base. Here I manually picked up individual droplets of quenched pyranine without Tris (**from Fig 4.13B,** grey data points, T = 1H) and formed a DIB with a droplet of 1 M NaOH. Instantly fluorescence was restored in the pyranine droplet, far above the initial level (**Figure 4.13C**), as hydroxide ions were either diffusing across the DIB or through the oil into the neighbouring droplet. This did not confirm that previously pyranine had been present but non-fluorescent, because the majority of pyranine might have diffused out of the droplet into the oil and the fluorescence of the remaining, lower concentration of pyranine been greatly enhanced by addition of base. As previously mentioned, this explanation was unlikely considering the hydrophilicity of pyranine.

I wanted to know whether this base-mediated fluorescence recovery was active at long distances and so I monitored the fluorescence of pyranine droplets with no buffer located approximately 1 cm away from a droplet of 1 M NaOH. After a one-

hour incubation I observed an increase in fluorescence, confirming that indeed the base could diffuse through the oil phase (**Figure 4.13D**). This opened up a possibility for base-treatment of ONT AR20, such as washing with Na_2CO_3 prior to use; and this will be investigated going forward. Unfortunately, due to droplet dehydration I was not able to measure any further fluorescent increases in experiment detailed in **Figure 4.13D**.

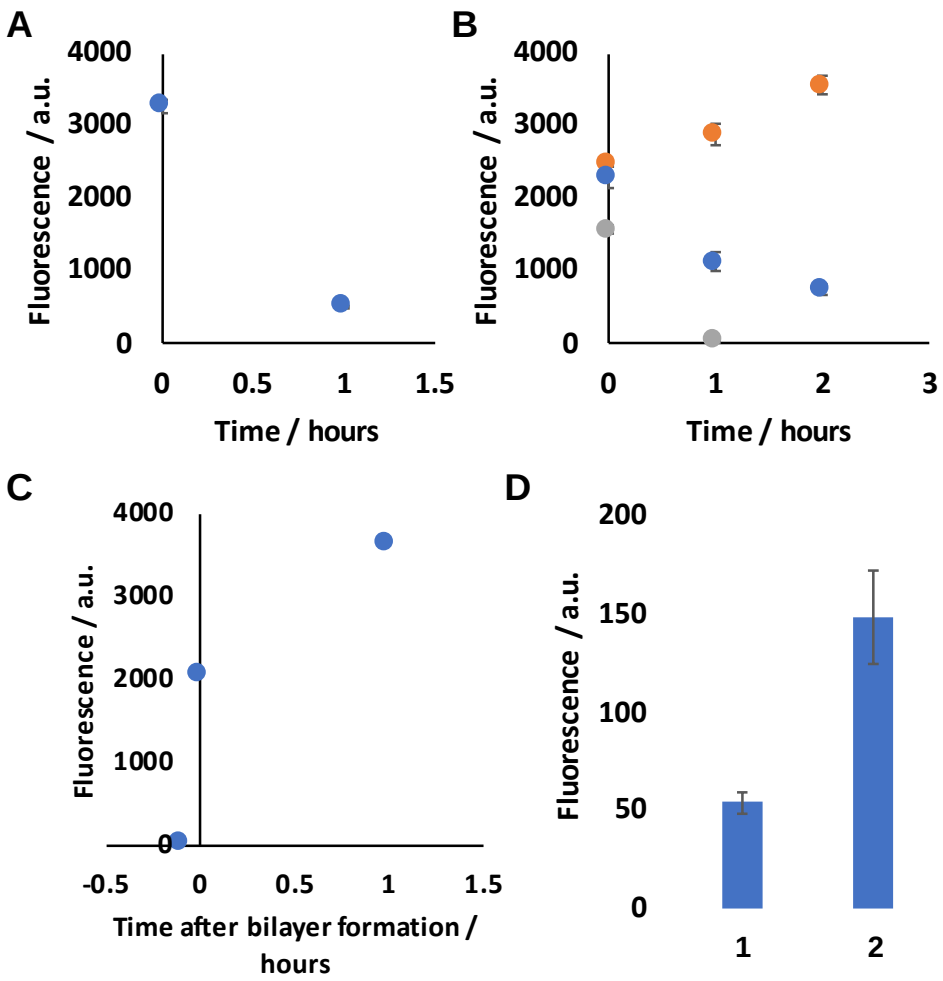

Figure 4.13 Droplet acidification. (**A**) Fluorescence of pyranine droplets incubated in 1:1 mixture of Hx:ONT AR20. 10.6 mM Tris present in solution. (**B**) Fluorescence of pyranine droplets incubated in 1:1 mixture of Hx:ONT AR20. Pyranine solutions contain 0 (grey), 10 (blue), or 200 (orange) mM Tris, pH 8.00. (**C**) Fluorescence of a pyranine droplet, deficient of buffer, before and after DIB formation with a droplet of 1 M NaOH. (**D**) Fluorescence of a pyranine droplet, deficient of buffer, before and after a droplet of 1 M NaOH was dispensed approximately 1 cm away. Fluorescence measured (**1**) prior to 1 M NaOH addition and (**2**) one hour after. **A** and **B**, each data point represents the mean of 5 droplets, each from the same experiment. Error bars represent one standard deviation about the mean. **C** and **D**, each data point is from one droplet.

4.2.5 Density of droplets

Numerous lab members of the Bayley group were using ONT AR20 in their experiments; however, I was the only one observing a change in droplet-based biochemical functionality upon washing ONT AR20. I hypothesised that this was due to the local environment of droplets. While others were constructing printed synthetic tissues containing between 56[47] and 560 droplets (Jorin Riexinger, unpublished work), I was looking at one or two droplets in isolation. Droplets at the periphery of a droplet network would buffer internal droplets against acidification. Furthermore, I hypothesised the hydration of oil may be crucial to the correct functioning of biochemical processes within droplets, in which case multiple droplets in close proximity would be beneficial; the cumulative diffusion of water from each droplet in the network into the oil phase would maintain a certain level of hydration.

To test this theory, I printed droplets containing an IVT cocktail, visualised by DFHBI-Choline (**Figure 4.14A**), either 800 μm apart or in close proximity in the same cuvette (**Figure 4.14A*ii-iv***). Droplets in close proximity did not have controlled inter-droplet distances, but were formed by firing the piezo at maximum speed while moving the printing nozzle across the cuvette. After a two-hour incubation a striking difference in fluorescence was observed; droplets spaced 800 μm displayed a lower fluorescence than those spaced closer together (Figure **4.14B**). I hypothesised that if this effect was caused by differences in oil hydration and droplets in close proximity maintained hydration of oil to a greater degree, then droplets spaced 800 μm apart would dehydrate at a faster rate. This would result

from droplets printed close together needing to yield individually only a fraction of the total amount of water to reach a certain level of oil hydration, compared to single droplets, where all water must come from that droplet. Looking at the diameter of the droplets described above over time, a clear increase in dehydration occurred when droplets were spaced 800 μm apart (**Figure 4.14C**). In contrast, droplets in close proximity to one another held consistent volumes.

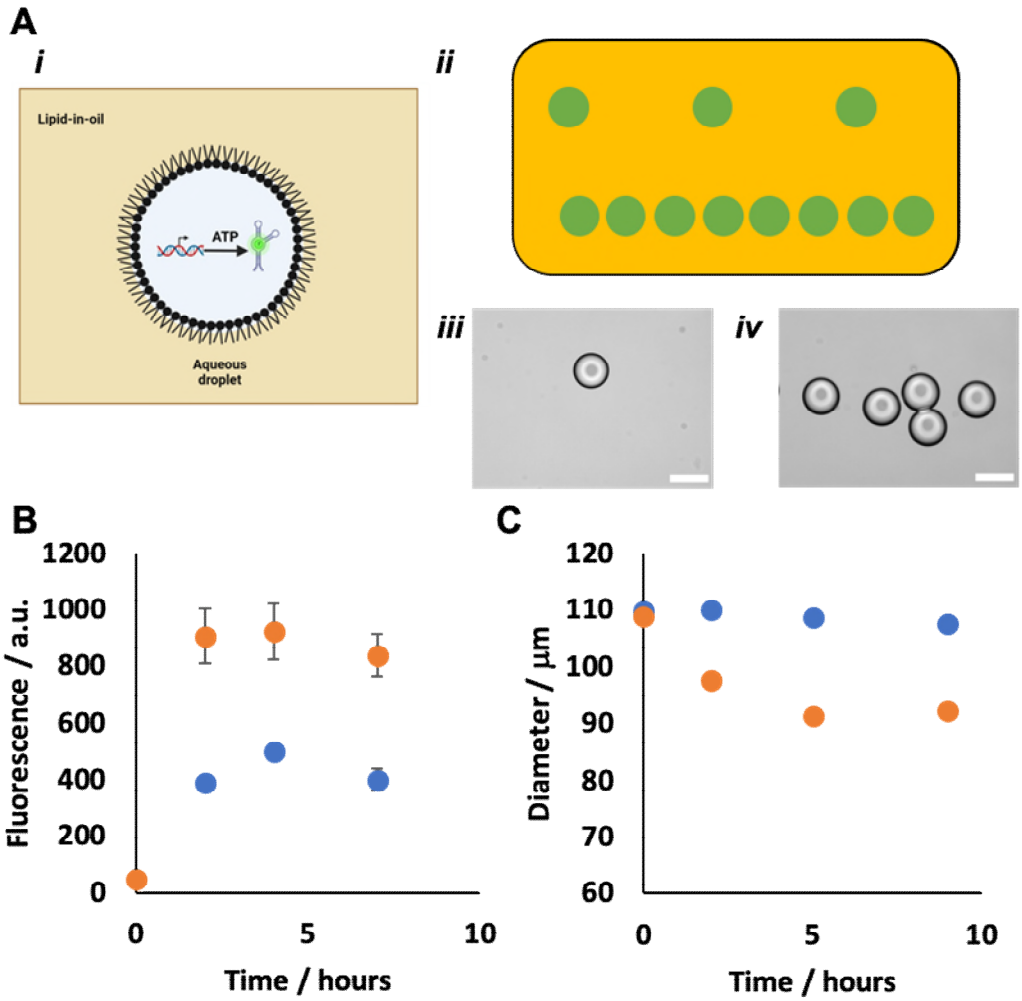

Figure 4.14 Density of printed droplets. (**A**) ***i*** ATP-driven IVT of a RNA aptamer in pL droplets ***ii*** Experimental setup. Droplets (green) were printed in a cuvette containing washed oil (yellow) either 800 μm or in close proximity. ***ii*** Representative image of low density droplets. ***iii*** Representative image of high density droplets. For ***ii*** and ***iii*** scale bars are 100 μm (**B**) Fluorescence from IVT in high (orange) and low (blue) density droplets. (**C**) Diameter of high (orange) and low (blue) density droplets. **B** and **C** data points represent the mean fluorescence of 10 droplets. Error bars represent one standard deviation about the mean.

From these findings, I found the density of droplets to be an important consideration when working with pL droplets My hypothesis was that this was linked to the hydration level of the oil surrounding droplets. Washing ONT AR20 with MQ water has most likely helped in this regard, although it raises the question whether the final wash with 250 mM glucose should be omitted, as this may extract water from ONT AR20. I plan to build droplet networks housing the systems that I have developed but in reaching this goal there are limitations surrounding DIB stability, ATP dilution, and printer set-up that necessitate optimising the system with droplet pairs. Issues with the printer set-up revolve mainly around the current maximum of two solutions printed simultaneously. Working with ATP synthesising droplet networks would require a minimum of three solutions but most likely four, due to requiring proteoliposome, αHL, spacer, and biological function droplets. Members of the group are working on upgrading the printer to handle more inks simultaneously.

4.2.6 Light-activated ATP synthesis powers IVT across lipid bilayers

Having optimised light-activated ATP synthesis, visualisation of IVT, and αHL-mediated DIB permeabilisation, as well as preventing inhibition of the aforementioned biochemical processes by acidification from ONT AR20, it was now time to combine these separate areas into a singular system. Here I would demonstrate the first example of light-activated ATP synthesis with ATP produced performing work in a separate compartment, in a synthetic system.

The potential for droplet dehydration (see **Chapter 4.2.5**) was of concern: therefore, to ensure formation of the correct structure (one proteoliposome droplet connected to one IVT/αHL droplet) droplet pairs were to be separated by 800 μm, a distance at which droplets were susceptible to dehydration. 800 μm was used to separate droplet pairs to ensure that when the cuvette was moved between the microscope and the incubator vibrations did not bring droplet pairs into contact with one another. If careless when moving the cuvette, droplets tended to cluster and coalesce at the centre of the cuvette. Designing and manufacturing custom cuvettes with either 3D-printed or etched channels to hold droplets in position is underway.

Dehydration was of particular concern due the addition of illumination. Excess infrared (IR) radiation emitted from the LED would increase the temperature of the aqueous droplet and thus increase dehydration. Therefore, to minimise IR radiation an IR blocking filter was attached to the LED. Additionally, I created a humid environment for droplets by enclosing the cuvette in a petri dish filled with a thin layer of water during incubation at 37 ^{o}C.

With these factors surrounding dehydration addressed, I proceeded to carry out light-activated ATP synthesis coupled to IVT across a DIB. I formed DIBs between pairs of droplets with a solution of proteoliposomes, and a solution IVT/αHL. Upon illumination of droplets I saw a large light-dependent increase in fluorescence in droplets containing T7 RNAP, signifying that ATP was successfully synthesised and diffusing across the DIB to facilitate Broccoli transcription (**Figure 4.15B)**. Both

mCherry and Broccoli fluorescence were fully compartmentalised by the DIB (**Figure 4.15C**). This experiment succinctly joins all previous major lines of investigation, validating the combined system and opening up the development of larger synthetic tissues with a multitude of unique biochemical processes powered by light-activated ATP synthesis.

Low fluorescence was observed in droplets shielded from light, albeit with a small trend of increasing fluorescence over time. This is most obvious comparing the on/off states, that is illumination vs non-illumination: the ratio decreased over time as ATP is made in the droplet shielded from light (**Figure 4.15D**). It is important to note that fluorescence of the on state at nine hours is not accurate due the detection limit of the microscope being reached. I hypothesised that the increase in fluorescence of droplets shielded from light was by either exposure to light whilst imaging or through droplet dehydration and the subsequent concentration of reagents varying droplet pH.

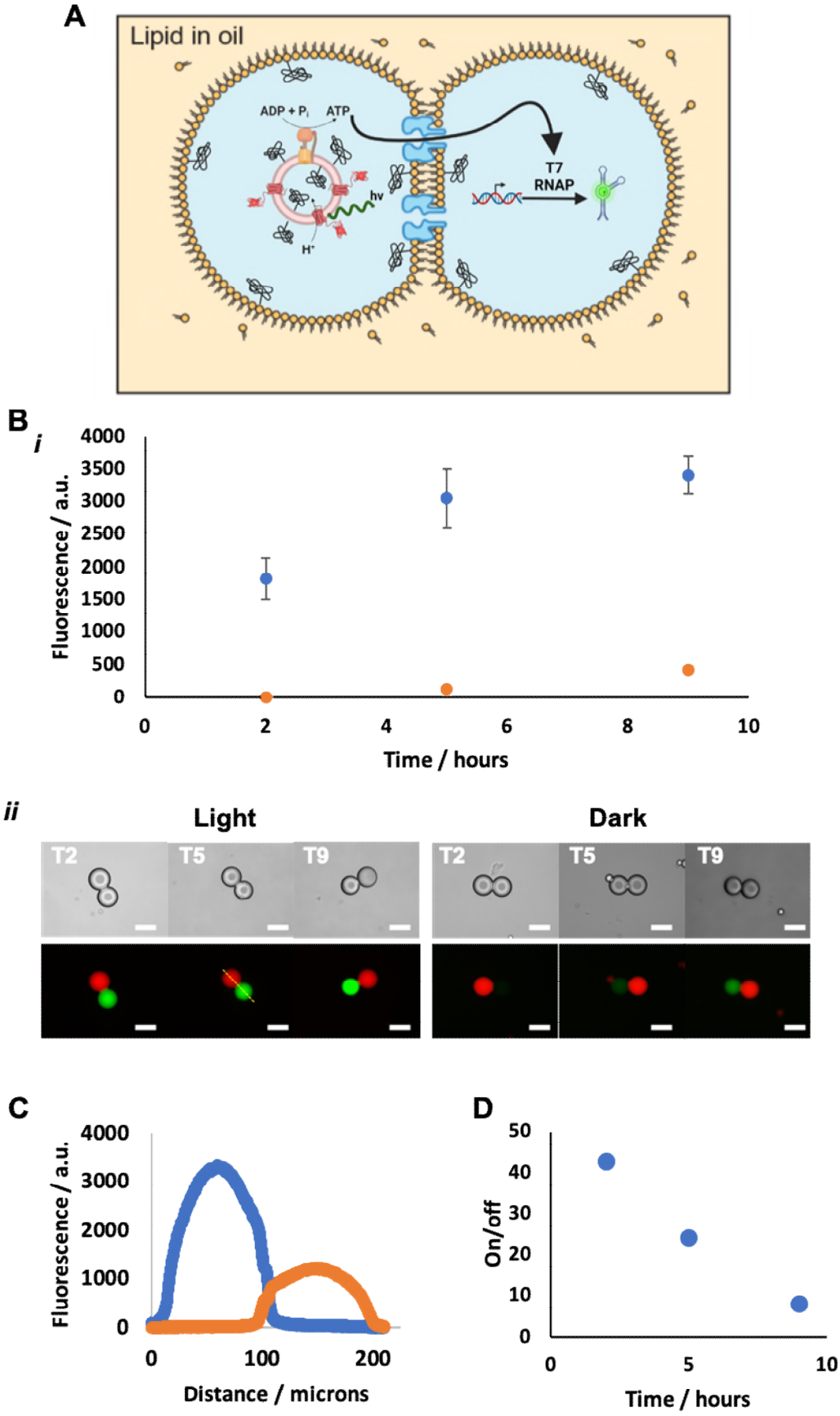
A
Lipid in oil
ADP + Pi
ATP
T7
RNAP
hv
H+
B
i
Fluorescence / a.u.
4000
3500
3000
2500
2000
1500
1000
500
0
0
2
4
6
8
10
Time / hours
ii
Light
Dark
T2
T5
T9
C
Fluorescence / a.u.
4000
3000
2000
1000
0
0
100
200
Distance / microns
D
On/off
50
40
30
20
10
0
0
5
10
Time / hours

Figure 4.15 Light-activated ATP synthesis powers IVT across a DIB. (**A**) Light-activated ATP synthesis powers the IVT of a fluorescent RNA aptamer is a compartment separated by a lipid bilayer. (**B**) ***i*** Fluorescence of IVT droplets when illuminated (blue) and shielded from light (orange). Each data point represents the mean fluorescence of 10 droplets. Error bars represent one standard deviation about the mean. ***ii*** Representative fluorescence microscopy images from ***i***. Scale bars are 100 μm (**C**) Line profiles of a droplet pair from ***ii*** showing compartmentalised mCherry (orange) and Broccoli/DFHBI-Choline fluorescence. (**D**) Fluorescence increase upon illumination at various time points from **B**.

In terms of refining the experimental set-up, I recognised it would be helpful to address the fact that the limit of detection was reached and fluorescence levels oversaturated at the settings chosen for the epifluorescence microscope (**Figure 4.15B,** + Light, 9 hours). I believed that my experimental set-up was the leading factor here, specifically the accuracy in which I was illuminating the cuvette: I had collimated the LED to provide a beam of illumination with radius approximately 0.5 cm; and with a cuvette of 2 cm by 1 cm I was illuminating at most around half of the available area. Droplet pairs at the periphery of illumination would not be energised to the same extent as those under direct illumination. To address this a 3D printed cuvette holder will be designed to improve the positioning of the cuvette relative to the LED.

4.3 Conclusion

To conclude the research developments presented in this thesis, I have shown how it is possible to create ATP-synthesising proteoliposomes and an optimised IVT reaction (described in **Chapters 2 and 3**, respectively) and in this chapter how these elements can be combined in separate compartments bound by lipids. WT αHL, a pore forming protein, was purified from *S. aureus* and utilised to facilitate chemical communication across DIBs. After addressing problems associated with

acidic AR20, I was able to achieve the first example of light-activated ATP synthesis coupled to a biochemical reaction in a distinct compartment in a synthetic biology system. This development is a step towards the design and fabrication of synthetic tissues with on-demand energy generation, in which illumination[159] could enable the spatiotemporal control of protein synthesis[14], carbon fixation[12], and enzyme activation.

5 Conclusions and future work

The development of synthetic tissues with an ability to regulate energy moves us closer to the design of biomedical devices capable, for example, of producing therapeutic proteins on demand. Furthermore, this objective is a key milestone towards the development of bottom-up artificial life. This thesis has described the development of a system capable of light-activated ATP synthesis in lipid-bound droplet networks, with synthesised ATP performing work across lipid bilayers in separate compartments.

In **Chapter 1.6**, I described the three objectives that were tackled in this thesis.

1. Light-activated ATP synthesis
2. An ATP-dependent biological process able to be visualised and functional in a droplet network
3. Generation of droplet networks, including stabilising droplet pairs against coalescence and permeabilising DIBs to hydrophilic chemicals.

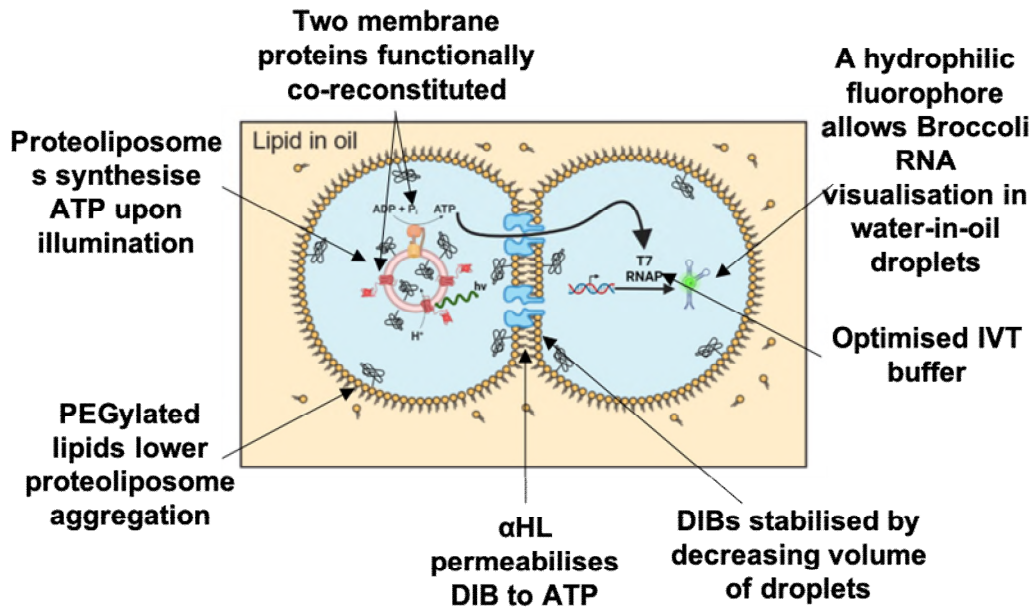

Figure 5.1. Optimisation required to achieve light-activated ATP synthesis and the subsequent powering of transcription across lipid bilayers.

In **Chapter 2**, I discussed the production of proteoliposomes capable of light-activated ATP synthesis to achieve objective one. Amongst other findings, I showed how the choice of detergent was crucial to preserving the activity of two membrane proteins, F1FO and pR during the reconstitution procedure. The incompatibility of the detergents required for F1FO and pR made it necessary to incorporate a new construct, pR-mCherry, in the reconstitution procedure. ATP impurities in commercial ADP were enzymatically removed with hexokinase. Maximum ATP synthesis rates of 53.2 nmol.min-1.mg ATP-1 were achieved with the inclusion of 30 mol% cholesterol in proteoliposome bilayers and ATP concentrations in the micromolar range were reached, accomplishing objective one. The proteoliposomes described within this chapter would enable the powering of biological processes in synthetic tissues.

In **Chapter 3**, I described the creation of a model system based on ATP-driven IVT in the aim of achieving objective two. After optimising transcription of the fluorescent Broccoli aptamer [126] in bulk in part through the addition of DTT to new aliquots of buffer every seven days due to the observation of decreased IVT output linked to DTT degradation, I described the light-activated transcription of Broccoli in nL-sized droplets with ATP supplied by proteoliposomes. Several challenges were overcome when translating the system from bulk solution to water-in-oil droplets; the crucial issue being lack of visualisation of the Broccoli aptamer, hindered by DFHBI solubility in oil. To this end, I designed a novel hydrophilic Broccoli fluorophore, DFHBI-Choline, to prevent loss of fluorophore to oil.

I observed acidification of pL droplets via AR20 which was inhibiting IVT and diminishing mCherry fluorescence. Acidic AR20 was neutralised through a wash step with water. This, combined with the work outlined in **Chapter 3**, completed objective two, as a biological function was powered by light-activated ATP synthesis in a droplet.

In **Chapter 4**, I described the development of the system from single droplets to droplet networks to achieve objective three. A pore-forming protein, □HL, permeabilised DIBs, enabling ATP to perform work across lipid bilayers. The addition of PEGylated lipids to both the oil phase and proteoliposomes prevented the association of proteoliposomes at the oil-water interface. Investigations into the optimal concentration of PEGylated lipids were undertaken to ensure that □HL insertion was not drastically limited by PEG shielding of DIBs. To stabilise DIBs and increase the rate at which the contents of droplet would equilibrate, droplet volume was lowered from 100 nL to 500 pL; droplet pairs were subsequently manufactured using the 3D droplet printer previously developed within the group[51]. This completed objective three.

In conclusion, I demonstrated the IVT of the Broccoli aptamer in a droplet pair, with ATP synthesised upon illumination and supplied from a compartment separated by a lipid bilayer, achieving the overall objective of this thesis.

Transcription of the Broccoli aptamer has created a model of a biologically relevant function, but the aim remains to assemble synthetic tissues on a larger scale with additional functions that will provide greater therapeutic benefits and better

recapitulate natural systems. The machinery of protein synthesis has been reconstituted in synthetic cells to drive the differentiation of neural cells[13] and represents an attractive option to energise in droplet networks. Stimuli-responsive protein synthesis has been performed in droplet networks using light-activated DNA[115]. However, the ultraviolet (UV) light required to uncage light-activated DNA is harmful to living tissues[160]. ATP-synthesising proteoliposomes, energised with non-ionising 530 nm light, represent a promising alternative to afford stimuli-responsive protein synthesis. To perform these experiments a number of complications must be overcome. For example, taking the NEB PURExpress IVTT kit, one must remove both ATP and the ATP regenerating systems: creatine kinase and nucleoside-diphosphate kinase. The NEB PURExpress IVTT kit is sold pre-mixed and so custom IVTT kits will be required to minimise the off state. Light-activated ATP synthesis has been coupled to IVTT in synthetic cells[14], but to date this goal has not been reached synthetic tissues.

Selectively powering multiple distinct biological functions within a single synthetic tissue would be an improvement over the tissues described within this thesis. This can be achieved either through the spatiotemporal control of ATP synthesis or by directing the flow of ATP. Previously, synthetic tissues were activated via light at single droplet resolution[159]; using this technology one could power ATP-dependent functionality at specific locations in synthetic tissues. Alternatively, the movement of synthesised ATP can be directed by applying a potential across the synthetic tissue; driving anionic ATP through αHL pores embedded in DIBs, similar to the electrophoresis of DNA during nanopore DNA sequencing.[153] This potential can

be applied across the synthetic tissue from electrodes[51] or from the generation of a proton or ion gradient[161].

Going forward, it may be possible to interface the synthetic tissues described within this thesis with living cells in order to influence their biological activity. This would require the synthetic tissues to undergo a phase transition to remove the external oil phase. Removal of the oil phase has recently been achieved in our group to afford synthetic tissues encapsulated within an external continuous lipid bilayer[55].

Acting as soft, implantable bio-factories, synthetic tissues could facilitate delivery of therapeutic proteins to living cells. One method of delivery would entail the IVTT of therapeutic proteins fused with cell-penetrating peptides (CPPs)[162]. CPPs are small peptides, often cationic, that facilitate the energy-independent translocation of hydrophilic macromolecules across lipid bilayers[163]. CPP fusion proteins are currently in development for the treatment of cancer[164], inflammation[165], and neurodegenerative diseases[166]. Alternatively, proteins may be delivered through disruption of the external bilayer via esterase-catalysed surfactant formation[22] or perfringolysin O (PFO)[13] insertion. PFO is a protein pore with an outer diameter of 25 – 30 nm [167] that permeabilises lipid bilayers to globular proteins[13]. Dilution of chemicals and reagents from lysed compartment to the bulk phase is a drawback of this system; dilution of an IVTT machinery and reagents preventing further protein synthesis. Lysing compartments of synthetic tissues precludes the controlled or extended release of therapeutic agents and so the use of CPPs may be advantageous.

Controlled substrate transport across the external lipid bilayer would represent a step change towards interfacing synthetic and living tissues. Substrates such as sugars and protons have been transported via membrane proteins in synthetic tissues[33,116] driven by a proton gradient or light, respectively. In addition to these functions, ATP-driven transporters have great potential for use in synthetic tissues. ATP binding cassette (ABC) transporters represent a superfamily of membrane proteins that transport a wide range of anionic substrates across cell bilayers, from ions to macromolecules[168]. Humans possess 48 proteins split into 7 subfamilies. One notable example is P-glycoprotein, also known as multidrug resistance protein 1 (MRP1), which confers multidrug resistance to tumour cells[169]. MRP1 has an additional function other than drug resistance, as evidenced by the ATP-dependent efflux of glutathione and the pro-inflammatory cysteinyl leukotriene C_4[169]. Bacterial ABC transporters are also known, such as McjD from *E. coli* that secretes Microcin J25, a 21 amino acid antimicrobial peptide[170].

Reconstituted into the external lipid bilayer of a synthetic tissue with the NBD orientated towards the droplet interior, ABC transporters would secrete small molecule drugs, peptides or chemicals to nearby living cells only upon ATP synthesis. A soft biocompatible processor able to controllably secrete drugs at specific locations would be of great therapeutic value, especially if said drugs are toxic. However, one issue may arise from the lipophilic nature of small molecule drugs. Many such drugs were designed to satisfy the Lipinksi Rule of 5 to increase their oral availability, restricting molecular weight, hydrogen bond donors and acceptors, and log P[171]. Care must be undertaken when selecting substrates to ensure an ATP-dependent mechanism of secretion.

P-type ATPases represent another class of ATP-dependent active transporters that transport cations[172]. One such P-type ATPase, the Na^+/K^+ ATPase, accounts for between 10-60% of the energy produced by cellular metabolism[173] depending on the situation. Excess energy released during ATP hydrolysis by the Na^+/K^+ ATPase and the subsequent dissipation of the resulting electrochemical gradient maintains thermogenesis in mammals [174]. Another subfamily of P-type ATPase is the Ca^{2+} ATPase with three subtypes, defined by their location, found in humans. As representative variants of each subtype are found in archaea and bacteria, this separation of function likely predates the emergence of eukaryotes[175]. One such example in bacteria is the Ca^{2+} ATPase from *Listeria monocytogenes*, *Listeria monocytogenes* Ca^{2+}-ATPase 1 (LMCA1)[176]. A 95 kDa single chain protein, LMCA1 shares a 38% sequence similarity with the sarco(endo)plasmic reticulum Ca^{2+}-ATPase (SERCA), its closest human variant[176]. With an optimal pH of 9.00 and requiring no cofactors, LMCA1 has a maximum turnover four times that of SERCA, but with a lower affinity for calcium by approximately two or three orders of magnitude[176].

In a follow up to the experiments in this thesis, I chose LMCA1 as a suitable ATP-dependent transporter to investigate. I knew proteoliposomes could generate ATP concentrations above the EC_{50} of 15 μM [108] and Ca^{2+} would not partition into the oil phase. I have conducted some preliminary work into the use of LMCA1. Having purified LMCA1 and investigated its ATPase activity in solution (**Figure 5.1A**), I reconstituted the protein in proteoliposomes. LMCA1 is a 1:1 H^+/Ca^{2+} antiporter[176] and so Ca^{2+} flux can be indirectly tracked via the encapsulation of pH-sensitive fluorophore, pyranine. After addition of Ca^{2+} and ATP, a rapid increase in pyranine

fluorescence was observed, as Ca^{2+} is transported in to the lumen of the proteoliposomes and H^+ out (**Figure 5.1B**). The addition of a Ca^{2+} chelator inhibits transport, indicating that a Ca^{2+}-dependent protein is responsible for the acidification. Following this promising initial work, the next step is to functionalise lipid bilayers in a synthetic tissue with LMCA1. Techniques to be evaluated include proteoliposome fusion[31,33], insertion of detergent solubilised protein[116], or insertion of protein produced in-situ via IVTT[33].

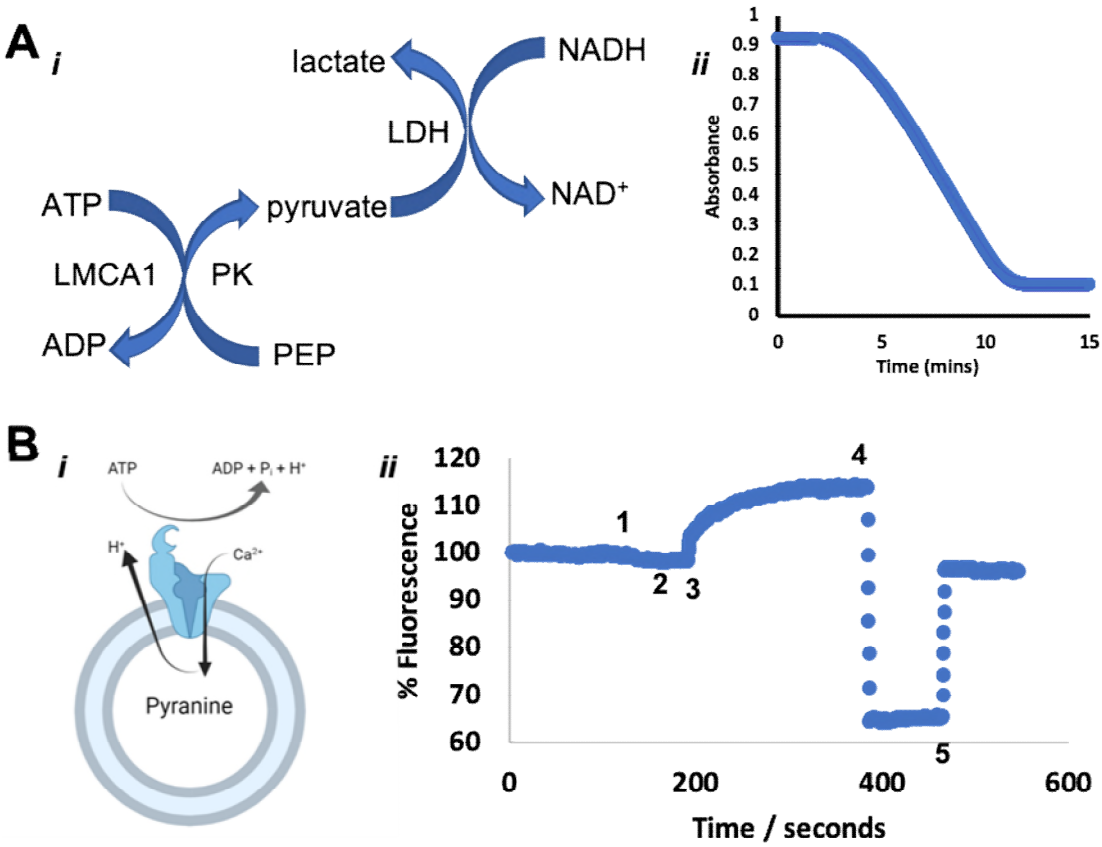

Figure 5.1 LMCA1 is an ATP-dependent H^+/Ca^{2+} antiporter. (**A**) ***i*** ATP regenerating assay ***ii*** NADH fluorescence after addition of solubilised LMCA1 (red arrow). (**B**) ***i*** LMCA1-dependent acidification of proteoliposomes ***ii*** Proton transport in LMCA1 proteoliposomes visualised by the pH-sensitive dye, pyranine. Additions are as follows: **1** 1 μM valinomycin **2** 100 μM $CaCl_2$ **3** 1 mM ATP **4** 1 μM A23187 **5** 10 μM CCCP

I plan to functionalise DIBs with LMCA1 and observe Ca^{2+} transport across the lipid bilayer by a Ca^{2+} sensitive fluorophore, before moving on to the activation of Ca^{2+} dependent enzymes, such as the calpains[177]. Additionally, LMCA1 reconstituted into external bilayers of a phase transitioned synthetic tissue would transport Ca^{2+} to adjacent Ca^{2+} sensitive cells, such as cardiomyocytes, to influence their behaviour. However, a large localised Ca^{2+} concentration would be required to effect cellular behaviour. The slow rate of Ca^{2+} movement across bilayers compared to channels and rapid diffusion of Ca^{2+} in the cell culture medium are issues that will require optimisation.

In the future, our group aims to design synthetic tissues of increasing complexity that possess a larger number of life-like characteristics and functionality. Synthetic tissues will interface with living tissues by secreting ions, growth factors, and therapeutic proteins to alter cellular activity. Sensing of metabolites or signalling molecules, for example quorum sensing molecules, will make it possible to establish two-way communication between cells and synthetic tissues to control the release of the aforementioned biologically active agents. Synthetic tissues with defined architecture and stimuli-responsive functions will provide spatiotemporal control when influencing cells and tissues.

6 Methods

This chapter describes the details off the experimental work described in this thesis, specifically the materials and methods used for experiments discussed in **Chapters 2**, **3**, **4,** and **5**.

6.1 Materials

All chemicals were purchased at the highest possible purity from Sigma-Aldrich unless otherwise specified.

Reagent	**Supplier**
1-palmitoyl-2-oleoyl-sn-glycero-3-phosphate (sodium salt) (POPA)	Avanti Polar Lipids
1,2-dioleoyl-sn-glycero-3-phosphocholine (DOPC)	Avanti Polar Lipids
1,2-diphytanoyl-sn-glycero-3-phosphocholine (DPhPC)	Avanti Polar Lipids
1,2-distearoyl-sn-glycero-3-phosphoethanolamine-N-[methoxy(polyethylene glycol)-2000] (DSPE-PEG2000)	Avanti Polar Lipids
2-(N-(7-Nitrobenz-2-oxa-1,3-diazol-4-yl)Amino)-2-Deoxyglucose (2-NBDG)	Thermo Fisher

3,5-Difluoro-4-hydroxybenzaldehyde	Fluorochem
Cholesterol (plant)	Avanti Polar Lipids
cOmplete EDTA-free protease inhibitor	Roche
n-Dodecyl-ß-D-maltoside (DDM)	Avanti Polar Lipids
n-Octyl-ß-D-glucoside	Avanti Polar Lipids
Ni-NTA Agarose	Qiagen
NTPs (100 mM)	Thermo Fisher
Nuclease-free water (Not DEPC treated)	Thermo Fisher
Silicone oil AR20	Sigma-Aldrich & Oxford Nanopore Technologies
Soybean PC	Avanti Polar Lipids
SP Sepharose Fast Flow resin	Cytiva
T7 RNA Polymerase	New England Biolabs
Tris pH 8.00 (1M)	Thermo Fisher
Tris(2-carboxyethyl)phosphine (TCEP)	Sigma-Aldrich
Ultrapure MilliQ water	Merck Millipore

6.2 Instruments

Instrument	**Manufacturer**
AKTA Pure	Cytiva USA
DMi8 inverted epifluorescent microscope	Leica, Germany
EZ4 stereo microscope	Leica, Germany

Hamilton microliter syringes	Hamilton, USA
PC-10 dual stage glass capillary puller	Narishige, Japan
SZX10 upright stereo microscope	Olympus, Japan
PTI QuantaMaster 8000 Spectrofluorometer Fluorometer	Horiba, Japan
MonoFab SRM-20	Roland DG, Japan

6.3 General Methods

6.3.1 Lipid-in-oil solutions

25 mg of lipid was dissolved in 1 mL chloroform. To make a 2 mM lipid-in-oil solution, 2 μmol of dissolved lipid was transferred to a glass vial, previously cleaned with IPA, and the chloroform evaporated under a steady stream of nitrogen. The resulting lipid film was further dried under reduced pressure overnight to ensure all residual chloroform had evaporated. 500 μL hexadecane, filtered through 22 μm PES filter, was added to the glass vial to dissolve the lipid film. 500 μL filtered AR20 was then added to afford a 2 mM lipid-in-oil solution with a 1:1 ratio of hexadecane:AR20. Lipid-in-oil solutions were used on the same day as their production and then discarded.

6.3.2 Formation of handmade nL droplets and droplet interface bilayers

Droplets were produced in a custom-made PMMA well array, produced with a computer numerical control (CNC) machine (monoFab SRM-20 Roland DG, Japan). Well arrays contained 200 μL of a lipid-in-oil solution prepared as described in **6.3.1**. A pipette (Pipetman Classic P2) dispensed solution into the lipid in oil. To form droplets of ≥ 200 nL the exact volume of solution was pipetted from bulk solution to the well away. To form droplets with volumes less than 200 nL an excess of aqueous solution was taken up by the pipette. The pipette tip was inserted into the oil and aqueous solution dispensed, while remaining attached to the tip. When the desired volume of solution had been dispensed the tip was brought up to the air-water interface which detached the droplet.

6.3.5 Printer setup

pL droplets were created using the 3D droplet printed described in previous work[51]. In short, a custom-made piezoelectric transducer generated controlled pressure waves to a chamber filled with MQ H_2O. Glass nozzles, fabricated from pulled capillaries with a tip diameter of ≈150 μm and subsequently bent at a 90^o angle by heating over a Bunsen burner. Nozzles were washed with H_2O and EtOH before use and treated by O_2 plasma cleaning to increase hydrophilicity. A ≈4 μL hexadecane plug was loaded into the nozzle to prevent mixing between MQ H_2O and printing solution. Printing solution (≈5 μL) was then loaded into the nozzle tip

which was subsequently lowered into a quartz cuvette (internal diameter 2 x 1 x 1 cm, Starna Scientific LTD, UK) which contained 300 μL lipid-in-oil solution. Upon generation of a pressure wave by the piezo actuator, a droplet of pL volume was generated at the nozzle tip and slowly sank to the bottom of the cuvette. The position of the cuvette was controlled by a motorised micromanipulator (PatchStar micromanipulator, Scientifica, 20-nm resolution). Synchronisation of micromanipulator movements and piezo actuation were controlled by a custom-built software developed in LabVIEW (National Instruments). Droplet deposition was monitored using a side-on stereomicroscope (Nikon® SMZ745T).

6.4 Chapter 2 Methods

6.4.1 Purification of F_1F_O

Purification of *E. coli* F_1F_O ATP synthase followed an adapted procedure from the literature[93]. *E. coli* strain DK8, an *atp* operon deletion strain containing a plasmid encoding a cysteine-free version of *E. coli* F_1F_O ATP synthase, pFV2, was used in the preparation of the protein. Cells were grown in 50 mL LB media, supplemented with 200 μg/mL ampicillin overnight at 37 °C with shaking. 1 L of LB, supplemented with 200 μg/mL ampicillin was inoculated with cells in a 1:100 dilution and grown at 37 °C with shaking for six hours. Cells were collected by centrifugation at 8,000 *x g* for 15 minutes at 4 °C. Cell pellets were stored at -80 °C until further use.

Cell pellets were thawed overnight at 4 °C prior to purification. Cell pellets were resuspended in French Press buffer (200 mM Tris, pH 7.77, 100 mM KCl, 5 mM

$MgCl_2$. 0.1 mM EDTA, and 2.5% glycerol) and homogenised. At this stage a small amount of DNaseI from bovine pancreas was added. The suspension was subjected to three passages through a French Press pressure cell at 16,000 p.s.i. Unbroken cells were collected by centrifugation at at 8,000 *x g* for 15 minutes at 4 ^{o}C and discarded. All subsequent manipulations were performed at 4 ^{o}C.

The supernatant fraction containing inverted membrane vesicles was centrifuged at 443,000 *x g* for 1 hour. Pellets of membrane from 2L culture were resuspended in 50 mL solubilisation buffer (50 mM Tris, pH 7.5, 100 mM KCl, 250 mM sucrose, 40 mM ε-aminocaproic acid, 15 mM *p*-aminobenzamidine, 5 mM $MgCl_2$, 0.1 mM EDTA, 0.2 mM DTT, 0.8% w/v soybean phosphatidylcholine, 1.5% w/v OG, 0.5% w/v sodium deoxycholate, 0.5% w/v cholate, 2.5% v/v glycerol, 30 mM imidazole). Solubilisation was performed for one hour on a rocking platform.

Unsolubilised membrane was collected by centrifugation at 443,000 *x g* for one hour and discarded. The supernatant fraction, containing solubilised membrane proteins, was applied to a column containing 0.75 mL Ni-NTA resin that had been previously equilibrated with solubilisation buffer. After loading, contaminating proteins were removed by washing the resin with 20 mL solubilisation buffer. F_1F_O was eluted with 2 mL solubilisation buffer supplemented with 150 mM imidazole. Protein concentration was determined by BCA assay (Thermo) before the sample was flash frozen in LN2 dropwise.

6.4.2 Purification of pR

E. coli strain C43(DE3) containing a plasmid encoding pR were used to produce this protein. Cells were grown in 50 mL LB media, supplemented with 200 μg/mL ampicillin overnight at 37 ^{o}C with shaking. 1 L of LB, supplemented with 200 μg/mL ampicillin was inoculated with cells in a 1:100 dilution and grown at 37 ^{o}C with shaking until an OD_{600} of 0.6 was achieved. pR expression was induced by addition 1 mM IPTG, 10 μM ATR was added, and growth continued for five hours. Cells were collected by centrifugation at 8,000 *x g* for 15 minutes at 4 ^{o}C. Cell pellets were stored at -80 ^{o}C until further use.

Cells pellets were thawed overnight at 4 ^{o}C prior to processing. Cell pellets were resuspended in French Press buffer (200 mM Tris, pH 7.77, 100 mM KCl, 5 mM $MgCl_2$. 0.1 mM EDTA, and 2.5% glycerol) and homogenised. At this stage a small amount of DNaseI from bovine pancreas was added. The suspension was subjected to three passages through a French Press pressure cell at 16,000 p.s.i. Unbroken cells were collected by centrifugation at at 8,000 *x g* for 15 minutes at 4 ^{o}C and discarded. All subsequent manipulations were performed at 4 ^{o}C.

The supernatant fraction containing inverted membrane vesicles was centrifuged at 443,000 *x g* for 1 hour. Pellets of membrane from 2 L culture were resuspended in 50 mL solubilisation buffer (100 mM NaCl, 50 mM MOPS, 1 mM $MgCl_2$, 30 mM imidazole, 2.5% v/v glycerol, 1.5% w/v DDM). Solubilisation was performed for two hours on a rocking platform.

Unsolubilised membrane was collected by centrifugation at 443,000 *x g* for one hour and discarded. The supernatant fraction, containing solubilised membrane proteins, was diluted 8-fold with DDM-free solubilisation buffer and applied to a column containing 0.75 mL Ni-NTA resin that had been previously equilibrated with solubilisation buffer. After loading, contaminating proteins were removed and detergent exchanged by washing the resin with 20 mL wash buffer (100 mM NaCl, 50 mM MOPS, 1 mM $MgCl_2$, 30 mM imidazole, 2.5% v/v glycerol, 1% w/v OG). pR was eluted with 2 mL solubilisation buffer supplemented with 370 mM imidazole. Protein concentration was determined by BCA assay (Thermo) before aliquots of protein were flash frozen in LN2.

6.4.3 Purification of pR-mCherry

Purification of *E. coli* F_1F_O ATP synthase followed an adapted procedure from the literature[57]. *E. coli* strain C43(DE3) containing a plasmid encoding pR-mCherry were used tp produce the protein. Cells were grown in 50 mL LB media, supplemented with 200 μg/mL ampicillin overnight at 37 °C with shaking. 1 L of LB, supplemented with 200 μg/mL ampicillin was inoculated with cells in a 1:100 dilution and grown at 37 °C with shaking until an OD_{600} of 0.6 was achieved. pR expression was induced by addition 1 mM IPTG, 10 μM ATR added, and growth continued for five hours. Cells were collected by centrifugation at 8,000 *x g* for 15 minutes at 4 °C. Cell pellets were stored at -80 °C until further use.

Cells pellets were thawed overnight at 4 °C prior to purification. Cell pellets were resuspended in French Press buffer (20 mM Tris, pH 7.4, 100 mM NaCl, 1 mM

TCEP) and homogenised. At this stage 100 μM PMSF and a small amount of DNaseI from bovine pancreas were added. The suspension was subjected to three passages through a French Press pressure cell at 16,000 p.s.i. Unbroken cells were collected by centrifugation at at 8,000 *x g* for 15 minutes at 4 ^{o}C and discarded. All subsequent manipulations were performed at 4 ^{o}C.

The supernatant fraction containing inverted membrane vesicles was centrifuged at 443,000 *x g* for 1 hour. Pellets of membrane from 2 L culture were resuspended in 50 mL solubilisation buffer (20 mM Tris, pH 7.4, 100 mM NaCl, 1 mM TCEP, 3% OG, 30 mM Imidazole, 250 mM sucrose). Solubilisation was performed overnight on a rocking platform.

Unsolubilised membrane was collected by centrifugation at 443,000 *x g* for one hour and discarded. The supernatant fraction, containing solubilised membrane proteins was applied to a column containing 1.5 mL Ni-NTA resin that had been previously equilibrated with solubilisation buffer. After loading, contaminating proteins were removed by washing the resin with 20 mL solubilisation buffer pR-mCherry was eluted with 2 mL solubilisation buffer supplemented with 150 mM imidazole. Protein concentration was determined by on nanodrop (MW 57.4 kDa - extinction coefficient of 115,865 M^{-1} cm^{-1}.) before aliquots of protein were flash frozen in LN2.

6.4.4 Proteoliposome reconstitution

Lipids stocks in chloroform were mixed in a glass vial previously cleaned with IPA to achieve the desired lipid concentration. Lipids were concentrated under a flow of N_2 and further dried under reduced pressure for 30 minutes. Reconstitution buffer (100 mM NaCl, 10 mM Tris pH 8.00, 1 mM $MgCl_2$) was added to a final lipid concentration of 10 mg/mL and allowed to swell for 30 min. The resulting solution was extruded through a mini liposome extruder 100 nm-sized pores 21 times to form liposomes.

Proteoliposomes were formed by first destabilizing liposomes by addition of 1 % w/v sodium cholate (final concentration) before addition of proteins. Single aliquots of protein were used for each reconstitution – freeze/thaw cycles were avoided. Reconstitution buffer was added to afford a total volume of 660 μL. The detergent/lipid/protein mixture was incubated at 4 ºC for 15 minutes on a rocking platform. A column packed with 5 mL Sephadex G-50 superfine resin previously equilibrated with reconstitution buffer was used to removed detergent. 500 μL fractions were collected and the OD_{600} measured to ascertain fractions containing proteoliposomes.

To store proteoliposomes, first proteoliposomes were concentrated using an Amicon Ultra-0.5 centrifugal filter with 100 kDa MWCO. Glycerol was then added to a final concentration of 33% v/v before aliquots of proteoliposomes were flash frozen in LN2.

6.4.5 ACMA assay

100 uL of proteoliposomes were added to of reaction buffer (100 mM NaCl, 10 mM Tris, pH 8.00, 1 mM $MgCl_2$) along with 1 μM ACMA and 1 μM valinomycin to a final volume of 2 mL. Under constant stirring and at room temperature, 1 mM ATP (final concentration) was added with ACMA fluorescence was excited at 419 nm and registered at 492 nm using a Horiba PTI QuantaMaster 8000 Spectrofluorometer Fluorometer. Proton gradients were dissipated by addition of 5 uM CCCP.

6.4.6 Hexokinase purification of ADP

ADP was dissolved in buffer (1 mM NaCl, 10 mM Tris, pH 8.00, 1 mM $MgCl_2$) to a final concentration of 100 mM. To this solution was added 1 mM glucose and 0.01 U/mL hexokinase (final concentrations). Eppendorfs were vortexed and spun down to ensure full mixing. Solutions were incubated at 37 ^oC for one hour with shaking before hexokinase was denatured at 99 ^oC for 30 minutes. Residual ATP contamination was checked with luciferase assay (see **section 6.4.8**). Aliquots of hexokinase-treated ADP were stored at -20 ^oC until use.

6.4.7 Anion exchange purification of ADP

Purification followed an adapted literature procedure[14]. Commercial ADP was dissolved in 10 mM TEAB pH 8.5 (buffer A) to a final concentration of 20 mM and pH adjusted to 7.5 with NaOH. Solution applied to a Mono-Q 1 mL column

previously equilibrated with buffer A at a flow rate of 2 mL/min. Elution proceeded with a gradient of 10 to 1000 mM TEAB, pH 8.5 over 20 CV at a flow rate of 1 mL/min. One large peak and three small peaks by UV trace. Major peak pooled and lyophilised to remove TEAB. ADP was redissolved and lyophilisation repeated five times, or until TEAB concentration no longer decreased as observed by NMR. Stock solution prepared of 100 mM ADP_{HPLC}, aliquot, and stored at -20 ^{o}C until further use.

6.4.8 ATP synthesis

936 μL activity buffer (100 mM NaCl, 10 mM Tris, pH 8.00, 1 mM $MgCl_2$), 1 μL 1M $MgCl_2$, and 3 uL pH 7.75 1 M NaP_i were mixed in a cuvette (Starna 3.10/Q/20) (reaction cuvette). Separately, 970 uL luciferase buffer (20 mM Tris, pH 7.75, 5 mM NaP_i, 5 mM $MgCl_2$) and 30 uL luciferin/luciferase cocktail (Sigma Aldrich CSL II) were added to a cuvette and mixed with a pipette (detection cuvette). Care was taken to avoid bubble formation. At this stage 5 μL from the reaction cuvette was added to the detection cuvette followed by luminescence recording in a luminometer (Sirius-L single tube luminometer, Titertek). 10 μL 100 mM ADP_{HK} (see **section 6.4.6)** was added to the reaction cuvette followed by 50 uL proteoliposomes. A similar 5 μL measurement was performed as described above after each addition. ATP synthesis was initiated through illumination with a 530 nm LED (Thor Labs M530L4) equipped with aspheric condenser lens (Thor Labs ACL2520U-A) and an IR blocking filter (Thor Labs TF1) at a power of 50 mW/cm^{-2}. Illumination continued for 30 minutes, with measurements taken at 5-minute intervals. At the end of the run ATP was calibrated through the addition of a

standard of 5 pmol ATP, thrice. To obtain the actual amount of ATP measured, the increase in luminescence counts of a given time point was subtracted from the previous level of luminescence. This gave the increase in luminescence over that period. This number was then divided by the value from the ATP standard to ascertain the amount of ATP made in pmol.

6.5 Chapter 3 Methods

6.5.1 Preparation of a linear Broccoli template

To prepare a linear DNA template for IVT, the Broccoli gene was amplified using the following primers with an annealing temperature of 57 ^{o}C over 25 cycles.

Forward primer: 5' GAAATTAATACGACTCAC

Reverse primer: 5' GATATAGTTCCTCCTTTCAG

6.5.2 Bulk *in-vitro* transcription

To transcribe and visualise the Broccoli aptamer in bulk studies, 10 mM ATP, 10 mM CTP, 10 mM UTP, 10 mM GTP, T7 RNAP (NEB), 8 ng/μL DNA, 60 μM fluorophore were prepared in buffer (10 mM Tris, pH 7.9, 50 mM $MgCl_2$, 2 mM Spermidine, 1 mM DTT, 10 mM NaN_3 – buffer was prepared weekly to avoid excess DTT oxidation). IVT cocktail was prepared at RT to avoid DNA-spermidine precipitation. Solution was mixed and centrifuged before two-hour incubation at 37 ^{o}C. 10 μL of IVT solution was diluted with 20 μL MQ H_2O and 25 μL of the resulting

solution was added to a 384 well flat bottom plate for analysis. Analysis was carried out on a Tecan Infinite M1000 Pro microplate reader with ex = 465-475 nm, em = 525-535 nm

6.5.3 Dissipation of proteoliposome pH gradient

Proteoliposomes were diluted 10-fold in a buffer containing 10 mM Tris, pH 7.9, 50 mM $MgCl_2$, 2 mM Spermidine, 1 mM DTT, 10 mM NaN_3, 10 mM CTP, 10 mM UTP, 10 mM GTP, T7 RNAP (NEB), 8 ng/μL DNA, 60 μM fluorophore and 10 mM NaP_i, pH 7.9. The solution was centrifuged to ensure complete mixing. The solution was incubated in the dark for two hours at which point 10 mM ADP_{HK} (see **section 6.4.6**) was added and the proteoliposome solution used in further experiments immediately (for example see **section 6.5.4**).

To test dissipation of the pH gradient the proteoliposome solution was incubated in the dark for a further two hours, at which point 10 μL of solution was diluted with 20 μL MQ H_2O and 25 μL of the resulting solution was added to a 384 well flat bottom plate for analysis. Analysis was carried out on a Tecan Infinite M1000 Pro microplate reader with ex = 465-475 nm, em = 525-535 nm

6.5.4 Light-activated ATP synthesis in nL droplets

100 nL droplets of an IVT cocktail containing proteoliposomes with dissipated pH gradient (see **section 6.5.2**) was dispensed into a lipid-containing oil (see **section**

6.3.1) in a custom-made PMMA well. To create a humid environment, the PMMA well was placed into a petri dish filled with water. Droplets were illuminated with a 530 nm LED (see **section 6.4.8**). Fluorescence outputs were measured with a Leica DMi8 epifluorescence microscope with the GFP filter cube equipped (ex: 450−490 nm, em: 500−550 nm). For quantification, fluorescence intensities were analysed on ImageJ/FIJI manually. A line profile was drawn across the centre of each droplet with the fluorescence intensities along the line averaged to give a single value.

6.5.5 Addition of DFHBI to oil

In a cleaned glass vial 120 μM DFHBI (final concentration) in DMSO was added to a 1:1 mixture of hexadecane and silicone oil. Although DMSO is insoluble in this oil mixture, DFHBI diffused from one phase to the other over time. The glass vial was wrapped in foil and stored at RT until further use. When required, an excess quantity of DFHBI-infused oil was transferred to a 1.5 mL Eppendorf and centrifuged at 20,000 *x g* for 10 minutes to minimise any DMSO suspended in solution. The DFHBI-infused oil was then charged to a lipid film (see **section 6.3.1**).

6.5.6 Synthesis of DFHBI analogues

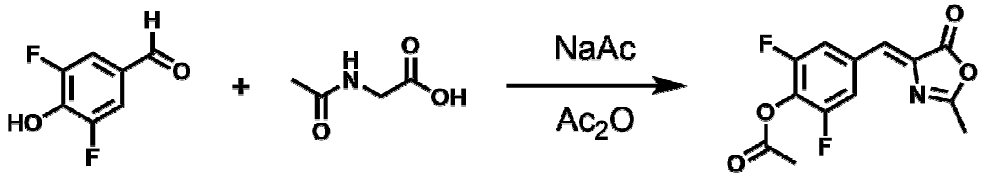

(Z)-2,6-difluoro-4-((2-methyl-5-oxooxazol-4(5H)-ylidene)methyl)phenyl acetate (**1**) was synthesised according to a literature procedure[122]. N-Acetylglycine (617 mg, 5.34mmol), anhydrous sodium acetate (432 mg, 5.34 mmol), 4-acetyloxy-3,5-difluorobenzaldehyde (832 mg, 5.34 mmol), and acetic anhydride (3 ml) were stirred at 110 ^{o}C for 5 h. After allowing the reaction to cool to room temperature, cold ethanol (20 ml) was added while stirring and the reaction was left stirring overnight at 4 ^{o}C. The resulting crystalline solid was then washed with a small amount of cold ethanol, hot water, hexanes and dried to afford 0.94 g (yield 62%) of **1** as a pale-yellow solid, which was used without further purification. ^{1}H NMR (400 MHz, DMSO) δ 8.14 – 8.05 (m, 2H), 7.23 (s, 1H), 2.50 – 2.41 (m, 6H).

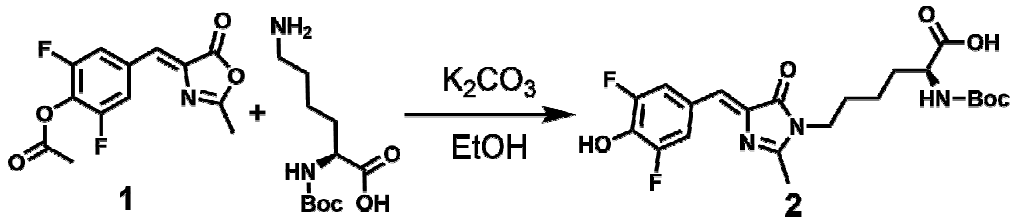

Compound **1** (122 mg, 0.44 mmol) was refluxed with 1.86 ml of ethanol, 130 mg Boc-Lys-OH (0.81 mmol), and 168 mg of potassium carbonate (1.2 mmol) for 4 h. The orange suspension was removed from heat and the solvent removed under

reduced pressure. The crude sample was redissolved in 1:1 EtOAc: 500 mM NaAcetate pH 3.00. The organic layer containing compound **2** was separated, dried with anhydrous sodium sulphate and solvent was removed under reduced pressure. The impure material was used directly without further purification.

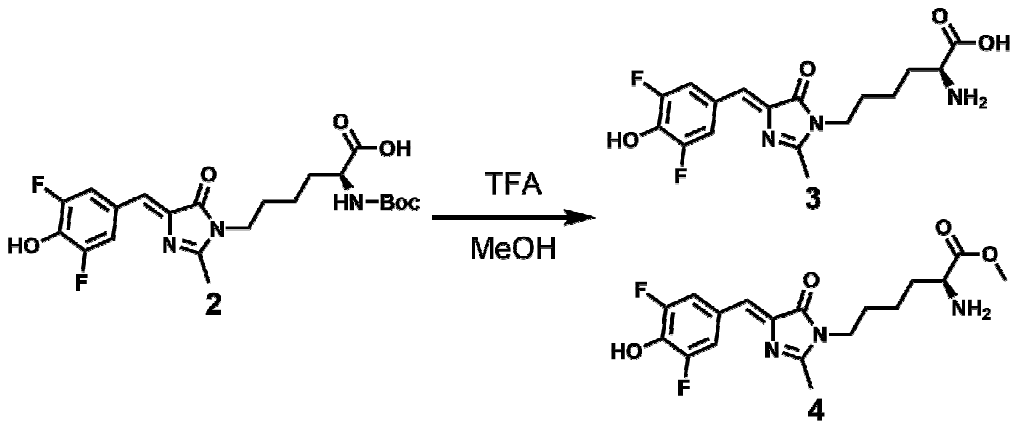

Compound **2** (10 mg, 20 μmol) was dissolved in 171 μL MeOH to which was added 57 μL TFA. The reaction was stirred at RT for five hours. Solvent was removed under reduced pressure. The film was dissolved in 1.2 mL of 1:6 ACN:H_2O and 100 μL injected onto a C18 150 mm column. Elution proceeded over 30 minutes with a gradient 5-22.5% ACN with 0.1% TFA in H_2O with 0.1% TFA at a flow rate of 4.5 mL min. This run was repeated for the remaining sample. Three peaks were collected and lyophilised – fraction one containing 0.8 mg compound **3** (yield 10.8%, LC/MS ESI+; 370.2 $[M+H]^+$), fraction two containing 0.7 mg compound **4** (yield 10.4%%, LC/MS ESI+; 384.2 $[M+H]^+$), and fraction three containing ^{t}BuOH.

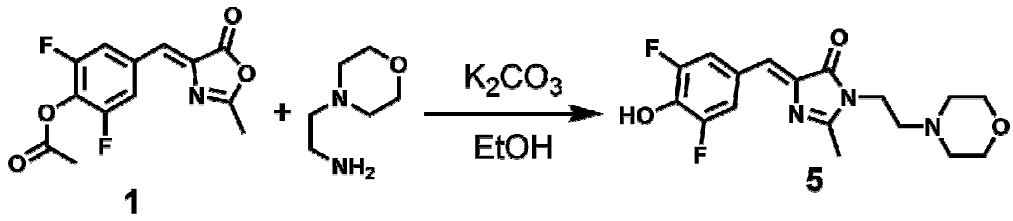

Compound **1** (100 mg, 0.355 mmol) was refluxed with 1.5 ml of ethanol, 90 mg 4-(2-Aminoethyl)morpholine (0.711 mmol), and 145 mg of potassium carbonate (1.2 mmol) for 18 h. The orange suspension was removed from heat and the solvent removed under reduced pressure. The crude sample was re-dissolved in 2.5mL 1:10 ACN with 0.1% TFA:H_2O with 0.1% TFA. 1.4 mL of sample was loaded onto a 25 cm C18 reverse phase column with elution gradient of 10-30% ACN with 0.1% TFA in H_2O with 0.1% TFA at a flow rate of 15 mL/min. Fractions containing compound 5 were pooled and lyophilised to give 10.6 mg compound **5** (yield 8.5%) as a yellow solid. ^{1}H NMR (400 MHz, D2O) δ 7.43 (dt, J = 8.7, 1.5 Hz, 2H), 6.74 (s, 1H), 4.25 – 2.96 (m, 12H). LC/MS ESI+; 352.2 $[M+H]^+$

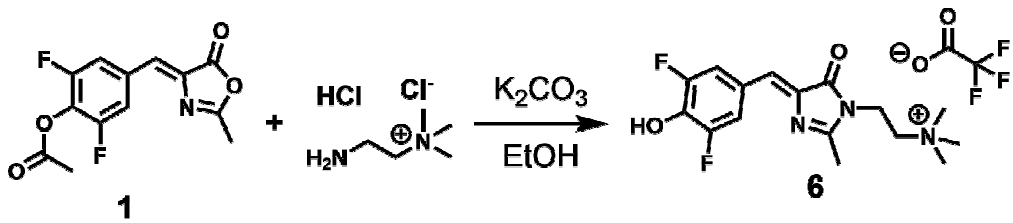

Compound **1** (100 mg, 0.355 mmol) was refluxed with 1.5 ml of ethanol, 124 mg (2-Aminoethyl)trimethylammonium chloride hydrochloride (0.711 mmol), and 145 mg of potassium carbonate (1.2 mmol) for 18 h. The orange suspension was removed from heat and the solvent removed under reduced pressure. The crude sample was re-dissolved in 3 mL H_2O with 0.1% TFA. Sample precipitated after

five minutes at RT. Mixture was centrifuged to remove precipitate and purification continued on supernatant. 1.5 mL of sample was loaded onto a 25 cm C18 reverse phase column with elution gradient of 5-35% ACN with 0.1% TFA in H_2O with 0.1% TFA at a flow rate of 15 mL/min. Fractions containing compound **6**, as determined by TLC, were pooled and lyophilised to afford 22.0 mg of compound **6** (yield 14.2%) as a yellow solid. ^{1}H NMR (400 MHz, D2O) δ 7.38 (dd, J = 8.2, 1.6 Hz, 2H), 6.65 (s, 1H), 4.12 – 4.03 (m, 2H), 3.58 – 3.48 (m, 2H), 3.20 (s, 9H), LC/MS ESI+; 324.2 $[M]^+$

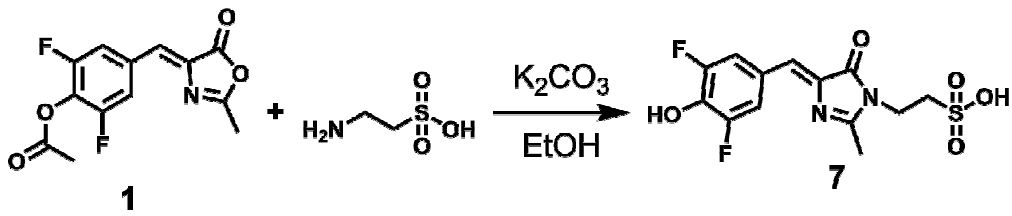

Compound **1** (100 mg, 0.355 mmol) was refluxed with 1.5 ml of ethanol, 88 mg taurine (0.711 mmol), and 145 mg of potassium carbonate (1.2 mmol) for 18 h. The orange suspension was removed from heat and the solvent removed under reduced pressure. The crude sample was re-dissolved in 2 mL H_2O with 0.1% TFA and adjust to pH 4.00. 1 mL of sample was loaded onto a 25 cm C18 reverse phase column with elution gradient of 5-40% ACN in 10 mM NH_4OAc at a flow rate of 15 mL/min. Fractions containing compound **7**, as determined by TLC, were pooled and lyophilised to give 9.8 mg **7** (yield 7.9%) as a yellow solid. LC/MS ESI-; 345.0 $[M-H]^+$

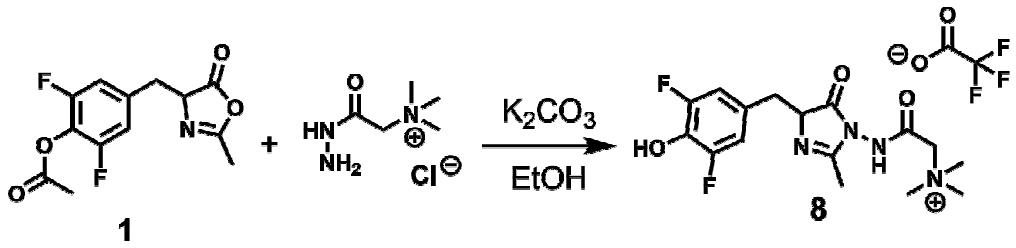

Compound **1** (100 mg, 0.355 mmol) was refluxed with 1.5 ml of ethanol, 120 mg (Hydrazinocarbonylmethyl)trimethylammonium chloride (0.711 mmol), and 145 mg of potassium carbonate (1.2 mmol) for five days. The orange suspension was removed from heat and the solvent removed under reduced pressure. The crude sample was re-dissolved in 2.5 mL H_2O with 0.1% TFA. 1 mL of sample was loaded onto a 25 cm C18 reverse phase column with elution gradient of 5-40% ACN with 0.1% TFA in H_2O with 0.1% TFA at a flow rate of 15 mL/min. Fractions containing compound **8**, as determined by TLC, were pooled and lyophilised to afford 14.0 mg of 8 (yield 11.2%) as a yellow solid. LC/MS ESI+; 353.0 $[M]^+$

6.5.7 Qualification of fluorophore lipophilicity

To investigate fluorophore solubility in oil, an IVT cocktail transcribing a Broccoli aptamer was prepared in the absence of fluorophore (see **section 6.5.3**) and incubated at 37 ^oC for two hours. After incubation, a second solution containing IVT buffer (10 mM Tris, pH 7.9, 50 mM $MgCl_2$, 2 mM Spermidine, 1 mM DTT, 10 mM NaN_3) and 60 μM fluorophore was prepared. A volume of 200 μL of lipid-containing oil solution was added to a PMMA well array, before 100 nL droplets of the two aqueous solutions were dispensed in the wells by pipette. Nine wells in a square pattern were used with droplets of the fluorophore-containing solution

dispensed in the eight outer wells, and a single droplet of transcribed Broccoli aptamer in the central well. Incubation was carried out at 37 ^{o}C in a humidified environment. Fluorescence in the central aptamer-containing droplet was quantified with the method described in **6.5.3**.

For investigations into fluorophore permeability across lipid bilayers one, 100 nL droplet of both two solutions described above were dispensed into a DPhPC-containing oil in a single well. After incubating droplets for five minutes to allow lipid monolayer formation the well array was tilted by hand to promote DIB formation. Incubation was carried out at 37 ^{o}C in a humidified environment. Fluorescence outputs were measured with a Leica DMi8 epifluorescence microscope with the GFP filter cube equipped (ex: 450−490 nm, em: 500−550 nm). For quantification, fluorescence intensities were analysed on ImageJ/FIJI manually. A line profile was drawn across the DIB and the fluorescence plotted.

6.6 Chapter 4 Methods

6.6.1 αHL purification

This protocol followed an adapted literature protocol[178]. *Staphylococcus aureus* strain Wood 46 was streaked onto a Tryptic Soy Broth (TSB) plate and grown overnight at 37 ^{o}C. A single colony was picked and used to inoculate into 1 L TSB which was subsequently incubated at 200 rpm at 37 ^{O}C for 26 hours. Cells at 8,000 x g for 30 minutes at 4 ^{o}C and discarded. 0.5 mM PMSF and 2 cOMPLETE protease inhibitor tablets (Roche) were added to the supernatant before dilution

with 1 L MQ water and the pH adjusted to 5.2. All subsequent manipulations were performed at 4 ^{o}C. The supernatant was charged to a manually packed SP-Sepharose FF ion exchange column (30 mL bed volume) previously equilibrated with 5CV of buffer A (10 mM Na acetate, 1 mM EDTA, pH 5.2). Bound protein was washed 350 mL buffer A, 100 mL buffer A supplemented with 150 mL NaCl, and eluted with 100 mL buffer A supplemented with 250 mM NaCl. 5 mL fractions in Falcon tubes were collected and analysed by SDS-PAGE gel analysis to identify fractions containing αHL. Fractions containing αHL were then flash frozen in LN2 and store at -80 until further use.

Fractions containing αHL were defrosted slowly on ice, combined and concentrated with a Sartorius Vivaspin 10k MWCO to ~5 mg/mL and ~2 mL at 6,000 *x g* for 3 minutes at a time, mixing the solution after each spin. The concentrated protein solution was loaded onto a Sephacryl 26/60 S100 previously equilibrated with 150 mM NaCl, 10 mM Tris pH 8.00. A flow rate of 1.2 mL/min was used to elute the protein, resulting in four peaks. The latter three peaks overlapped, with the last peak being αHL. Fraction purity as assessed by SDS-PAGE gel and protein concentration calculated by nanodrop spectrophotometer. Fractions containing pure αHL were pooled and concentrated to 1 mg/mL before flash freezing drop wise in LN2.

6.6.2 Hemolytic assay

500 mL of MBSA buffer was prepared and filtered (150 mM NaCl, 10 mM MOPS, pH 7.5, 1 mg/mL BSA). 450 μL of rabbit blood K2 EDTA was mixed with 900 μL

mBSA at 4 ^{o}C. Mixture was centrifuged at 1,200 rpm at RT for 2 minutes. The dark red-coloured supernatant was discarded. 900 μL MBSA was added and this procedure repeated 5-6 times until supernatant was rosy. At this point solution was removed until 100 μL of mixture remained. This was then diluted with MBSA 100-fold to afford 1% blood.

To a 96 well plate, 50 μL MBSA buffer was added to lanes 2-11. To lane 1 was added 95 μL MBSA buffer and 5 μL sample (αHL, MBSA control). Well was mixed with pipette, ensuring bubble formation was minimised. 50 μL from lane one was taken and deposited in lane 2, together with mixing. This dilution was repeated until lane 12, affording a dilution range of αHL. 50 μL of 1% blood was added to each well, starting from lane 12 and finishing at lane 1. The OD_{595} of each sample was analysed over time on a Tecan Infinite M1000 Pro microplate reader.

6.6.3 Permeabilisation of DIBs by αHL in nL droplets

In a well array containing a lipid-in-oil solution, 100 nL droplets of solution A (10 mM Tris, pH 8.00, 150 mM NaCl, 100 μM 2-NBDG) and solution B (10 mM Tris, pH 8.00, 150 mM NaCl, 100 μg/mL αHL) were dispensed in a well. After a 5-minute incubation to ensure monolayer formation the well array was tilted by hand to promote DIB formation. Small molecule diffusion through αHL was measured with a Leica DMi8 epifluorescence microscope with the GFP filter cube equipped (ex: 450−490 nm, em: 500−550 nm). For quantification, fluorescence intensities were

analysed on ImageJ/FIJI manually. A line profile was drawn across the DIB and the fluorescence plotted.

6.6.4 Permeabilisation of DIBs by αHL in nL droplets

The solutions described in **6.5.3** were printed in a 2 x 1 cm quartz cuvette in 100 μm diameter droplets using the 3D printer. Solution A was printed first, followed by a 2-minute incubation period to ensure monolayer formation. Solution B was then dispensed on top of each droplet of solution A, aiming at the shoulder of solution A. Droplet coalescence would occur if the droplet of solution B landed directly on top of solution A. Small molecule diffusion through αHL was measured with a Leica DMi8 epifluorescence microscope with the GFP filter cube equipped (ex: 450−490 nm, em: 500−550 nm). For quantification, fluorescence intensities were analysed on ImageJ/FIJI manually. A line profile was drawn across the DIB and the fluorescence plotted.

6.6.4 Silicone oil AR20 washing

8 mL MQ H_2O was added to 2 mL AR20 in a 15 mL falcon tube. The resulting biphasic system was violently shaken manually to form an emulsion which was left for three minutes before the two layers were separated by centrifugation at 2,900 *x g* for five minutes at RT. The top aqueous layer was removed and the wash step repeated twice. After the third wash a solution of 250 mM glucose was used to wash the AR20 instead of MQ H_2O and the emulsion formation/centrifugation step

was repeated. After the centrifugation step the AR20 was now the top layer, making for facile removal. AR20 was pipetted into a 1.5 mL Eppendorf, taking care to avoid any aqueous phase, and centrifuged at 20,000 *x g* for 15 minutes. AR20 was removed from the Eppendorf tube, again ensuring no aqueous phase was picked up. Washed AR20 was immediately used to make lipid in oil solutions.

6.6.5 Light-activated ATP synthesis in DIBs

In a 2 x 1 cm quartz cuvette containing 300 μL of a lipid in oil solution, 100 um diameter droplets of a solution one, consisting of buffer A (10 mM Tris, pH 7.9, 50 mM $MgCl_2$, 2 mM Spermidine, 1 mM DTT, 10 mM NaN_3, 10 mM CTP, 10 mM ADP_{HK}, 10 mM UTP, 10 mM GTP, 120 μM DC and 10 mM NaP_i) and proteoliposomes (pH gradient dissipated – see **6.5.4**), were printed in a row, 800 um apart.

After a 5-minute incubation time to ensure monolayer formation, solution two, consisting of buffer A and T7 RNAP (NEB), 8 ng/μL DNA, and 100 μg/mL αHL, was dispensed onto each droplet of solution one. It was critical to ensure that droplets of solution two landed on the shoulder of the droplets of solution one as coalescence occurred if a droplet landed directly on top of another droplet. After a two-minute incubation period to ensure bilayer formation the cuvette was transferred to a hydrated petri dish and illuminated with a 530 nm LED (Thor Labs M530L4) equipped with aspheric condenser lens (Thor Labs ACL2520U-A) and an IR blocking filter (Thor Labs TF1) at a power of 50 mW/cm^{-2}. Fluorescence outputs were measured with a Leica DMi8 epifluorescence microscope with the GFP filter

cube equipped (ex: 450−490 nm, em: 500−550 nm). For quantification, fluorescence intensities were analysed on ImageJ/FIJI manually. A line profile was drawn across the centre of each droplet with the fluorescence intensities along the line averaged to give a single value.

6.7 Chapter 5 Methods

6.7.1 LMCA1 purification

LMCA1 was purified by a protocol adapted from the literature[176]. *E. coli* strain C43(DE3) containing a plasmid encoding LMCA1, LMCA1-pET-22b, was used in the preparation of the protein. Cells were grown in 50 mL TB media, supplemented with 100 μg/mL ampicillin overnight at 37 ^{o}C with shaking. 2 L of LB, supplemented with 100 μg/mL ampicillin were inoculated with cells in a 1:100 dilution and grown at 37 ^{o}C with shaking. Expression was induced at OD_{600} = 0.6-0.8 with 1 mM IPTG, the temperature lowered to 20 ^{o}C for a further 20 hours of growth. Cells were collected by centrifugation at 8,000 *x g* for 15 minutes at 4 ^{o}C. Cell pellets were resuspended in French Press buffer (50 mM Tris-HCl, pH 7.6, 200 mM KCl, 20% v/v glycerol) and stored at -80 ^{o}C until further use.

Cells suspensions were thawed at 4 ^{o}C and the supplemented with a small amount of DNaseI from bovine pancreas, 1 mM PMSF and 1 EDTA-free cOMPLETE tablet (Roche). The suspension was subjected to three passages through a French Press pressure cell at 16,000 p.s.i. Unbroken cells were collected by centrifugation at 27,000 *x g* for 30 minutes at 4 ^{o}C and discarded. All subsequent manipulations

were performed at 4 ºC. The supernatant fraction containing inverted membrane vesicles was centrifuged at 443,000 *x g* for 1 hour. Pellets of membrane were resuspended in 50 mL solubilisation buffer (20 mM Tris-HCl, pH 7.6, 200 mM KCl, 20% v/v glycerol, 5 mM βME, 3 mM $MgCl_2$, 0.1 mM $CaCl_2$, 1% w/v DDM, 1 mM PMSF). Solubilisation was carried out for one hour on a rocking platform.

Unsolubilised membrane was collected by centrifugation at 443,000 *x g* for one hour and discarded. The supernatant fraction, containing solubilised membrane proteins, was applied to a column containing 1 mL HisTrap previously equilibrated with wash buffer (20 mM Tris-HCl, pH 7.5, 200 mM KCl, 20% v/v glycerol, 5 mM βME, 1 mM $MgCl_2$, 0.1 mM $CaCl_2$, 30 mM Imidazole, 0.25 mg/ml C12E8 (6.6 CMC))). After loading, contaminating proteins were removed by washing the resin with 20 mL wash buffer. LMCA1 was eluted with 10 mL solubilisation buffer supplemented with 220 mM imidazole. Fractions were analysed for LMCA1 by SDS-PAGE gel. Protein concentration was determined by BCA assay (Thermo) before the sample was flash frozen in LN2 dropwise.

6.7.2 LMCA1 reconstitution

LMCA1 was reconstituted into proteoliposomes by a protocol adapted from the literature[176]. 200 nm 20 mg/mL DOPC liposomes were produced in reconstitution buffer (10.6 mm Tris-HCl, pH 7.6, 17% glycerol, 90 mm KCl, 0.9 mm $MgCl_2$, 0.8 mm NaN_3), and 0.29 mM pyranine by microextrusion. 10 mg/mL liposomes were mixed with 400 μg/mL LMCA1 and 15 mg/mL OG (all final concentrations) in a total volume of 500 μL. To this lipid/protein/detergent mixture biobeads[38] were added at

a concentration of 80 mg/mL for two hours, 80 mg/mL for one hour, 160 mg/mL for one hour 160 mg/mL for two hours. To remove external pyranine proteoliposomes were passed through a PD-10 spin column previously equilibrated with reconstitution buffer. Proteoliposomes were assessed for activity on the same day as their reconstitution. Proteoliposomes were flash frozen in LN2 in 5 μL aliquots.

6.7.3 LMCA1 activity

Calcium pumping was observed indirectly in LMCA1 proteoliposomes with encapsulated pyranine following a literature method[176]. 100 μL of LMCA1 proteoliposomes (**6.6.2**) were added to 1900 μL activity buffer (10.6 mm Tris-HCl, pH 7.6, 17% glycerol, 90 mm KCl, 0.9 mm $MgCl_2$, 0.8 mm NaN_3) under continuous stirring and fluorescence changes tracked upon addition of 1 μM valinomycin, 100 μM $CaCl_2$, and 1 mM ATP. Fluorescence was tracked on a PTI QuantaMaster 8000 Spectrofluorometer Fluorometer (Horiba) with excitation wavelength 450-460 nm, emission wavelength 507-517 nm.

6.8 Sequences

6.8.1 pR-pBAD

pR has been highlighted in bold.

CAGACATTGCCGTCACTGCGTCTTTTACTGGCTCTTCTCGCTAACCAAACCG
GTAACCCCGCTTATTAAAAGCATTCTGTAACAAAGCGGGACCAAAGCCATGA
CAAAAACGCGTAACAAAAGTGTCTATAATCACGGCAGAAAAGTCCACATTGA
TTATTTGCACGGCGTCACACTTTGCTATGCCATAGCATTTTTATCCATAAGAT

TAGCGGATCCTACCTGACGCTTTTTATCGCAACTCTCTACTGTTTCTCCATAC

CCGTTTTTTTGGGCTAGAAATAATTTTGTTTAACTTTAAGAAGGAGATATACA

TACCC**ATGGGTAAATTATTACTGATATTAGGTAGTGTTATTGCACTTCCTAC**

ATTTGCTGCAGGTGGTGGTGACCTTGATGCTAGTGATTACACTGGTGTTTC

TTTTTGGTTAGTTACTGCTGCTTTATTAGCATCTACTGTATTTTTCTTTGTTG

AAAGAGATAGAGTTTCTGCAAAATGGAAAACATCATTAACTGTATCTGGTC

TTGTTACTGGTATTGCTTTCTGGCATTACATGTACATGAGAGGGGTATGGA

TTGAAACTGGTGATTCGCCAACTGTATTTAGATACATTGATTGGTTACTAAC

AGTTCCTCTATTAATATGTGAATTCTACTTAATTCTTGCTGCTGCAACTAAT

GTTGCTGGATCATTATTTAAGAAATTACTAGTTGGTTCTCTTGTTATGCTTG

TGTTTGGTTACATGGGTGAAGCAGGAATCATGGCTGCATGGCCTGCATTC

ATTATTGGGTGTTTAGCTTGGGTATACATGATTTATGAATTATGGGCTGGA

GAAGGAAAATCTGCATGTAATACTGCAAGTCCTGCTGTGCAATCAGCTTAC

AACACAATGATGTATATTATCATCTTTGGTTGGGCGATTTATCCTGTAGGTT

ATTTCACAGGTTACCTGATGGGTGACGGTGGATCAGCTCTTAACTTAAACC

TTATCTATAACCTTGCTGACTTTGTTAACAAGATTCTATTTGGTTTAATTATA

TGGAATGTTGCTGTTAAAGAATCTTCTAATGCTAAGGGCGAGCTTGAAGGT

AAGCCTATCCCTAACCCTCTCCTCGGTCTCGATTCTACGCGTACCGGTCAT

CATCACCATCACCATTGAGTTTAAACGGTCTCCAGCTTGGCTGTTTTGGCG

GATGAGAGAAGATTTTCAGCCTGATACAGATTAAATCAGAACGCAGAAGCG

GTCTGATAAAACAGAATTTGCCTGGCGGCAGTAGCGCGGTGGTCCCACCTG

ACCCCATGCCGAACTCAGAAGTGAAACGCCGTAGCGCCGATGGTAGTGTG

GGGTCTCCCCATGCGAGAGTAGGGAACTGCCAGGCATCAAATAAAACGAAA

GGCTCAGTCGAAAGACTGGGCCTTTCGTTTTATCTGTTGTTTGTCGGTGAAC

GCTCTCCTGAGTAGGACAAATCCGCCGGGAGCGGATTTGAACGTTGCGAAG

CAACGGCCCGGAGGGTGGCGGGCAGGACGCCCGCCATAAACTGCCAGGC

ATCAAATTAAGCAGAAGGCCATCCTGACGGATGGCCTTTTTGCGTTTCTACA

AACTCTTTTTGTTTATTTTTCTAAATACATTCAAATATGTATCCGCTCATGAGA

CAATAACCCTGATAAATGCTTCAATAATATTGAAAAAGGAAGAGTATGAGTAT

TCAACATTTCCGTGTCGCCCTTATTCCCTTTTTTGCGGCATTTTGCCTTCCTG

TTTTTGCTCACCCAGAAACGCTGGTGAAAGTAAAAGATGCTGAAGATCAGTT

GGGTGCACGAGTGGGTTACATCGAACTGGATCTCAACAGCGGTAAGATCCT

TGAGAGTTTTCGCCCCGAAGAACGTTTTCCAATGATGAGCACTTTTAAAGTT

CTGCTATGTGGCGCGGTATTATCCCGTGTTGACGCCGGGCAAGAGCAACTC

GGTCGCCGCATACACTATTCTCAGAATGACTTGGTTGAGTACTCACCAGTCA

CAGAAAAGCATCTTACGGATGGCATGACAGTAAGAGAATTATGCAGTGCTG

CCATAACCATGAGTGATAACACTGCGGCCAACTTACTTCTGACAACGATCGG

AGGACCGAAGGAGCTAACCGCTTTTTTGCACAACATGGGGGATCATGTAAC

TCGCCTTGATCGTTGGGAACCGGAGCTGAATGAAGCCATACCAAACGACGA

GCGTGACACCACGATGCCTGTAGCAATGGCAACAACGTTGCGCAAACTATT

AACTGGCGAACTACTTACTCTAGCTTCCCGGCAACAATTAATAGACTGGATG

GAGGCGGATAAAGTTGCAGGACCACTTCTGCGCTCGGCCCTTCCGGCTGG

CTGGTTTATTGCTGATAAATCTGGAGCCGGTGAGCGTGGGTCTCGCGGTAT

CATTGCAGCACTGGGGCCAGATGGTAAGCCCTCCCGTATCGTAGTTATCTA

CACGACGGGGAGTCAGGCAACTATGGATGAACGAAATAGACAGATCGCTGA

GATAGGTGCCTCACTGATTAAGCATTGGTAACTGTCAGACCAAGTTTACTCA

TATATACTTTAGATTGATTTAAAACTTCATTTTTAATTTAAAAGGATCTAGGTG

AAGATCCTTTTTGATAATCTCATGACCAAAATCCCTTAACGTGAGTTTTCGTT

CCACTGAGCGTCAGACCCCGTAGAAAAGATCAAAGGATCTTCTTGAGATCC

TTTTTTTCTGCGCGTAATCTGCTGCTTGCAAACAAAAAAACCACCGCTACCA

GCGGTGGTTTGTTTGCCGGATCAAGAGCTACCAACTCTTTTTCCGAAGGTAA

CTGGCTTCAGCAGAGCGCAGATACCAAATACTGTCCTTCTAGTGTAGCCGT

AGTTAGGCCACCACTTCAAGAACTCTGTAGCACCGCCTACATACCTCGCTCT

GCTAATCCTGTTACCAGTGGCTGCTGCCAGTGGCGATAAGTCGTGTCTTAC

CGGGTTGGACTCAAGACGATAGTTACCGGATAAGGCGCAGCGGTCGGGCT

GAACGGGGGGTTCGTGCACACAGCCCAGCTTGGAGCGAACGACCTACACC

GAACTGAGATACCTACAGCGTGAGCTATGAGAAAGCGCCACGCTTCCCGAA

GGGAGAAAGGCGGACAGGTATCCGGTAAGCGGCAGGGTCGGAACAGGAG

AGCGCACGAGGGAGCTTCCAGGGGGAAACGCCTGGTATCTTTATAGTCCTG

TCGGGTTTCGCCACCTCTGACTTGAGCGTCGATTTTTGTGATGCTCGTCAG

GGGGGCGGAGCCTATGGAAAAACGCCAGCAACGCGGCCTTTTTACGGTTC

CTGGCCTTTTGCTGGCCTTTTGCTCACATGTTCTTTCCTGCGTTATCCCCTG

ATTCTGTGGATAACCGTATTACCGCCTTTGAGTGAGCTGATACCGCTCGCC

GCAGCCGAACGACCGAGCGCAGCGAGTCAGTGAGCGAGGAAGCGGAAGA

GCGCCTGATGCGGTATTTTCTCCTTACGCATCTGTGCGGTATTTCACACCGC

ATATGGTGCACTCTCAGTACAATCTGCTCTGATGCCGCATAGTTAAGCCAGT

ATACACTCCGCTATCGCTACGTGACTGGGTCATGGCTGCGCCCCGACACCC

GCCAACACCCGCTGACGCGCCCTGACGGGCTTGTCTGCTCCCGGCATCCG

CTTACAGACAAGCTGTGACCGTCTCCGGGAGCTGCATGTGTCAGAGGTTTT

CACCGTCATCACCGAAACGCGCGAGGCAGCAGATCAATTCGCGCGCGAAG

GCGAAGCGGCATGCATAATGTGCCTGTCAAATGGACGAAGCAGGGATTCTG

CAAACCCTATGCTACTCCGTCAAGCCGTCAATTGTCTGATTCGTTACCAATT

ATGACAACTTGACGGCTACATCATTCACTTTTTCTTCACAACCGGCACGGAA

CTCGCTCGGGCTGGCCCCGGTGCATTTTTTAAATACCCGCGAGAAATAGAG

TTGATCGTCAAAACCAACATTGCGACCGACGGTGGCGATAGGCATCCGGGT

GGTGCTCAAAAGCAGCTTCGCCTGGCTGATACGTTGGTCCTCGCGCCAGCT

TAAGACGCTAATCCCTAACTGCTGGCGGAAAAGATGTGACAGACGCGACGG

CGACAAGCAAACATGCTGTGCGACGCTGGCGATATCAAAATTGCTGTCTGC

CAGGTGATCGCTGATGTACTGACAAGCCTCGCGTACCCGATTATCCATCGG

TGGATGGAGCGACTCGTTAATCGCTTCCATGCGCCGCAGTAACAATTGCTC

AAGCAGATTTATCGCCAGCAGCTCCGAATAGCGCCCTTCCCCTTGCCCGGC

GTTAATGATTTGCCCAAACAGGTCGCTGAAATGCGGCTGGTGCGCTTCATC

CGGGCGAAAGAACCCCGTATTGGCAAATATTGACGGCCAGTTAAGCCATTC

ATGCCAGTAGGCGCGCGGACGAAAGTAAACCCACTGGTGATACCATTCGCG

AGCCTCCGGATGACGACCGTAGTGATGAATCTCTCCTGGCGGGAACAGCAA

AATATCACCCGGTCGGCAAACAAATTCTCGTCCCTGATTTTTCACCACCCCC

TGACCGCGAATGGTGAGATTGAGAATATAACCTTTCATTCCCAGCGGTCGG

TCGATAAAAAAATCGAGATAACCGTTGGCCTCAATCGGCGTTAAACCCGCCA

CCAGATGGGCATTAAACGAGTATCCCGGCAGCAGGGGATCATTTTGCGCTT

CAGCCATACTTTTCATACTCCCGCCATTCAGAGAAGAAACCAATTGTCCATA

TTGCAT

6.8.2 *E. coli* F_1F_O-pVF2

Subunits have been highlighted in bold.

AGCTTTCAAAGTTCTGGCGATGTTGGTGTTACTGGTGGTGGCGTTGGCGGT

TTTAAAGGCGGTATTCTTGCCGCTGATCGTTACGTGGGTTTTGGTGCTGGTG

GTTCAGATACTGGCACCGGCTGTAATTAACAACAAAGGGTAAAAGGCATC**AT**

GGCTTCAGAAAATATGACGCCGCAGGATTACATAGGACACCACCTGAATA

ACCTTCAGCTGGACCTGCGTACATTCTCGCTGGTGGATCCACAAAACCCC

CCAGCCACCTTCTGGACAATCAATATTGACTCCATGTTCTTCTCGGTGGTG

CTGGGTCTGTTGTTCCTGGTTTTATTCCGTAGCGTAGCCAAAAAGGCGACC

AGCGGTGTGCCAGGTAAGTTTCAGACCGCGATTGAGCTGGTGATCGGCTT

TGTTAATGGTAGCGTGAAAGACATGTACCATGGCAAAAGCAAGCTGATTG

CTCCGCTGGCCCTGACGATCTTCGTCTGGGTATTCCTGATGAACCTGATGG

ATTTACTGCCTATCGACCTGCTGCCGTACATTGCTGAACATGTACTGGGTC

TGCCTGCACTGCGTGTGGTTCCGTCTGCGGACGTGAACGTAACGCTGTCT

ATGGCACTGGGCGTATTTATCCTGATTCTGTTCTACAGCATCAAAATGAAA

GGCATCGGCGGCTTCACGAAAGAGTTGACGCTGCAGCCGTTCAATCACTG

GGCGTTCATTCCTGTCAACTTAATCCTTGAAGGGGTAAGCCTGCTGTCCAA

ACCAGTTTCACTCGGTTTGCGACTGTTCGGTAACATGTATGCCGGTGAGCT

GATTTTCATTCTGATTGCTGGTCTGTTGCCGTGGTGGTCACAGTGGATCCT

GAATGTGCCGTGGGCCATTTTCCACATCCTGATCATTACGCTGCAAGCCTT

CATCTTCATGGTTCTGACGATCGTCTATCTGTCGATGGCGTCTGAAGAACA

TTAATTTACCAACACTACTACGTTTTAACTGAAACAAACTGGAGACTGTC**ATG**

GAAAACCTGAATATGGATCTGCTGTACATGGCTGCCGCTGTGATGATGGG

TCTGGCGGCAATCGGTGCTGCGATCGGTATCGGCATCCTCGGGGGTAAAT

TCCTGGAAGGCGCAGCGCGTCAACCTGATCTGATTCCTCTGCTGCGTACT

CAGTTCTTTATCGTTATGGGTCTGGTGGATGCTATCCCGATGATCGCTGTA

GGTCTGGGTCTGTACGTGATGTTCGCTGTCGCGTAGTAAGCGTTGCTTTTA

TTTAAAGAGCAATATCAGAACGTTAACTAAATAGAGGCATTGTGCTGTGAAT

CTTAACGCAACAATCCTCGGCCAGGCCATCGCGTTTGTCCTGTTCGTTCTGT

TCGCC**ATGAAGTACGTATGGCCGCCATTAATGGCAGCCATCGAAAAACGT**

CAAAAAGAAATTGCTGACGGCCTTGCTTCCGCAGAACGAGCACATAAGGA

CCTTGACCTTGCAAAGGCCAGCGCGACCGACCAGCTGAAAAAAGCGAAA

GCGGAAGCCCAGGTAATCATCGAGCAGGCGAACAAACGCCGCTCGCAGA

TTCTGGACGAAGCGAAAGCTGAGGCAGAACAGGAACGTACTAAAATCGT

GGCCCAGGCGCAGGCGGAAATTGAAGCCGAGCGTAAACGTGCCCGTGAA

GAGCTGCGTAAGCAAGTTGCTATCCTGGCTGTTGCTGGCGCCGAGAAGAT

CATCGAACGTTCCGTGGATGAAGCTGCTAACAGCGACATCGTGGATAAAC

TTGTCGCTGAACTGTAAGGAGGGAGGGGCTG**ATGTCTGAATTTATTACGGT**

AGCTCGCCCCTACGCCAAAGCAGCTTTTGACTTTGCCGTCGAACACCAAA

GTGTAGAACGCTGGCAGGACATGCTGGCGTTTGCCGCCGAGGTAACCAA

AAACGAACAAATGGCAGAGCTTCTCTCTGGCGCGCTTGCGCCAGAAACGC

TCGCCGAGTCGTTTATCGCAGTTGCTGGTGAGCAACTGGACGAAAACGGT

CAGAACCTGATTCGGGTTATGGCTGAAAATGGTCGTCTTAACGCGCTCCC

GGATGTTCTGGAGCAGTTTATTCACCTGCGTGCCGTGAGTGAGGCTACCG

CTGAGGTAGACGTCATTTCCGCTGCCGCACTGAGTGAACAACAGCTCGCG

AAAATTTCTGCTGCGATGGAAAAACGTCTGTCACGCAAAGTTAAGCTGAAT

GCCAAAATCGATAAGTCTGTAATGGCAGGCGTTATCATCCGAGCGGGTGA

TATGGTCATTGATGGCAGCGTACGCGGTCGTCTTGAGCGCCTTGCAGACG

TCTTGCAGTCTTAAGGGGACTGGAGC**ATGCAACTGAATTCCACCGAAATC**

AGCGAACTGATCAAGCAGCGCATTGCTCAGTTCAATGTTGTGAGTGAAGC

TCACAACGAAGGTACTATTGTTTCTGTAAGTGACGGTGTTATCCGCATTCA

CGGCCTGGCCGATGCTATGCAGGGTGAAATGATCTCCCTGCCGGGTAACC

GTTACGCTATCGCACTGAACCTCGAGCGCGACTCTGTAGGTGCGGTTGTT

ATGGGTCCGTACGCTGACCTTGCCGAAGGCATGAAAGTTAAGGCTACTGG

ACGTATCCTGGAAGTTCCGGTTGGCCGTGGCCTGCTGGGCCGTGTGGTTA

ACACTCTGGGTGCACCAATCGACGGTAAAGGTCCGCTGGATCACGACGG

CTTCTCTGCTGTAGAAGCAATCGCTCCGGGCGTTATCGAACGTCAGTCCGT

AGATCAGCCGGTACAGACCGGTTATAAAGCCGTTGACTCCATGATCCCAA

TCGGTCGTGGTCAGCGTGAATTGATCATCGGTGACCGTCAGACAGGTAAA

ACCGCACTGGCTATCGATGCCATCATCAACCAGCGCGATTCCGGTATCAA

AGCTATCTATGTCGCTATCGGCCAGAAAGCGTCCACCATTTCTAACGTGGT

ACGTAAACTGGAAGAGCACGGCGCACTGGCTAACACCATCGTTGTGGTAG

CAACCGCGTCTGAATCCGCTGCACTGCAATACCTGGCACCGTATGCCGGT

GCCGCCATGGGTGAATACTTCCGTGACCGCGGTGAAGATGCGCTGATCAT

TTACGATGACCTGTCTAAACAGGCTGTTGCTTACCGTCAGATCTCCCTGCT

GCTCCGTCGTCCGCCAGGACGTGAAGCATTCCCGGGCGACGTTTTCTACC

TCCACTCTCGTCTGCTGGAGCGTGCTGCACGTGTTAACGCCGAATACGTT

GAAGCCTTCACCAAAGGTGAAGTGAAAGGGAAAACCGGTTCTCTGACCGC

ACTGCCGATTATCGAAACTCAGGCGGGTGACGTTTCTGCGTTCGTTCCGA

CCAACGTAATCTCCATTACCGATGGTCAGATCTTCCTGGAAACCAACCTGT

TCAACGCCGGTATTCGTCCTGCGGTTAACCCGGGTATTTCCGTATCCCGTG

TTGGTGGTGCAGCACAGACCAAGATCATGAAAAAACTGTCCGGTGGTATC

CGTACCGCTCTGGCACAGTATCGTGAACTGGCAGCGTTCTCTCAGTTTGCA

TCCGACCTTGACGATGCAACACGTAACCAGCTTGACCACGGTCAGAAAGT

GACCGAACTGCTGAAACAGAAACAGTATGCGCCGATGTCCGTTGCGCAGC

AGTCTCTGGTTCTGTTCGCAGCAGAACGTGGTTACCTGGCGGATGTTGAA

CTGTCGAAAATTGGCAGCTTCGAAGCCGCTCTGCTGGCTTACGTCGACCG

TGATCACGCTCCGTTGATGCAAGAGATCAACCAGACCGGTGGCTACAACG

ACGAAATCGAAGGCAAGCTGAAAGGCATCCTCGATTCCTTCAAAGCAACC

CAATCCTGGTAACGTCTGGCGGGTACCCTTAGGGCAGGCCGCAAGGCATT

GAGGAGAAGCTC**ATGGCCGGCGCAAAAGACATACGTAGTAAGATCGCAA**

GCGTCCAGAACACGCAAAAGATCACTAAAGCGATGGAGATGGTCGCCGC

TTCCAAAATGCGTAAATCGCAGGATCGCATGGCGGCCAGCCGTCCTTATG

CAGAAACCATGCGCAAAGTGATTGGTCACCTTGCACACGGTAATCTGGAA

TATAAGCACCCTTACCTGGAAGACCGCGACGTTAAACGCGTGGGCTACCT

GGTGGTGTCGACCGACCGTGGTTTGGCGGGTGGTTTGAACATTAACCTGT

TCAAAAAACTGCTGGCGGAAATGAAGACCTGGACCGACAAAGGCGTTCA

AGCCGACCTCGCAATGATCGGCTCGAAAGGCGTGTCGTTCTTCAACTCCG

TGGGCGGCAATGTTGTTGCCCAGGTCACCGGCATGGGGGATAACCCTTCC

CTGTCCGAACTGATCGGTCCGGTAAAAGTGATGTTGCAGGCCTACGACGA

AGGCCGTCTGGACAAACTTTACATTGTCAGCAACAAATTTATTAACACCAT

GTCTCAGGTTCCGACCATCAGCCAGCTGCTGCCGTTACCGGCATCAGATG

ATGATGATCTGAAACATAAATCCTGGGATTACCTGTACGAACCCGATCCG

AAGGCGTTGCTGGATACCCTGCTGCGTCGTTATGTCGAATCTCAGGTTTAT

CAGGGCGTGGTTGAAAACCTGGCCAGCGAGCAGGCCGCCCGTATGGTGG

CGATGAAAGCCGCGACCGACAATGGCGGCAGCCTGATTAAAGAGCTGCA

GTTGGTATACAACAAAGCTCGTCAGGCCAGCATTACTCAGGAACTCACCG

AGATCGTCTCGGGGGCCGCCGCGGTTTAAACAGGTTAACTAGTAGAGGATT

TAAG**ATGAGAGGATCTCACCATCACCATCATCATGGCATGGCTACTGGAA**

AGATTGTCCAGGTAATCGGCGCCGTAGTTGACGTCGAATTCCCTCAGGAT

GCCGTACCGCGCGTGTACGATGCTCTTGAGGTGCAAAATGGTAATGAGCG

TCTGGTGCTGGAAGTTCAGCAGCAGCTCGGCGGCGGTATCGTACGTACCA

TCGCAATGGGTTCCTCCGACGGTCTGCGTCGCGGTCTGGATGTAAAAGAC

CTCGAACACCCGATTGAAGTCCCGGTAGGTAAAGCGACTCTGGGCCGTAT

CATGAACGTACTGGGTGAACCGGTCGACATGAAAGGCGAGATCGGTGAA

GAAGAGCGTTGGGCGATTCACCGCGCAGCACCTTCCTACGAAGAGCTGTC

AAACTCTCAGGAACTGCTGGAAACCGGTATCAAAGTTATCGACCTGATGG

CCCCGTTCGCTAAGGGCGGTAAAGTTGGTCTGTTCGGTGGTGCGGGTGTA

GGTAAAACCGTAAACATGATGGAGCTCATTCGTAACATCGCGATCGAGCA

CTCCGGTTACTCTGTGTTTGCGGGCGTAGGTGAACGTACTCGTGAGGGTA

ACGACTTCTACCACGAAATGACCGACTCCAACGTTATCGACAAAGTATCC

CTGGTGTATGGCCAGATGAACGAGCCGCCGGGAAACCGTCTGCGCGTTG

CTCTGACCGGTCTGACCATGGCTGAGAAATTCCGTGACGAAGGTCGTGAC

GTTCTGCTGTTCGTTGACAACATCTATCGTTACACCCTGGCCGGTACGGAA

GTATCCGCACTGCTGGGCCGTATGCCTTCAGCGGTAGGTTATCAGCCGAC

CCTGGCGGAAGAGATGGGCGTTCTGCAGGAACGTATCACCTCCACCAAAA

CTGGTTCTATCACCTCCGTACAGGCAGTATACGTACCTGCGGATGACTTGA

CTGACCCGTCTCCGGCAACCACCTTTGCGCACCTTGACGCAACCGTGGTA

CTGAGCCGTCAGATCGCGTCTCTGGGTATCTACCCGGCCGTTGACCCGCT

GGACTCCACCAGCCGTCAGCTGGACCCGCTGGTGGTTGGTCAGGAACACT

ACGACACCGCGCGTGGCGTTCAGTCCATCCTGCAACGTTATCAGGAACTG

AAAGACATCATCGCCATCCTGGGTATGGATGAACTGTCTGAAGAAGACAA

ACTGGTGGTAGCGCGTGCTCGTAAGATCCAGCGCTTCCTGTCCCAGCCGT

TCTTCGTGGCAGAAGTATTCACCGGTTCTCCGGGTAAATACGTCTCCCTGA

AAGACACCATCCGTGGCTTTAAAGGCATCATGGAAGGCGAATACGATCAC

CTGCCGGAGCAGGCGTTCTACATGGTCGGTTCCATCGAAGAAGCTGTGGA

AAAAGCCAAAAAACTTTAACGCCTTAATCGGAGGGTGAT**ATGGCAATGACT**

TACCACCTGGACGTCGTCAGCGCAGAGCAACAAATGTTCTCTGGTCTGGT

CGAGAAAATCCAGGTAACGGGTAGCGAAGGTGAACTGGGGATCTACCCT

GGCCACGCACCGCTGCTCACCGCCATTAAGCCTGGTATGATTCGCATCGT

GAAACAGCACGGTCACGAAGAGTTTATCTATCTGTCTGGCGGCATTCTTGA

AGTGCAGCCTGGCAACGTGACCGTTCTGGCCGACACCGCAATTCGCGGC

CAGGATCTCGACGAAGCGCGAGCCATGGAAGCGAAACGTAAGGCTGAAG

AGCACATTAGCAGCTCTCACGGCGACGTAGATTACGCTCAGGCGTCTGCG

GAACTGGCCAAAGCGATCGCGCAGCTGCGCGTTATCGAGTTGACCAAAAA

AGCGATGTAACACCGGCTTGAAAAGCACAAAAGCCAGTCTGGAAACAGGCT

GGCTTTTTTTTGCGCGTGTGACCCGTCCTGAATAGCGTTCACATAGATCCTG

CTGATATAAAACCCCCCTGTTTTCCTGTTTATTCATTGATCGAAATAAGAGCA

AAAACATCCACCTGACGCTTAAATTAAGGTACTGCCTTAATTTTCTGCAGACA

AAAGGCGTGACGATGGTCGAAAATGGCGCTTTCGTCAGCGGGGATAATCCG

TTATTGAACAATTTATCCTCTGTCCATTTCACGATGAAAAAAATGTAGTTTTTT

CAAGGTGAAGCGGTTTGACTCTAGAGTCGACTCTAGCGGAGTGTATACTGG

CTTACTATGTTGGCACTGATGAGGGTGTCAGTGAAGTGCTTCATGTGGCAG

GAGAAAAAAGGCTGCACCGGTGCGTCAGCAGAATATGTGATACAGGATATA

TTCCGCTTCCTCGCTCACTGACTCGCTACGCTCGGTCGTTCGACTGCGGCG

AGCGGAAATGGCTTACGAACGGGGCGGAGATTTCCTGGAAGATGCCAGGA

AGATACTTAACAGGGAAGTGAGAGGGCCGCGGCAAAGCCGTTTTTCCATAG

GCTCCGCCCCCCTGACAAGCATCACGAAATCTGACGCTCAAATCAGTGGTG

GCGAAACCCGACAGGACTATAAAGATACCAGGCGTTTCCCCCTGGCGGCTC

CCTCGTGCGCTCTCCTGTTCCTGCCTTTCGGTTTACCGGTGTCATTCCGCTG

TTATGGCCGCGTTTGTCTCATTCCACGCCTGACACTCAGTTCCGGGTAGGC

AGTTCGCTCCAAGCTGGACTGTATGCACGAACCCCCCGTTCAGTCCGACCG

CTGCGCCTTATCCGGTAACTATCGTCTTGAGTCCAACCCGGAAAGACATGC

AAAAGCACCACTGGCAGCAGCCACTGGTAATTGATTTAGAGGAGTTAGTCTT

GAAGTCATGCGCCGGTTAAGGCTAAACTGAAAGGACAAGTTTTGGTGACTG

CGCTCCTCCAAGCCAGTTACCTCGGTTCAAAGAGTTGGTAGCTCAGAGAAC

CTTCGAAAAACCGCCCTGCAAGGCGGTTTTTTCGTTTTCAGAGCAAGAGATT

ACGCGCAGACCAAAACGATCTCAAGAAGATCATCTTATTAAGGGGTCTGAC

GCTCAGTGGAACGAAAACTCACGTTAAGGGATTTTGGTCATGAGATTATCAA

AAAGGATCTTCACCTAGATCCTTTTAAATTAAAAATGAAGTTTTAAATCAATCT

AAAGTATATATGAGTAAACTTGGTCTGACAGTTACCAATGCTTAATCAGTGA

GGCACCTATCTCAGCGATCTGTCTATTTCGTTCATCCATAGTTGCCTGACTC

CCCGTCGTGTAGATAACTACGATACGGGAGGGCTTACCATCTGGCCCCAGT

GCTGCAATGATACCGCGAGACCCACGCTCACCGGCTCCAGATTTATCAGCA

ATAAACCAGCCAGCCGGAAGGGCCGAGCGCAGAAGTGGTCCTGCAACTTT

ATCCGCCTCCATCCAGTCTATTAATTGTTGCCGGGAAGCTAGAGTAAGTAGT

TCGCCAGTTAATAGTTTGCGCAACGTTGTTGCCATTGCTGCAGGCATCGTG

GTGTCACGCTCGTCGTTTGGTATGGCTTCATTCAGCTCCGGTTCCCAACGAT

CAAGGCGAGTTACATGATCCCCCATGTTGTGCAAAAAAGCGGTTAGCTCCTT

CGGTCCTCCGATCGTTGTCAGAAGTAAGTTGGCCGCAGTGTTATCACTCAT

GGTTATGGCAGCACTGCATAATTCTCTTACTGTCATGCCATCCGTAAGATGC

TTTTCTGTGACTGGTGAGTACTCAACCAAGTCATTCTGAGAATAGTGTATGC

GGCGACCGAGTTGCTCTTGCCCGGCGTCAACACGGGATAATACCGCGCCA

CATAGCAGAACTTTAAAAGTGCTCATCATTGGAAAACGTTCTTCGGGGCGAA

AACTCTCAAGGATCTTACCGCTGTTGAGATCCAGTTCGATGTAACCCACTCG

TGCACCCAACTGATCTTCAGCATCTTTTACTTTCACCAGCGTTTCTGGGTGA

GCAAAAACAGGAAGGCAAAATGCCGCAAAAAAGGGAATAAGGGCGACACG

GAAATGTTGAATACTCATACTCTTCCTTTTTCAATATTATTGAAGCATTTATCA

GGGTTATTGTCTCATGAGCGGATACATATTTGAATGTATTTAGAAAAATAAAC

AAATAGGGGTTCCGCGCACATTTCCCCGAAAAGTGCCACCTGACGTCTAAG

AAACCATTATTATCATGACATTAACCTATAAAAATAGGCGTATCACGAGGCC

CTTTCGTCTTCAAGAATTTTATAAACCGTGGAGCGGGCAATACTGAGCTGAT

GAGCAATTTCCGTTGCACCAGTGCCCTTCTGATGAAGCGTCAGCACGACGT

TCCTGTCCACGGTACGCCTGCGGCCAAATTTGATTCCTTTCAGCTTTGCTTC

CTGTCGGCCCTCATTCGTGCGCTCTAGGATCA

6.8.3 pR-mCherry

Construct was cloned onto pET3A between Nde1- Blp1 restriction sites.

ATGGGTAAATTATTACTGATATTAGGTAGTGTTATTGCACTTCCTACATTTGC

TGCAGGTGGTGGTGACCTTGATGCTAGTGATTACACTGGTGTTTCTTTTTGG

TTAGTTACTGCTGCTTTATTAGCATCTACTGTATTTTTCTTTGTTGAAAGAGAT

AGAGTTTCTGCAAAATGGAAAACATCATTAACTGTATCTGGTCTTGTTACTGG

TATTGCTTTCTGGCATTACATGTACATGAGAGGGGTATGGATTGAAACTGGT

GATTCGCCAACTGTATTTAGATACATTGATTGGTTACTAACAGTTCCTCTATT

AATATGTGAATTCTACTTAATTCTTGCTGCTGCAACTAATGTTGCTGGATCAT

TATTTAAGAAATTACTAGTTGGTTCTCTTGTTATGCTTGTGTTTGGTTACATG

GGTGAAGCAGGAATCATGGCTGCATGGCCTGCATTCATTATTGGGTGTTTA

GCTTGGGTATACATGATTTATGAATTATGGGCTGGAGAAGGAAAATCTGCAT

GTAATACTGCAAGTCCTGCTGTGCAATCAGCTTACAACACAATGATGTATAT

TATCATCTTTGGTTGGGCGATTTATCCTGTAGGTTATTTCACAGGTTACCTGA

TGGGTGACGGTGGATCAGCTCTTAACTTAAACCTTATCTATAACCTTGCTGA

CTTTGTTAACAAGATTCTATTTGGTTTAATTATATGGAATGTTGCTGTTAAAGA

ATCTTCTAATGCTCTCGAGGGAGGAAGTCTGGAAGTTCTGTTCCAGGGGCC

CGTCGACGGCGGCTCCGGATCCGAAAACTTGTATTTCCAGGGCATGCATAG

CAAGGGCGAGGAGGATAACATGGCCATCATCAAGGAGTTCATGCGCTTCAA

GGTGCACATGGAGGGCTCCGTGAACGGCCACGAGTTCGAGATCGAGGGCG

AGGGCGAGGGCCGCCCCTACGAGGGCACCCAGACCGCCAAGCTGAAGGT

GACCAAGGGTGGCCCCCTGCCCTTCGCCTGGGACATCCTGTCCCCTCAGTT

CATGTACGGCTCCAAGGCCTACGTGAAGCACCCCGCCGACATCCCCGACTA

CTTGAAGCTGTCCTTCCCCGAGGGCTTCAAGTGGGAGCGCGTGATGAACTT
CGAGGACGGCGGCGTGGTGACCGTGACCCAGGACTCCTCCTTGCAGGACG
GCGAGTTCATCTACAAGGTGAAGCTGCGCGGCACCAACTTCCCCTCCGACG
GCCCCGTAATGCAGAAGAAGACCATGGGCTGGGAGGCCTCCTCCGAGCGG
ATGTACCCCGAGGACGGCGCCCTGAAGGGCGAGATCAAGCAGAGGCTGAA
GCTGAAGGACGGCGGCCACTACGACGCTGAGGTCAAGACCACCTACAAGG
CCAAGAAGCCCGTGCAGCTGCCCGGCGCCTACAACGTCAACATCAAGTTG
GACATCACCTCCCACAACGAGGACTACACCATCGTGGAACAGTACGAACGC
GCCGAGGGCCGCCACTCCACCGGCGGCATGGACGAGCTGTACAAGGGCG
GCTCCGGCGGCTCCGGCAAACTGGCGGCGGCGCTGGAACACCATCACCAT
CACCATTAA

6.8.4 F30-2xdBroccoli

Construct was cloned onto pET3A between HindIII – BglII restriction sites.

CGATCCCGCGAAATTAATACGACTCACTATAGGTTGCCATGTGTAT
GTGGGAGACGGTCGGGTCCATCTGAGACGGTCGGGTCCAGATATT
CGTATCTGTCGAGTAGAGTGTGGGCTCAGATGTCGAGTAGAGTGT
GGGCTCCCACATACTCTGATGATCCAGACGGTCGGGTCCATCTGA
GACGGTCGGGTCCAGATATTCGTATCTGTCGAGTAGAGTGTGGGC
TCAGATGTCGAGTAGAGTGTGGGCTGGATCATTCATGGCAACTAG
CATAACCCCTTGGGGCCTCTAAACGGGTCTTGAGGGGTTTTTTGCT
GAAAGGAGGAACTATATCCGGATATCCACAGGACGGGTGTGGTCG
CCATGATCGCGTAGTCGATAGTGGCTCCAAGTAGCGAAGCGAGCA
GGACTGGGCGGCGGCCAAAGCGGTCGGACAGTGCTCCGAGAACG

GGTGCGCATAGAAATTGCATCAACGCATATAGCGCTAGCAGCACG

CCATAGTGACTGGCGATGCTGTCGGAATGGACGATATCCCGCAAG

AGGCCCGGCAGTACCGGCATAACCAAGCCTATGCCTACAGCATCC

AGGGTGACGGTGCCGAGGATGACGATGAGCGCATTGTTAGATTTC

ATACACGGTGCCTGACTGCGTTAGCAATTTAACTGTGATAAACTAC

CGCATTA

6.8.5 LMCA1-pET-22b

LMCA1-pET-22b was a kind gift from Professor Poul Nissen. The construct was ligated into pET-22b between NdeI and XhoI.

ATGGTTATTGTTTTAGTCATCGCTGCCTTGGTGCAGTTGGTTTTAGGCGAAG

TAGTCGAATCGCTTATTATCTTTTTAGTGCTGATTGTGAACTCGATAATTAGC

GTAGTTCAAACGCGAAAAGCAGAAAGTTCGCTTGATGCGTTACGAGAAATGT

CTGCGCCAGTTGCCAAAGTTATTCGTGATGGTTCTAAGCAAAGTATTCATGC

GCGCGAACTTGTTCCGGGTGACGTCGTTATTTTGGATGCAGGTGATTTCGT

CCCAGCAGACGGCCGTTTGTTCGAAAGTGGCTCCTTGAAAATCGACGAAGG

GATGCTTACTGGAGAATCGGAGGCAGTCGAGAAATATATCGATACCATTCCA

GATGAAGTAGGACTTGGCGACCGTGTGAATATGGTTTTCAGCGGGTCCCTC

GTTGTATATGGTCGCGGGATGTTTGTTGTAACAGGCACAGCGAGCGAAACG

GAAATCGGTAAAATTGCCGGATTACTTGAAACGGCAGAAGCAAAACAAACAC

CACTACAAAGAAAACTAGAATCATTCAGTAAAAAGCTAGGACTCGGTATTTTA

GCACTCTGTGTACTTATTTTTGCTGTCGAAGCTGGTCGCGTATTACTCGGCG

ACAATTCAGCGGATATGGCAACAGCGATTTTAAATGCCTTTATGTTTGCCGT

GGCCGTAGCTGTAGCAGCCATTCCAGAAGCACTTTCTTCTATTGTAACGATT

GTACTTGCGGTCGGAACAAACAAAATGGCAAAGCAGCACGCGATTATTAGA

AAGCTCCCAGCTGTTGAAACACTAGGCTCCACCAGCGTTATTTGTACAGACA

AAACCGGAACATTAACACAAAATAAAATGACTGTAGTCGATTATTATTTACCC

GATGGAACAAAAGAAAATTTCCCAGAAAGTCCAGAAAATTGGTCAGAAGGG

GAACGTCGTTTGATTCATATTGCGGTACTTTGTAACGATTCAAATATTAACAG

TGAGGGCAAGGAGTTAGGCGACCCGACCGAAGTGGCGCTAATTGCCTTTA

GTAATAAAAATAATCAAGATTACAATGAAATTCGAGAAAAATTCATCCGTGAA

GGCGAAATTCCCTTTGATTCAGATCGTAAGTTAATGTCTACGCTTCATACCTT

TAATGAAAACAAGGCAATGCTAACAAAAGGTGGACCAGACGTGATGTTCGC

GCGTTGCAGTTATGTTTTCCTTGATGGGGAAGAAAAGCCAATGACAGAAGAA

ATTTTAGCGAAACTAAAAGAAACAAACGAAGAATTTTCGAATCAAGCCTTAC

GTGTCCTCGCATACGGCTACAAACGGATGCCTGCTGATACAACCGAATTAA

AATTAGAAGATGAGCAAGATATCGTTCTAGTTGGTTTAACAGCAATGATTGA

CCCACCACGTGAAGCCGTGTATGCATCCATTGAAGAGTCCAAAAAAGCGGG

TATTCGCACGGTTATGATTACTGGTGACCATAAAACAACGGCACAAGCAATC

GGCCGGGACATTGGTTTAATGGATGCTGATGATATCGCATTAACAGGTCAA

GAACTAGACGCAATGCCAGAAGAAGAACTCGACAAAAAACTAGAACATATC

GCAGTCTACGCCCGAGTTTCACCAGAAAACAAAATCCGTATCGTCAAAGCTT

GGCAGAAAAAAGGCAAAATCACCGCAATGACTGGTGATGGTGTCAATGATG

CGCCAGCTCTAAAACAAGCCGATATTGGTGTCGCAATGGGTAGCGGAACAG

ACGTTGCGAAAGACTCCGCTGCAATGATTCTAACAGATGATAATTTCGTTTC

GATTGTGGATGCAGTTGGCGTAGGTAGAACCGTTTTTGACAATATTAAGAAA

TCAATTGCTTATCTATTTGCAGGAAACCTAGGTGCGATTATTGCGATTTTATT

CGCGCTAGTGCTGGACTGGATCAACCCGTTCACTGCATTACAATTACTATTT

ATCAACTTAGTCAATGACTCCTTACCAGCAATCGCACTAGGTATGGAAAAAG

CAGAACCTGACGTAATGAAACGCAAACCAAGAGATATAAACGAAGGTATTTT

TGCTGGTGGAACAATGCGCGCCGTTATCAGTCGTGGTGTATTAATCGGTAT

CGCCGTTATCATCTCACAATACATTGGTATGCAAATTTCACCAGAGATGAGT

GTTGCAATGGCATTTACTACGCTTATCCTAGCACGCACATTACAAACATTTG

CAGCTCGTTCGAATGTCCAAACCGCATTTGGCGCAGGATTCTTCAGCAACA

AATACGTAATCGGTGCAGTATTGCTTTGTTTCGTCCTATACGGAATTACTGTA

CTACCAGGAGCTCGCGAAATCTTCTCAATCCCAGCATCATTTGGCCTACATG

AATGGTCGATTGCAGCCGGGCTAGCACTTGCAGCAGTTGTAATGATGGAGA

TTATTAAAGTAGTTCAGAATAAGTTTTTCAAATAAGATTATGATATTCCGACCA

CCENLYFGCACCACCACCACCACCACCACCACCAC

7 Supplementary figures

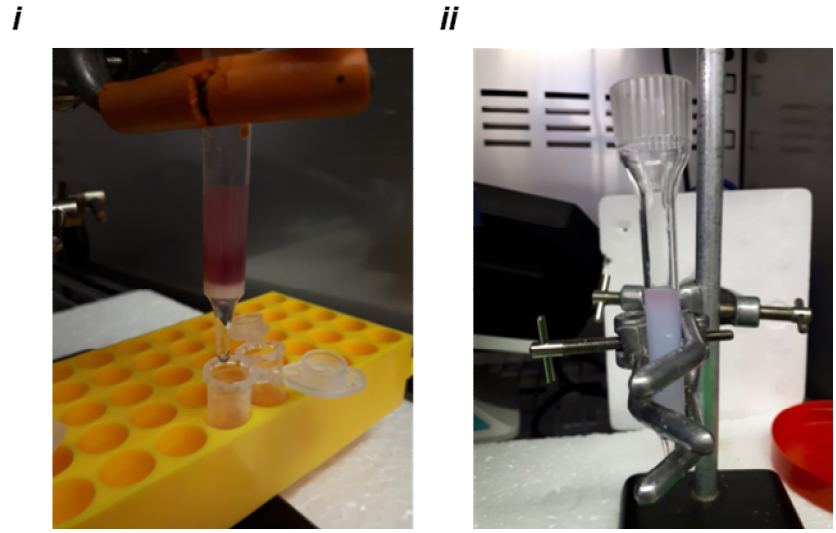

Figure 7.1 Irreversible pR binding to Ni-NTA resin. (***i***) pR remains bound to Ni-NTA resin after elution with buffer containing 500 mM imidazole. (***ii*****)** pR eluted with 180 mM imidazole after dilution of mixture of solublised pR to a DDM concentration of 0.15% w/v.

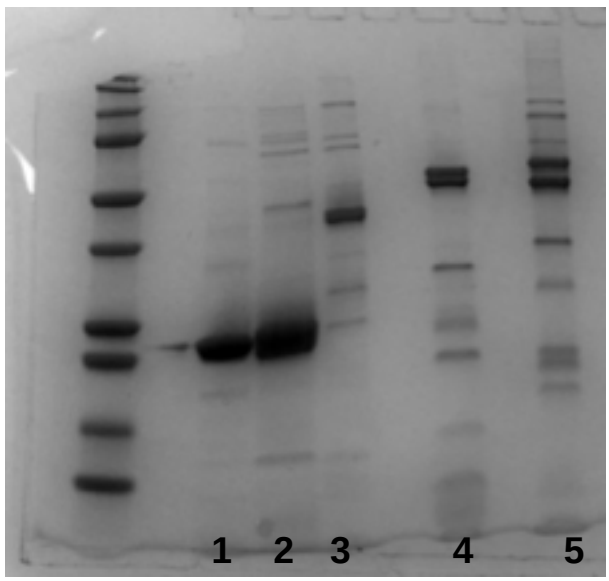

Figure 7.2 Proteins used for ATP synthesis. Lane 1 – pR. Lane 2 – Sodium pumping pR (not used in this thesis). Lane 3 – pR-mCherry. Lane 4 – *E. coli* F_1F_O. Lane 5 – TA2 F_1F_O from a thermoalkaliphilic bacterium (not used in this thesis). Ladder (kDa): 180, 130, 100, 70, 55, 40, 35, 25, 15, 10.

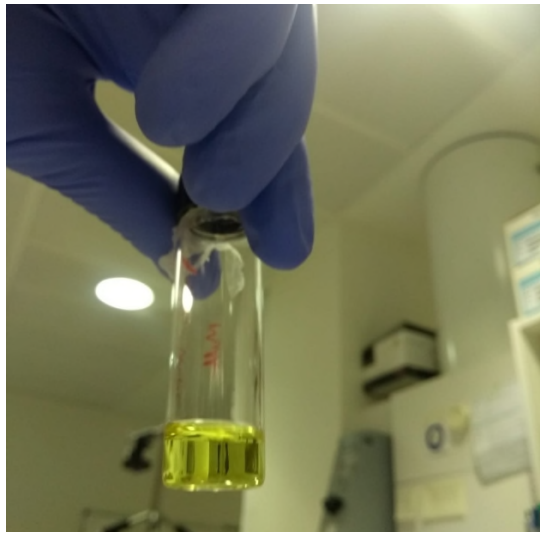

7.3 DFHBI partitioning into oil phase. Intense discolouration of a mixture of 1:1 Hx:Si incubated with 60 μM DFHBI.

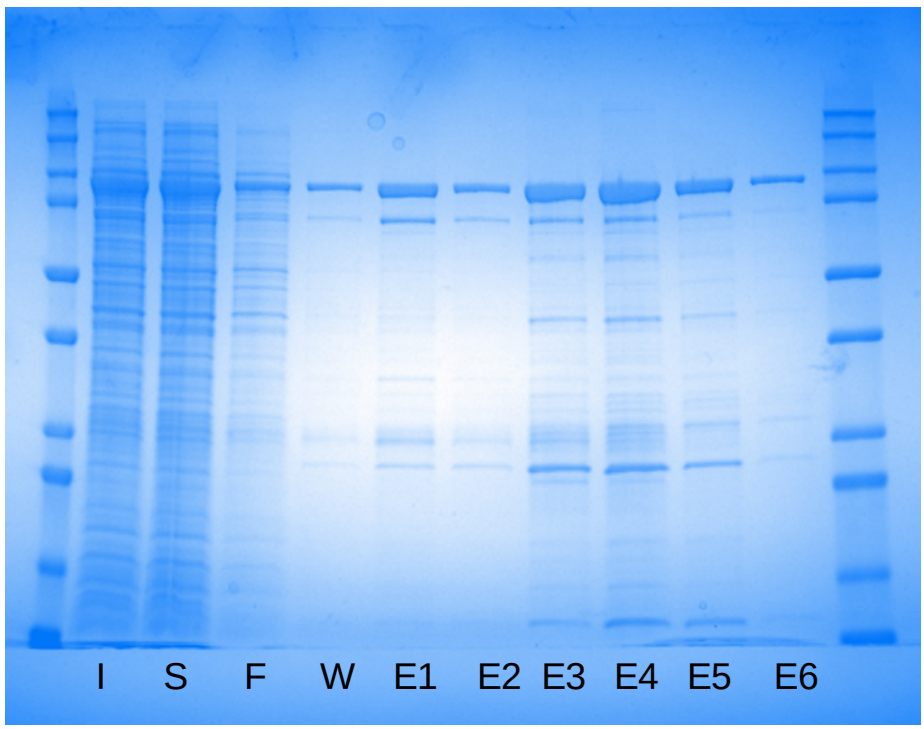

Figure 7.4 Stages of LMCA1 purification. P – Inverted membrane vesicles. S – Solubilised membranes. F – Ni-NTA flow-through. W – Wash. E1 – E6 – Elution fractions. Ladder (kDa): 250, 150, 100, 75, 50, 37, 25, 20, 15, 10

8 Bibliography

1. Cazimoglu, I., Booth, M. J. & Bayley, H. A Lipid-Based Droplet Processor for Parallel Chemical Signals. *ACS Nano* **15**, 20214–20224 (2021).
2. Booth, M. J., Cazimoglu, I. & Bayley, H. Controlled deprotection and release of a small molecule from a compartmented synthetic tissue module. *Commun Chem* **2**, 142 (2019).
3. Schild, V. R., Booth, M. J., Box, S. J., Olof, S. N., Mahendran, K. R. & Bayley, H. Light-Patterned Current Generation in a Droplet Bilayer Array. *Sci Rep* **7**, 46585 (2017).
4. Mansy, S. S., Schrum, J. P., Krishnamurthy, M., Tobé, S., Treco, D. A. & Szostak, J. W. Template-directed synthesis of a genetic polymer in a model protocell. *Nature* **454**, 122–125 (2008).
5. Deshpande, S., Brandenburg, F., Lau, A., Last, M. G. F., Spoelstra, W. K., Reese, L., Wunnava, S., Dogterom, M. & Dekker, C. Spatiotemporal control of coacervate formation within liposomes. *Nat Commun* **10**, 1800 (2019).
6. Huang, X., Li, M., Green, D. C., Williams, D. S., Patil, A. J. & Mann, S. Interfacial assembly of protein–polymer nano-conjugates into stimulus-responsive biomimetic protocells. *Nat Commun* **4**, 2239 (2013).
7. Mason, A. F., Buddingh', B. C., Williams, D. S. & van Hest, J. C. M. Hierarchical Self-Assembly of a Copolymer-Stabilized Coacervate Protocell. *J Am Chem Soc* **139**, 17309–17312 (2017).
8. Sokolova, E., Spruijt, E., Hansen, M. M. K., Dubuc, E., Groen, J., Chokkalingam, V., Piruska, A., Heus, H. A. & Huck, W. T. S. Enhanced transcription rates in membrane-free protocells formed by coacervation of cell lysate. *Proceedings of the National Academy of Sciences* **110**, 11692–11697 (2013).
9. Holden, M. A., Needham, D. & Bayley, H. Functional Bionetworks from Nanoliter Water Droplets. *J Am Chem Soc* **129**, 8650–8655 (2007).
10. van Stevendaal, M. H. M. E., Vasiukas, L., Yewdall, N. A., Mason, A. F. & van Hest, J. C. M. Engineering of Biocompatible Coacervate-Based Synthetic Cells. *ACS Appl Mater Interfaces* **13**, 7879–7889 (2021).
11. Qiao, Y., Li, M., Booth, R. & Mann, S. Predatory behaviour in synthetic protocell communities. *Nat Chem* **9**, 110–119 (2017).
12. Lee, K. Y., Park, S.-J., Lee, K. A., Kim, S.-H., Kim, H., Meroz, Y., Mahadevan, L., Jung, K.-H., Ahn, T. K., Parker, K. K. & Shin, K. Photosynthetic artificial organelles sustain and control ATP-dependent reactions in a protocellular system. *Nat Biotechnol* **36**, 530 (2018).
13. Toparlak, Ö. D., Zasso, J., Bridi, S., Serra, M. D., Macchi, P., Conti, L., Baudet, M.-L. & Mansy, S. S. Artificial cells drive neural differentiation. *Sci Adv* **6**, eabb4920 (2020).
14. Berhanu, S., Ueda, T. & Kuruma, Y. Artificial photosynthetic cell producing energy for protein synthesis. *Nat Commun* **10**, 1325 (2019).
15. Deshpande, S., Spoelstra, W. K., van Doorn, M., Kerssemakers, J. & Dekker, C. Mechanical Division of Cell-Sized Liposomes. *ACS Nano* **12**, 2560–2568 (2018).

16. Steinkühler, J., Knorr, R. L., Zhao, Z., Bhatia, T., Bartelt, S. M., Wegner, S., Dimova, R. & Lipowsky, R. Controlled division of cell-sized vesicles by low densities of membrane-bound proteins. *Nat Commun* **11**, 905 (2020).
17. Abdelmohsen, L. K. E. A., Nijemeisland, M., Pawar, G. M., Janssen, G.-J. A., Nolte, R. J. M., van Hest, J. C. M. & Wilson, D. A. Dynamic Loading and Unloading of Proteins in Polymeric Stomatocytes: Formation of an Enzyme-Loaded Supramolecular Nanomotor. *ACS Nano* **10**, 2652–2660 (2016).
18. Chen, Z., Wang, J., Sun, W., Archibong, E., Kahkoska, A. R., Zhang, X., Lu, Y., Ligler, F. S., Buse, J. B. & Gu, Z. Synthetic beta cells for fusion-mediated dynamic insulin secretion. *Nat Chem Biol* **14**, 86 (2017).
19. Peters, R. J. R. W., Marguet, M., Marais, S., Fraaije, M. W., van Hest, J. C. M. & Lecommandoux, S. Cascade Reactions in Multicompartmentalized Polymersomes. *Angewandte Chemie International Edition* **53**, 146–150 (2014).
20. Bayley, H., Cazimoglu, I. & Hoskin, C. E. G. Synthetic tissues. *Emerg Top Life Sci* **3**, 615–622 (2019).
21. Wauer, T., Gerlach, H., Mantri, S., Hill, J., Bayley, H. & Sapra, K. T. Construction and Manipulation of Functional Three-Dimensional Droplet Networks. *ACS Nano* **8**, 771–779 (2014).
22. Langton, M. J., Scriven, L. M., Williams, N. H. & Hunter, C. A. Triggered Release from Lipid Bilayer Vesicles by an Artificial Transmembrane Signal Transduction System. *J Am Chem Soc* **139**, 15768–15773 (2017).
23. Lister, F. G. A., le Bailly, B. A. F., Webb, S. J. & Clayden, J. Ligand-modulated conformational switching in a fully synthetic membrane-bound receptor. *Nat Chem* **9**, 420–425 (2017).
24. Carrara, P., Stano, P. & Luisi, P. L. Giant Vesicles "Colonies": A Model for Primitive Cell Communities. *ChemBioChem* **13**, 1497–1502 (2012).
25. Hadorn, M., Boenzli, E. & Hanczyc, M. M. Specific and Reversible DNA-Directed Self-Assembly of Modular Vesicle-Droplet Hybrid Materials. *Langmuir* **32**, 3561–3566 (2016).
26. Bolognesi, G., Friddin, M. S., Salehi-Reyhani, A., Barlow, N. E., Brooks, N. J., Ces, O. & Elani, Y. Sculpting and fusing biomimetic vesicle networks using optical tweezers. *Nat Commun* **9**, 1882 (2018).
27. Booth, M. J., Schild, V. R., Downs, F. G. & Bayley, H. Functional aqueous droplet networks. *Mol Biosyst* **13**, 1658–1691 (2017).
28. Hwang, W. L., Chen, M., Cronin, B., Holden, M. A. & Bayley, H. Asymmetric Droplet Interface Bilayers. *J Am Chem Soc* **130**, 5878–5879 (2008).
29. Barlow, N. E., Smpokou, E., Friddin, M. S., Macey, R., Gould, I. R., Turnbull, C., Flemming, A. J., Brooks, N. J., Ces, O. & Barter, L. M. C. Engineering plant membranes using droplet interface bilayers. *Biomicrofluidics* **11**, 024107 (2017).
30. Devaux, P. F. Static and dynamic lipid asymmetry in cell membranes. *Biochemistry* **30**, 1163–1173 (1991).
31. Lee, S. & Bayley, H. Reconstruction of the Gram-Negative Bacterial Outer-Membrane Bilayer. *Small* 2200007 (2022) doi:10.1002/smll.202200007.
32. Bayley, H., Cronin, B., Heron, A., Holden, M. A., Hwang, W. L., Syeda, R., Thompson, J. & Wallace, M. Droplet interface bilayers. *Mol Biosyst* **4**, 1191 (2008).

33. Findlay, H. E., Harris, N. J. & Booth, P. J. In vitro synthesis of a Major Facilitator Transporter for specific active transport across Droplet Interface Bilayers. *Sci Rep* **6**, 39349 (2016).
34. Syeda, R., Holden, M. A., Hwang, W. L. & Bayley, H. Screening Blockers Against a Potassium Channel with a Droplet Interface Bilayer Array. *J Am Chem Soc* **130**, 15543–15548 (2008).
35. El-Arabi, A. M., Salazar, C. S. & Schmidt, J. J. Ion channel drug potency assay with an artificial bilayer chip. *Lab Chip* **12**, 2409 (2012).
36. Qing, Y., Tamagaki-Asahina, H., Ionescu, S. A., Liu, M. D. & Bayley, H. Catalytic site-selective substrate processing within a tubular nanoreactor. *Nat Nanotechnol* **14**, 1135–1142 (2019).
37. Qing, Y., Ionescu, S. A., Pulcu, G. S. & Bayley, H. Directional control of a processive molecular hopper. *Science (1979)* **361**, 908–912 (2018).
38. Rigaud, J.-L. & Lévy, D. Reconstitution of Membrane Proteins into Liposomes. in 65–86 (2003). doi:10.1016/S0076-6879(03)72004-7.
39. Lichtenberg, D., Ahyayauch, H. & Goñi, F. M. The Mechanism of Detergent Solubilization of Lipid Bilayers. *Biophys J* **105**, 289–299 (2013).
40. Booth, M. J., Schild, V. R., Graham, A. D., Olof, S. N. & Bayley, H. Light-activated communication in synthetic tissues. *Sci Adv* **2**, e1600056 (2016).
41. Dupin, A. & Simmel, F. C. Signalling and differentiation in emulsion-based multi-compartmentalized in vitro gene circuits. *Nat Chem* **11**, 32–39 (2019).
42. Villar, G., Graham, A. D. & Bayley, H. A Tissue-Like Printed Material. *Science (1979)* **340**, 48–52 (2013).
43. Maglia, G., Heron, A. J., Hwang, W. L., Holden, M. A., Mikhailova, E., Li, Q., Cheley, S. & Bayley, H. Droplet networks with incorporated protein diodes show collective properties. *Nat Nanotechnol* **4**, 437–440 (2009).
44. Yasuga, H., Kawano, R., Takinoue, M., Tsuji, Y., Osaki, T., Kamiya, K., Miki, N. & Takeuchi, S. Logic Gate Operation by DNA Translocation through Biological Nanopores. *PLoS One* **11**, e0149667 (2016).
45. Downs, F. G., Lunn, D. J., Booth, M. J., Sauer, J. B., Ramsay, W. J., Klemperer, R. G., Hawker, C. J. & Bayley, H. Multi-responsive hydrogel structures from patterned droplet networks. *Nat Chem* **12**, 363–371 (2020).
46. Friddin, M. S., Bolognesi, G., Elani, Y., Brooks, N. J., Law, R. v., Seddon, J. M., Neil, M. A. A. & Ces, O. Optically assembled droplet interface bilayer (OptiDIB) networks from cell-sized microdroplets. *Soft Matter* **12**, 7731–7734 (2016).
47. Krishna Kumar, R., Meiller-Legrand, T. A., Alcinesio, A., Gonzalez, D., Mavridou, D. A. I., Meacock, O. J., Smith, W. P. J., Zhou, L., Kim, W., Pulcu, G. S., Bayley, H. & Foster, K. R. Droplet printing reveals the importance of micron-scale structure for bacterial ecology. *Nat Commun* **12**, 857 (2021).
48. Alcinesio, A., Cazimoglu, I., Kimmerly, G. R., Restrepo Schild, V., Krishna Kumar, R. & Bayley, H. Modular Synthetic Tissues from 3D-Printed Building Blocks. *Adv Funct Mater* **32**, 2107773 (2022).
49. Alcinesio, A., Meacock, O. J., Allan, R. G., Monico, C., Restrepo Schild, V., Cazimoglu, I., Cornall, M. T., Krishna Kumar, R. & Bayley, H. Controlled packing and single-droplet resolution of 3D-printed functional synthetic tissues. *Nat Commun* **11**, 2105 (2020).

50. Mruetusatorn, P., Boreyko, J. B., Venkatesan, G. A., Sarles, S. A., Hayes, D. G. & Collier, C. P. Dynamic morphologies of microscale droplet interface bilayers. *Soft Matter* **10**, 2530 (2014).
51. Villar, G., Graham, A. D. & Bayley, H. A Tissue-Like Printed Material. *Science (1979)* **340**, 48–52 (2013).
52. Sadtler, V. M., Imbert, P. & Dellacherie, E. Ostwald Ripening of Oil-in-Water Emulsions Stabilized by Phenoxy-Substituted Dextrans. *J Colloid Interface Sci* **254**, 355–361 (2002).
53. Zhou, L., Wolfes, A. C., Li, Y., Chan, D. C. W., Ko, H., Szele, F. G. & Bayley, H. Lipid-Bilayer-Supported 3D Printing of Human Cerebral Cortex Cells Reveals Developmental Interactions. *Advanced Materials* **32**, 2002183 (2020).
54. Villar, G., Heron, A. J. & Bayley, H. Formation of droplet networks that function in aqueous environments. *Nat Nanotechnol* **6**, 803–808 (2011).
55. Alcinesio, A., Krishna Kumar, R. & Bayley, H. Functional Multivesicular Structures with Controlled Architecture from 3D-Printed Droplet Networks. *ChemSystemsChem* (2021) doi:10.1002/syst.202100036.
56. Amati, A. M., Graf, S., Deutschmann, S., Dolder, N. & Ballmoos, C. von. Current problems and future avenues in proteoliposome research. *Biochem Soc Trans* **48**, 1473–1492 (2020).
57. Ritzmann, N., Thoma, J., Hirschi, S., Kalbermatter, D., Fotiadis, D. & Müller, D. J. Fusion Domains Guide the Oriented Insertion of Light-Driven Proton Pumps into Liposomes. *Biophys J* **113**, 1181–1186 (2017).
58. von Ballmoos, C., Wiedenmann, A. & Dimroth, P. Essentials for ATP Synthesis by F $_1$ F $_0$ ATP Synthases. *Annu Rev Biochem* **78**, 649–672 (2009).
59. Imamura, H., Huynh Nhat, K. P., Togawa, H., Saito, K., Iino, R., Kato-Yamada, Y., Nagai, T. & Noji, H. Visualization of ATP levels inside single living cells with fluorescence resonance energy transfer-based genetically encoded indicators. *Proceedings of the National Academy of Sciences* **106**, 15651–15656 (2009).
60. Knowles, J. R. Enzyme-Catalyzed Phosphoryl Transfer Reactions. *Annu Rev Biochem* **49**, 877–919 (1980).
61. Junge, W. & Nelson, N. ATP Synthase. *Annu Rev Biochem* **84**, 631–657 (2015).
62. David G. Nicholls & Stuart J. Ferguson. *Bioenergetics*. (2013).
63. Berry, B. J., Trewin, A. J., Amitrano, A. M., Kim, M. & Wojtovich, A. P. Use the Protonmotive Force: Mitochondrial Uncoupling and Reactive Oxygen Species. *J Mol Biol* **430**, 3873–3891 (2018).
64. Sobti, M., Smits, C., Wong, A. S., Ishmukhametov, R., Stock, D., Sandin, S. & Stewart, A. G. Cryo-EM structures of the autoinhibited E. coli ATP synthase in three rotational states. *Elife* **5**, (2016).
65. Senior, A. E., Nadanaciva, S. & Weber, J. The molecular mechanism of ATP synthesis by F1F0-ATP synthase. *Biochimica et Biophysica Acta (BBA) - Bioenergetics* **1553**, 188–211 (2002).
66. Sobti, M., Walshe, J. L., Wu, D., Ishmukhametov, R., Zeng, Y. C., Robinson, C. v., Berry, R. M. & Stewart, A. G. Cryo-EM structures provide insight into how E. coli F1Fo ATP synthase accommodates symmetry mismatch. *Nat Commun* **11**, 2615 (2020).

67. Ueno, H., Suzuki, T., Kinosita, K. & Yoshida, M. ATP-driven stepwise rotation of FoF1-ATP synthase. *Proceedings of the National Academy of Sciences* **102**, 1333–1338 (2005).
68. Cook, G. M., Keis, S., Morgan, H. W., von Ballmoos, C., Matthey, U., Kaim, G. & Dimroth, P. Purification and Biochemical Characterization of the F_1F_o-ATP Synthase from Thermoalkaliphilic *Bacillus* sp. Strain TA2.A1. *J Bacteriol* **185**, 4442–4449 (2003).
69. Devenish, R. J., Prescott, M. & Rodgers, A. J. W. The Structure and Function of Mitochondrial F1F0-ATP Synthases. in 1–58 (2008). doi:10.1016/S1937-6448(08)00601-1.
70. Dimroth, P. Primary sodium ion translocating enzymes. *Biochimica et Biophysica Acta (BBA) - Bioenergetics* **1318**, 11–51 (1997).
71. Duan, L., He, Q., Wang, K., Yan, X., Cui, Y., Möhwald, H. & Li, J. Adenosine Triphosphate Biosynthesis Catalyzed by FoF1 ATP Synthase Assembled in Polymer Microcapsules. *Angewandte Chemie* **119**, 7126–7130 (2007).
72. Xu, X., Fei, J., Xu, Y., Li, G., Dong, W., Xue, H. & Li, J. Boric Acid-Fueled ATP Synthesis by FoF1 ATP Synthase Reconstituted in a Supramolecular Architecture. *Angewandte Chemie International Edition* (2021) doi:10.1002/anie.202016253.
73. Li, J.-H., Wang, Y.-F., Ha, W., Liu, Y., Ding, L.-S., Li, B.-J. & Zhang, S. Cyclodextrin-Based Microcapsules as Bioreactors for ATP Biosynthesis. *Biomacromolecules* **14**, 2984–2988 (2013).
74. Gutiérrez-Sanz, Ó., Natale, P., Márquez, I., Marques, M. C., Zacarias, S., Pita, M., Pereira, I. A. C., López-Montero, I., De Lacey, A. L. & Vélez, M. H_2-Fueled ATP Synthesis on an Electrode: Mimicking Cellular Respiration. *Angewandte Chemie* **128**, 6324–6328 (2016).
75. Hu, H., Zhu, J., Cao, L., Wang, Z., Gao, Y., Yang, L., Lin, W. & Wang, C. Light-driven proton transport across liposomal membranes enabled by Janus metal-organic layers. *Chem* (2021) doi:10.1016/j.chempr.2021.10.020.
76. Xu, Y., Fei, J., Li, G., Yuan, T. & Li, J. Compartmentalized Assembly of Motor Protein Reconstituted on Protocell Membrane toward Highly Efficient Photophosphorylation. *ACS Nano* **11**, 10175–10183 (2017).
77. Racker, E. & Stoeckenius, W. Reconstitution of Purple Membrane Vesicles Catalyzing Light-driven Proton Uptake and Adenosine Triphosphate Formation. *Journal of Biological Chemistry* **249**, 662–663 (1974).
78. Pitard, B., Richard, P., Duñarach, M., Girault, G. & Rigaiud, J. ATP Synthesis by the F0F1 ATP Synthase from Thermophilic Bacillus PS3 Reconstituted into Liposomes with Bacteriorhodopsin. *Eur J Biochem* **235**, 769–778 (1996).
79. Ishmukhametov, R. R., Russell, A. N. & Berry, R. M. A modular platform for one-step assembly of multi-component membrane systems by fusion of charged proteoliposomes. *Nat Commun* **7**, 13025 (2016).
80. Weiss, M., Frohnmayer, J. P., Benk, L. T., Haller, B., Janiesch, J.-W., Heitkamp, T., Börsch, M., Lira, R. B., Dimova, R., Lipowsky, R., Bodenschatz, E., Baret, J.-C., Vidakovic-Koch, T., Sundmacher, K., Platzman, I. & Spatz, J. P. Sequential bottom-up assembly of mechanically stabilized synthetic cells by microfluidics. *Nat Mater* **17**, 89–96 (2018).
81. Bamann, C., Bamberg, E., Wachtveitl, J. & Glaubitz, C. Proteorhodopsin. *Biochimica et Biophysica Acta (BBA) - Bioenergetics* **1837**, 614–625 (2014).

82. Miller, T. E., Beneyton, T., Schwander, T., Diehl, C., Girault, M., McLean, R., Chotel, T., Claus, P., Cortina, N. S., Baret, J.-C. & Erb, T. J. Light-powered CO 2 fixation in a chloroplast mimic with natural and synthetic parts. *Science (1979)* **368**, 649–654 (2020).
83. McKellar, I. R. C., Charles, A. M. & Butler, B. J. Some properties of adenylate kinase from chemolithotrophically grown Thiobacillus novellus. *Arch Microbiol* **124–124**, 275–284 (1980).
84. Jia, Y. & Li, J. Reconstitution of FoF1-ATPase-based biomimetic systems. *Nat Rev Chem* **3**, 361–374 (2019).
85. Itoh, H., Takahashi, A., Adachi, K., Noji, H., Yasuda, R., Yoshida, M. & Kinosita, K. Mechanically driven ATP synthesis by F1-ATPase. *Nature* **427**, 465–468 (2004).
86. Rögner, M., Ohno, K., Hamamoto, T., Sone, N. & Kagawa, Y. Net ATP synthesis in H+-ATPase macroliposomes by an external electric field. *Biochem Biophys Res Commun* **91**, 362–367 (1979).
87. Steinberg-Yfrach, G., Rigaud, J.-L., Durantini, E. N., Moore, A. L., Gust, D. & Moore, T. A. Light-driven production of ATP catalysed by F0F1-ATP synthase in an artificial photosynthetic membrane. *Nature* **392**, 479–482 (1998).
88. Choi, H.-J. & Montemagno, C. D. Artificial Organelle: ATP Synthesis from Cellular Mimetic Polymersomes. *Nano Lett* **5**, 2538–2542 (2005).
89. Pyrkova, D. v., Tarasova, N. K., Pyrkov, T. v., Krylov, N. A. & Efremov, R. G. Atomic-scale lateral heterogeneity and dynamics of two-component lipid bilayers composed of saturated and unsaturated phosphatidylcholines. *Soft Matter* **7**, 2569 (2011).
90. Dickey, A. & Faller, R. Examining the Contributions of Lipid Shape and Headgroup Charge on Bilayer Behavior. *Biophys J* **95**, 2636–2646 (2008).
91. Xu, Y., Fei, J., Li, G., Yuan, T., Li, Y., Wang, C., Li, X. & Li, J. Enhanced Photophosphorylation of a Chloroplast-Entrapping Long-Lived Photoacid. *Angewandte Chemie International Edition* **56**, 12903–12907 (2017).
92. Béjà, O., Aravind, L., Koonin, E. v., Suzuki, M. T., Hadd, A., Nguyen, L. P., Jovanovich, S. B., Gates, C. M., Feldman, R. A., Spudich, J. L., Spudich, E. N. & DeLong, E. F. Bacterial Rhodopsin: Evidence for a New Type of Phototrophy in the Sea. *Science (1979)* **289**, 1902–1906 (2000).
93. Ishmukhametov, R. R., Galkin, M. A. & Vik, S. B. Ultrafast purification and reconstitution of His-tagged cysteine-less Escherichia coli F1Fo ATP synthase. *Biochimica et Biophysica Acta (BBA) - Bioenergetics* **1706**, 110–116 (2005).
94. Senior, A. E. The Proton-Translocating ATPase of Escherichia Coli. *Annu Rev Biophys Biophys Chem* **19**, 7–41 (1990).
95. Chae, P. S., Rasmussen, S. G. F., Rana, R. R., Gotfryd, K., Chandra, R., Goren, M. A., Kruse, A. C., Nurva, S., Loland, C. J., Pierre, Y., Drew, D., Popot, J.-L., Picot, D., Fox, B. G., Guan, L., Gether, U., Byrne, B., Kobilka, B. & Gellman, S. H. Maltose–neopentyl glycol (MNG) amphiphiles for solubilization, stabilization and crystallization of membrane proteins. *Nat Methods* **7**, 1003–1008 (2010).
96. Stetsenko, A. & Guskov, A. An Overview of the Top Ten Detergents Used for Membrane Protein Crystallization. *Crystals (Basel)* **7**, 197 (2017).
97. Slotboom, D. J., Duurkens, R. H., Olieman, K. & Erkens, G. B. Static light scattering to characterize membrane proteins in detergent solution. *Methods* **46**, 73–82 (2008).

98. Lorber, B., Bishop, J. B. & DeLucas, L. J. Purification of octyl β-d-glucopyranoside and re-estimation of its micellar size. *Biochimica et Biophysica Acta (BBA) - Biomembranes* **1023**, 254–265 (1990).
99. Sohlenkamp, C. & Geiger, O. Bacterial membrane lipids: diversity in structures and pathways. *FEMS Microbiol Rev* **40**, 133–159 (2016).
100. Su, Z., Brown, E. C., Wang, W. & MacKinnon, R. Novel cell-free high-throughput screening method for pharmacological tools targeting K^+ channels. *Proceedings of the National Academy of Sciences* **113**, 5748–5753 (2016).
101. Pitard, B., Richard, P., Duñach, M. & Rigaud, J. ATP Synthesis by the F0F1 ATP Synthase from Thermophilic Bacillus PS3 Reconstituted into Liposomes with Bacteriorhodopsin. *Eur J Biochem* **235**, 779–788 (1996).
102. Rigaud, J.-L., Chami, M., Lambert, O., Levy, D. & Ranck, J.-L. Use of detergents in two-dimensional crystallization of membrane proteins. *Biochimica et Biophysica Acta (BBA) - Biomembranes* **1508**, 112–128 (2000).
103. Shastri, S., Vonck, J., Pfleger, N., Haase, W., Kuehlbrandt, W. & Glaubitz, C. Proteorhodopsin: Characterisation of 2D crystals by electron microscopy and solid state NMR. *Biochimica et Biophysica Acta (BBA) - Biomembranes* **1768**, 3012–3019 (2007).
104. Wiedenmann, A., Dimroth, P. & von Ballmoos, C. Δψ and ΔpH are equivalent driving forces for proton transport through isolated F0 complexes of ATP synthases. *Biochimica et Biophysica Acta (BBA) - Bioenergetics* **1777**, 1301–1310 (2008).
105. Tunuguntla, R., Bangar, M., Kim, K., Stroeve, P., Ajo-Franklin, C. M. & Noy, A. Lipid Bilayer Composition Can Influence the Orientation of Proteorhodopsin in Artificial Membranes. *Biophys J* **105**, 1388–1396 (2013).
106. Stanley, P. E. & Williams, S. G. Use of the liquid scintillation spectrometer for determining adenosine triphosphate by the luciferase enzyme. *Anal Biochem* **29**, 381–392 (1969).
107. Arnold, S., Siemann, M., Scharnweber, K., Werner, M., Baumann, S. & Reuss, M. Kinetic modeling and simulation of in vitro transcription by phage T7 RNA polymerase. *Biotechnol Bioeng* **72**, 548–561 (2001).
108. Dyla, M., Terry, D. S., Kjaergaard, M., Sørensen, T. L.-M., Andersen, J. L., Andersen, J. P., Knudsen, C. R., Altman, R. B., Nissen, P. & Blanchard, S. C. Dynamics of P-type ATPase transport revealed by single-molecule FRET. *Nature* **551**, 346 (2017).
109. Yeagle, P. L. Cholesterol and the cell membrane. *Biochimica et Biophysica Acta (BBA) - Reviews on Biomembranes* **822**, 267–287 (1985).
110. Kaddah, S., Khreich, N., Kaddah, F., Charcosset, C. & Greige-Gerges, H. Cholesterol modulates the liposome membrane fluidity and permeability for a hydrophilic molecule. *Food and Chemical Toxicology* **113**, 40–48 (2018).
111. Arcisio-Miranda, M., Abdulkader, F., Brunaldi, K., Curi, R. & Procopio, J. Proton flux induced by free fatty acids across phospholipid bilayers: New evidences based on short-circuit measurements in planar lipid membranes. *Arch Biochem Biophys* **484**, 63–69 (2009).
112. Levitan, I., Singh, D. K. & Rosenhouse-Dantsker, A. Cholesterol binding to ion channels. *Front Physiol* **5**, (2014).

113. Pegg, D. E. Principles of Cryopreservation. in 39–57 (2007). doi:10.1007/978-1-59745-362-2_3.
114. Vagenende, V., Yap, M. G. S. & Trout, B. L. Mechanisms of Protein Stabilization and Prevention of Protein Aggregation by Glycerol. *Biochemistry* **48**, 11084–11096 (2009).
115. Booth, M. J., Schild, V. R., Graham, A. D., Olof, S. N. & Bayley, H. Light-activated communication in synthetic tissues. *Sci Adv* **2**, (2016).
116. Restrepo Schild, V., Booth, M. J., Box, S. J., Olof, S. N., Mahendran, K. R. & Bayley, H. Light-Patterned Current Generation in a Droplet Bilayer Array. *Sci Rep* **7**, 46585 (2017).
117. CHAMBERLIN, M., MCGRATH, J. & WASKELL, L. New RNA Polymerase from Escherichia coli infected with Bacteriophage T7. *Nature* **228**, 227–231 (1970).
118. Tunitskaya, V. L. & Kochetkov, S. N. Structural-functional analysis of bacteriophage T7 RNA polymerase. *Biochemistry (Moscow)* **67**, 1124–1135 (2002).
119. Cheetham, G. M. & Steitz, T. A. Insights into transcription: structure and function of single-subunit DNA-dependent RNA polymerases. *Curr Opin Struct Biol* **10**, 117–123 (2000).
120. Klement, J. F., Moorefiedl, M. B., Jorgensen, E., Brown, J. E., Risman, S. & McAllister, W. T. Discrimination between bacteriophage T3 and T7 promoters by the T3 and T7 RNA polymerases depends primarily upon a three base-pair region located 10 to 12 base-pairs upstream from the start site. *J Mol Biol* **215**, 21–29 (1990).
121. Pavco, P. A. & Steege, D. A. Characterization of elongating T7 and SP6 RNA polymerases and their response to a roadblock generated by a site-specific DNA binding protein. *Nucleic Acids Res* **19**, 4639–4646 (1991).
122. Paige, J. S., Wu, K. Y. & Jaffrey, S. R. RNA Mimics of Green Fluorescent Protein. *Science (1979)* **333**, 642–646 (2011).
123. Strack, R. L., Disney, M. D. & Jaffrey, S. R. A superfolding Spinach2 reveals the dynamic nature of trinucleotide repeat–containing RNA. *Nat Methods* **10**, 1219–1224 (2013).
124. Autour, A., Jeng, S. C. Y., Cawte, A. D., Abdolahzadeh, A., Galli, A., Panchapakesan, S. S. S., Rueda, D., Ryckelynck, M. & Unrau, P. J. Fluorogenic RNA Mango aptamers for imaging small non-coding RNAs in mammalian cells. *Nat Commun* **9**, 656 (2018).
125. Kim, H. & Jaffrey, S. R. A Fluorogenic RNA-Based Sensor Activated by Metabolite-Induced RNA Dimerization. *Cell Chem Biol* **26**, 1725-1731.e6 (2019).
126. Filonov, G. S., Moon, J. D., Svensen, N. & Jaffrey, S. R. Broccoli: Rapid Selection of an RNA Mimic of Green Fluorescent Protein by Fluorescence-Based Selection and Directed Evolution. *J Am Chem Soc* **136**, 16299–16308 (2014).
127. Chen, X., Zhang, D., Su, N., Bao, B., Xie, X., Zuo, F., Yang, L., Wang, H., Jiang, L., Lin, Q., Fang, M., Li, N., Hua, X., Chen, Z., Bao, C., Xu, J., Du, W., Zhang, L., Zhao, Y., *et al.* Visualizing RNA dynamics in live cells with bright and stable fluorescent RNAs. *Nat Biotechnol* 1–7 (2019) doi:10.1038/s41587-019-0249-1.
128. Filonov, G. S. & Jaffrey, S. R. RNA Imaging with Dimeric Broccoli in Live Bacterial and Mammalian Cells. *Curr Protoc Chem Biol* **8**, 1–28 (2016).

129. Filonov, G. S., Kam, C. W., Song, W. & Jaffrey, S. R. In-Gel Imaging of RNA Processing Using Broccoli Reveals Optimal Aptamer Expression Strategies. *Chem Biol* **22**, 649–660 (2015).
130. Iwata, M., Izawa, M., Sasaki, N., Nagumo, Y., Sasabe, H. & Hayashizaki, Y. T7 RNA polymerase activation and improvement of the transcriptional sequencing by polyamines. *Bioorg Med Chem* **8**, 2185–2194 (2000).
131. King, G. C., Martin, C. T., Thang T. Pham & Coleman, J. E. Transcription by T7 RNA polymerase is not zinc-dependent and is abolished on amidomethylation of cysteine-347. *Biochemistry* **25**, 36–40 (1986).
132. Brunelle, J. L. & Green, R. In Vitro Transcription from Plasmid or PCR-amplified DNA. in 101–114 (2013). doi:10.1016/B978-0-12-420037-1.00005-1.
133. Milligan, J. F. & Uhlenbeck, O. C. [5] Synthesis of small RNAs using T7 RNA polymerase. *Methods Enzymol* **180**, 51–62 (1989).
134. Kartje, Z. J., Janis, H. I., Mukhopadhyay, S. & Gagnon, K. T. Revisiting T7 RNA polymerase transcription in vitro with the Broccoli RNA aptamer as a simplified real-time fluorescent reporter. *Journal of Biological Chemistry* **296**, 100175 (2021).
135. Cavac, E., Ramírez-Tapia, L. E. & Martin, C. T. High-salt transcription of DNA cotethered with T7 RNA polymerase to beads generates increased yields of highly pure RNA. *Journal of Biological Chemistry* **297**, 100999 (2021).
136. Tahirov, T. H., Temiakov, D., Anikin, M., Patlan, V., McAllister, W. T., Vassylyev, D. G. & Yokoyama, S. Structure of a T7 RNA polymerase elongation complex at 2.9 Å resolution. *Nature* **420**, 43–50 (2002).
137. Stevens, R., Stevens, L. & Price, N. The stabilities of various thiol compounds used in protein purifications. *Biochem Educ* **11**, 70 (1983).
138. Bowler, M. W., Montgomery, M. G., Leslie, A. G. W. & Walker, J. E. How azide inhibits ATP hydrolysis by the F-ATPases. *Proceedings of the National Academy of Sciences* **103**, 8646–8649 (2006).
139. de Gennes, P. G. Polymers at an interface; a simplified view. *Adv Colloid Interface Sci* **27**, 189–209 (1987).
140. Karatekin, E. & Rothman, J. E. Fusion of single proteoliposomes with planar, cushioned bilayers in microfluidic flow cells. *Nat Protoc* **7**, 903–920 (2012).
141. Paredes, R. M., Etzler, J. C., Watts, L. T., Zheng, W. & Lechleiter, J. D. Chemical calcium indicators. *Methods* **46**, 143–151 (2008).
142. Li, X., Kim, H., Litke, J. L., Wu, J. & Jaffrey, S. R. Fluorophore-Promoted RNA Folding and Photostability Enables Imaging of Single Broccoli-Tagged mRNAs in Live Mammalian Cells. *Angewandte Chemie International Edition* (2020) doi:10.1002/anie.201914576.
143. Song, W., Strack, R. L., Svensen, N. & Jaffrey, S. R. Plug-and-Play Fluorophores Extend the Spectral Properties of Spinach. *J Am Chem Soc* **136**, 1198–1201 (2014).
144. Grosberg, R. K. & Strathmann, R. R. The Evolution of Multicellularity: A Minor Major Transition? *Annu Rev Ecol Evol Syst* **38**, 621–654 (2007).
145. Bell, G. & Mooers, A. O. Size and complexity among multicellular organisms. *Biological Journal of the Linnean Society* **60**, 345–363 (1997).
146. Trivio, A., de Hoz, R., Rojas, B., Gallego, B. I., Ramrez, A. I., Salazar, J. J. & Ramrez, J. M. Effects of Hypercholesterolaemia in the Retina. in *Ocular Diseases* (InTech, 2012). doi:10.5772/48359.

147. Coulombe, P. A., Hutton, M. E., Vassar, R. & Fuchs, E. A function for keratins and a common thread among different types of epidermolysis bullosa simplex diseases. *Journal of Cell Biology* **115**, 1661–1674 (1991).
148. Amodeo, A. A. & Skotheim, J. M. Cell-Size Control. *Cold Spring Harb Perspect Biol* **8**, a019083 (2016).
149. Elani, Y., Law, R. v. & Ces, O. Vesicle-based artificial cells as chemical microreactors with spatially segregated reaction pathways. *Nat Commun* **5**, 5305 (2014).
150. Song, L., Hobaugh, M. R., Shustak, C., Cheley, S., Bayley, H. & Gouaux, J. E. Structure of Staphylococcal α-Hemolysin, a Heptameric Transmembrane Pore. *Science (1979)* **274**, 1859–1865 (1996).
151. Hildebrand, A., Pohl, M. & Bhakdi, S. Staphylococcus aureus alpha-toxin. Dual mechanism of binding to target cells. *J Biol Chem* **266**, 17195–200 (1991).
152. Virreira Winter, S., Zychlinsky, A. & Bardoel, B. W. Genome-wide CRISPR screen reveals novel host factors required for Staphylococcus aureus α-hemolysin-mediated toxicity. *Sci Rep* **6**, 24242 (2016).
153. Maglia, G., Restrepo, M. R., Mikhailova, E. & Bayley, H. Enhanced translocation of single DNA molecules through -hemolysin nanopores by manipulation of internal charge. *Proceedings of the National Academy of Sciences* **105**, 19720–19725 (2008).
154. Clarke, J., Wu, H.-C., Jayasinghe, L., Patel, A., Reid, S. & Bayley, H. Continuous base identification for single-molecule nanopore DNA sequencing. *Nat Nanotechnol* **4**, 265–270 (2009).
155. van Meer, G., Voelker, D. R. & Feigenson, G. W. Membrane lipids: where they are and how they behave. *Nat Rev Mol Cell Biol* **9**, 112–124 (2008).
156. Doherty, G. P., Bailey, K. & Lewis, P. J. Stage-specific fluorescence intensity of GFP and mCherry during sporulation In Bacillus Subtilis. *BMC Res Notes* **3**, 303 (2010).
157. Osumi-Davis, P. A., Sreerama, N., Volkin, D. B., Middaugh, C. R., Woody, R. W. & Woody, A.-Y. M. Bacteriophage T7 RNA Polymerase and Its Active-site Mutants. *J Mol Biol* **237**, 5–19 (1994).
158. Avnir, Y. & Barenholz, Y. pH determination by pyranine: Medium-related artifacts and their correction. *Anal Biochem* **347**, 34–41 (2005).
159. Booth, M. J., Schild, V. R., Box, S. J. & Bayley, H. Light-patterning of synthetic tissues with single droplet resolution. *Sci Rep* **7**, 9315 (2017).
160. Olejniczak, J., Carling, C.-J. & Almutairi, A. Photocontrolled release using one-photon absorption of visible or NIR light. *Journal of Controlled Release* **219**, 18–30 (2015).
161. Hoskin, C. E. G., Schild, V. R., Vinals, J. & Bayley, H. Parallel transmission in a synthetic nerve. *Nat Chem* (2022) doi:10.1038/s41557-022-00916-1.
162. Xie, J., Bi, Y., Zhang, H., Dong, S., Teng, L., Lee, R. J. & Yang, Z. Cell-Penetrating Peptides in Diagnosis and Treatment of Human Diseases: From Preclinical Research to Clinical Application. *Front Pharmacol* **11**, (2020).
163. Derakhshankhah, H. & Jafari, S. Cell penetrating peptides: A concise review with emphasis on biomedical applications. *Biomedicine & Pharmacotherapy* **108**, 1090–1096 (2018).
164. Coriat, R., Faivre, S., Mir, O., Dreyer, C., Ropert, S., Bouattour, M., Desjardins, R., Goldwasser, F. & Raymond, E. Pharmacokinetics and safety of DTS-108, a human

oligopeptide bound to SN-38 with an esterase-sensitive cross-linker in patients with advanced malignancies: a Phase I study. *Int J Nanomedicine* **Volume 11**, 6207–6216 (2016).
165. Chiquet, C., Aptel, F., Creuzot-Garcher, C., Berrod, J.-P., Kodjikian, L., Massin, P., Deloche, C., Perino, J., Kirwan, B.-A., de Brouwer, S., Combette, J.-M. & Behar-Cohen, F. Postoperative Ocular Inflammation: A Single Subconjunctival Injection of XG-102 Compared to Dexamethasone Drops in a Randomized Trial. *Am J Ophthalmol* **174**, 76–84 (2017).
166. Kang, Y. C., Son, M., Kang, S., Im, S., Piao, Y., Lim, K. S., Song, M.-Y., Park, K.-S., Kim, Y.-H. & Pak, Y. K. Cell-penetrating artificial mitochondria-targeting peptide-conjugated metallothionein 1A alleviates mitochondrial damage in Parkinson's disease models. *Exp Mol Med* **50**, 1–13 (2018).
167. Czajkowsky, D. M., Hotze, E. M., Shao, Z. & Tweten, R. K. Vertical collapse of a cytolysin prepore moves its transmembrane β-hairpins to the membrane. *EMBO J* **23**, 3206–3215 (2004).
168. Rees, D. C., Johnson, E. & Lewinson, O. ABC transporters: the power to change. *Nat Rev Mol Cell Biol* **10**, 218–227 (2009).
169. Cole, S. P. C. Multidrug Resistance Protein 1 (MRP1, ABCC1), a "Multitasking" ATP-binding Cassette (ABC) Transporter. *Journal of Biological Chemistry* **289**, 30880–30888 (2014).
170. Gu, R.-X., Corradi, V., Singh, G., Choudhury, H. G., Beis, K. & Tieleman, D. P. Conformational Changes of the Antibacterial Peptide ATP Binding Cassette Transporter McjD Revealed by Molecular Dynamics Simulations. *Biochemistry* **54**, 5989–5998 (2015).
171. Lipinski, C. A., Lombardo, F., Dominy, B. W. & Feeney, P. J. Experimental and computational approaches to estimate solubility and permeability in drug discovery and development settings 1PII of original article: S0169-409X(96)00423-1. The article was originally published in Advanced Drug Delivery Reviews 23 (1997) 3–25. 1. *Adv Drug Deliv Rev* **46**, 3–26 (2001).
172. Pedersen, B. P., Buch-Pedersen, M. J., Preben Morth, J., Palmgren, M. G. & Nissen, P. Crystal structure of the plasma membrane proton pump. *Nature* **450**, 1111–1114 (2007).
173. Skou, J. C. The Identification of the Sodium-Potassium Pump (Nobel Lecture). *Angewandte Chemie International Edition* **37**, 2320–2328 (1998).
174. Clarke, R. J., Catauro, M., Rasmussen, H. H. & Apell, H.-J. Quantitative calculation of the role of the Na+,K+-ATPase in thermogenesis. *Biochimica et Biophysica Acta (BBA) - Bioenergetics* **1827**, 1205–1212 (2013).
175. Vangheluwe, P., Sepúlveda, M. R., Missiaen, L., Raeymaekers, L., Wuytack, F. & Vanoevelen, J. Intracellular Ca2+ and Mn2+ Transport ATPases. *Chem Rev* **109**, 4733–4759 (2009).
176. Faxén, K., Andersen, J. L., Gourdon, P., Fedosova, N., Morth, J. P., Nissen, P. & Møller, J. V. Characterization of a Listeria monocytogenes Ca2+ Pump A SERCA-TYPE ATPase WITH ONLY ONE Ca2+-BINDING SITE. *Journal of Biological Chemistry* **286**, 1609–1617 (2011).
177. Croall, D. E. & Ersfeld, K. The calpains: modular designs and functional diversity. *Genome Biol* **8**, 218 (2007).

178. Maglia, G., Henricus, M., Wyss, R., Li, Q., Cheley, S. & Bayley, H. DNA Strands from Denatured Duplexes are Translocated through Engineered Protein Nanopores at Alkaline pH. *Nano Lett* **9**, 3831–3836 (2009).